Experimental Analysis of Disc Thickness Variation Development in Motor Vehicle Brakes

A thesis submitted in fulfilment of the requirements for the degree of

Doctor of Philosophy

Alexander J. Rodriguez

B. Eng.

School of Aerospace, Mechanical & Manufacturing Engineering (SAMME)

Science, Engineering and Technology (SET) Portfolio

RMIT University

December 2006

Declaration

I certify that except where due acknowledgement has been made, the work is that of the author alone; the work has not been submitted previously, in whole or in part, to qualify for any other academic award; the content of the thesis is the result of work which has been carried out since the official commencement date of the approved research program; and, any editorial work, paid or unpaid, carried out by a third party is acknowledged.

Alexander J. Rodriguez Date:

Acknowledgements

I would like to give my thanks to my two supervisors: Prof. Pavel Trivailo (RMIT University) and Dr. Jacek Skoraczynski (Holden Ltd) for their continued staunch support for this research program.

I would also like to thank Dr. Xi Huang (Holden Ltd) and Dr. Claire Davis (Air Vehicles Division, DSTO) for giving extra support and guidance during the experimental phase of the research program.

In addition, I would like to thank a number of companies and organizations for lending or giving various pieces of equipment and expertise to this project, namely: Holden Ltd, MMTC RMIT University, Bendix, PBR, Warsash Scientific, EEE Melbourne University and DSTO - without their support this research program could not have progressed experimentally, thank you.

I would also like to thank the great bunch of fellow postgraduates and staff from SAMME RMIT in particular I would like to thank: Dmitri Shmatkov, Duc Do, Behzad Nigjeh, Trenton Gilbert, Erica Abbot, Chris Blanksby, Sang-Wook Chu, Toh Yen Pang and Takeo Watanabe.

I would also like to thank my good friends Richard Murray and Leon Hunter for believing in my ability and continued moral support throughout the research program.

I would also like to thank the Lord for showing me the path to my salvation.

Finally, I would to thank my family and my loving wife Hong.

Abstract

Over the past decade vehicle judder caused by Disc Thickness Variation (DTV) has become of major concern to automobile manufacturers worldwide. Judder is usually perceived by the driver as minor to severe vibrations transferred through the chassis during braking [1–9].

In this research, DTV is investigated via the use of a Smart Brake Pad (SBP). The SBP is a tool that will enable engineers to better understand the processes which occur in the harsh and confined environment that exists between the brake pad and disc whilst braking. It is also a tool that will enable engineers to better understand the causes of DTV and stick-slip the initiators of low and high frequency vibration in motor vehicle brakes. Furthermore, the technology can equally be used to solve many other still remaining mysteries in automotive, aerospace, rail or anywhere where two surfaces may come in contact.

The SBP consists of sensors embedded into an automotive brake pad enabling it to measure pressure between the brake pad and disc whilst braking. The two sensor technologies investigated were Thick Film (TF) and Fibre Optic (FO) technologies. Each type was tested individually using a Material Testing System (MTS) at room and elevated temperatures. The chosen SBP was then successfully tested in simulated driving conditions.

A preliminary mathematical model was developed and tested for the TF sensor and a novel Finite Element Analysis (FEA) model for the FO sensor.

A new method called the Total Expected Error (TEE) method was also developed to simplify the sensor specification process to ensure consistent comparisons are made between sensors.

Most importantly, our achievement will lead to improved comfort levels for the motorist.

Contents

List of Figures

List of Tables

List of Acronyms and Abbreviations

AD	After (Christ's) Death. Alternatively, Common Era (CE).
ADINA	Automatic Dynamic Incremental Nonlinear Analysis
AODS	Animated Operational Deflection Shape
BC	Before Christ. Alternatively, Before Common Era (BCE).
BEM	Boundary Element Modelling
BLUERR	Blue Road Research
BLUERR-SP	Blue Road Research Smart Probe
BTV	Brake Torque Variation
CAD	Computer Aided Design. Also, Computer Assisted Drafting.
CAM	Computer Aided Manufacturing
CFD	Computational Fluid Dynamics
CNC	Computer Numerical Controlled
CW	Continuous-wave
DAQS	Data Acquisition System
DE	Differential Equation
DoF	Degrees of Freedom
X^{o} C	X Degrees Celsius. The present internationally acceptable way to write Degrees Celsius in symbolic form is, X ^{o}C, other variations are X^{o}C or X^{o} C.

DSTO Defence Science and Technology Organisation

DTC Discharge Time Constant

DTS Distributed Temperature Sensing

DTV Disc Thickness Variation

dyne dynamometer. Also known as a *dyno*.

E Modulus of Elasticity

EEE Department of Electrical and Electronic Engineering

EFPI Extrinsic Fabry Perot Interferometer

EM Electro-Magnetic

FBG Fibre Bragg Grating

FC Fibre Connector

FEA Finite Element Analysis

FDA Finite Difference Analysis

FO Fibre Optic

FOS Fibre Optic Sensor

F-P Fabry-Perot

FSR^{TM} Force Sensitive Resistor

FS Full ScaleThe FS is the largest useable range utilised by a device; such as a sensor. Please see Appendix B.

G-TF-DE-V General Thick Film Differential Equation for Voltage Output

G-TF-DE-R General Thick Film Differential Equation for Resistance Output

Hz Hertz

IMRC International Microelectronics Research Corporation

LoBF Line of Best Fit

LPSt Left Peak Strains

LPS Left Peak Shift

MEMS Micro Electro Mechanical Systems

MMTC Microelectronics and Materials Technology Centre

MPa Mega Pascals

MOIS Micron Optics Interrogation System

MTS Material Testing System. The term *MTS* is also a brand name of a company that manufactures Compression/Tensile Testing Machines (CTTM) or Material Testing Systems. MTS is used synonymously with CTTM by employees of structural testing laboratories; though the acronym *CTTM* itself would not be well known.

NAO Non-Asbestos Organic

Off-BW Off Brake Wear

On-BW On Brake Wear

OSA Optical Spectral Analyser

PCB Printed Circuit Board

PDE Partial Differential Equation

PVDF Polyvinylidene fluoride

PVF_2 Polyvinylidene difluoride

R Registered

RMIT Royal Melbourne Institute of Technology

RPS Right Peak Shift

RPSt Right Peak Strains

RSSE Root of Sum of Square Errors

RT Room Temperature

SAC	Senko Advanced Components
SAE	Sum of Absolute Errors
SAC-SP	Senko Advanced Components Smart Probe
SBP	Smart Brake Pad
SBP-dt	Smart Brake Pad diagnostics technology
SBPdt	SBP diagnostic technology
SBP-SDC	Smart Brake Pad Sensor Design Criteria
SCE	Scientific Computing Environments
SDC	Sensor Design Criteria
sig. figs.	significant figures
S-LDV	Scanning Laser Doppler Vibrometer
SP	Smart Probe
STF	Set Time Frame
ϵ_{n}	Normalised strain represents strain data that has been limited between selected bounds to aid in its analysis. It is ideally used between different sets where the upper and lower limits may be very different from test to test.
T/C	Thermocouple
TEE	Total Expected Error
TEI	Thermal Elastic Instability
TF	Thick Film
TFDH	Transfer Film Destruction Hypothesis
TIR	Total Internal Reflection
$_{TM}$	Trade Mark

VIW Vibration Induced Wear

VIWL Vibration Induced Wear Law . In order to create wear with the shape of a sinusoid or other waveform, we need an input from one or more external sources with the same shape and frequency. The frequency needs to be a summation or integer multiple of the base frequency of the *problem* vibration.

WDM Wavelength Division Multiplexing

wrt with respect to

Summary

In **Chapter 1** we set the scene for the project discussing: a preliminary literature review, locations where the project will be executed, scope, objectives and rational for the project which included: benefits to the community, scientific advancement and industry. We also included methods used to successfully reach our objectives; among these we included a simple flow chart of thesis structure.

In **Chapter 2** we conduct a full literature review which covers the latest research in the field of DTV development in motor vehicle brakes.

In **Chapter 3** we investigate and develop a SBP the technology that will enable us and others to pin point the root causes of DTV and other brake related problems into the future. In section 1 we introduced the concept of a SBP. In section 2 we developed a thorough set of specifications for a SBP to enable us to fulfil our objectives. In section 3 we conducted a review on applicable force measurement technologies to use with the SBP to enable us to match the specifications developed in section 2. In section 4 we investigated TF technology and in section 5 we investigated FO technology. FO technology was found to be the most suitable sensor for the SBP pad.

In **Chapter 4**, we conducted a test with a Scanning Laser Doppler Vibrometer (S-LDV) in the hope that it would more quickly enable us to answer the research questions in **Chapter 2**.

In **Chapter 5**, we showed the highlights from our successful SBP calibration and subsequent dynamometer tests.

Finally, in **Chapter 6**, we concluded the thesis and discussed recommendations and directions for future work.

Chapter 1

Thesis Introduction

1.1 Background

Over the past decade vehicle judder caused by DTV has become of major concern to automobile manufacturers worldwide. Judder is usually perceived by the driver as minor to severe vibrations transferred through the chassis during braking [1–9]. The judder phenomenon can be classified into two distinct subgroups; they are Hot (Thermal) or Cold Judder.

Hot judder is usually produced as a result of longer more moderate braking from high speed where the vehicle does not come to a complete stop [25]. It commonly occurs when a motorist decelerates from speeds of around 120-km/h to about 60-km/h, which results in severe vibrations being transmitted to the driver. These vibrations are the result of uneven thermal distributions believed to be the result of phenomena called Hot Spots. Hot Spots are classified as concentrated thermal regions that alternate between both sides of a disc that distort it in such a way that produces a sinusoidal waviness around its edges. Once the brake pads (friction material) comes in contact with the sinusoidal surface during braking severe vibrations are induced as a result and can produce hazardous conditions for the person driving the vehicle [13, 14, 26–28].

Cold judder on the other hand is the result of uneven disc wear patterns or DTV. These variations in the disc surface are usually the result of extensive vehicle road usage. DTV is usually attributed to the following causes; waviness of rotor surface, misalignment of axis (Runout), elastic deflection, thermal distortion, wear and friction material transfers [3, 27–29]. Whilst many institutions and companies are currently involved in research in this area there is very little published data on the DTV phenomenon as compared to

other such effects like squeal. This is probably due to judder having inherent complexities and the relative shortage of analytical models that can predict its behaviour satisfactorily. With a research program such as this, an experimental program would seem the logical, but essential step forward in furthering knowledge in this area.

1.2 Location

The candidate was based at SAMME for the majority of the project; however, periods were spent at DSTO and Holden Ltd Port Melbourne.

1.3 Scope

The scope of this research is to investigate the effects of DTV and its influence on low frequency (10−60 Hz) Rigid Body vibration commonly known as Brake Judder/Shudder [6, 8, 10]. This research will be limited to low frequency vibration.

1.4 Objectives

- To develop and test an experimental rig, system or method that will enable us to study DTV and the factors that may contribute to its development, such as: disc runout, contact pressure, dynamic braking conditions, temperature on disc surface, other disc surface conditions, driving styles etc.
- To come up with recommendations to develop these systems or methods towards assisting brake developers towards the minimization of brake judder and its effects in motor vehicles
- To develop analytical or empirical models of the systems or methods used
- To propose possible directions for future work

1.5 Rational

Car manufactures spend tens of millions of dollars annually on DTV related wear [30]. The rationale for this research program is to address the issue of DTV in automotive brakes.

Ultimately, this will improve the comfort and safety of the motorist whilst reducing the costs of the motor vehicles industry.

1.6 Research Questions

- Is it possible to measure contact pressure between brake pad and disc dynamically?
- How does the brake contact pressures effect DTV development in motor vehicle brakes?
- How do the experimental results compare to the analytical modelling of the brake pad and disc system?
- What measures are needed to minimise or eliminate DTV generation in motor vehicles disc brakes?

1.7 Schematic of Thesis Structure

Please see Figure 1.1 for a flow chart of the thesis structure.

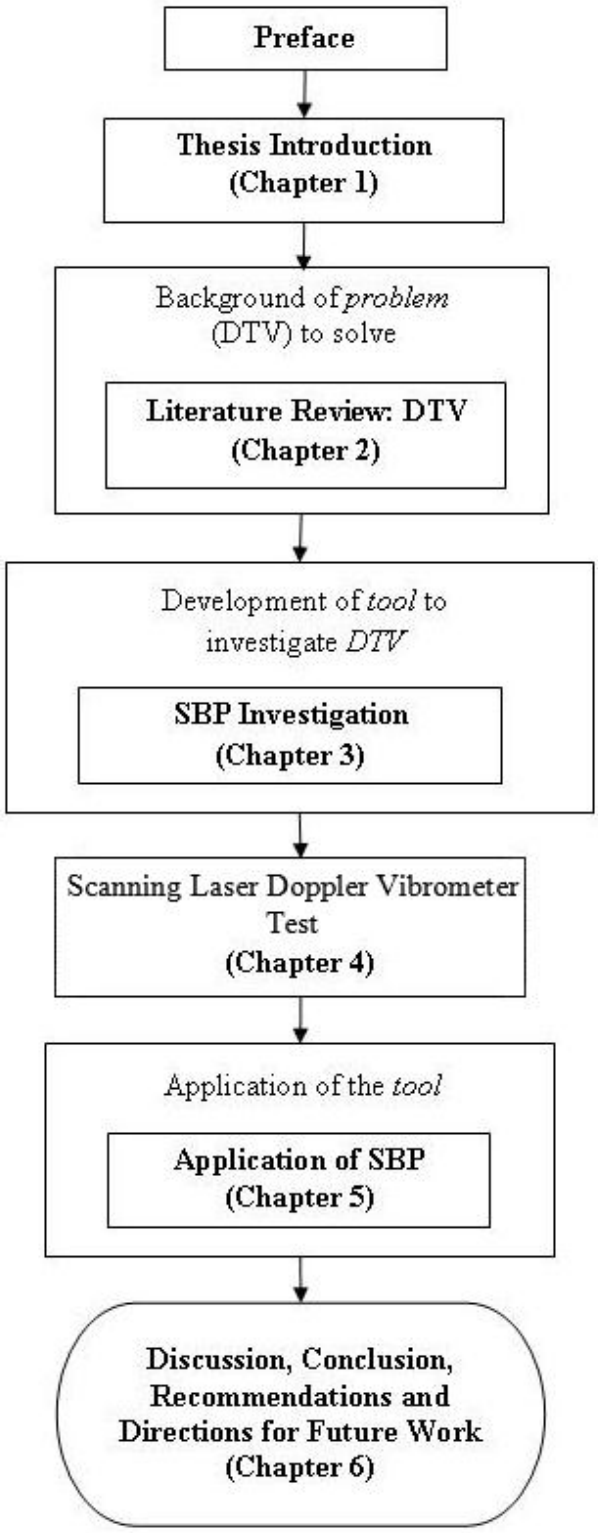

Figure 1.1: Thesis structure

1.8 Outcomes

1.8.1 Research Question Outcomes

- Using a SBP we are able to measure the contact pressure between brake pad and disc dynamically; this will enable us to gain a better understanding of DTV and other brake vibrations problems

- As a result of experimental work and experience gained through the research program we were able to suggest methods to minimise or eliminate the occupants' awareness of vibrations resulting from DTV

1.8.2 Publication and Scholarly Interactions

- Alexander Rodriguez, *Experimental Analysis of Disc Thickness Variation Development in Motor Vehicle Brakes - Project Highlights*, RMIT University, 2002

- Alexander Rodriguez, *Experimental Analysis of Disc Thickness Variation Development in Motor Vehicle Brakes - Update*, Sir Lawrence Wackett Centre for Aerospace Design Technology, RMIT University, Australia, 31-May-2001

- Alexander Rodriguez, *Experimental Analysis of Disc Thickness Variation Development in Motor Vehicle Brakes*, Sir Lawrence Wackett Centre for Aerospace Design Technology, RMIT University, Australia, 06-April-2000

1.8.3 Internal Reports

- Numerous (20+) in-house reports, presentations and discussions

Chapter 2

Literature Review: DTV

2.1 Introduction

In this Chapter we conduct a classical literature review on DTV by covering the following topics:

1. Classification of Vibrations in Automotive Brake Systems
2. Approaches used to study DTV
3. Causes: Excitation Mechanisms
4. Effects: Transfer Mechanisms
5. Disc and Friction Materials
6. Analytical Techniques

As a result of discussions of these topics a list of research questions will be formulated to investigate DTV; the answering of these questions will lead us to the causes of DTV and its possible solutions.

2.2 Classification of Vibration in Automotive Brake Systems

Vibration in an automotive brake system is usually categorized according to their dominant frequency measured in Hertz (Hz). Vibration ranges from low rigid body judder vibration; to high stick-slip self excited vibration (please refer to Figure 2.1).

As apposed to methods, here, we will continue to use phenomenological descriptions such as judder, squeal etc in the classification of vibrations within brake systems.

2.3 Approaches used to study DTV

The study of vibrations and the mechanisms that cause those vibrations are very complex in nature thus a number of different approaches have been formulated to assist researchers in the study of these phenomena, namely the:

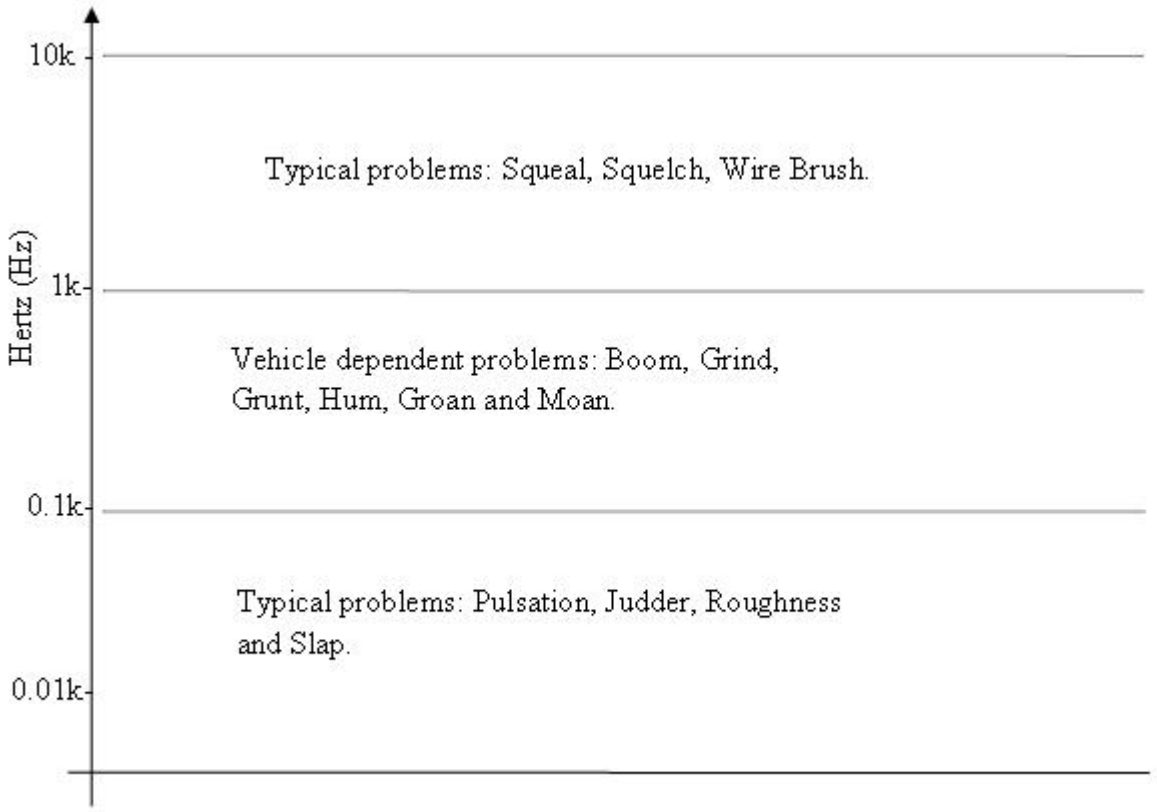

Figure 2.1: Range of brake noises and vibrations grouped by representative frequency [10]

- Cause
- Effect
- Systems, and
- Frequency Sweep Approaches

Examples and explanations of these approaches follow:

- The cause of a phenomenon called Thermal Elastic Instability (TEI)[1] is believed to be the result of brake disc material irregularities, such as high-spots. Studying high-spots would be an example of applying the cause approach to the understanding of TEI. A type of TEI is called a hotspot[2].
- An application of the effect approach would be to study the paths vibration takes from the source of the vibration, through the vehicle chassis, to the driver. Jacobsson [7] displayed graphically both the cause and effect approaches (please refer to Figure 2.2).

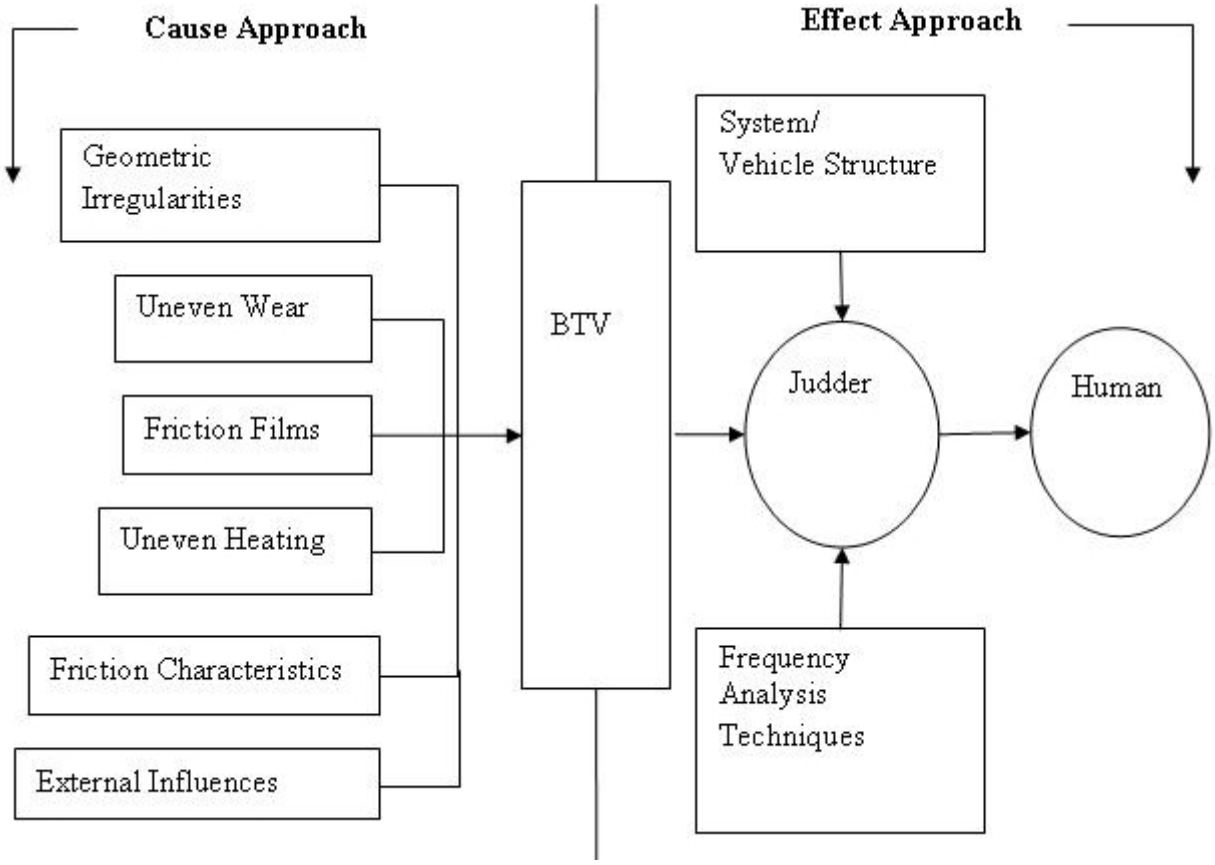

Figure 2.2: Jacobsson's Cause and Effect Approach [7]

- With the *systems* approach the vehicle is treated as one large system with several smaller subsystems. When applying the systems approach to a vehicle the idea is to systematically investigate the interactions between the subsystems. For example, Engel [3] applied the systems approach to the study of brake judder. In that investigation, Engel studied the interaction between the excitation and transfer mechanisms that caused brake judder.

The *systems* approach used by Engel can be considered an *effect* approach as it analyses the flow on effect of excitation but does not deal with the root cause of that vibration.

[1] TEI will be discussed later on page 13
[2] Hotspots will be discussed later on page 17

- The *frequency sweep* approach involves taking measurements whilst the wheel speed is changing. Normally, analyses and measurements are made of judder at a constant speed; brake line pressure and temperature to simplify analysis [7]. Jacobsson [7] also mentioned that Aviles [31] used this approach to study braking with constant deceleration.

The *frequency sweep* approach like the systems approach can be considered an *effect* approach. It can also be thought of as a sub-approach to be used within one of previously mentioned approaches.

Here the *cause* approach will be utilized, as it is believed that it is most important not to ignore the root cause of a problem by looking at its effect. Thus DTV will be analysed as a possible cause of cold judder.

2.4 Causes: Excitation Mechanisms

2.4.1 DTV

DTV is a variation in the thickness of a brake disc (please refer to Figure 2.3). The figure depicts two main cases of DTV:

1. A disc with one *thin spot*
2. A disc with two *thin spots*

These two main cases of DTV combined with different wheel diameters can produced vibration in the frequency range of between 10 and 60 Hz.

2.4.1.1 Classification of DTV

DTV related disc wear is normally classified according to how the wear was produced. In a automotive brake system the terms used are: Off Brake Wear (Off-BW) or On Brake Wear (On-BW) for when the wear was caused in either the *off* or *on* brake condition.

2.4.1.2 Mechanisms that can cause DTV

When brakes are applied onto a disc with runout On-BW it is believed to cause minimal wear, compared to the condition that is caused by Off-BW which is widely believed to be the cause of DTV and hence cold judder. Though research by industry and others indicates this is not necessarily true.

Off Brake Wear

Off-BW DTV generation is quite often referred to, as the only cause of uneven wear which leads to judder. The majority of tests procedures developed and technical papers presented are addressed towards this theory. The conditions and assumptions necessary to produce DTV by Off-BW are as follows:

- Discs are installed with a level of lateral runout; the amount of lateral runout varies from car to car and from design to design.
- The amount of calliper roll back is generally not enough to completely remove contact between friction material and disc whilst the brakes are in the off-brake condition.

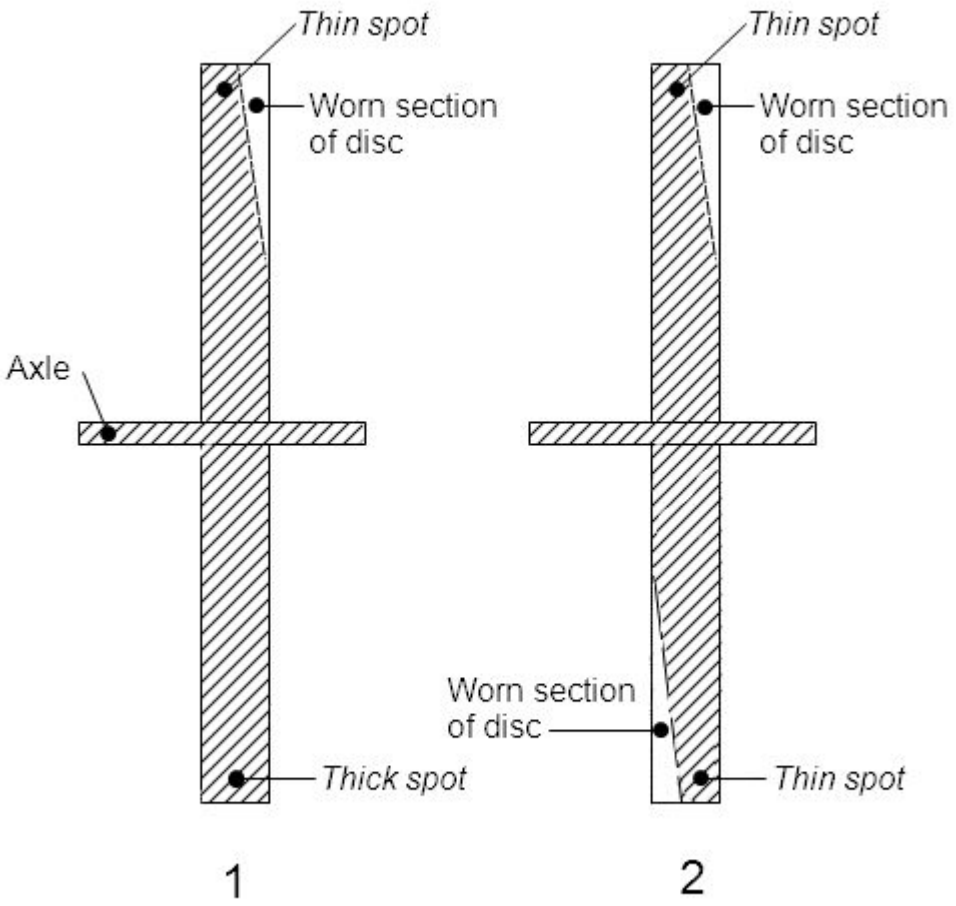

Figure 2.3: DTV

- Whilst the car is moving and the brakes are in the off-brake position, the disc comes in contact with the friction material at the highest point of lateral runout; the disc gets worn away in these areas.

The disc material at the highest points of lateral runout is gradually being removed, whereas, other areas of the disc are not in contact during these periods [32]. A variation on this is: "The rotor [disc] surface being worn away on the *rise of the hill* rather than the peak [33], p. 2." Evidence of both forms of wear patterns has been found to occur on seemingly identical brake systems, with no explanation available as to the different results. This rise of the hill wear could be linked to On-BW.

This is summarised in the following way:

- *Wear at peaks* leads to wear only occurring at peaks. Can happen on both sides of the disc, or just one producing two thin sections or just one. Alternatively,

- *Wear at rise of hill* occurs when the friction material comes in contact at an earlier part of the disc, just before the highest point of lateral runout [33].

The surface pressure between friction material and disc during the rise is greatest. This increase in pressure could be caused by dynamic slide force interactions which could be effected by calliper inertia and slide pin friction. Vries [2] confirmed these theories, he mentioned the importance of assuring clearance between pad and disc whilst the brakes are not applied to avoid causing DTV and if contact is made make it as uniform as possible [2].

On Brake Wear

When the friction material of the pads is in contact with the disc, the on-brake condition causes negligible uneven wear to the disc compared to the off-brake condition.

There is certainly documented evidence that the thin point of DTV wear does not always occur at the maximum runout position. As mentioned previously, sometimes the discs' thin point occurs on the *rise of the hill* [33].

Manufacturing and Installations Defects

During manufacture, casting and machining operations can result in a waviness of the disc surface that can lead to DTV [32]. Mistakes in installation procedures of wheels and bearings can also lead to the generation of DTV in discs of automotive brake systems [2].

2.4.1.3 Mechanisms that can reduce DTV or its Influence

Machine Tool Cleaning Theory

The pads can act as machine tools and clean the surface of the disc. This is accomplished via the following steps.

1. The calliper-pad assembly acts like a fixed set of disc machining tools.

2. As a thick section of the disc passes through the calliper-pad assembly the increased surface pressure generated increases the disc wear rate.

3. This localised ON-BW rate increase counteracts the DTV generation to some extent.

The length of time the friction material of the pads are exposed to the disc is critical in establishing if the ON-BW characteristics are capable of maintaining or reducing DTV levels [33].

Pad Compressibility Theory

The friction material can also affect the severity of any given level of DTV within a brake

system. This is classed as affecting the overall vehicle sensitivity or the amount of judder felt compared to the level of DTV.

A common theory relates to the compressibility of the friction material. A highly compressible (soft) friction material, in theory, will allow for a disc thickness change with less surface pressure increase and therefore less BTV [33].

Pad Friction Level versus Surface Pressure Theory

This theory relates the friction level versus surface pressure which affects the BTV. For example, a friction material, which increases its friction level with an increase in surface pressure, would exaggerate the DTV effect and have a high BTV for a given level of DTV [33].

2.4.1.4 Experimental Approaches used to Study DTV

A system developed by Gassmann [4] measured DTV dynamically via the use of non contact sensors. The sensors were mounted on the steering knuckle using a specially designed bracket. The bracket positioned the sensors so that the disc spun between them in an analogous manner to a brake calliper and pads, where the pads have been replaced with a fixed set of sensors; one on each side.

The system was tested in a street going vehicle in order to understand the actual forces affecting the steering knuckle and disc in the production of DTV. The data from the sensors led to a better understanding of the excitation mechanism of judder. In the same test, accelarometers were placed along the transfer path from the source (brake system), to the steering wheel which enabled a better understanding of the transfer mechanism of judder.

Using similar techniques, Stringham [9], carried out an experimental program. The aim of this program was to get a better understanding of the forces involved in braking and their role in the production of brake roughness (judder). This was achieved by developing two new measurement techniques. One measurement technique was able to measure DTV non-intrusively, like that of Gassmann [4]. The other sensor technique used a non-intrusive BTV technique. As a result of these advances in measurement, they were able to come up with the following conclusions:

- The disc BTV is a non-stationary function and its frequency content is a function of rotational speed.
- DTV increases linearly with increasing temperature.
- The disc BTV signature is dominated by first order (once per revolution) component and that DTV is the primary contributor.

Vehicle *brake roughness* is a resonant response characteristic, which is influenced by suspension and steering column resonances and the degree of roughness is associated with the resonance amplification factor.

Together with the work of others previously mentioned these conclusions indicate a link between rotational speed, BTV, and DTV. This also strengthens the belief that geometrical rather than frictional (stick-slip) is the phenomenon that creates DTV. It also indicates the link between DTV and temperature.

2.4.2 Thermo Elastic Instability

Barber [11] was one of the first to show experimentally the TEI process; he did this in two novel experiments (please see Figure 2.4).

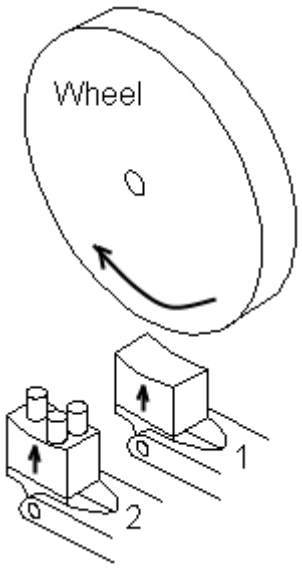

Figure 2.4: Barber's wheel & block rig [11]

In the first experiment a smooth cast iron block with a surface area of 25 mm^2 and with the same curvature as its mating wheel (please see Figure 2.4, block 1). The block via a lever mechanism (out of the figure) was able to apply a normal load of up to 1.472 kN. The sliding speed was variable from 5 to 35 m/s. Using this apparatus he showed that irregularities, such as highspots on the surface of the cast iron block caused the contact pressure to be non-uniform. These highspots (maxima) became hotter (*heating phase*) than the surrounding material causing them to expand at a greater rate, protrude further and wear more due to a greater exposure. In the *cooling phase* the once highspots become depressions (minima) in the surface of the material. It was also shown with the aid of thermocouples that these hotspots seem to move around the block every few seconds as a result of the decay (*cooling phase*) of the previous hotspots.

To investigate the TEI process further, Barber [11] devised a second experiment using three pins (please see Figure 2.4, No. 2). The idea was to simply show the cyclic nature of the process by which a once highspot decayed and transferred the load to another point on the surface every few seconds. The experiment was a success, he was able to show that initially one pin carried most of the load, then it would contract (due to the TEI process) leaving an air gap between the pin and the wheel; the load was then passed, in a matter of moments, to another pin and the cycle would continue. The limit to the cycle is when the wear rate exceeds the rate of expansion of the pins.

Empirical models were also produced to support this work.

Barber's [11] work gave us these important results:

- The concept of TEI
- Proof of the cyclic nature of TEI provided by the surface separation (three pins) experimental results
- Knowledge of possible limits to the TEI cycle, such as:
  - When the wear rate equals the rate of expansion
  - When the amount of heat input equals that of heat lost

- It is most likely that two surfaces that slide over each other with the absence of lubricant, such as: in automotive and railway brakes, would be most affected by the production of TEI
- TEI can be reduced or prevented by
  - Ensuring adequate lubrication between rubbing surfaces
  - Ensuring the rubbing surfaces have a low thermal conductivity
  - Have a high wear rate so that highspots are quickly removed preventing the development of the TEI process or
  - Have a very low wear rate so that all the load is effectively taken by one point

Barber [11] suggested the major assumption that underlies the TEI theory is that the wear process is continuous rather than the result of the removal of individual wear particles.

2.4.2.1 Effect of Temperature on Thermo Elastic Instability

Barber [25], studied the effect of constant deceleration and different stopping periods on thermal growth and TEI creation. When a vehicle is braking, rapid stops were found to give insufficient time for hotspots to develop, whereas with slow stops there was sufficient time for them to develop. For very slow stops, hotspots may be completely developed before any great reduction in speed has occurred. Barber [25] suggested that brakes be applied sequentially and for the pads to consist of a number of discrete elements rather than continuously with pads that have no discrete segments.

This result indicates that gently squeezing on the brakes from high speed provides enough time and sufficient heat to generate TEI.

This dependence of TEI on temperature was further supported by the work of Lee [34]. It was observed, that on the application of the brakes under drag brake conditions, it took five to ten minutes before TEI occurred. This was attributed to the dependence on pad temperature, since an increase in sliding time gives increased pad temperature.

2.4.2.2 Effect of Finite Disc Thickness on Thermo Elastic Instability

When modelling systems in the physical world it is desirable to limit the number of variables needed to describe them. Lee [12] represented a brake system as consisting of the following ideal geometry and conditions: A disc of finite (uniform) thickness, stationary half planes (brake pads), a disc simulating constant sliding velocity and brake pads applying a constant pressure. The model was represented in two dimensions.

Lee [12] used this model to investigate TEI; the focus was on what effect the finite uniform thickness would have on a theoretical model of a brake disc (please refer to Figure 2.5). The stationary half planes are pressed together by a uniform pressure and the disc, slides between them at a constant velocity V.

Using this model, the critical speed to develop TEI was estimated. However the results of the simulation were unrealistic. A major downfall of the model is the assumption of uniform pressure which disagrees with earlier research conducted by Barber [11].

One important result, from this theoretical analysis is the prediction of the mode of instability. Lee [12] was able to predict that the resulting unstable perturbation is anti-asymmetric and this matched what was found in practice by Thoms [13] (please refer to Figure 2.6).

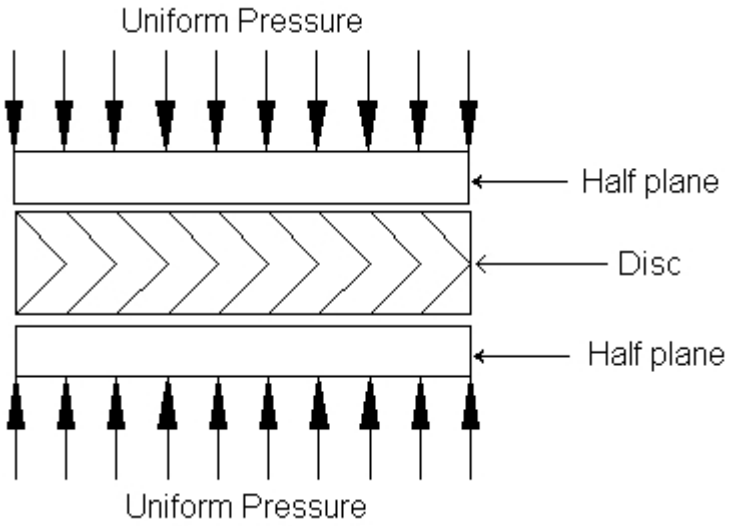

Figure 2.5: Lee's theoretical model of brake system [12]

Figure 2.6: Thoms' anti-symmetric mode [13]

Lee [15] later improved his earlier model by studying the effect of intermittent contact and TEI. This later research realistically simulated the critical speed for the development of TEI and thus confirming the relationship between non-uniform contact and the development of TEI.

2.4.2.3 Classification of Thermo Elastic Instability and Hotspots

Anderson [14] categorized hotspots into groups. Figure 2.7 illustrates common types of worn disc contact surface phenomena. In the figure, the types of hotspots are named: 1. Asperity, 2. Focal, 3. Band, 4. Distortional, 5. Regional and 6. Mixed. Figure 2.8 illustrates the surface characteristics of the accompanying friction material required to form each type of worn disc featured in Figure 2.7.

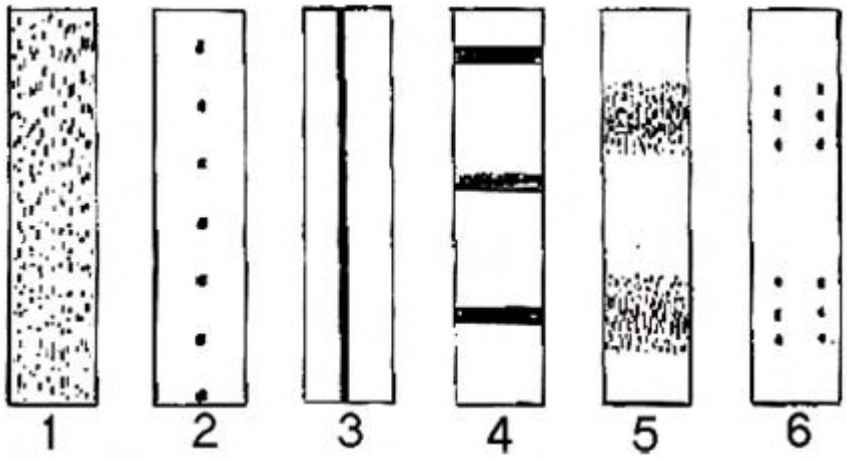

Figure 2.7: Worn disc contact surface phenomena [14]

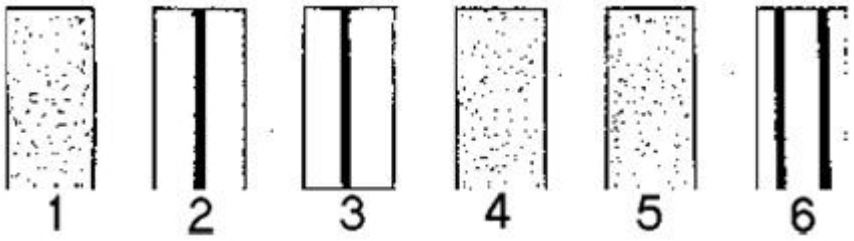

Figure 2.8: Worn friction material contact surface phenomena [14]

The descriptions of the types of hotspots and TEI follow:

1. Asperity hotspots have peak temperatures around 1000^{o} C and are brief, only lasting less than 1 millisecond in duration. Asperity hotspots affect the entire surface, however leave no marks once the brake is stopped and inspected. The only way of knowing that asperity marks were produced during a brake application is by the satin appearance left behind which is found on inspection as a result of the oxidization film they impart [14].

2. Focal hotspots are defined as small contact sites that are generated as a result of local TEI on a ferrous surface. Focal hotspots are usually generated in the same site

Table 2.1: Physical properties of hotspots [14]

Type	Width (mm)	Temp (C^o)	Duration (s)
Asperity	< 1	$\rightarrow$ 1200 peak	$< 0.001^a$
Focal	$5 - 20$	$750 - 1200$ peak	$0.5 - 20$
Distortional	$20 - 100$	$100 - 700\ \Delta T$	10
Regional	$50 - 200$	$10 - 100\ \Delta T$	10

[a]For cast iron only; pad asperities may have longer contact times.

repetitively at high speed, as a result witness marks tends to disappear as regional boundary markings are formed. Passenger vehicles brakes with short arcs of contact usually don't produce focal hotspots. Trucks where the arc of contact is larger may generate hotspots at high speed as more friction material is in contact with the disc surface. In truck brakes less time is available for the disc to cool between subsequent applications of the pad, thus more time is available for the growth of regions of TEI [14].

3. Band type TEI (also referred to as hot banding as previously discussed) often forms prior to the developed of focal hotspots. Figure 2.8 (No. 3) features a singular convex friction material surface that produces a singular rubbing track on the disc at low speeds when the speed increases focal hotspots form [14].

4. Distortional hotspots are a consequence of rubbing on a warped disc similar to that described by Thom's (please see Figure 2.5). Distortional hotspots are formed on the ridges or hills of such discs. The most common number of ridges and troughs is three. On rare occasions five may result from uneven tightening of wheel nuts [14].

5. Regional type TEI is the result of uneven contact pressure, metal thickness or non-linear friction characteristics of the material. They may also be the result of oval disc and drum brakes that have high lateral runout and thus form opposing pairs of regional hotspots. Regional hotspots typically affect about 10 % - 30% of the rubbing path and are usually singular [14].

6. Mixed type TEI may form as a result of a number of previously mentioned phenomena.

Focal hotspots are seen as the most commonly occurring hotspots. Anderson [14] concluded by saying that:

- Non-uniform contact is believed to be the precursor for hot spotting.
- An increase in highway speeds and a change from asbestos-based to non-asbestos-based materials is likely to increase the presence of TEI.

Anderson also said, that: "Until researchers are able to model complete frictional systems and experimentalists have catalogue values for the many required input conditions, an approach is suggested that combines both the computer model and system experiment [14], p. 337."

Anderson's [14] data featured in Table 2.1 is a useful guide to the physical descriptions of hotspots such as width, temperature and duration.

2.4.2.4 Mechanisms that can cause Hotspots

Just below the critical speed, areas of TEI occur and in time form bands around the disc. The pads during this time begin to heat up, expand and become convex. The temperature distribution around the disc circumference remains constant however, due to the shape of the pad the temperature at the center of the friction track is greatly increased. In time, this leads to hot banding [13, 15] (please refer to Figure 2.9).

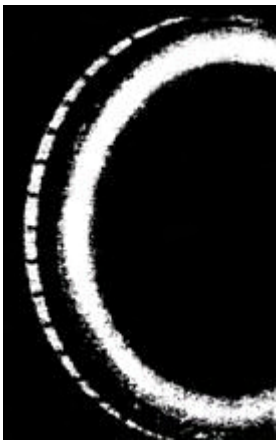

Figure 2.9: Thermal image of hot banding on a brake disc [15]

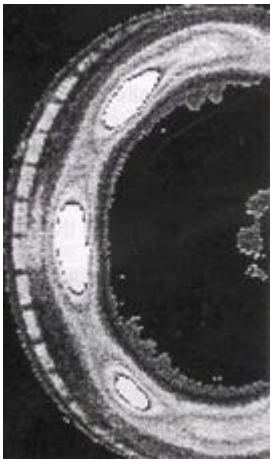

Figure 2.10: Thermal image of hot spotting on a brake disc [15]

On and just above the critical speed the thermal distributions become concentrated around a few different spots on the disc. The resulting phenomena are called hotspots (please refer to Figure 2.10).

2.4.2.5 Experimental Approaches used to Study Hotspots

Using an infrared camera, Abendroth [35] was able to show visually the temperature distribution of a brake disc whilst juddering with use of a de-rotator and thermal camera. Using this visualization technique, one is clearly able to see the outline of five or six hotspots more or less equally spaced around each face of each side of the disc's surface. Later, Lee [32], used high-speed thermal imaging techniques to capture images of hot banding and hot spotting whilst braking.

Using another technique, Inoue [26], developed a system using fibre optic cables to measure the thermal characteristics of a brake disc. The apparatus resulted in the production of key conclusions about the effects of high-speed judder and its cause. They were also able to confirm the anti-symmetric mode of hotspots and with the addition of FEA techniques they were able to show that the thermal deformation of the disc was two fold in action:

- Produced sinusoidal buckling of the disc
- Produced thickness variations in the rotational directions

With this key information they suggested an improved model for the design of the brake disc.

Thoms [13] confirmed through experimentation the various stages in the development of hotspots. Though, Thoms and Inoue [13, 26] separately had made the connection between hotspots and judder, Rhee [28] proposed a similar connection. This involved imagining a pad the length of two neighbouring hills on a disc surface (something similar to Figure 2.6), when the pad was in motion it would ride over the bumps causing (judder) vibration. Though, this was nothing new, Rhee added by saying that once vibration was initiated; this could cause other parts, such as, the callipers or discs to go into a state of resonance. This hints towards the transfer mechanism characteristics of the chassis.

2.4.3 Friction Material Films

When the temperature of a disc increases rapidly in a short amount of time the friction material film or glaze that tends to be present on pads can degrade. This degradation of the friction film can cause the pad material to transfer on to the brake disc at a very high rate producing DTV. On braking the resultant DTV can cause vibrations. This effect is sometimes referred to as the: "Transfer Film Destruction Hypothesis" TFDH [28], p. 4. For one group of researchers the TFDH did not fit their experimental results [28]. In the tests they conducted, noise and vibration occurred when the glaze was well established. The development of stable wear and friction occurred in the temperature range of $200 - 300^{o}$C.

Judder is known to occur as a result of moderate braking from high speed which gives time for TEI to occur, however this moderate braking causes a greater increase in temperature than rapid stops. Thus both TEI and transference of pad material could be occurring in some brake systems.

2.4.4 External Influences

Mostly, the source of judder has been attributed to internal causes of the disc brake system, such as hotspots formation and DTV and so on. However a number of authors have mentioned external causes may play an important role in the diagnosis of brake judder. Vries [2] found that the cause of brake judder does not always relate to the brake system but rather other components within the system. Previously this point has been hinted at by Rhee [28], it was mentioned that once hammering (vibration) was initiated this could cause other parts such as the calliper or the disc to vibrate and go into a state of resonance.

As a result, a number of researchers have moved away from dealing with the root cause of the brake judder problem and instead have concentrated their efforts on the transfer of the initial excitation of the brake system to minimise judder.

2.5 Effects: Transfer Mechanisms

2.5.1 Systems Approaches

Transfer of the initial excitation from a disc brake system through a vehicle was found to be a most important factor [2]. Others have hinted at the amplification and transfer path as the direction towards a solution for brake judder.

Using a systems approach, Engel [3] made a couple of recommendations to reduce judder. The first recommendation was to decrease judder by minimising DTV and lateral runout. The second one was to optimize the vibration transfer. This could be achieved by:

- Shifting the eigenfrequencies above the 1st order wheel excitation.
- Insuring modal separation of eigenfrequencies of components in the transfer path, particularly if the previous frequency targets cannot be met due to other constraints.

Here, Engel [3] suggested that by changing the stiffness of the bushings, the natural frequency of the suspension can be altered; however this can lead to poor performance of the suspension system and thus provide the passenger with poorer ride qualities.

Using statistical methods Kim [29] like Engel [3] found that the suspension system was the key to the reduction of judder. A main influencing factor in the generation of judder was believed to be the swaying of the vehicle in a backward and forwards motion due to the inertia of the vehicle and the performance of the suspension system. During driving to avoid brake judder initiated resonance of the suspension system, they suggested shifting the eigenfrequencies of the suspension system to a higher frequency. To achieve this they postulated that the stiffness of the lower control arm bushing should be changed. As a result of changing the stiffness of the bushing by 50% in the radial direction, their simulations suggest that a 5 Hz shift in eigenfrequencies of the suspension vibrational mode is achievable, however this would have to be a vehicle dependent assumption as has been mentioned by literature and industry.

We already know that the range of vibration for judder to occur is typically between 10 and 60 Hz and is termed low frequency vibration. Thus resonance between that of the excitation mechanism and chassis must occur within this range. When a brake system passes through the critical speed, about 95 km/h depending on vehicle, the natural frequency of the suspension has been found to be approximately 14 Hz [6]. On the other hand, the excitation, which occurs within the disc brake system, also, occurs within this range; hence the possibility of resonance between the braking system and suspension. Previously, Engel and Kim [3, 29] separately noted this. Steering wheel torque responses have also been found to contain between 10 and 15 Hz peak responses, thus giving another path of vibration amplification and transfer [36].

2.5.2 Frequency Approaches

The importance of speed in hot judder is evident from previous sections; however, it is also important in the area of cold judder.

Cold judder seems to be the result of runout initiated DTV; the reason is that the frequency of vibration at the critical speed is a multiple of wheel speed. Runout induced DTV with one thin section, would produce one pulse response per revolution. If the disc has two thinner sections, the frequency would be double; whereas, vibration as the result of hotspots, would produce about $4-5$ pulses per revolution equating to a higher frequency

and eliminating it as a cause of DTV - this is also supported by research conducted by Lee [10].

Different researchers have conducted modelling of the critical speed. Oscillations produced in the engagement of clutches has been shown by Balakin and Jacobsson [5, 37]. Similar oscillations are produced in automotive brake systems and were shown to grow dramatically when the wheel passed through the critical speed. Later, Jacobsson [7] conducted an analytical and an experimental study and developed a function that describes the variation in vibration amplitude with time. The results of the experiments found that shapes of the theoretically generated amplitude functions were very close to those measured, the eigenfrequencies of the brake system for all three tests conducted, were found to be around 13.8 Hz which falls in the range of judder frequencies.

2.6 Disc and Friction Materials

Around the 1960's disc brakes were introduced into motor vehicles. They were mainly constructed of grey cast iron discs and pads with asbestos friction material. Even today, grey cast iron is still being used. What has changed in that time is the ingredients and machining processes used to manufacture modern discs. Asbestos friction material has been abandoned in most parts of the world since the asbestos contained within the pad can cause a fatal lung disease called asbestosis.

Earlier disc materials *GG25* that were tried consisted of high modulus iron with chromium, nickel and molybdenum. This configuration of material properties led to the development of a grey cast iron disc with excellent wear properties. The material was a poor conductor of heat and hence hotspots formed as the heat was unable to dissipate quickly enough. Later, other cast iron materials such as *GG15* were designed to provide high thermal conductivity and the ability to withstand heating and cooling cycles. The material has also reduced hot spotting, thermal stress and no carbide formation [38]. Today, cast iron discs are still widely used and it is only in the last couple of years that carbon fibre discs and their derivatives are being used for high performance motor vehicles, particularly in racing however, at a substantial cost. For example, in 1998 Porsche joined forces with SGL Technologies to produce a carbon-ceramic disc for the Porsche 911 C4s [39]. SGL Technologies describe the carbon-ceramic disc as: "Carbon-ceramic is a ceramic composite material, composed of carbon fiber [fibre] within a silicon carbide matrix; so-called carbon fiber [fibre] reinforced silicon carbide (C/SiC) [39]." These discs are not affected by hot judder, though a set of such discs and pads for a high performance car such as a Porsche cost between (US) $17 000 and $20 000 [40] which puts it out of the range even for a large family car.

Since the use of asbestos based pads in conventional braking systems subsided, the problems of hot spotting had more or less diminished due to the advances in both the friction and disc materials. Nevertheless, the introduction of environmentally friendly organic friction material has caused a re-emergence of hot spotting and judder.

Non-Asbestos Organic (NAO) friction material has caused the re-emergence of hot judder due to the inconsistency of the microstructure of the material. NAO friction material has much lower thermal conductivity compared to semi-metallic pads. As a result more heat is transferred into the disc during braking, aiding in the initiation of TEI.

High conductivity of the friction material can lead to other problems. Lee [32] indicated that if the thermal conductivity of a friction material is increased, the heat will be transferred away from the disc towards the brake system. Too much heat transferred to the brake system will result in such problems as boiling of the brake fluid which can cause

brakes to fail. On the other hand, if too much heat is reflected into the disc, problems such as TEI may result.

To counter these conflicting desires indicated by Lee [32] brake designers have introduced innovations such as ventilated and cross drilled discs especially on the front of vehicle's where the majority of vehicles forward momentum is translated into heat. These types of improvements allow brake designers to have pads with friction material with low conductivities and any excess heat is dissipated from the disc through the rotation of the wheel during driving.

2.7 Analytical Techniques

Hohmann [41] use the ADINA FEA[1] package to analyse the contact conditions that may occur as a result of a stick-slip motion in an automotive disc brake system. The paper shows stress distributions of the friction material-calliper interface. These pressure distributions of the contact area, are believed to be particularly important in the study of DTV [42]. Stringham and later Suzuki [9, 43] believed that contact pressure distributions are important for the study of stick-slip vibration. It is mentioned in a paper by Jacobsson [8] that the level of BTV cannot be controlled during a brake stop as the instantaneous temperature and pressure on the brake disc during a brake application affect the level.

Hohmann [41], also suggests that the ADINA packages is capable of heat transfer and elastic-mechanical calculations, this would be particularly helpful when studying the effects of TEI and hotspots on the discs surface.

2.8 Discussion and Conclusion

- Literature Review: DTV -

Much of the literature focuses on the transfer of vibrations and its mechanisms rather than its excitation mechanisms. It seems likely that the cause of DTV lay between the brake-calliper and disc. On the one hand we have DTV and on the other we have TEI, hotspots and thermal buckling of the disc as illustrated by Thoms (please see Figure 2.6).

Though, traditionally, DTV is thought of as a cold wear problem, Stringham [9], showed that DTV linearly increases with increasing temperature. Stringham [9] also concluded that BTV is a function of wheel speed. Since BTV is a variation in torque, the most likely way to get a variation of torque is if there is an interaction between applied brakes and disc assuming that all other components are in adequate condition. Stringham [9] as a result of these experiments inferred that there was a relationship between BTV and DTV; Lee [10] also agrees with these inferences.

Apart from the mechanisms that can cause DTV there were a number of theories that are thought to reduce DTV, among these the *Pad Friction Level versus Surface Pressure Theory.* This theory seems quite plausible since if you have a sanding block and you apply a greater pressure you would expect to remove more material from the surface. However, if the pressure was too great you may lessen the effectiveness (crush) the grit or cause it to shear off and thus reduce the effectiveness of the material removal.

In conclusion, it seems there are many people investigating the transfer mechanisms of judder. However, there are a fewer number of people investigating what is actually occurring between brake pad and disc. As a result of this we believe the following questions need to be answered in order to get closer to the root cause of DTV and its solution:

- Is it possible to measure contact pressure between pad and disc dynamically?

[1] See Appendix A, for: "A brief Introduction to Analytical Techniques."

- How does the brake contact pressures effect DTV development in motor vehicle brakes?
- How do the experimental results compare to the analytical modelling of the brake pad and disc system?
- What measures are needed to minimise or eliminate DTV generation in motor vehicles disc brakes?

In the next Chapter, we investigate and develop a SBP as the technology that will enable us to measure the contact pressure between brake pad and disc. Thereby in time, enable us to answer all of the research questions posed above and more.

Chapter 3

Smart Brake Pad Investigation

3.1 Introduction

A SBP is a brake pad with sensors embedded into it. Here we investigate the development of a SBP by reviewing, selecting and testing different force sensing technologies.

To achieve this aim, we will cover the following topics:

1. Smart Brake Pad Sensor Design Criteria
2. Review of Force Measurement Technologies
3. Thick Film Investigation
4. Fibre Optic Investigation

In the next section we develop the Smart Brake Pad Sensor Design Criteria (SBP-SDC). The SBP-SDC will assist us in choosing the best force measurement technology to drive the SBP. Figures 3.1 and 3.2 illustrate the force measurement options that we have available to us.

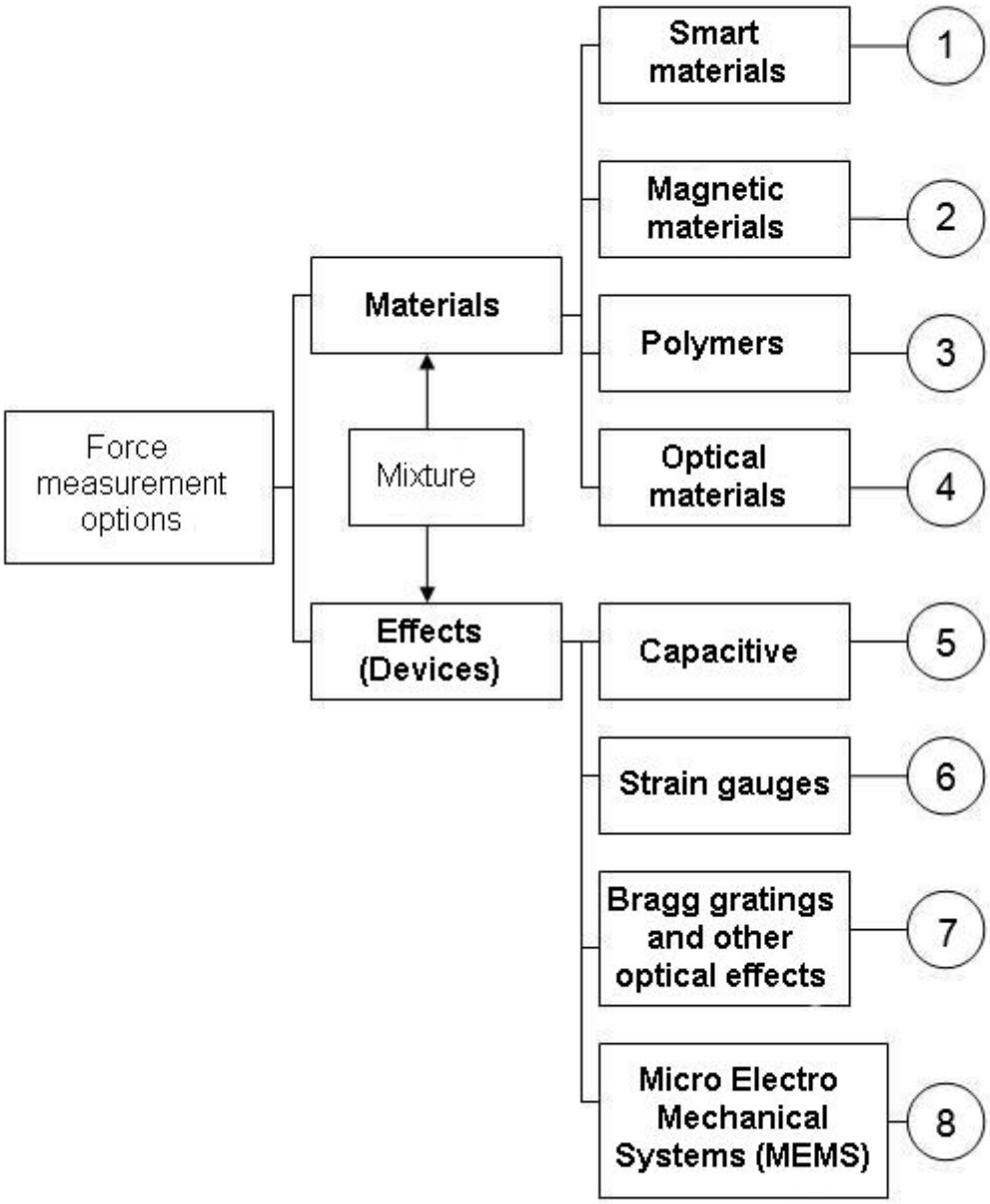

Figure 3.1: Force measurement options [16]: Part A

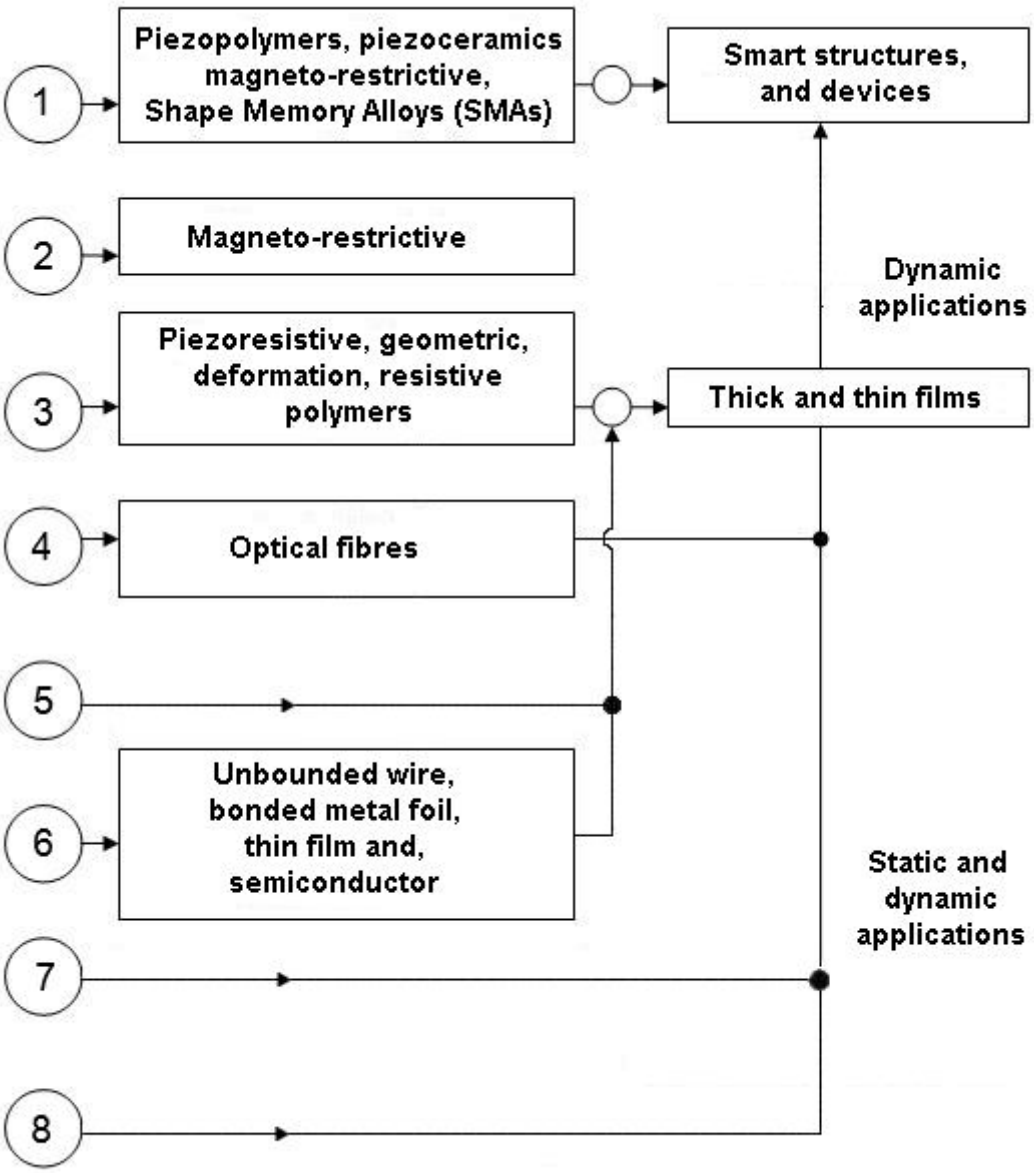

Figure 3.2: Force measurement options [16]: Part B

3.2 Smart Brake Pad Sensor Design Criteria

3.2.1 Introduction

The SBP-SDC need to be established to guide and ensure the most appropriate sensor technology is chosen as the key component of a functional SBP.

To develop the SBP-SDC we investigate the following:

1. Location
2. Environmental Factors
3. Sensor Reliability
4. Materials
5. Range
6. Accuracy, Precision, Repeatability and Confidence
7. Uncertainty Analysis

3.2.2 Location

Figures 3.3 and 3.4 illustrates the surrounding components and location of the SBP.

3.2.3 Environmental Factors

The environmental factors consist of:

1. Temperature Constraints
2. Operative Restraints and Sensor Mounting Considerations
3. Geometry
4. Sensor Lead Attachment Considerations

3.2.3.1 Temperature Constraints

As a result of the literature review we have established a probable range of temperatures a SBP needs to operate within, this is: -30 to 200^o C.

Based on this statement the chosen specifications are:

- SBP desired operating temperature: -30 to 200^o C

3.2.3.2 Operative Restraints and Sensor Mounting Considerations

Since brake pads experience compressive loads the preference is for a sensor that measures compression directly rather than longitudinal[1] strain.

There are three types of mounting configurations considered; mounting sensors (please refer to Figure 3.5):

1. On the rear of the backing plate

[1]Parallel with the backing plate

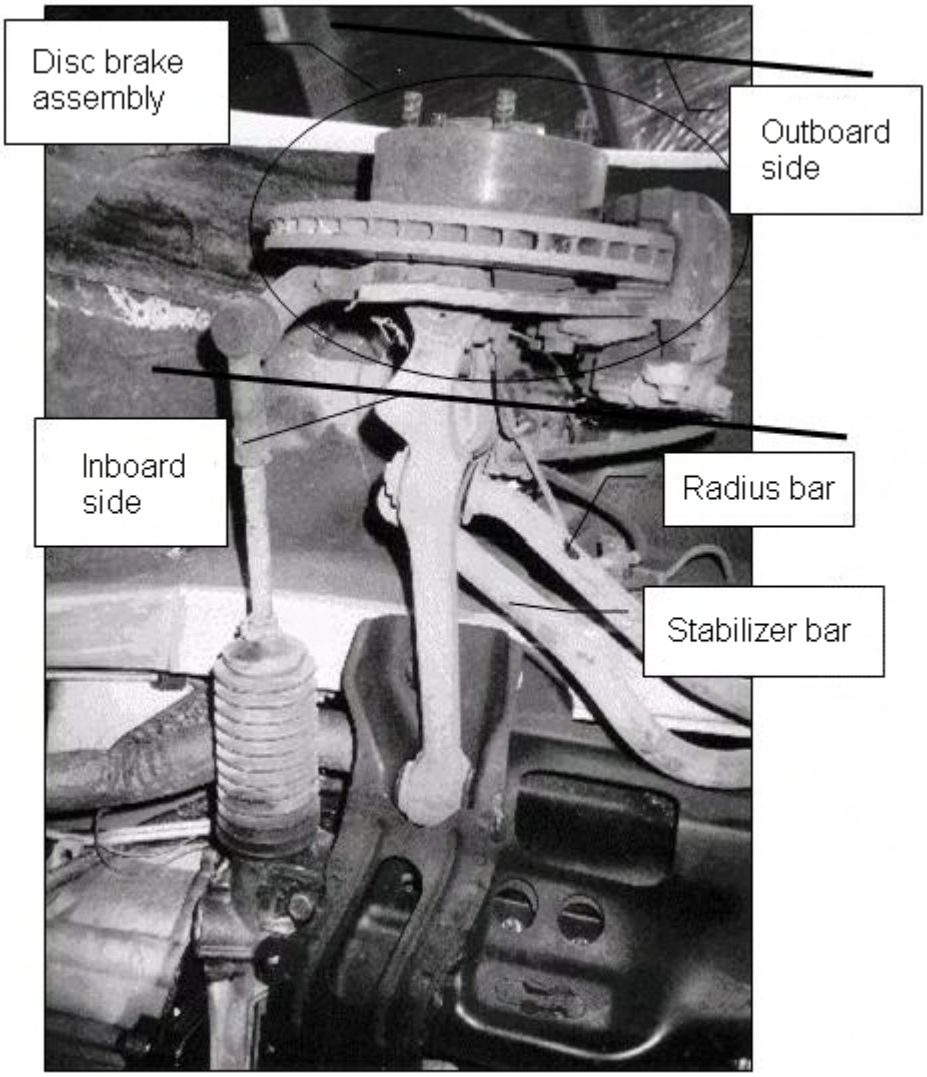

Figure 3.3: Underside of right-hand front corner of a test vehicle

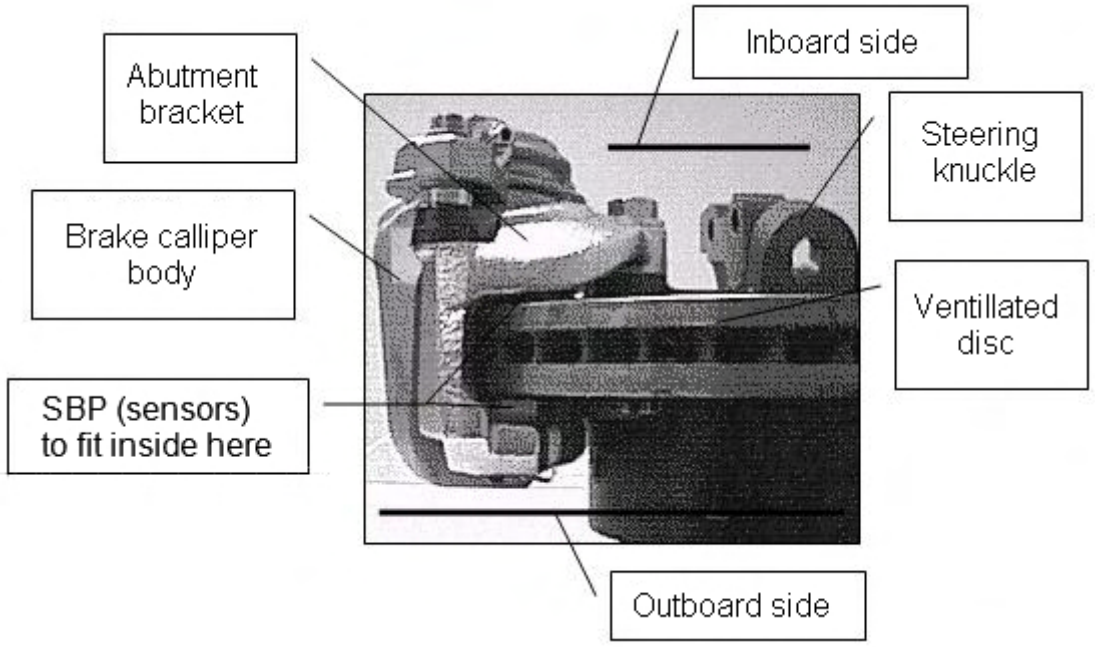

Figure 3.4: Right-hand disc brake and calliper

2. In between the backing plate and friction material

3. Embedded into the friction material

The first choice is dismissed because of the influence the backing plate material would have on the brake pad, the non-linearity of the brake pad material, and the temperature limitation of suitable sensors for this purpose. The second and third choices are possibilities. Which position is chosen, will depend on the mounting needs of the sensor.

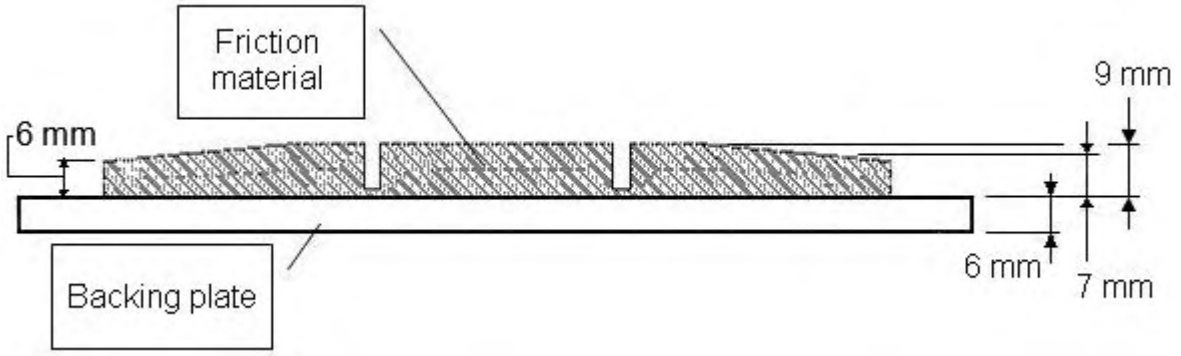

Figure 3.5: Cross-section of brake pad

Based on this discussion the chosen specifications are:

- Sensors' to measure compressive loads
- Sensors' to be fitted between friction material and backing plate or embedded into friction material

3.2.3.3 Geometry

The placement of sensors within the brake pad is limited to the volume of the friction material. As can be seen from Figure 3.5 the thickness of the brake pad is approximately 9 mm thick[1] affixed to a mild steel backing plate. With a thickness of 9 mm, and 2 mm allowable wear thickness, this leaves a total of less than 7 mm of thickness to embed the sensors within, in order to lessen possible damage to the sensors whilst in service.

The other physical restraint is the area. It is envisaged that the SBP would need fifteen equally distributed sensing cells in order to develop a pressure distribution of the brake pad surface (please refer to Figure 3.6). This number has now been revised down to six points per pad because of data acquisition limitations and cost.

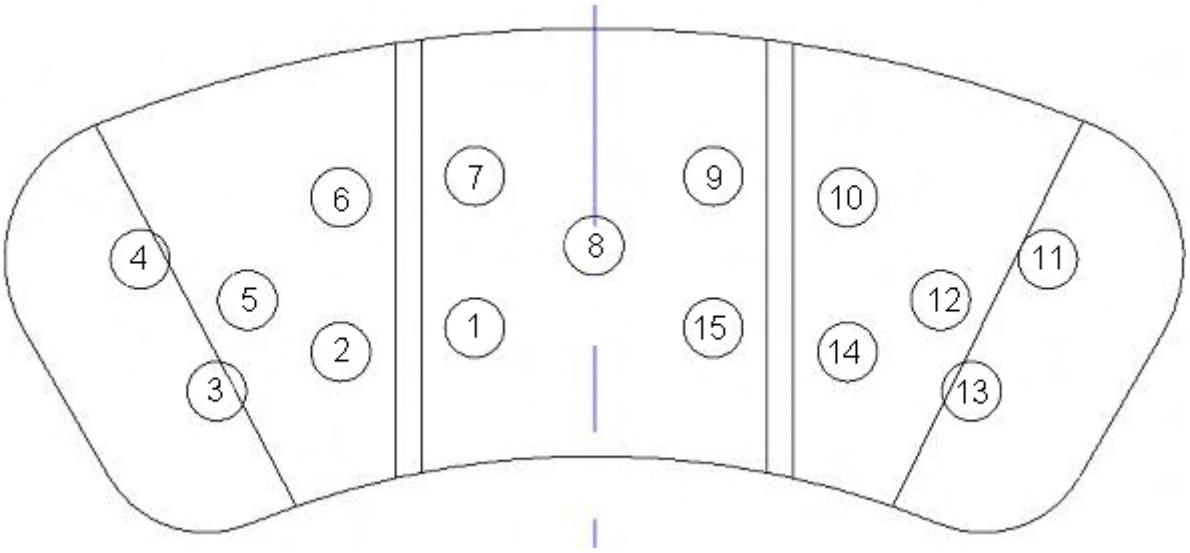

Figure 3.6: Brake pad with fifteen equally distributed sensing cells

[1] when new, depending on brand, type and loading condition

Based on this discussion the chosen specifications are:

- Sensors' to be a maximum of 7 mm thick
- 15 or 6 sensing cells per pad

3.2.3.4 Sensor Lead Attachment Considerations

The sensor leads[1] exit the SBP toward the axis of the wheel a distance of approximately 200 mm in order to clear the calliper. They also need to be able to withstand the operating conditions of the SBP without detachment.

Based on this discussion the chosen specifications are:

- The sensor leads which exit the SBP need to withstand the operating conditions without detachment, and
- The sensor leads need to be 200 mm long

3.2.4 Sensor Reliability

Sensor reliability relates to how many loading cycles the sensor can handle till failure. As a minimum, we would like the SBP to be used for at least one standard judder test in a brake dynamometer. The sensor reliability ϱ can be calculated by using Equation 3.1.

$$\varrho = \omega_{max}\, t \tag{3.1}$$

Where:

ω_{max}	maximum vibration frequency during test
t	time duration of test

For a SBP judder test we have,

ω_{max}	equals the maximum likely judder frequency, which is: 60 Hz
t	equals the length of the judder test in seconds, which is: 1 209 600 s or 14 days

Therefore,

$$\begin{aligned} \varrho &= 60 \times 1209600 \\ &\approx 73 \times 10^6 \text{ cycles} \end{aligned} \tag{3.3}$$

Based on this discussion and calculation the chosen specifications are:

- Each sensor is to successfully complete one judder test or withstand a minimum of 73 000 000 loading cycles

3.2.5 Materials

The Modulus of Elasticity (E) for the test vehicle's friction material is known to be around 0.5 GPa. In order for the sensor not to influence the braking performance of the SBP the sensor ought to have an E value greater than or equal to 0.5 GPa.

Based on this discussion the chosen specifications are:

- Sensors' Modulus of Elasticity: E $\geq$ 0.5 GPa

[1] This will be demonstrated in later figures

3.2.6 Range

When we think of *range* we are thinking of a measurement interval or measurement space, refer to Figure 3.7. In our case, the minimum pressure would be when the brakes are *not applied* whereas maximum pressure level between brake pad and disc would be 5 MPa which occurs during *panic braking* [42]. For our application, the sensors' range is determined by the following simple Equations 3.4 and 3.5.

$$F = PA \tag{3.4}$$

Where:

F	force
P	applied pressure
A	cross-sectional area

$$\vartheta = \frac{\Upsilon}{NoSC} \tag{3.5}$$

Where:

ϑ	SBP sensor range
Υ	*Panic braking* equivalent force value
NoSC	Number of sensing cells

Given,

$$\begin{aligned} P &= 5 \times 10^6\,\text{Pa} \\ A &= 2.77 \times 10^{-3}\text{m}^2 \end{aligned}$$

Therefore, we have,

$$\begin{aligned} F &= 5 \times 10^6 (2.77 \times 10^{-3}) \\ &= 13.85\ \text{kN} \end{aligned} \tag{3.6}$$

We then use Equation 3.5 to calculated the range for the sensor; and so, we have,

$$\begin{aligned} \Upsilon &= 13.85\ \text{kN} \\ \text{NoSC} &= 15 \end{aligned}$$

Therefore, we have,

$$\begin{aligned} \vartheta &= \frac{13.85 \times 10^3}{15} \\ &= 923\,\text{N} \\ &\approx 1\,\text{kN} \end{aligned}$$

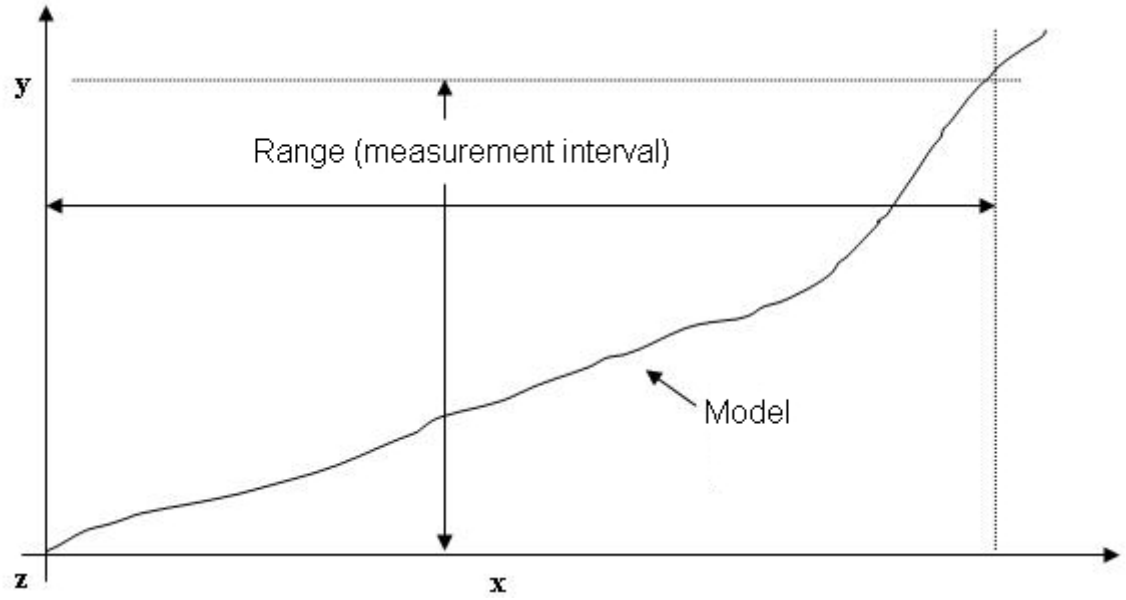

Figure 3.7: Representation of *range* with regards to a hypothetical sensors' response

Referring to Figure 3.7, the range can be defined as the interval between the maximum and minimum values of: x, y or z (z - not shown).

Based on this discussion the chosen specifications are:

- Range: $0 - 1\,\text{kN}$ in compression for each of fifteen sensing cells

3.2.7 Accuracy, Precision, Repeatability and Confidence

Accuracy is most easily understood in terms of archery; an archer fires a *volley of arrows* at a practice target with concentric rings and a *bull's eye'*. The accuracy is how close the arrows are to the bull's eye. The precision or repeatability is how close a group of arrows are to each other but not necessarily close to the target (please refer to Figure 3.8) [44].

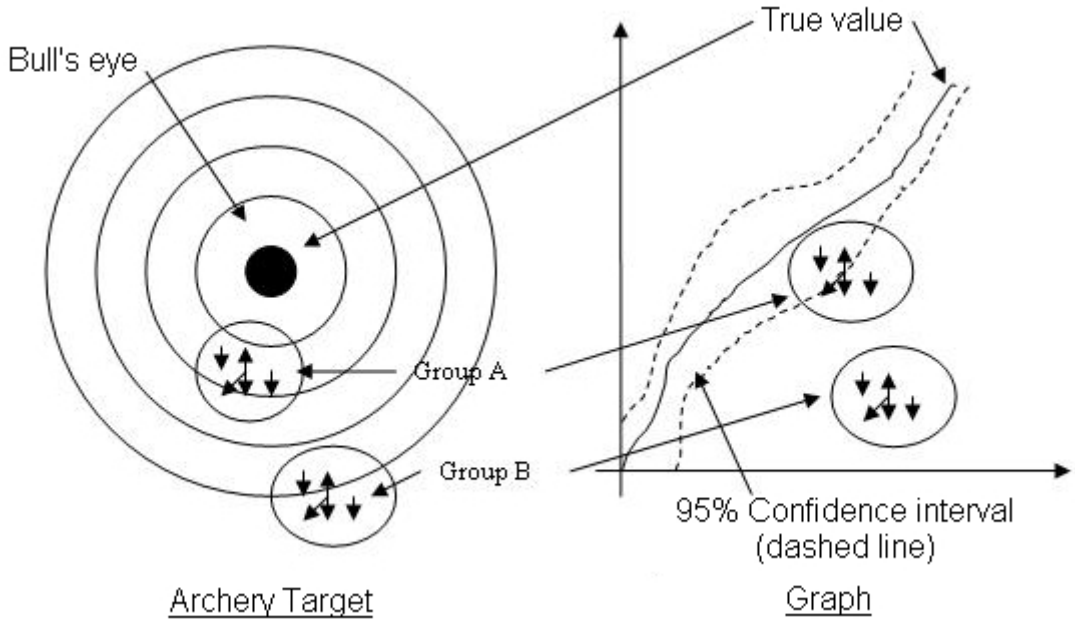

Figure 3.8: Accuracy, precision, repeatability and confidence

If you cast your eyes on the archery target in Figure 3.8, the bull's eye represents the optimal or true value of a measurement, this value is typically called the nominal or average value depending on the probability distribution. The accuracy is by how much the values, say in, groups *A or B* vary[1] from the nominal[2] value[3]. The precision or repeatability relates to how close successive measurements are to each other. In this case, both groups *A and B* have the same repeatability but only *A* has the greatest accuracy. Our confidence of obtaining such measurements is often represented by dashed curves, see graph in Figure 3.8. The degree to which the dashed curves are offset is related to a probability distribution, typically either the *normal*, or t distributions, depending on the size of the population of data. A subset of a population is the sample.

In order to specify a sensors' accuracy, we normally refer to a *tolerance* or *margin of error*. This quantity can not be calculated we must a guess to the amount which will suit our application. One thing to note though is, that a large tolerance, will normally cost less.

In our case, the range of operation of each sensing cell ought to be between: $0 - 1$ kN in compression. However, thinking of this range will not help us, we need to think of the array of fifteen cells for one SBP in order to make it suit our application. So for panick braking (as already discussed) we have a maximum pressure of 5 MPa and a tolerance of $\pm$ 0.25 MPa; as a percentage 5 %. Relating this back to the cell range, we have: 1 kN $\pm$ 5 % with a desired 95 % confidence interval specified by industry.

[1] Variance
[2] Mean
[3] Bull's eye

Based on this discussion the chosen specifications are:

- Sensor accuracy (tolerance): $\pm$ 5 %
- Confidence interval: 95 %

3.2.8 Uncertainty Analysis

Uncertainty or error ϵ in any measurement is the difference between the true value a and what is measured $\tilde{a}$ or approximated mathematically, as in the case of a numerical analysis procedure:

$$\epsilon = a - \tilde{a} \tag{3.7}$$

Re-arranging in terms of a, we have:

$$a = \tilde{a} + \epsilon \tag{3.8}$$

In terms of experimental measurements the error ϵ[1] term in Equation 3.8 can be further broken down into three further subcomponents which are shown in Equation 3.9:

$$\epsilon_t = \epsilon_i + \epsilon_r + \epsilon_s \tag{3.9}$$

Where:

ϵ_t	total error
ϵ_i	illegitimate error
ϵ_r	random error
ϵ_s	systematic error

3.2.8.1 Illegitimate Error

Illegitimate errors are one-off errors caused by accidental events such: as parallax error, reading the wrong scale, putting in the wrong values etc. These errors can usually be eliminated at the time of processing the data or running the program.

Removal of illegitimate errors is done by carefully tracing the cause of, say, a *far outlier* in a graph of data. If there is a known fault then remove the offending data points. However, if no fault can be found, it is unwise to remove the data.

3.2.8.2 Random Error

Random errors are present every time you make a measurement, but which vary positively or negatively in a uniform way. Typical examples of random error in a MTS, are:

- Grips aligned, however not square
- Compression platens, not exactly square
- Backlash in screws and threads etc

Nevertheless, it has been shown that if we take a group of measurements the random errors fluctuate around a mean of a normal distribution. It has also been shown that the sum of such errors, as the number of samples approaches infinity, is equal to zero.

[1] Also known as total error ϵ_t

3.2.8.3 Systematic Error

Systematic errors are typically errors which vary in a predictable way such as:

- Rounding error's in computations (please refer to Appendix J)
- Measurement errors due to *limit of reading* of a scale or resolution of instrumentation
- Model fitting errors

Measurement Errors We will always have measurement errors; though sometimes they will be so small we can neglect them. In Figure 3.9, we have a ruler used to take a measurement. You will notice in the figure that the limit of reading is equal to 0.5 cm; we guess the error in any measurement taken with this ruler to be *plus or minus half the limit of reading*, or $\pm$ 0.25 cm.

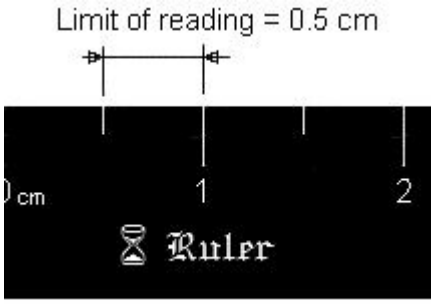

Figure 3.9: Part of a ruler

If we took multiple readings with a ruler or other similar instruments, we could simply take the Sum of Absolute Errors (SAE), as demonstrated in Equation 3.10 to find an estimate of the total error. Alternatively, we could use Equation 3.11 to find the, Root of Sum of Square Errors (RSSE).

$$SAE = |\epsilon_1| + |\epsilon_2| + \cdots + |\epsilon_n| \tag{3.10}$$

$$RSSE = \sqrt{(\epsilon_1)^2 + (\epsilon_2)^2 + \cdots + (\epsilon_n)^2} \tag{3.11}$$

This first type of measurement method we can call a *direct measurement method* because there is no mechanical, electrical, optical or other means between the device making the measurement and us estimating the error from that measurement.

The second type of measurement method we can call a *indirect measurement method* because there is some means between us and our ability to accurately estimate its error, examples of this type are:

- A Data Acquisition System (DAQS) for retrieving data from sensors
- A multimeter for taking electrical measurements
- An automotive speedometer

In the above three listed examples, it is not enough to gauge the amount of error by relying on what is written on the screen. We must look at the mechanism which is used to take the initial measurement. For example, if we have a 12 bit DAQS, with 10 volts Full Scale (FS); how would we find its equivalent *limit of reading*? The answer is, we use its smallest resolvable unit, which is its resolution *RES* which can be calculated using Equation 3.12.

$$\begin{aligned} RES &= \frac{10}{2^{12}} \\ &= 0.002441\,\text{v} \quad (4 \text{ sig. figs.}) \end{aligned} \tag{3.12}$$

Using Equation 3.12, it is not necessary to use half the limit of reading as we would do for a direct measurement, since there is no possibility of parallax error.

Model Fitting Errors Once data from sensors is obtained either manually or by using a DAQS and a model is fitted, this introduces *model fitting errors*; since no model perfectly fits its data. Given a model of the form 3.13, we estimate the model fitting errors with Equation 3.14 [45].

$$y = f(x_1, x_2 \ldots x_n) \tag{3.13}$$

$$\delta y = \frac{\partial y}{\partial x_1}\delta x_1 + \frac{\partial y}{\partial x_2}\delta x_2 + \cdots + \frac{\partial y}{\partial x_n}\delta x_n \tag{3.14}$$

Along, with the model fitting errors that can be derived mathematically as illustrated above, once the data is plotted, a number of other errors become evident, for example:

- Null or Voltage Offset
- Null Temperature Shift
- Sensitivity Temperature Shift
- Linearity Error
- Drift Error
- Hysteresis Error

Drift and hysteresis errors will be discussed here; the remainder of the list will be discussed further in Appendix B.

In Figure 3.10 we have a plot of data from a force sensor under constant load. You can see from the figure, that the data is drifting away from the horizontal by $d_1 - d_0$, over a period of $t_1 - t_0$. This is called *drift*. Drift $\bigwedge$ is expressed mathematically in Equation 3.15. Drift is most often expressed as a percentage of FS.

$$\bigwedge = \frac{d_1 - d_0}{t_1 - t_0} \tag{3.15}$$

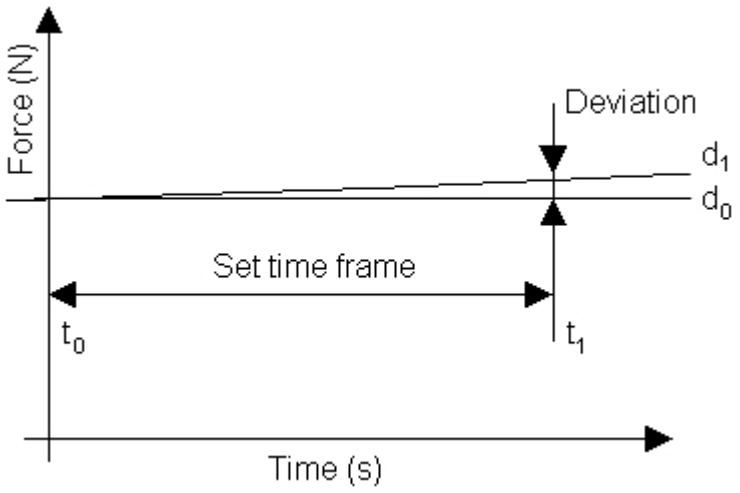

Figure 3.10: Drift

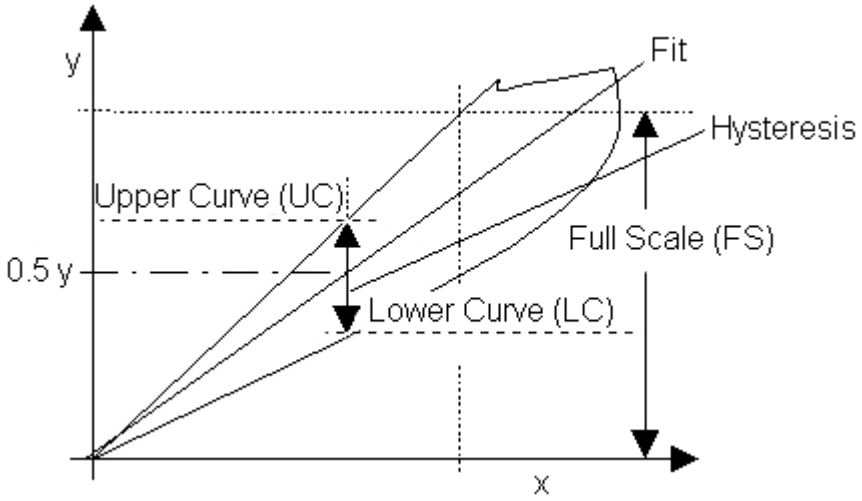

Figure 3.11: Hysteresis

If a force sensor went through one loading cycle and there was a gap between the loading and unloading curves the output would have hysteresis (please see Figure 3.11). Hysteresis Ξ is expressed mathematically in Equation 3.16; Hysteresis is most often expressed as a percentage of FS.

$$\Xi = \frac{UC - LC}{FS} \tag{3.16}$$

Based on this discussion the chosen specifications are:

- A sensor for a SBP must have zero drift over a period of one minute. This measurement must be within one decimal place

3.2.8.4 Total Expected Error

The standard practice used by many manufacturers of scientific equipment is to use Equation 3.11 and sum: sensitivity temperature shift, linearity, drift and hysteresis errors to find the root sum of square errors. This method is fine for sensors with a linear output but not practical otherwise.

An alternative method, that we will use here is simply to use the 95 % error bounds to calculate a TEE value or total error, if other errors are small (please see Figure 3.12).

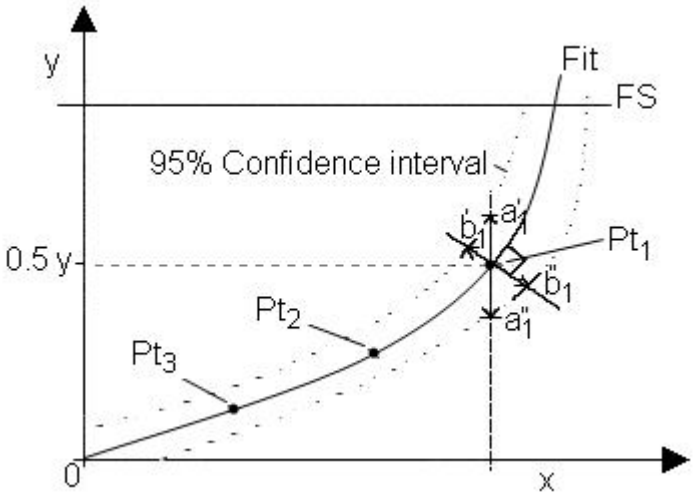

Figure 3.12: TEE

The TEE value may be calculated by choosing the most appropriate case below whilst referring to Figure 3.12.

TEE Cases

Case 1: If, $|a'\,a''| \parallel |b'\,b''|$ OR $|a'\,a''| \approx\parallel |b'\,b''|$ then use Equation 3.17,

$$TEE = \frac{|a'\,a''|}{FS} \times 100 \tag{3.17}$$

Else,

Case 2: If, $|a'\,a''| \nparallel |b'\,b''|$ then use Equation 3.18

$$TEE = \frac{|b'\, b''|}{FS} \times 100 \tag{3.18}$$

Else,

Case 3: If, $|a'\, a''| \nparallel |b'\, b''|$ and has a highly irregular 95 % confidence interval (users' judgement) then use Equation 3.19.

$$TEE = \frac{100}{3FS}(|b_1'\, b_1''| + |b_2'\, b_2''| + |b_3'\, b_3''|) \tag{3.19}$$

Where[1],

$\parallel$	is parallel to
$\approx\parallel$	approximately parallel to
$\lvert a'\, a''\rvert$	interval aa
$\lvert b'\, b''\rvert$	interval bb
$\lvert b_1'\, b_1''\rvert$	interval bb for point 1
$\lvert b_2'\, b_2''\rvert$	bb for point 2
$\lvert b_3'\, b_3''\rvert$	bb for point 3

As previously mentioned, we require the sensor to have accuracy of $\pm$ 5 % with 95 % confidence. Using the TEE method, divide the TEE value by two and compare that value with our required tolerance. If the required value is less than or equal to half the TEE value, then we have obtained the required sensor tolerance.

A limitation of this method, is that you are unable to tell what plotting errors[2] comprise the TEE value. This is not an issue from the researchers perspective. It may be an issue for some consumers though.

Based on this discussion the chosen specifications are:

- Use the TEE method to account for uncertainty

3.2.9 Discussion and Conclusion
- Smart Brake Pad Sensor Design Criteria -

The most obvious components of a SBP-SDC are the: location, environmental factors, sensor reliability, materials and range of operation. These were briefly discussed within the relevant sections. We also thoroughly investigated errors an important area and developed the TEE method. We could accept the TEE method is simply a re-labeling of hysteresis error with slight modifications. It simplifies the connection between taking a measurement and linking that measurement with a specified tolerance. Some may argue, why bother specifying a tolerance for a preliminary technology or an application of that technology? Well, if no tolerance is specified, there is no way of knowing whether the output will be useful for the specified purpose.

In conclusion and based on the discussions within this section the SBP-SDC consists of the following criterion:

- SBP desired operating temperature: -30 to 200^o C
- Sensors to measure compressive loads

[1] Collectively, for Equations: 3.17, 3.18, 3.19

[2] Please see Appendix B

- Sensors to be fitted between friction material and backing plate or embedded into friction material
- Sensors to be a maximum of 7 mm thick
- 15 or 6 sensing cells per pad
- The sensor leads which exit the SBP need to withstand the operating temperature without detachment
- The sensor leads need to be 200 mm long
- Each sensor is to successfully complete one judder test or withstand a minimum of 73 million loading cycles (worst case)
- Sensors modulus of elasticity: $E \geq 0.5$ GPa.
- Sensors range: $0 - 1\,\text{kN}$ for each of 15 sensing cells
- Sensor accuracy (tolerance): $\pm 5\,\%$
- Confidence interval: $95\,\%$
- A sensor for a SBP must have zero drift over a period of 1 minute. Within one decimal place
- Use the TEE method to account for uncertainty

3.3 Review of Force Measurement Techniques

3.3.1 Introduction

In the last section we investigated the SBP-SDC required in order to satisfy the needs of a SBP.

In this section, we discuss[1] applicable force measurement techniques to satisfy the SBP-SDC, namely:

1. Strain Gauges
2. Piezo Sensors
3. Thin and Thick Film Sensors
4. Fibre Optic Sensors[2]

3.3.2 Strain Gauges

3.3.2.1 Introduction

In a seminar to the Royal Philosophical[3] Society, Lord Kelvin describe an experiment where a piece of copper or iron if strained produced a change in resistance; thus the possibility of a *strain gauge* was born [46].

Today, strain gauges are the most commonly used device for the measurement of small displacements or strains. When a strain gauge is calibrated, it is possible to translate measured strains to equivalent forces. So, although strain gauges measure strain, they can be configured to measure strain, force and pressure.

3.3.2.2 Description

Typically, there are 4 main types of strain gauges:

1. Unbounded wire
2. Bonded metal foil
3. Thin film
4. Semiconductor

It is beyond the scope of the thesis to discuss each of these types in detail.

Either of these four types of strain gauges are typically glued to the surface of the body to be strained. In the case of a SBP, this would be at the rear of the backing plate. However, if mounted in this position, it would be difficult to accurately determine the forces at the brake pad surface. This is due to the non-linearity and non-homogenous nature of the friction material.

As space is limited at the rear of the backing plate, placement of such gauges without some type of *false back*[4] would not be practical.

[1] Only a few pertinent references have been included out of the hundreds that are available

[2] Please see a subsequent review in Chapter 3, page 53

[3] In the early days, *natural philosophy* implied physics

[4] Typically, a false back was a concealed section of a hardcover book where a lover may leave a message for their sweetheart. In this case, the false back would form part of the backing plate where a sensor could be embedded

Strain gauges are often *packaged* in two main types of devices called *load cells or load washers*; however, either type are are usually over 7 mm thick, and are still susceptible to heat and thus failing several criterion in the SBP-SDC.

3.3.2.3 Discussion and Conclusion - Strain Gauges -

Although strain gauges can be configured to measure force they are unable to measure it directly. Strain gauges are also highly susceptible to heat. Lastly, strain gauges are unable to be mounted on a brake pad due to the limited space and non-linearity of the friction material.

3.3.3 Piezo Sensors

3.3.3.1 Introduction

Pierre and Jacques Curie conducted an experiment in 1880 which confirmed the existence of piezoelectricity; electricity which resulted from applying stress to certain crystals[1] [47].

However, it was not until 1881 that a mathematician, Lippmann showed theoretically the reverse property would be possible, mechanical stress resulting from placing the crystal near an electric field. This latter effect is the driver for modern quartz wrist watches and computer clocks [47].

Today, these sensors along with an inertial mass are predominantly used in accelaromeeters for vibration analysis.

3.3.3.2 Description

Typically, there are two main types of piezo sensors:

1. Thin film[2]
2. Semiconductor

Apart from these types, there is a further technological subclassification, into either:

- Piezoelectric
- Piezoresistive

Here we will focus on the piezoelectric sensor since they are known to withstand the environmental conditions of the automotive braking environment [10].

These sensors utilize the piezo electric effect to operate. Natural crystals such as quartz (please refer to Figure 3.13) exhibit a piezoelectric effect when placed under stress σ. Charge builds up across the opposing ends of the crystal.

In addition to quartz crystals, there are many other materials that exhibit the piezoelectric effect. Among them are: man-made piezoceramic and polycrystalline materials. These materials are made to exhibit piezoelectric properties by an application of an electric field. An advantage of such materials is that they can exhibit a larger than normal charge output compared to natural materials, which can make them better for sensor applications (please refer to Table 3.1) [24].

As piezoelectric materials only produce charge when acted upon by applied force. When the force is at rest or removed the charge that was produced leaks back to zero

[1] Tourmaline, quartz, topaz, cane sugar and rochelle salt (sodium potassium tartrate tetrahydrate)
[2] Treated more fully in the next section

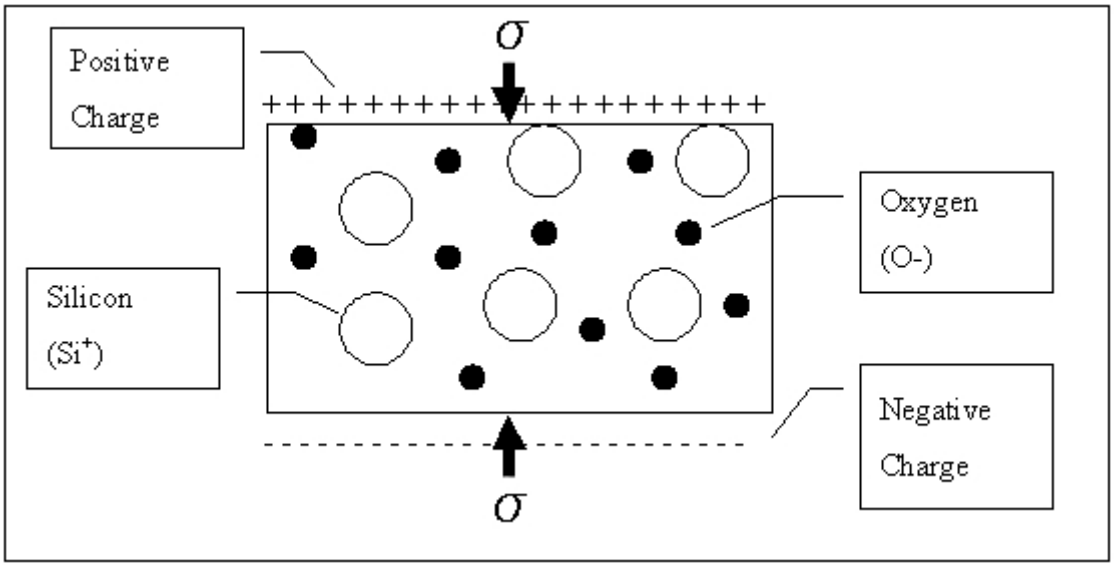

Figure 3.13: Piezoelectric quartz crystal under stress

Table 3.1: Comparison between quartz and a polycrystalline ceramic material [24]

Quartz Crystal (a piezoceramic)	**Polycrystalline Ceramic**
Natural piezoelectric material	Artificially polarized, man-made material
High voltage sensitivity	High charge sensitivity
Stiffness comparable to steel	Unlimited availability of sizes and shapes
Exhibits excellent long term stability	Materials available which operate at 540^o C
Non-pyroelectric	Output due to thermal transients (pyroelectric)
Low temperature coefficient	Characteristics vary with temperature

along the path of least resistance, like a capacitor that is grounded. The rate at which this leakage of charge occurs is determined by the, Discharge Time Constant (DTC), which varies depending on type of piezo sensor. If a piezoelectric sensor is acted upon by a rapid event, such as a mass hitting the bonnet of a car and the DTC is sufficiently long the event can be recorded. However, if the same sensor were acted upon by a slow or static event such as a mass resting on the bonnet, the DTC may not be sufficiently long enough, thus no charge will be present and no event will be able to be recorded. This is why piezo sensors are generally used for vibration measurement a dynamic event.

3.3.3.3 Discussion and Conclusion - Piezo Sensors -

The beauty of a piezoelectric sensor is that it is generally made of a ceramic material enabling it to withstand the temperatures existing in the brake environment. Though the disadvantage is that it is generally used for the measurement of transient events; like vibration rather than static loads. A further disadvantage is that there are no packaged piezo sensors of a sufficiently thin cross-section to meet the needs of the SBP-SDC.

Therefore, in conclusion, piezo sensors can not be used for a SBP application.

3.3.4 Thin and Thick Film Sensors

3.3.4.1 Introduction

Thin and thick film sensors are seen as *tactile* sensors used to measure the equivalent of human touch, or the measurement of pressure over a given area. If these sensors are calibrated they can be made to measure force directly.

3.3.4.2 Description

Thin and thick films are classified as polymer sensors which focus on the material properties of the sensor rather than a specific device or effect such as a strain gauge. Polymer sensors can be further classified into the simple groups of either thin or thick film; where the differentiation comes down to the thicknesses of the deposited film and the methods used to manufacture[1] them (please refer to Figure 3.14).

There are two basic groups of *sensor film structures*, namely:

1. Piezoelectric and Piezoresistive Devices
2. Geometric Deformation and Resistive Polymers

There descriptions follow:

1. **Piezoelectric and Piezoresistive Devices** Piezoelectric devices are structured around the principals of the piezo electric effect and so are limited to dynamic force measurement as previously described. Nevertheless, the films such as Polyvinylidene difluoride (PVF_2) and Polyvinylidene fluoride (PVDF) have significant applicability for the measurement of contact forces as they are extremely rugged even in thin sheets [17]. These devices can also be effectively used for measurement of heat and have successfully been implemented as extremely sensitive fire detection devices. However this can also be seen as a disadvantage especially when measuring contact force in hot environments.

[1] Please see Appendix C for: "Techniques to Manufacture Thin and Thick Films"

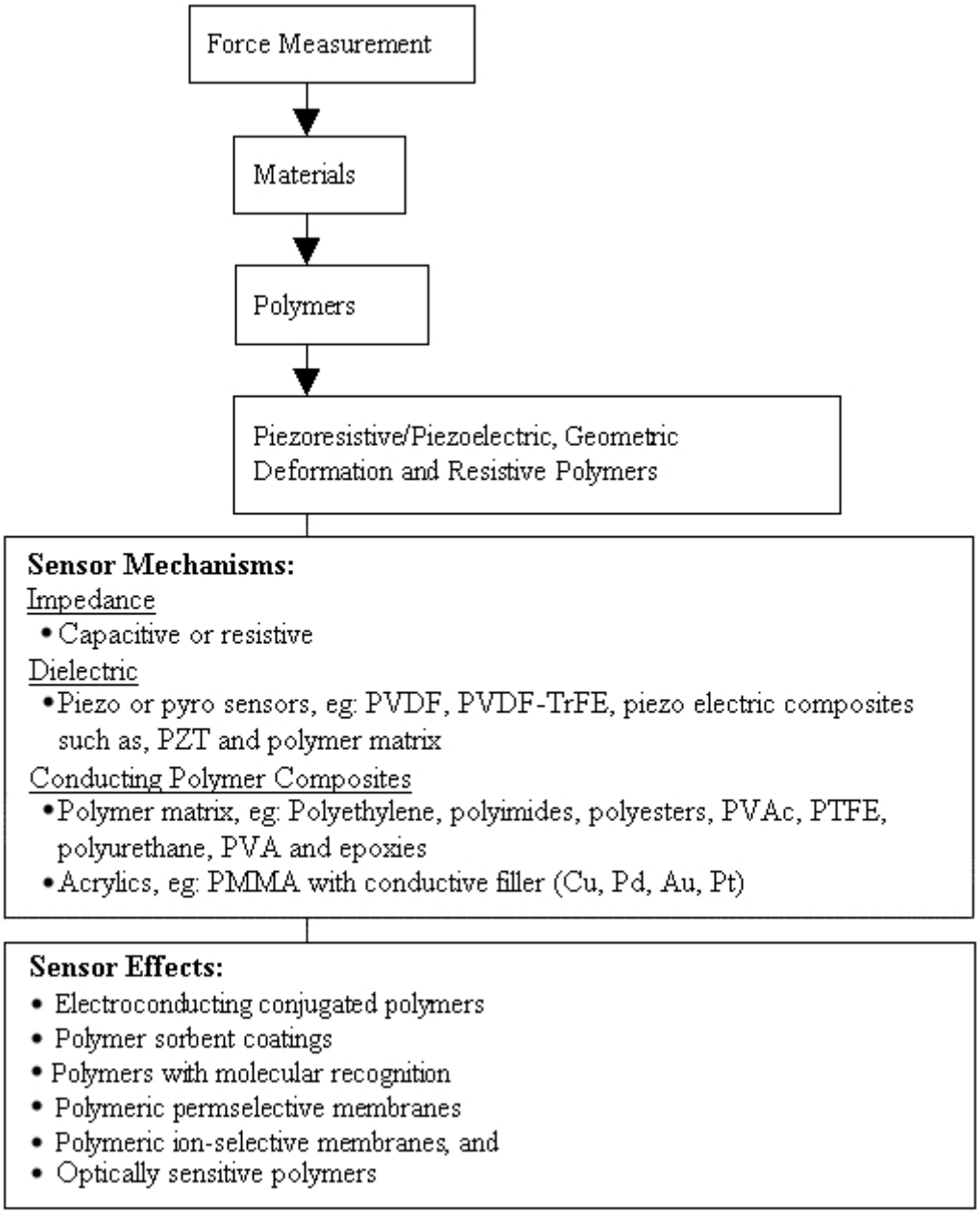

Figure 3.14: Classification of force sensors for force measurement

There are a number of different structures; Figure 3.15 is one of the earlier designs though many others are hybrids of this. These hybrids are manufactured using different techniques, and the size of sensors are now greatly reduced.

On the right side of Figure 3.15 we have an exploded view of the structure of this sensor. Starting with a protective sheeting to protect the sensor from harsh environments, then *row electrodes* printed on the top side of a PVDF sheet[1] to form apart of the sensor circuit. Beneath this, there is another layer, which has circular islands of conductive material, embedded in a non conducting rubber. This acts as the path for charge to flow. The next two layers are: a layer with holes, that allows a varying amount of conducting rubber from above, to pass through to the bottom printed circuit board, thereby completing the capacitive circuit. On the left side of the drawing demonstrates the operation of the sensor (please see Figure 3.15).

2. **Geometric Deformation and Resistive Polymers** There are two basic types:

   1. Conductive Elastomers
   2. Force Sensitive Resistor^{TM} and allied techniques

   There descriptions follow:

   1. **Conductive Elastomers** Elastomers such as foams or rubbers are traditionally non-conductive; however, they can be made conductive by the addition of finely ground good conductors like copper and silver. Materials manufactured this way can have intriguing properties. Deform the material and you have a better conductor because a greater number of conducting pathways will be in contact with each other; thus load can be determined via the change in resistance of the elastomers. Figure 3.16 is a conductive elastomer in a sandwich type construction.

      The great weakness of these sensors is their performance; they do have the ability to bend around and conform to various surfaces and are thin in cross-section and are flexible seemingly like human skin, yet they lack the durability that is required in robotic applications and for that matter for a SBP. Conductive Elastomers also have a lack luster performance when it comes to temperature tolerability thus a further reason to eliminate them for use in a SBP application [17, 48].

   2. **Force Sensitive Resistor^{TM} and allied techniques** Conductive elastomers offer a reduced size but at the cost of high temperature sensitivity and low durability. On the other hand, Force Sensitive Resistor (FSR^{TM}), are difficult to purchase for experimental usage, yet are used extensively in many technologies such as:

      - Keyboards
      - Pointing devices
      - Musical instruments

[1] Capacitive material

The device is based on polymer thick film technology. Externally, it resembles a membrane switch, but rather than being a switch, on–off, its output varies continuously with applied load. If testing such a device, at the *no load* position, the resistance measured would be infinitely high and upon loading the output follows an approximate power law relationship (please refer to Figure 3.17). Above certain loads depending on the specified force range, the sensor would reach saturation point, that is a point where no further relationship between resistance and force is viable, this depends on various factors, such as:

- The spacing between the interleaving electrode fingers
- The composition of the polymer FSR [18].

Figure 3.18 is simple drawing of the sensors' design and structure of one style of electrode configuration for a FSR. This drawing can be considered the drawing of a single cell of an array of similar cells if this was to be used in many applications including that of the SBP. Sensitivity of such sensors is related to the semi-conductor[1] mixture, the electrode design and the type of extra overlay, indenter shape that can be applied over the top of the sensor to improve force distribution. The effect of a rubber overlay is an increase in the slope of the response at low forces and a decrease in slope of the curve at high forces compared to that of a hard actuator. A key determinant in proper FSR design is the selection of the size of gap between interleaving fingers - a large gap less fingers are in contact a smaller gap more fingers are in contact. These factors all affect the sensitivity of a given sensor. Another sensor performance characteristic is that of drift, which is key issue in load measurement. The drift for this sensor if measure over several minutes is 10 to 20 % of the initial value. This can be improved by better sensor design according to the paper [18].

On the left hand side of Figure 3.18 we have a semi-conducting polymer, on the right we have the interleaving of electrode fingers (similar to 2D clasping of one's fingers). On assembly of these two layers voltage can pass from one electrode finger through the semi-conducting polymer back into the other completing a circuit; when load is applied to the assembled package a variable output roughly following that of a power law relationship between resistance and force ensues.

The FSR is a rugged and durable device in service. The operating temperature range of such a device can extend to 170^o C and up to 400^o C for some devices. The temperature sensitivity of the sensor at room temperature is a matter of a simple function, nevertheless at temperatures above 68^o C a more complicated function is needed for temperature compensation[18].

3.3.4.3 Discussion and Conclusion - Thin and Thick Film Sensors -

It is likely that a film based piezoelectric sensor can withstand the rigors of the automotive testing environment. Though, the major disadvantage of a piezo type device it is ideally suited to measuring transient events. The thickness of the commercially available device

[1] Sometimes a sintered polymer ink

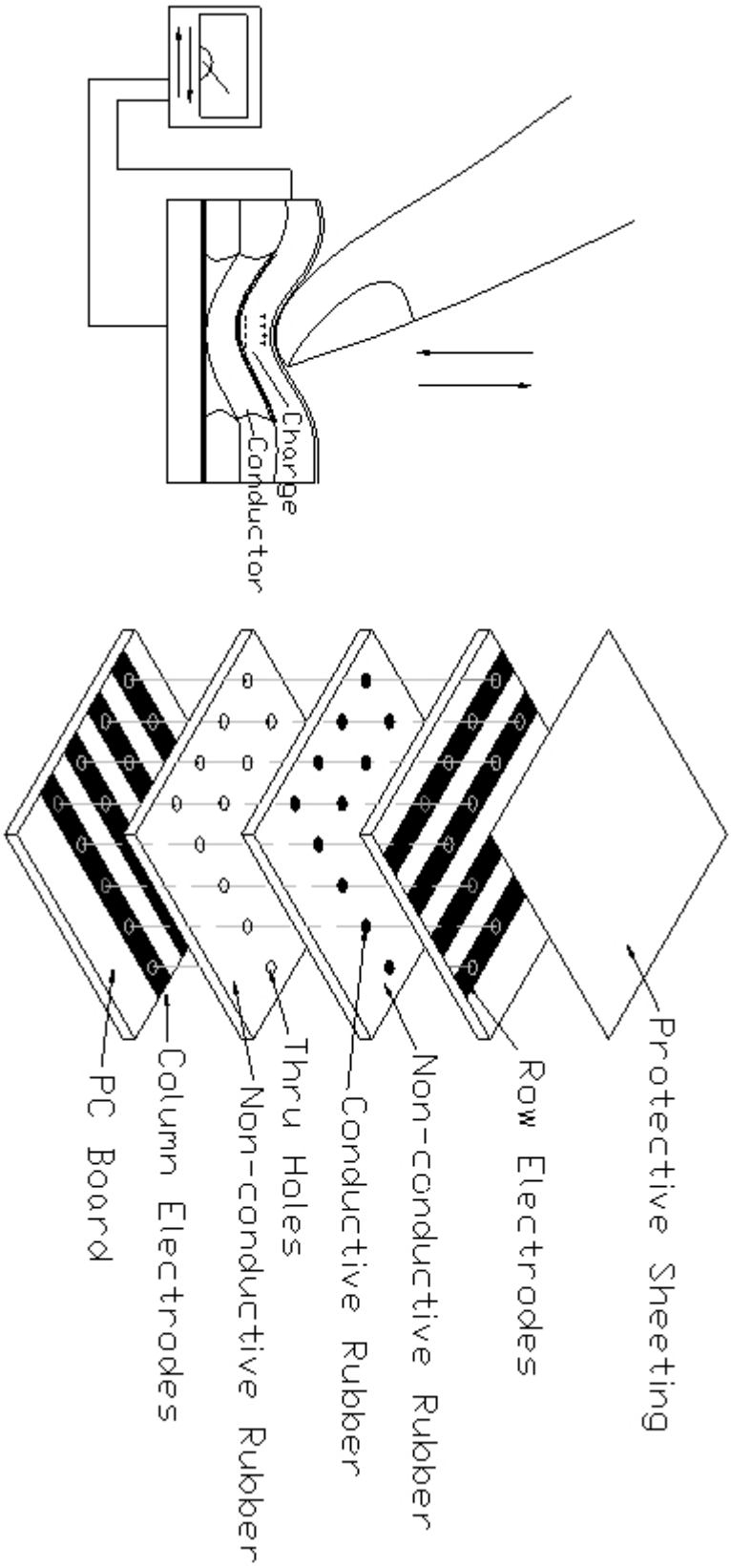

Figure 3.15: The structure of a sample piezo electric device [17]

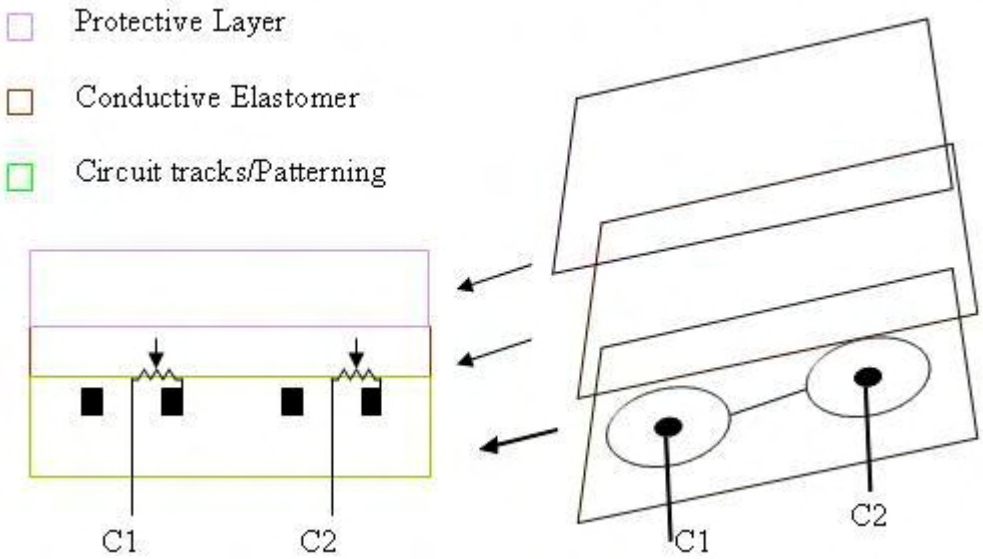

Figure 3.16: The structure of a conductive elastomer device [17]

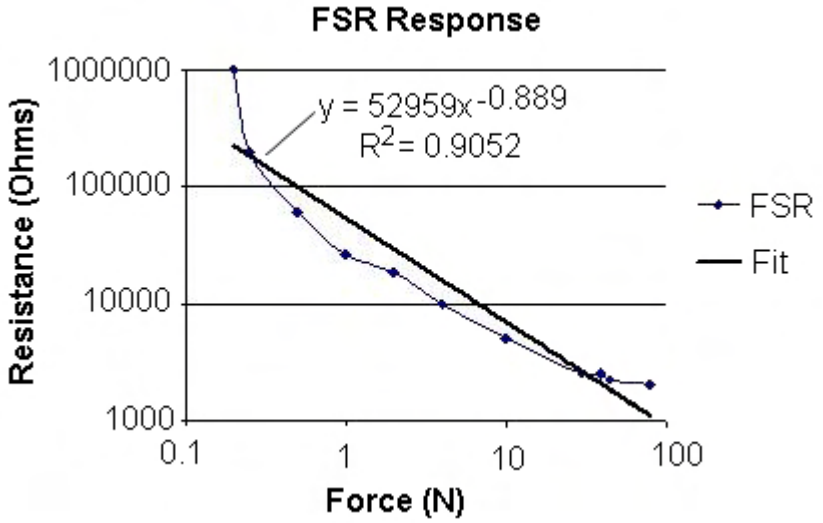

Figure 3.17: The typical response of a FSR [18]

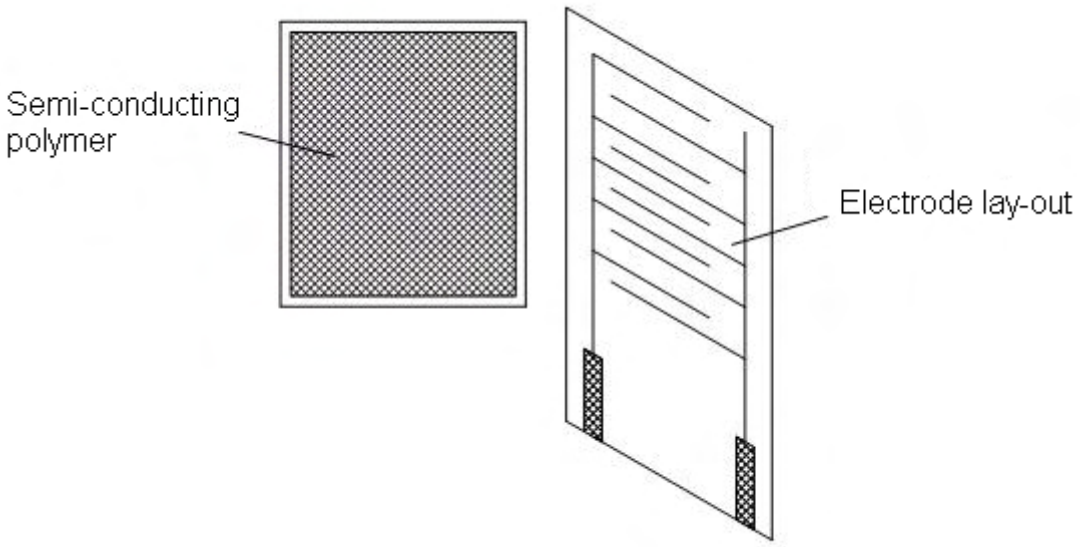

Figure 3.18: A FSR [18]

also presents us with some challenges. On the other hand, conductive elastomers offer a reduced size but at the cost of high temperature sensitivity and low durability. Whereas, the FSR, is durable, withstands temperature of up to 400^o C and can measure static and transient loads though at the cost of high drift of 10 to 20 % (depending on sensor design) of the initial value and has a non-linear output at high temperatures. The further disadvantage of FSR sensors is that they are difficult to purchase *off the shelf*.

In conclusion, it is difficult from this discussion to pick a clear winner, since all of the different sensor film techniques have their problems. However, the FSR sensor despite its disadvantages if a sensor can be custom fabricated, it may be able to be used for a SBP application.

Please note: In the previous sections we reviewed electronic force measurement techniques. This review took place near the start of the project. As the project proceeded, it became clear that photon based techniques would perhaps suit our application better. In the coming section we review these techniques. Appendices D and E contains review material for this coming section.

3.3.5 Fibre Optic Sensors

3.3.5.1 Introduction

FO technology forms a wide spectrum of concepts and techniques; here we focus on Fibre Optic Sensor (FOS). Generally, FOS have no moving parts, and are a modified section of the fibre rather than a separate sensor. When a FOS is calibrated, it is possible to translate measured strains to equivalent forces, just like a strain gauge, but with several distinct advantages.

3.3.5.2 Description

FOSs rely on different methods to function, the three most common methods are:

1. Scatter based Methods
2. Interference based Methods
3. Reflection based Methods

There descriptions follow:

1. Scatter based Methods The most common types of scattering are named after their inventors: Lord Rayleigh (1842 – 1919), Raman (1888 – 1970), Compton (1892 – 1962), Tyndall (1820 – 1893) and Brillouin (1889 – 1969), these can most easily be demonstrated in Figures 3.19 - 3.23.

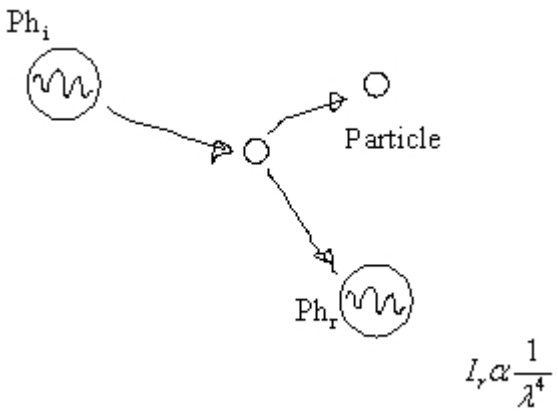

Figure 3.19: Rayleigh scattering [19]

In Rayleigh scattering (please refer to Figure 3.19, on the left) a high energy incident photon Ph_i strikes a suspended particle and rebounds elastically after the collision, the reflected photonsintensity of reflected light, is equal to the inverse of the wavelength to the power of 4. This is known as *Rayleighs Law*. Rayleigh scatter relates to the elastic scattering of light on particles smaller in diameter than the wavelength

of light. It usually occurs in transparent media, such as: solids, liquids, but more commonly in gases, such as air. For scattering of particles larger in diameter than the wavelength of light this is covered by *Mie* scattering.

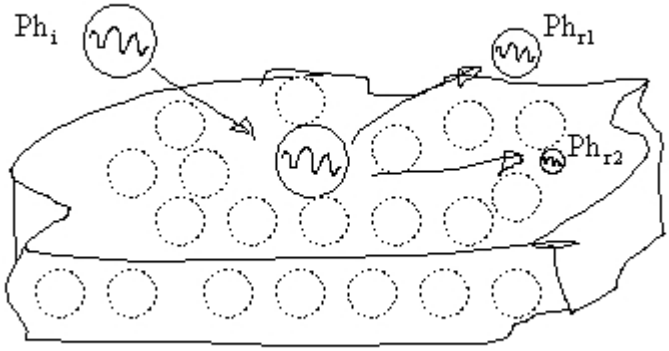

Figure 3.20: Raman scattering [20]

In Raman scattering (please refer to Figure 3.20), an incident photon Ph_i strikes a piece of material. The majority of light reflects at the same frequency as the incident light a small portion of the reflected light (Raman Scattering, Ph_{r2}) is shifted in frequency by the atoms of the constituent material. By using Raman spectroscopy scientists can determine the type of vibration frequencies of the atoms and thus the physical and chemical structure of the material under observation. Sensors developed using derivatives of this effect can accurately measure temperature over lengths of up to 10 km, with a temperature resolution of 10^o C and spatial resolutions of 0.1 metres [20]. Unfortunately, the spatial resolution is still too large to use in a SBP.

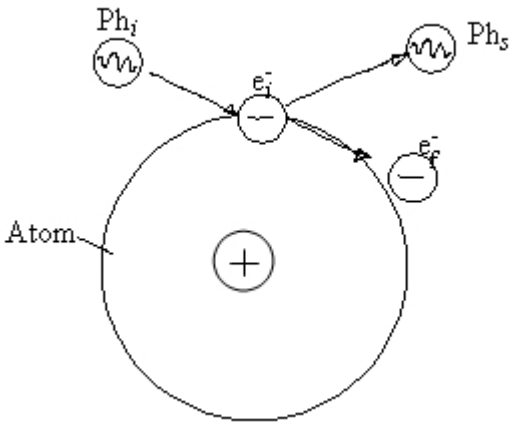

Figure 3.21: Compton scattering [21]

Whereas in Compton scattering (please refer to Figure 3.21), an incident photon Ph_i elastically strikes an orbiting electron and it ejects it from the outer shell. Most

of the energy from the collision is not absorbed but given to the scattered Photon, Ph_s in true *particle like fashion* [21].

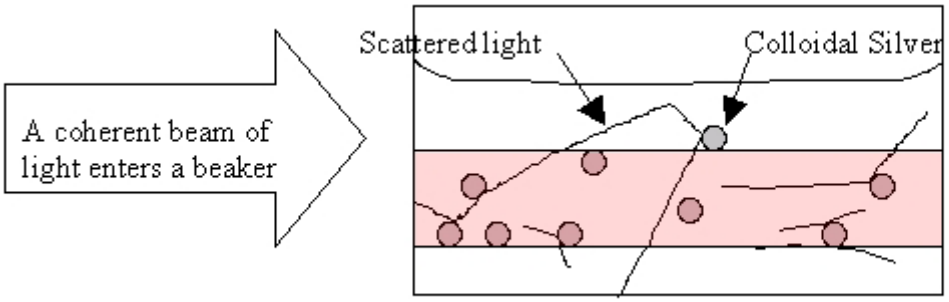

Figure 3.22: The Tyndall Effect [22]

With the Tyndall effect, a beam of coherent light such as a laser,(please refer to Figure 3.22) enters the side of a beaker of liquid containing colloids[1] of silver. The beam strikes some of the particles producing a visible coherent beam of light through the medium. This effect can be used to test the presence of particles in a liquid.

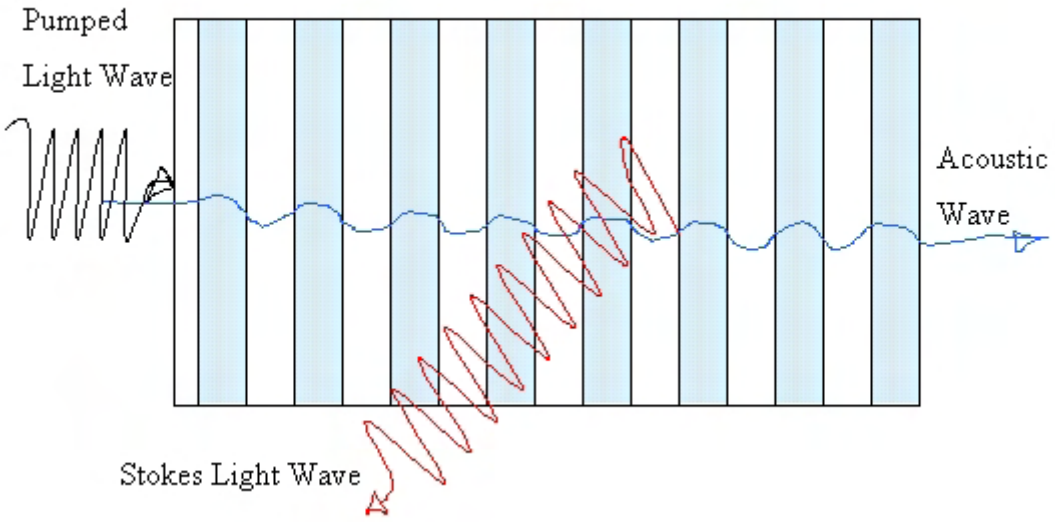

Figure 3.23: Spontaneous Brillouin scattering [23]

In Brillouin scattering, pumped laser light enters a transparent medium (please see Figure 3.23). In the same medium, an acoustic *standing wave*[2] is present. An interaction occurs between the laser light and the standing wave producing a backscattered *stokes* component, of a lower frequency to the incident pumped light wave and a change in frequency of the acoustic wave. By studying the shift in frequencies, we can accurately measure temperature continuously over a length of fibre. Such techniques have been used to study the curing rates of concrete. They have also

[1] Tiny divided particles
[2] A standing or stationary wave is created by opposing waves interfering with each other

been used to measure the time and temperatures changes in a lake utilising an already installed optical communication cable [23]. Stimulated Brillouin scattering can enhance the effectiveness of systems based on this effect [20].

Of these types of scattering: Rayleigh, Raman and Brillouin are commonly found in FOS development. Both Brillouin and Raman techniques have been used for distributed temperature measurement. Raman Distributed Temperature Systems (DTS) are expensive compared to other systems though they are self calibrating and can be used over tens of kilometres with a temperature resolution in the order of 1^o C and an interrogation length in the order of metres [49, 50]. These systems are ideally suited to logging temperature field in oil wells, Fire alarm DTS for use in tunnels and long process ovens . Another, great advantage of the Raman system is that temperature is measured independently thus there is no cross-sensitivity with strain . Parker [51] achieved both strain and temperature measurement by making use of the Brillouin shift and power levels.

2. Interference based Methods The most common types of interferometric sensors are Mach-Zehnder, Michelson and Fabry-Perot (F-P). F-P is best suited to embedded applications. A&M University in 1988 [27] presented a new approach towards measuring thermal and strain effects. The team developed a simple intrinsic F-P interferometer by assembling two lots of cleaved single mode fibre ends together, via a special fusion splicing technique. Before assembling the fibre ends, they were coated with titanium dioxide via chemical vapour deposition to create a small semi-reflective mirror on one of faces of the fused fibre. Multi-sections of these mirrored faces were assembled to create the interferometer, see Figure 3.24 a. and b. Another basic type of F-P is the extrinsic version, see Figure 3.24 c. This type of device is easier to fabricate. The gap and alignment of the fibres is achieved by a small glass tube which holds the faces together rather than being integral to the fibre. It also has the benefit of not suffering from loss of fringe due to polarisation effects of the fibre as does the intrinsic type [52].

Either intrinsic or extrinsic type F-P sensors have difficulty in distinguishing between whether a specimen is in compression or tension. A transmission type Extrinsic Fabry Perot Interferometer (EFPI) type device solves this problem.

Figure 3.25 gives a basic theoretical geometry for the F-P technique. Incident light on the left hand side of the figure enters at angle α. The light refracts at the interface between the atmosphere and the core of the fibre and refracts again as it enters the polished interfaces of the F-P interferometer. As the surfaces are highly polished some of the light reflects a number of times between the gap, whilst the remainder of the beam continues on it journey down the fibre. Strain and temperature can be measured by analysing the relative output power that occurs as a result of changes in the spacing d. Changes in the spacing causes phase changes and subsequent fluctuations between constructive and destructive interference between successive beams and thus changes in the relative output power [53].

In summary, F-P based sensors have promise yet as they are dependent on constructive and destructive interference. They are also susceptible to losses in the fibre caused by fusion splicing and sharp bends. Another disadvantage of this technique is that it would require careful processing to produce multiple sets of sensors over a small area as required in SBP development. Though the processing of data is relatively simple, the processing of multiple sensors on one fibre using as in a *quasi-distributed network* would be difficult, but very impractical over multiple fibres.

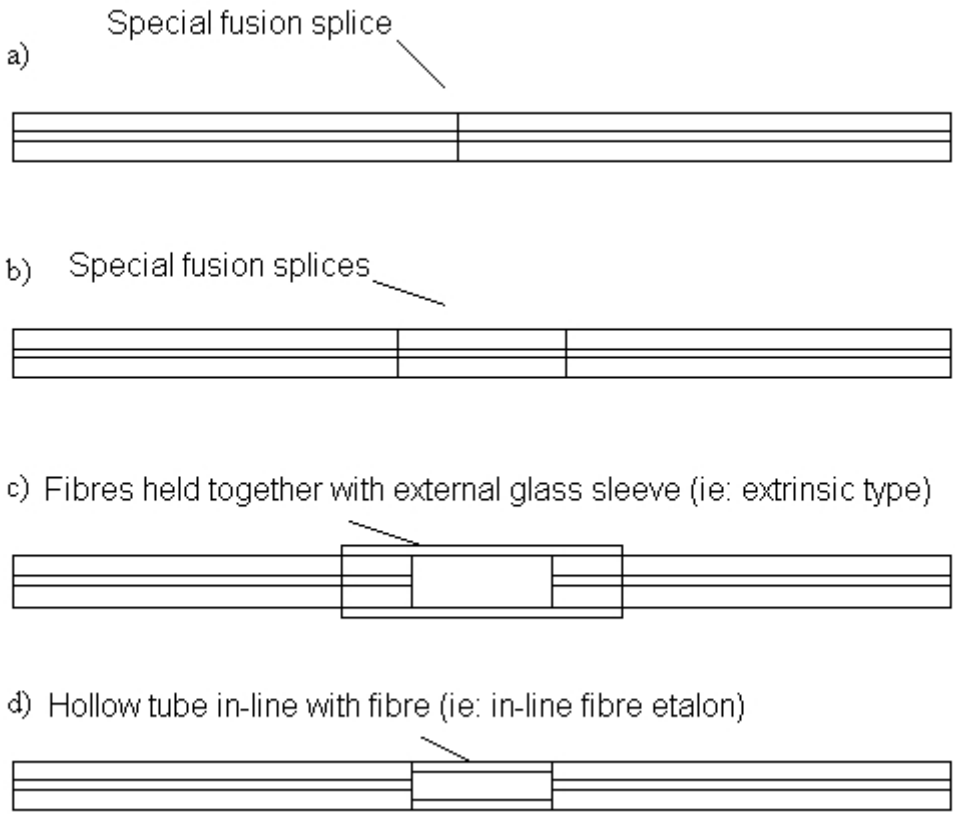

Figure 3.24: Interference based methods

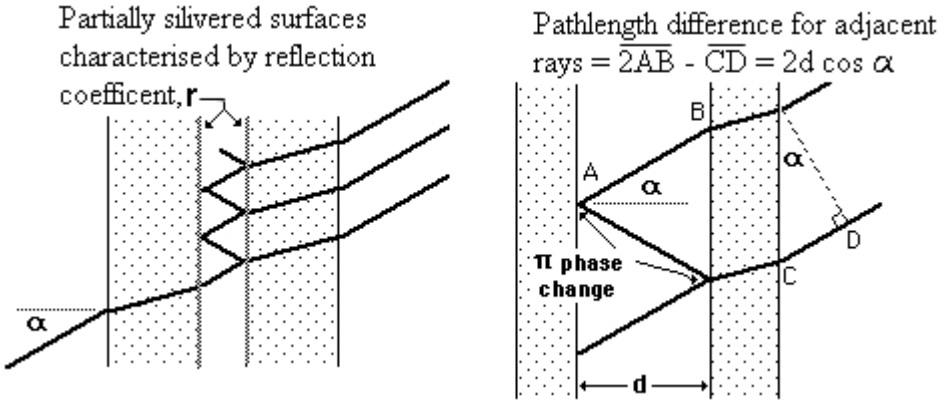

Figure 3.25: Geometry of a F-P interferometer [19]

This is a further reason for not using this type of sensor for SBP development.

3. Reflection based Methods One of the simplest and most adaptable of optical fibre sensing technologies is the Fibre Bragg Grating (FBG) sensor. FBG sensors were discovered in 1978 accidentally by Ken Hill et al in Canada whilst investigating Continuous-wave (CW) Fibre Raman Lasers [54]. A standard FBG sensor is a small (5 to 10 mm long) integral section of a single mode optical fibre that has been specially processed using a laser[1] to produce alternating regions of differing refractive index. The sensor works by monitoring a shift in wavelength of the reflected signal, called *Bragg signal* or *Bragg wavelength* (please refer to Figure 3.26).

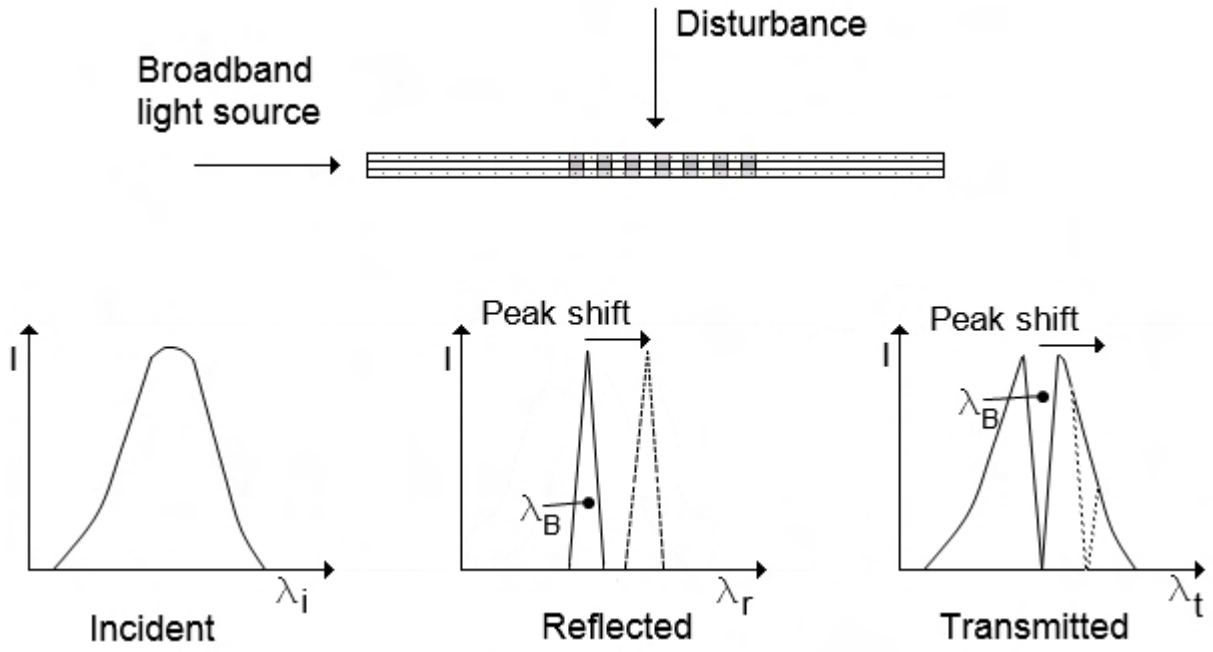

Figure 3.26: FBG sensor and spectrums

Light from a spectrally broad light source (please refer to Figure 3.26) is launched into a fibre containing a Bragg grating. When light of the Bragg wavelength strikes the grating it is reflected but all other wavelengths are allowed to pass through the device. If a disturbance is witnessed by the Bragg grating, a shift of the centre wavelength occurs. By recording the shifts in wavelengths a linear relationship develops between the strain and peak shift. Straining or physically disturbing the fibre shifts the launched spectrum in one direction and temperature shifts in the opposite direction. Often a separate grating is needed to measure temperature unless birefringent[2] fibre is used. FBG are not dramatically affected by losses in the fibre due to fusion splicing or tight bends as the measurements are reliant on peak shifts not intensity like other methods.

The Bragg wavelength, λ_B is related to the refractive index of the material, n and the grating pitch, Λ by Equation 3.20 [20].

$$\lambda_B = 2n\Lambda \tag{3.20}$$

[1] Holographically or mask
[2] double refracting

Mechanical strain will cause a change in pitch of the grating and thus a linearly corresponding change in Bragg wavelength. Strain being the change in the gauge length over the original length gives Equation 3.21

$$\varepsilon = \frac{\Delta\Lambda}{\Lambda_{OB}} \tag{3.21}$$

Where:

ε	strain
$\Delta\Lambda$	change in pitch
Λ_{OB}	is the original FBG pitch

In terms of wavelength we have,

$$\varepsilon = \frac{\Delta\lambda}{\lambda_{OB}} \tag{3.22}$$

Where:

$\Delta\lambda$	change in wavelength
λ_{OB}	original wavelength

And to account for temperature we have [55],

$$\varepsilon = k\left(\frac{\Delta\lambda}{\lambda_{OB}} - \xi\Delta T\right) \tag{3.23}$$

Where:

k	is a constant which is a function of: refractive index, Poisson's ratio and strain-optic constants of the fibre
ξ	is the thermo-optic coefficient
ΔT	is change in temperature

Equation 3.23 is suitable for compensating for the effects of temperature in an optical fibre sensor which measures both strain and temperature simultaneously. It may also be used in FBG sensors that measure strain only if extreme care were taken with placement and selection of thermocouples.

Some FBG sensors have been used at operating temperatures of up to 300^o C[1] with linear output [56]. Often thin[2] polymer coatings such as polyimide are applied on top of the cladding to increase or maintain high operating temperatures such as this. Bragg gratings also come in a variety of types, mainly short[3], long[4] and chirped[5] gratings. Gratings are also commercially available yet costs are in the order of AUD $500 dollars per grating, are fragile, and easily broken making testing expensive and time consuming. Yet some birefringent gratings offer the ability to perform multi-axis strain and temperature measurements simultaneously with the advantage of

[1] The temperature at which FBG's can be created using ultraviolet light
[2] Measured in microns
[3] 5−10 mm
[4] 10−300 mm
[5] A normal fibre where the pitch of the periodic change in the reflected index varies along the grating

the grating being as thick as 160 μm and a interrogation length of between 5 and 10 mm [57]. Some interrogation system manufacturers boast scan rates of up to 250 Hz for 125 FBG on a single fibre [58]. A similar strain gauge system would involve many more cables and act as an antennae for Electro-Magnetic (EM) Radiation [49]. FBG systems can be multiplexed allowing the continuous monitoring of up to 512 sensors at 125 Hz [58]. These systems typically use Wavelength Division Multiplexing (WDM) [20]. What makes this achievable is that, FBG sensors require a spectrally broad source (50 nm). Each grating has a unique wavelength and thus each grating has its own unique address. These sensors are presently used in civil engineering for structural health monitoring of bridges, buildings, defence[1] and in the oil industry where they are used to measure deep−hole oil pressure [57, 58].

3.3.5.3 Discussion and Conclusion
- Fibre Optic Sensors -

Raman Distributed Temperature Sensing (DTS) is an excellent method for large continuous monitoring of various civil and other structures where this type of sensing is needed, though the measuring of temperature is a secondary benefit and not a primary aim of the SBP. It was shown that Brillouin techniques are feasible for combined temperature and strain measurements, but are not suitable for this application, though they may be in the future. F-P interference based techniques could possibly be used as they are easy to interface to existing technologies, yet it would be difficult and time consuming to process a series of F-Ps over a small distance in comparison to other techniques such as FBG, which can now be processed fairly rapidly used mask laser techniques. In addition, F-Ps would be difficult to network in series a requirement for a SBP. The FBG sensors along with encompassing the great benefits of optical sensor technology: not being susceptible to EM radiation, being able to be easily networked and multiplexed with minimum amount of cabling are also smaller than many of the other sensors and could easily fit into a SBP given the right packaging. Yet a down side to optical technology in general, is the high cost of the associated hardware, though the benefits surely out way this detriment.

[1] For materiel life-extension research programs

3.3.6 Discussion and Conclusion
- Review of Force Measurement Techniques -

From our initial analysis thick film sensor based on FSR^{TM} and allied techniques were found to be the most applicable techniques based on the literature investigation. As the research program progressed the need for another technique arose since the allied sensor we had purchased did not live up to that predicted by the literature or our expectations. At this time our awareness of FOS was emerging as the technique was starting to appear on the edges of accessible usage. Of these it is the FBG sensors which we believe will take us to our final destination: i.e. a useable SBP for laboratory and test track usage.

3.4 Thick Film Investigation

3.4.1 Introduction

In the last section we reviewed force measurement techniques and chose two different techniques to investigate.

In this section, we investigate *thick film sensors*; this will be covered in the following subsections:

1. Thick Film Smart Brake Pad Design Summary
2. Thick Film Sensor Development
3. Thick Film Theory
4. Thick Film Smart Brake Pad Room Temperature Tests
5. Thick Film Smart Brake Pad Elevated Temperature Tests

3.4.2 Thick Film Smart Brake Pad Design Summary

Earlier in the chapter, (please refer to section 2) we discussed several possibilities of where to place a sensor within a SBP. For the TF sensor, we had opted for placing the film between the friction material and the backing plate. This is analogous to a *push button light switch*, where each of the three friction material segments would be *individual friction material buttons* held down by a fixture constructed of steel, affixed to the backing plate (please refer to Figure 3.27).

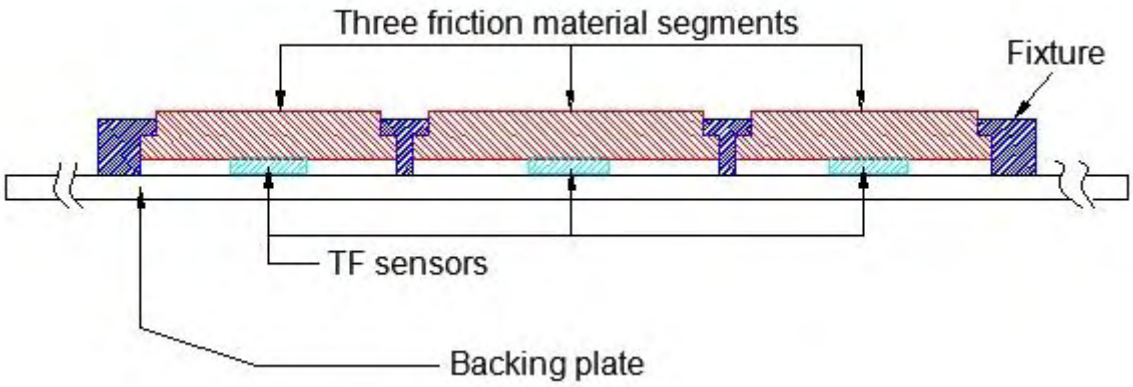

Figure 3.27: Cross-section of a SBP designed for the TF sensor

This method has following advantages:

- The load is dispersed across three separate pad elements which reduce measurement error compared to using one large element
- It is reusable – environmentally friendly and cost effective
- It is robust – withstands the rigours of the testing environment
- Easily manufactured and assembled with minimum number of pieces
- Different types of pad materials can easily be tested individually or as sets
- The sensor need only be a flat sheet or embedded into a flat sheet allowing multiple types of sensor technologies to be tested individually or simultaneously
- It could be assembled by lab technicians

3.4.3 Thick Film Sensor Development

The TF sensor for the SBP was developed in cooperation with the International Microelectronics Research Corporation (IMRC). Our sensor array used his electrode configuration[1] with the trademark, *Prescon*^{TM} as the underlying technology. Figure 3.28, shows the schematic for the Prescon^{TM} electrode configuration[2].

Once the TF technology manufacturer was chosen that best met the SBP-SDC, we were able over many months to design a sensor array to fulfil our requirements. For the schematic diagram of the sensor array and a photo of the finished sensor (please refer to Figures 3.29 and 3.30).

Please refer to Appendix C for approximate techniques used to manufacture the sensor.

3.4.4 Thick Film Theory

The technology provided to us by IMRC is not that of a FSR according to the President. What is known about its operation is that it ought to have an operating temperature up to 180^o C. It also has a conduction curve which appears similar to that of a conductive elastomer.

After investigating similar technologies, here we develop a basic theory of operation for this sensor; since none existed at the time. First we investigate the structure of the device (please refer to Figure 3.31)[3]

If we now notice the top Kapton sheet of the sensor (No. 14). The underside is screen printed with a resistive polymer (No. 17). Since only one side of this top sheet is screen printed and fired, the resulting stresses have caused a dimple (please refer to Figure 3.32). The middle sheet (please refer to Figure 3.31, No. 13) is to compensate for the thickness of the copper (No. 10) and the resistive polymer. The sheets were most probably joined together via heat activated glue forming a strong durable cell. The underside of the lower layer (No. 12) also has a self-adhesive pull-off film allowing the sensor to be stuck to an object for measurement.

Once the layers are heat-sealed together, and a further disc of Kapton (sticker) is stuck on to the upper layer of the film to compensate for the dimple. The cell is then ready for testing.

[1] Individually addressable load cell
[2] The actual one we used is slightly different
[3] Please see Appendix F for dimensions of the components.

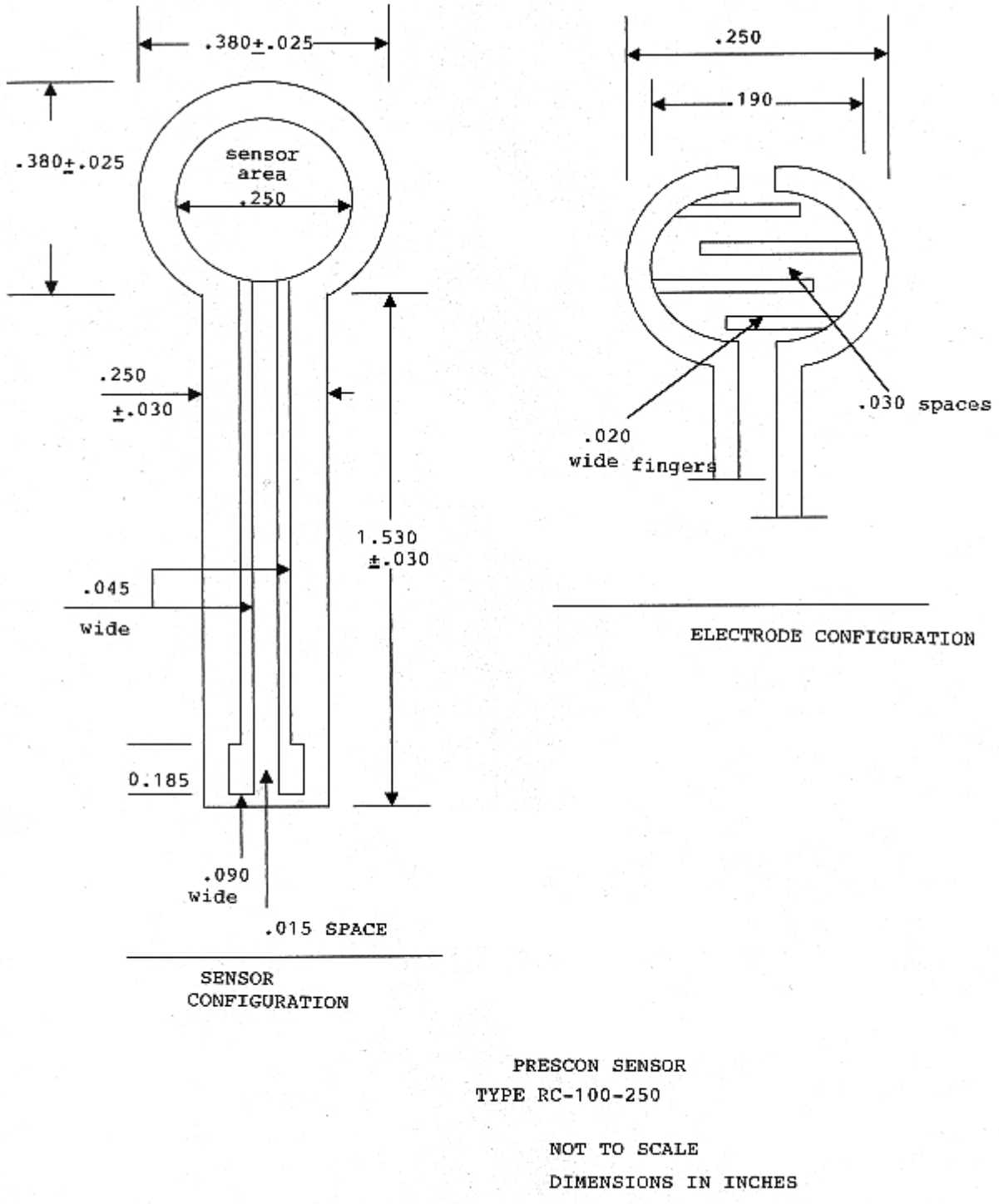

Figure 3.28: Prescon^{TM} electrode configuration

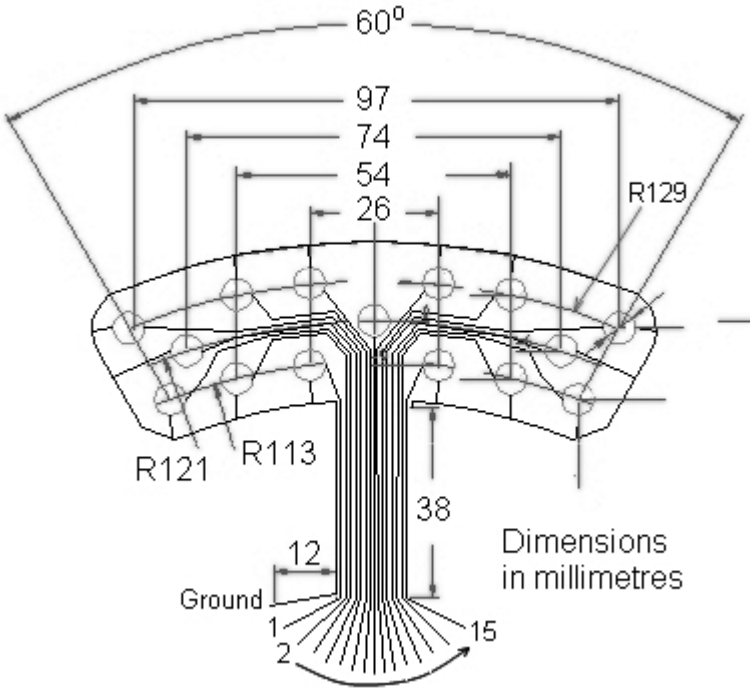

Figure 3.29: SBP TF sensor design

Figure 3.30: Manufactured SBP TF sensor

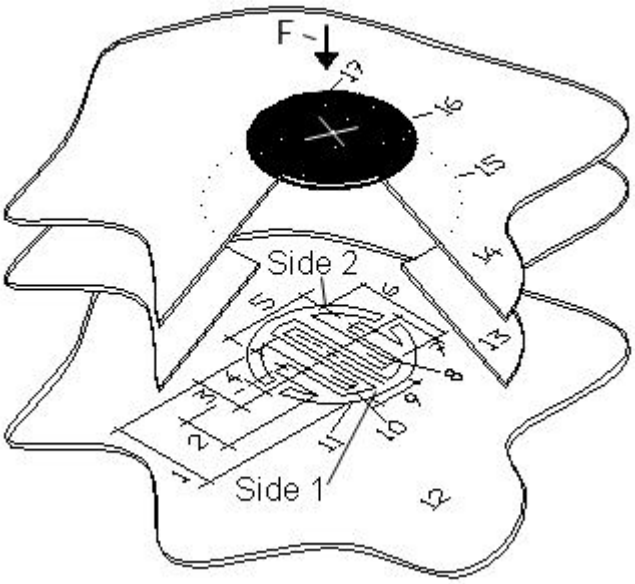

Figure 3.31: Structure of a single TF sensor cell

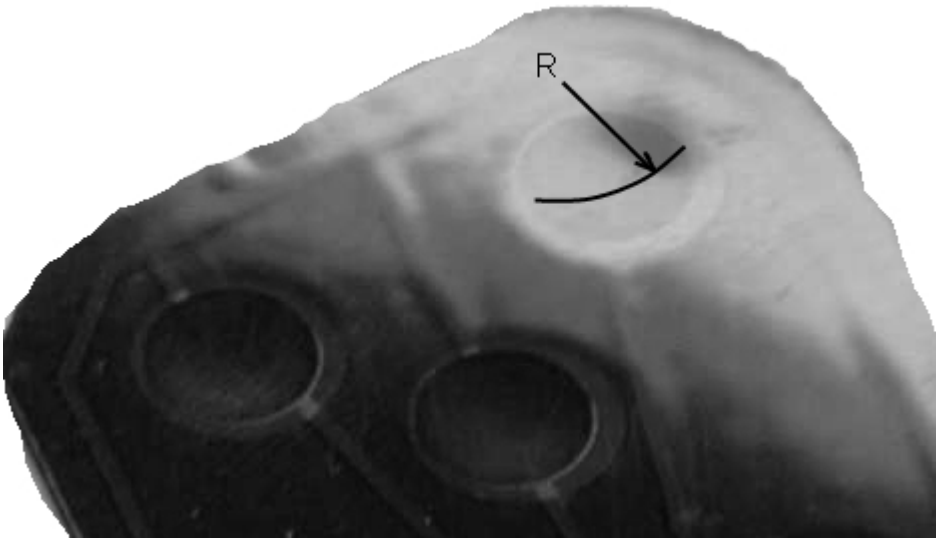

Figure 3.32: Close-up of TF sensor cell with dimple

If such a sensor (please refer to Figure 3.31) is tested, we would expect to get a conduction curve similar to that shown in Figure 3.33. The data in this example was provided to us by IMRC. The function fitted to the data is of the form of Equation 3.24.

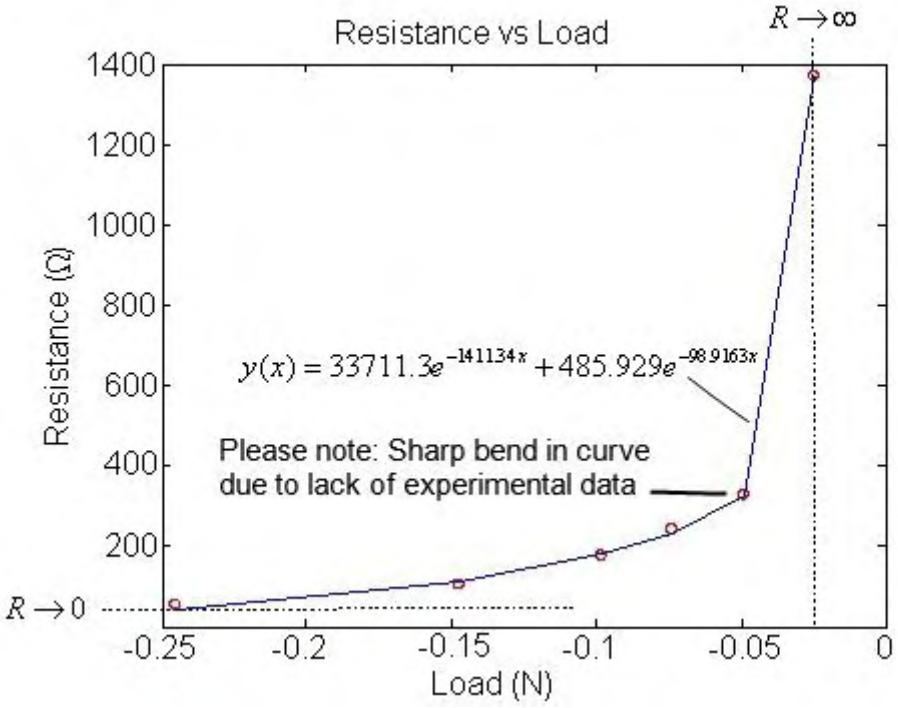

Figure 3.33: Conduction curve for a IMRC TF sensor cell

$$R_T = Ae^{-\beta_1 F} + Be^{-\beta_2 F} \tag{3.24}$$

Where:

R_T	total resistance for a thick film sensor cell
F	force
A, B, β_1 and β_2	are parameters to be found

The missing parameters of Equation 3.24 were found by using the data supplied to us by IMRC and a Gauss-Newton Least Squares optimisation routine utilising MatLab®'s Optimisation toolbox.

We now derive the theory of operation of the sensor by examining how it functions.

Assumptions

- The material and operation of the sensor is assumed to be linear elastic[1] and homogenous for the strains and displacement encountered during its operation
- The possible capacitive effects in the Resistive Polymer (RP) are minimal and therefore we neglect them
- In the RP we assume there are small gaps between subsequent discretised volumes; rather than one continuous layer

[1]Unless, otherwise noted

At the no-load position, there is a very large or near infinite resistance (please refer to Figure 3.33). As the load is increased the resistance drops sharply following an exponentially decreasing relationship. The key to the sensor's non-linearity, is believed to be the result of the RP. As the load is applied contact is made between the RP and the lower electrode (please refer to Figure 3.31, item 10) allowing current to flow between the two sides of the electrode. The amount of current I that is allowed to flow is determined by the amount of resistance R which is related by Ohms law given in Equation 3.25.

$$V = IR \tag{3.25}$$

or,

$$I = \frac{V}{R}$$

The following two cases describe possible relationships between resistance and the sensors' geometry:

Case 1 (C1)

If you imagine the discretised width (please refer to Figure 3.34, item 8) of the resistive polymer having a particular resistance. If this length was increased by an amount dw (please refer to Figure 3.35) as a result of the applied force depicted in Figure 3.35 there would be a corresponding increase in resistance between adjacent fingers, analogously to increasing the length of a traditional resistor. Increasing this length would be achieved by increasing the gap between the fingers. Having a thinner *film thickness* (h in Figure 3.35) and a longer *Length of Fingers in Contact* (L_{fl}) ($L + dL$ in Figure 3.35) would decrease the cross-sectional area A_I and increase the resistance. Thus these relationships would follow the law of resistivity in a metal wire expressed in Equation 3.26.

$$R_{C1} = \rho_{C1}\frac{w}{A_I} \tag{3.26}$$

Where:

R_{C1}	resistance for Case 1
ρ_{C1}	specific resistance of RP for C1
w	width in Figure 3.35
A_I	Area. $A_I = h \times L$ in Figure 3.35

Case 2 (C2)

Suppose a load is applied onto the unstressed conductor thereby compressing h; traditionally this would increase the resistance as in C1 (please refer to Figure 3.35). However, since the RP is dispersed with metal particles decreasing the thickness, would actually decrease the resistance. Equation 3.27 expresses this mathematically.

$$R_{C2} = \rho_{C2}\mathfrak{V}_T \tag{3.27}$$

Where:

R_{C2}	resistance for C2
ρ_{C2}	specific resistance of RP for C2
$\mathfrak{V}_T$	total volume of RP per cell

Using symmetry, the total volume of RP $\mathfrak{V}_T$ is discretised into three convenient shapes (please refer to Figure 3.34, No. 2, 3 and 4). To find the total volume we then double this value since the whole electrode is covered in resistive polymer.

Before we continue, using Figure 3.34, we now define a number of components needed for the ensuing formulation:

1. Film thickness h
2. Large rectangular area R_{al} of RP. $\mathfrak{V}_1 = R_{al} \times h$
3. Small rectangular area R_{as} of RP. $\mathfrak{V}_2 = R_{as} \times h$
4. Small triangular area T_{as} of RP. $\mathfrak{V}_3 = T_{as} \times h$
5. Finger width f_w
6. Finger spacing f_s
7. Length of finger in contact *long* L_{fl}
8. Length of finger in contact *short* L_{fs}
9. Height of triangle H_t. $H_t = L_{fl} - L_{fs}$
10. Width of rectangle W_r. $W_r = f_s + f_w$
11. Copper electrode
12. Capacitor
13. Variable resistor

The three areas and volumes of RP (R_{al}, R_{as}, T_{as}, $\mathfrak{V}_1$, $\mathfrak{V}_2$, $\mathfrak{V}_3$ and $\mathfrak{V}_T$) are calculated in Equations 3.28, 3.29, 3.30, 3.31, 3.32, 3.33 and 3.39.

$$R_{al} = L_{fl}(f_s + f_w) \tag{3.28}$$

$$R_{as} = L_{fs}(f_s + f_w) \tag{3.29}$$

$$T_{as} = 1/2(f_s + f_w)(L_{fl} - L_{fs}) \tag{3.30}$$

$$\mathfrak{V}_1 = R_{al}h \tag{3.31}$$

$$\mathfrak{V}_2 = R_{as}h \tag{3.32}$$

$$\mathfrak{V}_3 = T_{as}h \tag{3.33}$$

$$\mathfrak{V}_T = 2[\mathfrak{V}_1 + \mathfrak{V}_2 + \mathfrak{V}_3] \approx 4\mathfrak{V}_1 \tag{3.34}$$

The total resistance for the TF sensor is the sum of both C1 and C2, however $C2 \gg C1$ and therefore we ignore the influence of C1 and use C2 and Equation 3.39 for the rest of the formulation.

Equation 3.24 has a Differential Equation (DE) of the form[1]:

$$\frac{d^2R_T}{dF^2} + (|\beta_1| + |\beta_2|)\frac{dR_T}{dF} + (|\beta_1| \times |\beta_2|)R_T = 0 \tag{3.35}$$

Equation 3.24 is also the solution of this DE. This said, Equation 3.35, is a DE which represents the operation of the TF sensor.

However, as in our case, if the data is captured via a DAQS and expressed in terms of negative voltage, and negative load (implying compression), the sign ($\pm$) will change from positive $+$ to negative $-$. Thus Equations 3.24 and 3.35 will become Equations 3.36 and 3.37. Equation 3.38 is the resistance version of Equation 3.37 that we will use for the derivation and only change back to voltage at the end; because it is easier to think in terms of resistance rather than voltage.

[1]The general numerical form of this equation came from a table of generic results presented in Stroud [45], page 693.

$$V = Ae^{\beta_1 F} + Be^{\beta_2 F} \tag{3.36}$$

The DE is,

$$\frac{d^2V}{dF^2} - (|\beta_1| + |\beta_2|)\frac{dV}{dF} + (|\beta_1| \times |\beta_2|)V = 0 \tag{3.37}$$

And, the resistance version of the DE, is,

$$\frac{d^2R_T}{dF^2} - (|\beta_1| + |\beta_2|)\frac{dR_T}{dF} + (|\beta_1| \times |\beta_2|)R_T = 0 \tag{3.38}$$

First, we start by finding a relation for volume with respect to (wrt) height,

$$\mathfrak{V}_T = 4A_{ii}h \tag{3.39}$$

$$\frac{\partial \mathfrak{V}_T}{\partial h} = 4A_{ii} \tag{3.40}$$

Giving,

$$\partial \mathfrak{V}_T = 4A_{ii}\partial h \tag{3.41}$$

Second, a relation for force wrt height,

$$\sigma = E\varepsilon \tag{3.42}$$

$$\varepsilon = \frac{dh}{h} \tag{3.43}$$

Substitute Equation 3.43 into 3.42, giving,

$$\sigma = E\frac{dh}{h} \tag{3.44}$$

As,

$$\sigma = \frac{F}{A_{ii}} \tag{3.45}$$

Then substitute Equation 3.45 into Equation 3.44,

$$\frac{dF}{A_{ii}} = E\frac{dh}{h} \tag{3.46}$$

$$dF = \frac{A_{ii}E}{h}dh \tag{3.47}$$

Third, we find a relationship for resistance wrt height,

$$R_T = \rho 4A_{ii}h \tag{3.48}$$

$$\frac{\partial R_T}{\partial h} = \rho 4A_{ii} \tag{3.49}$$

$$\partial R_T = \rho 4A_{ii}\partial h \tag{3.50}$$

Now, substituting Equation 3.41 into Equation 3.47 (in terms of dh), we have,

$$dF = \frac{E}{h4} d\mathfrak{V}_T \tag{3.51}$$

Substituting Equation 3.41 into Equation 3.51, we have,

$$dF = \frac{EA_{ii}}{h} dh \tag{3.52}$$

Substituting Equation 3.50 into Equation 3.52, giving,

$$dF = \frac{E}{h\rho 4} dR_T \tag{3.53}$$

$$\frac{dR_T}{dF} = \frac{h\rho 4}{E} \tag{3.54}$$

Finding the second derivative,

$$\frac{d^2 R_T}{dF^2} = 0 \tag{3.55}$$

Substituting Equations 3.54 and 3.55 into Equation 3.38, giving,

$$0 - (\beta_1 + \beta_2)\frac{h\rho 4}{E} + (\beta_1 + \beta_2)\rho 4 A_{ii} = 0 \tag{3.56}$$

Arrange in terms of β_1 and β_2 and expand the brackets,

$$\frac{h}{A_{ii}E}\beta_1 = \left(\frac{\beta_1 + \beta_2}{\beta_2}\right) \tag{3.57}$$

$$\frac{h}{A_{ii}E}\beta_2 = \left(\frac{\beta_1 + \beta_2}{\beta_1}\right) \tag{3.58}$$

$$(\beta_1 + \beta_2) = \frac{h}{A_{ii}E}\left(\frac{\beta_1^2 + \beta_2^2 + 2\beta_1\beta_2}{\beta_1\beta_2}\right) \tag{3.59}$$

$$(\beta_1 \times \beta_2) = \left(\frac{h}{A_{ii}E}\right)^2 \left(\frac{\beta_1^2 + \beta_2^2 + 2\beta_1\beta_2}{\beta_1\beta_2}\right) \tag{3.60}$$

Let,

$$\beta_T = \left(\frac{\beta_1^2 + \beta_2^2 + 2\beta_1\beta_2}{\beta_1\beta_2}\right) \tag{3.61}$$

Then substituting Equations 3.59, 3.60 and 3.61 into Equation 3.62, giving,

$$\underbrace{1}_{a}\frac{d^2 R_T}{dF^2} - \underbrace{\beta_T\left(\frac{h}{A_{ii}E}\right)}_{b}\frac{dR_T}{dF} + \underbrace{\beta_T\left(\frac{h}{A_{ii}E}\right)^2}_{c} R_T = 0 \tag{3.62}$$

We now compare the Beta β components of Equations 3.62 and 3.38, giving,

$$(|\beta_1| + |\beta_2|) = \beta_{Tb}\left(\frac{h}{A_{ii}E}\right) \tag{3.63}$$

$$\beta_{Tb} = (|\beta_1| + |\beta_2|)\left(\frac{A_{ii}E}{h}\right) \tag{3.64}$$

$$(|\beta_1| \times |\beta_2|) = \beta_{Tc}\left(\frac{h}{A_{ii}E}\right)^2 \tag{3.65}$$

$$\beta_{Tc} = (|\beta_1| \times |\beta_2|)\left(\frac{A_{ii}E}{h}\right)^2 \tag{3.66}$$

Where the sub-sub scripts b and c denote the components of Equation 3.62.
Substituting, Equations 3.63 and 3.65 into Equation 3.38, giving,

$$\underbrace{1}_{a}\frac{d^2R_T}{dF^2} - \underbrace{\beta_{Tb}\left(\frac{h}{A_{ii}E}\right)}_{b}\frac{dR_T}{dF} + \underbrace{\beta_{Tc}\left(\frac{h}{A_{ii}E}\right)^2}_{c}R_T = 0 \tag{3.67}$$

Equation 3.67 is a second order DE with constant coefficients. Since it is a second order differential equation, there will be two solutions with two arbitrary constants; one for each. The sum of these solutions forms the complete solution, Equation 3.72. We can now write Equation 3.67 in the form of an auxiliary equation 3.68 to find the unknown exponents of that solution.

$$(a)m^2 + (b)m + (c) = 0 \tag{3.68}$$

Substituting components, a, b and c of Equation 3.67 into Equation 3.68, giving,

$$(1)m^2 + \left(\beta_{Tb}\left(\frac{h}{A_{ii}E}\right)\right)m + \left(\beta_{Tc}\left(\frac{h}{A_{ii}E}\right)^2\right) = 0 \tag{3.69}$$

Knowing the Quadratic Equation ie,

$$m_{1,2} = \frac{-b \pm \sqrt{b^2 - 4ac}}{2a} \tag{3.70}$$

Then substituting a, b and c components of Equation 3.69 into Equation 3.70, giving,

$$m_{1,2} = \frac{\beta_{Tb}\frac{h}{A_{ii}E} \pm \frac{h}{A_{ii}E}\sqrt{\beta_{Tb}^2 - 4\beta_{Tc}}}{2} \tag{3.71}$$

Using Equation 3.71, the complete solution to Equation 3.67 is,

$$R_T = Ae^{m_1 F} + Be^{m_2 F} \tag{3.72}$$

To get the G-TF-DE-V we would use averaged values of Equations 3.64 and 3.66 ($\beta_{Tb\,avg}$ and $\beta_{Tc\,avg}$) gained from several sets of data and substitute them into Equation 3.72.

So the G-TF-DE-V and solution in terms of voltage are,

$$\frac{d^2V}{dF^2} - \beta_{Tb\,avg}\left(\frac{h}{A_{ii}E}\right)\frac{dV}{dF} + \beta_{Tc\,avg}\left(\frac{h}{A_{ii}E}\right)^2 V = 0 \tag{3.73}$$

$$V = Ae^{m_{1\,avg}F} + Be^{m_{2\,avg}F} \tag{3.74}$$

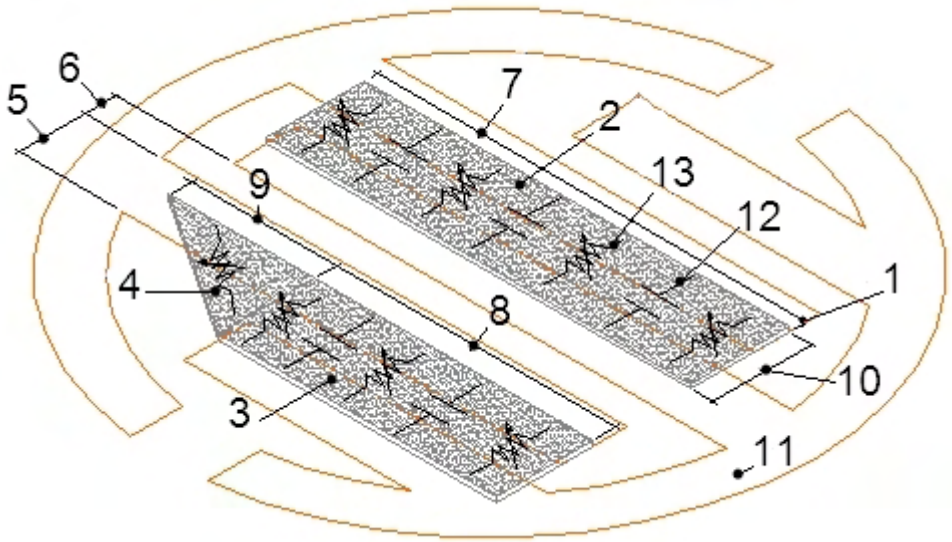

Figure 3.34: TF electrode with an overlay of resistive polymer sections

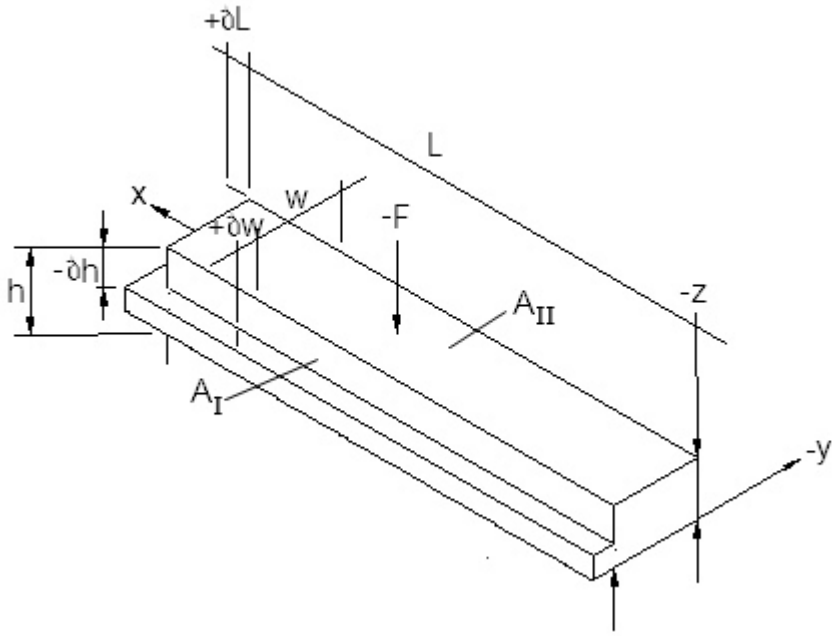

Figure 3.35: Close-up of Figure 3.34 No. 2 being strained

3.4.5 Thick Film Smart Brake Pad Room Temperature Tests

3.4.5.1 Introduction

The following tests were performed at Room Temperature (RT):

1. Thick Film Smart Brake Pad Room Temperature Compression Tests
2. Thick Film Room Temperature *cell by cell* Compression Test
3. Thick Film Room Temperature *glass disc* Compression Test
4. Thick Film Room Temperature *metal disc* Compression Test

These tests follow.

1. Thick Film Smart Brake Pad Room Temperature Compression Tests

   (a) **Introduction**
   Here we test two TF SBP's at varying compression at RT. The data will be plotted and the TF model will be fitted against data.

   (b) **Objectives**

   - To test the effectiveness of the SBP fixture
   - To try and calibrate the TF Sensors' whilst assembled in the fixture
   - To test the TF model against the data

   (c) **Methods**
   Using the MTS shown in Figure 3.36 with compression platens (flat plates) instead of jaws, apply a load from 0 to 4.5 kN and return onto each of the three segments of the SBP (each segment contains five TF cells). The data from the TF sensor is recorded using a separate signal conditioning and DAQS; the applied load is also recorded using this system via a separate load cell fitted underneath the test specimen.

   (d) **Specimens**
   Two specimens are tested *SBP 2* and *SBP 4*. Both specimens are similar to that depicted in Figure 3.30.

   (e) **Experimental Set-up**
   Please refer to Figure 3.37 for the experimental set-up used in the RT SBP tests.

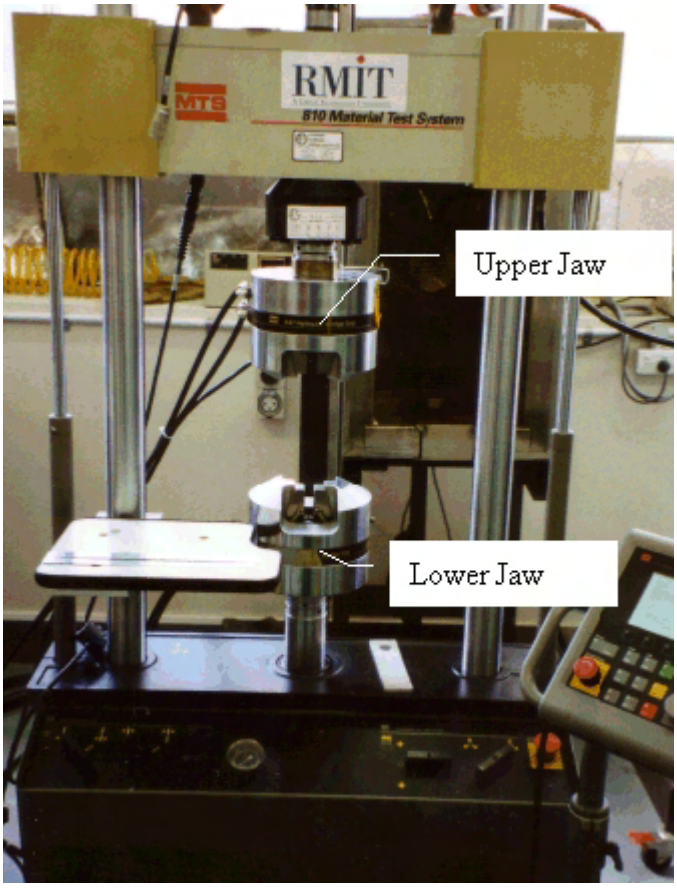

Figure 3.36: Type of MTS used in most of our tests

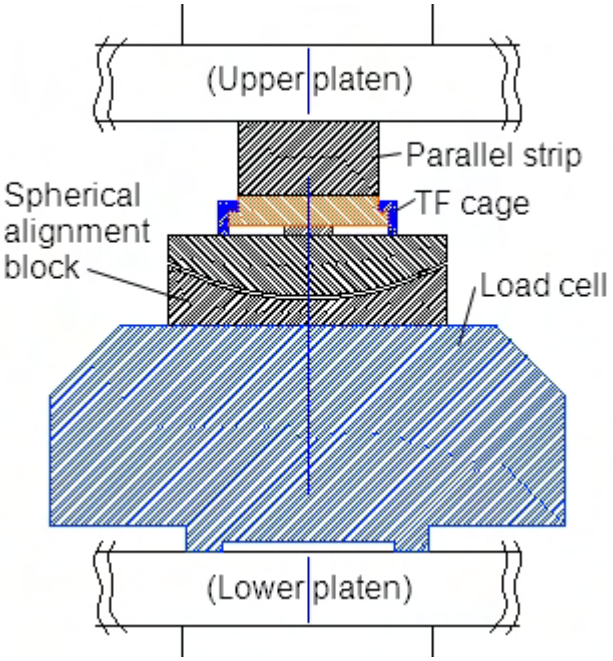

Figure 3.37: MTS set-up used between the platens of the MTS

(f) **Results**

Figure 3.38 is the mathematical model plotted against the experimental data with 68 % (dotted) and 95 % (dashed) confidence intervals.

Figure 3.39 is the plot of residuals[1] for the model in Figure 3.38. The generalised items in the Figure are [44]:

(a) A histogram of the input data The histogram gives us an idea of the form of the input and what are possible causes of outliers in the residuals.

(b) A histogram of sensor response data The histogram give us an idea of the form of the response and what are possible causes of outliers in the residuals.

(c) Residuals of fit vs input To see if there is any correlation between the residuals and the input. If there is a correlation, then the data will be non-random.

(d) Residuals vs response To see if there is any correlation between the residuals and the response. If there is a correlation, then the data will be non-random.

(e) Run plot of residuals The run plot is a plot of the residuals. It will tell us if there is any drift in the location of the data. It will also tell us if there are any shifts in variation of the data.

(f) Lag plot Indicates if there is a linear correlation between successive points or drift. This also helps us decide what sought of model ought to be used with the data.

(g) Histogram of residuals The histogram helps us answer these questions: i) What kind of population do the data belong to? ii) Where are the data located? iii) How spread out are the data? iv) Are the data symmetric or skewed? v) Are there any outliers?

(h) Normal probability plot of residuals The normal probability plot helps us answer these questions: i) Are the data normally distributed? ii) Is it skewed? iii) Does it have longer or shorter tails?

These plots will be used in pertinent places throughout the remainder of the thesis.

[1] The residuals are the difference between the mathematical model and the data

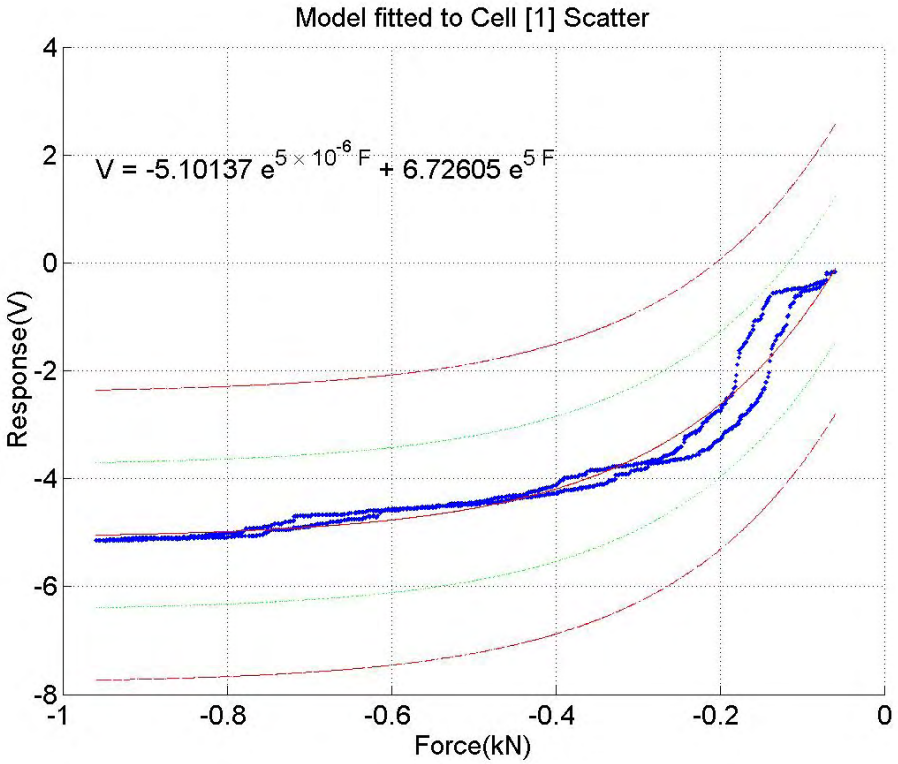

Figure 3.38: SBP 2, cell 1, model and data

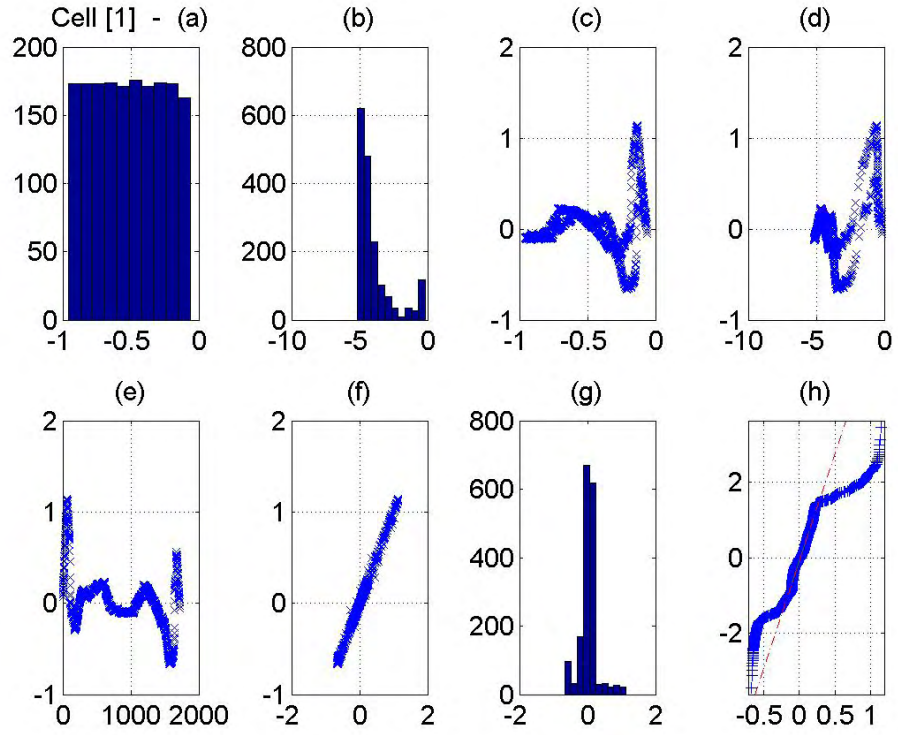

Figure 3.39: SBP 2, cell 1, plots of residuals

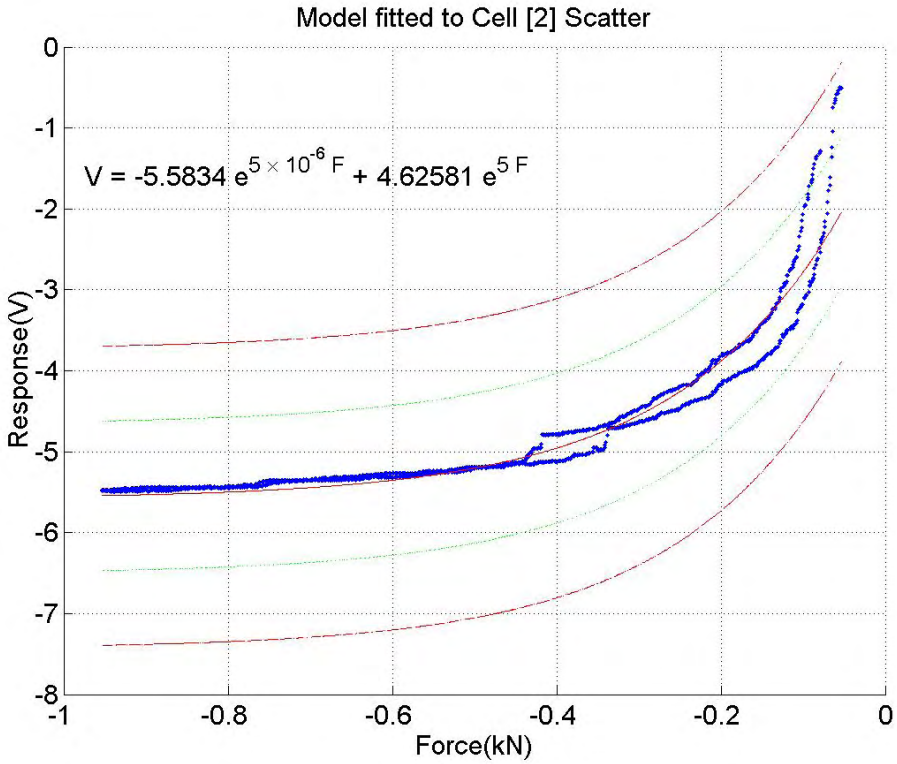

Figure 3.40: SBP 2, cell 2, model and data

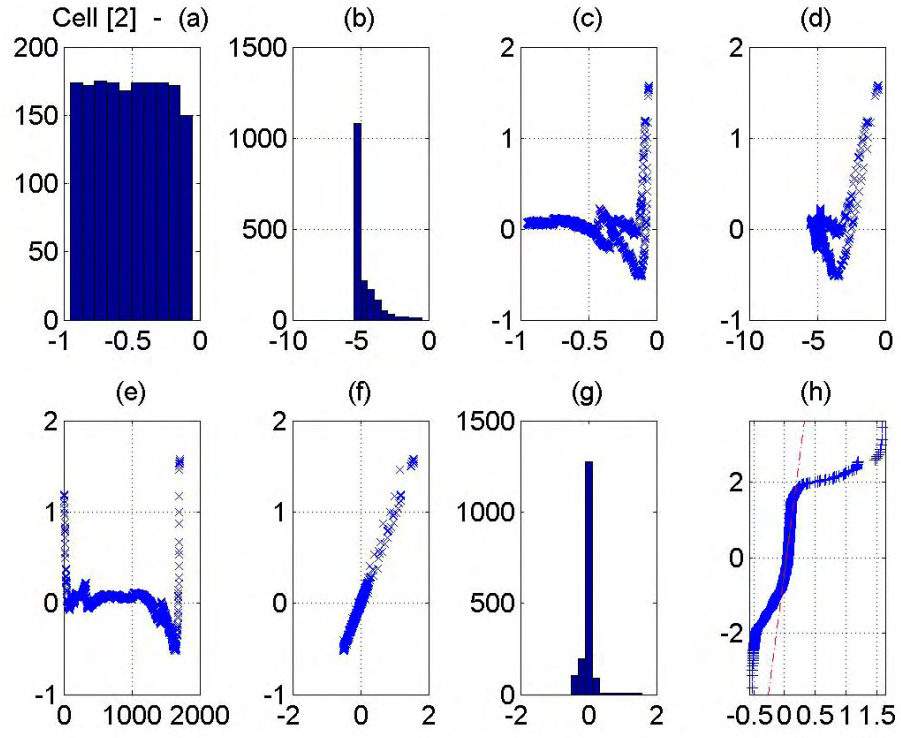

Figure 3.41: SBP 2, cell 2, plots of residuals

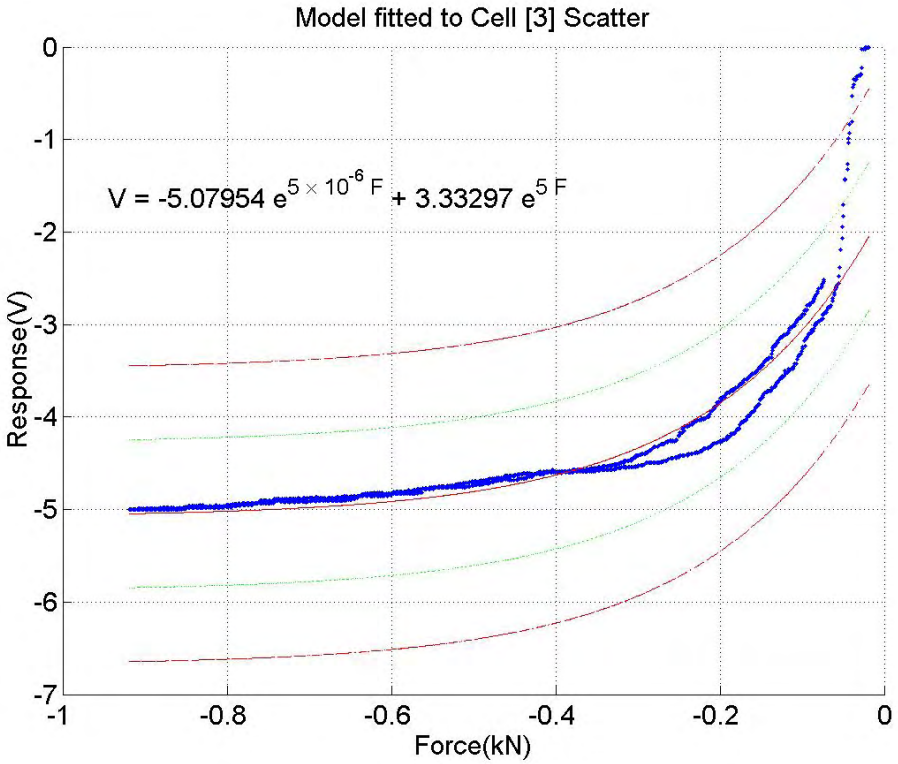

Figure 3.42: SBP 2, cell 3, model and data

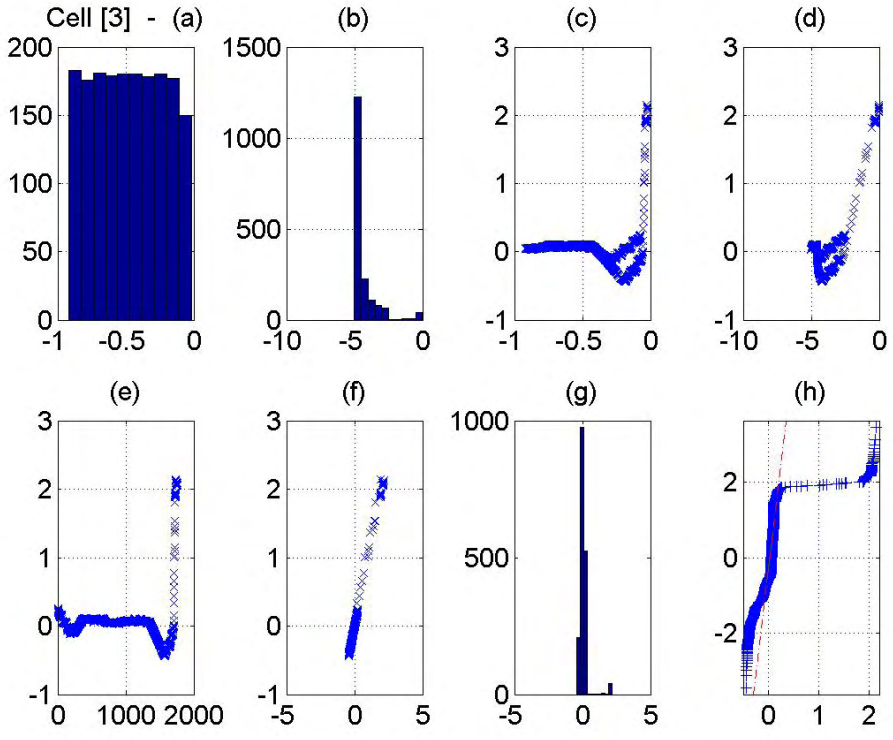

Figure 3.43: SBP 2, cell 3, plots of residuals

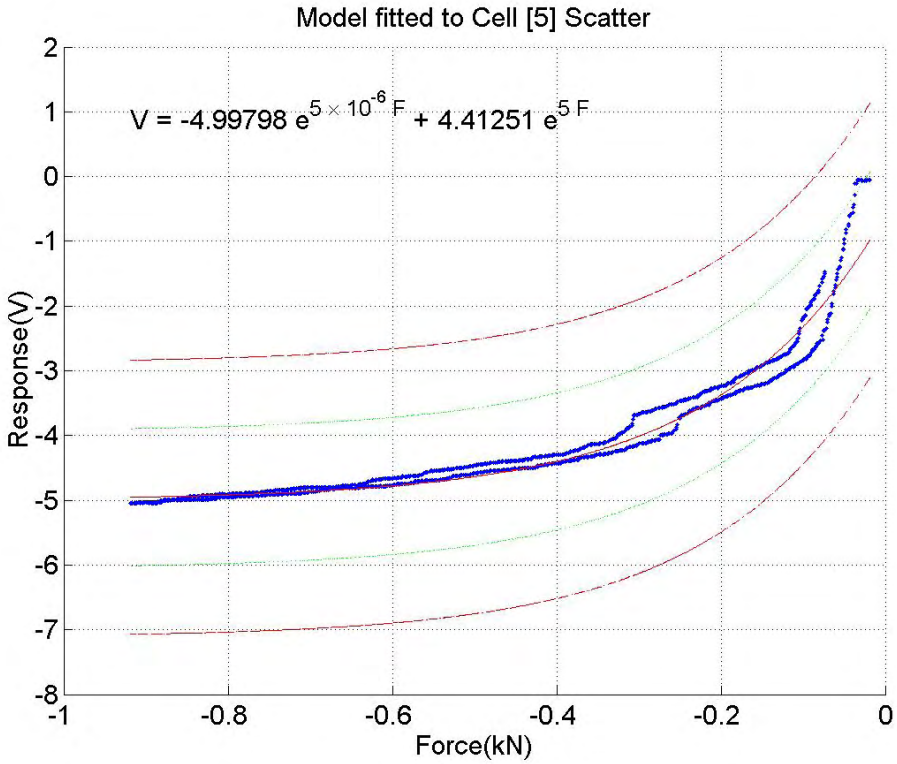

Figure 3.44: SBP 2, cell 5, model and data

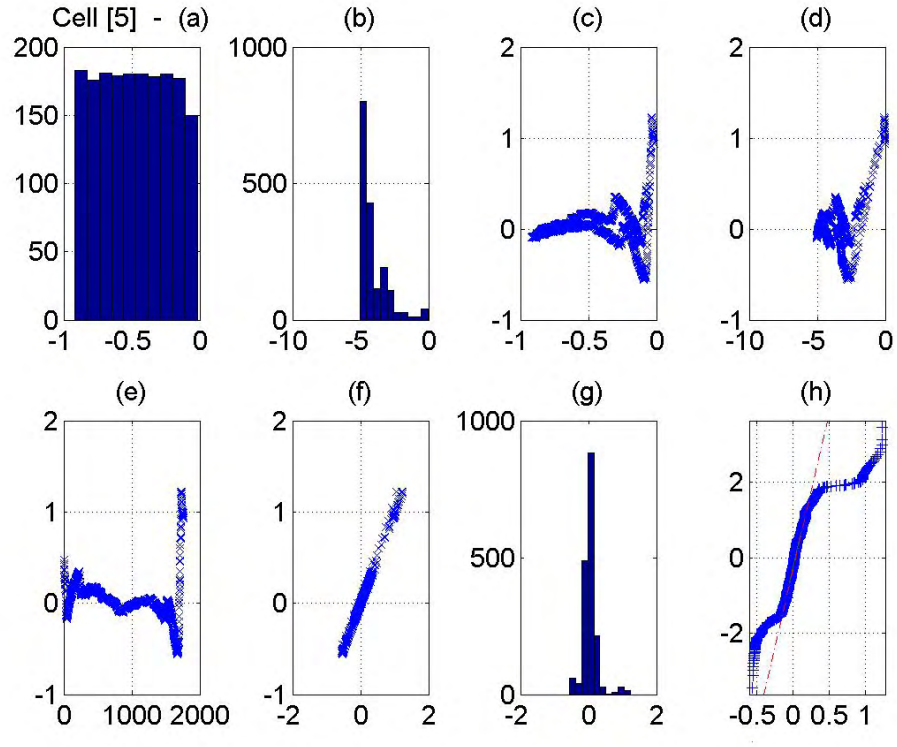

Figure 3.45: SBP 2, cell 5, plots of residuals

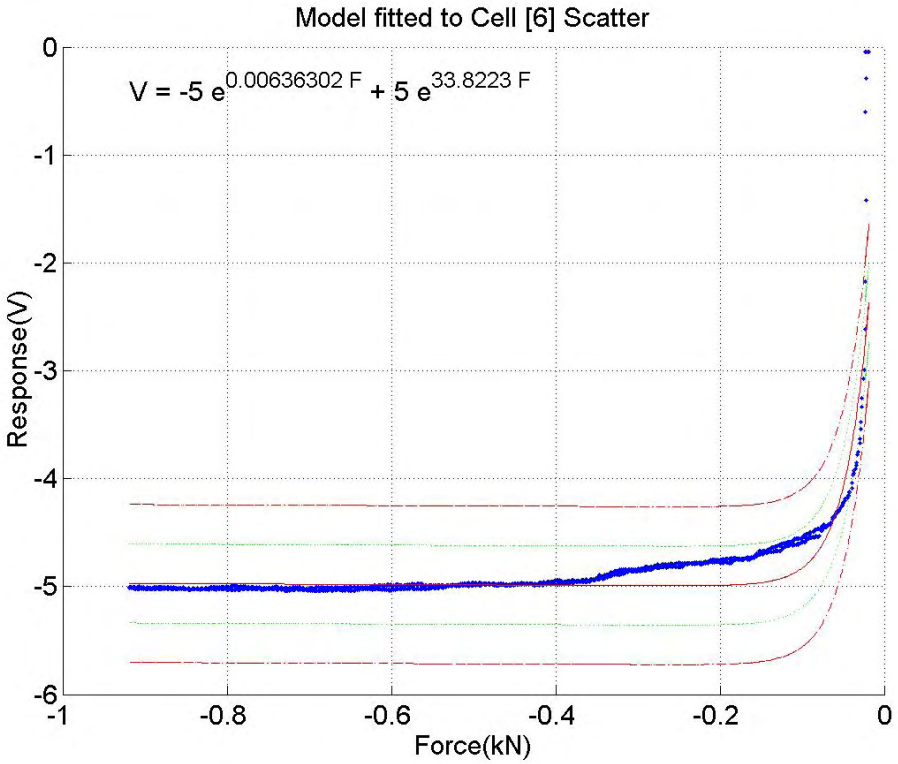

Figure 3.46: SBP 2, cell 6, model and data

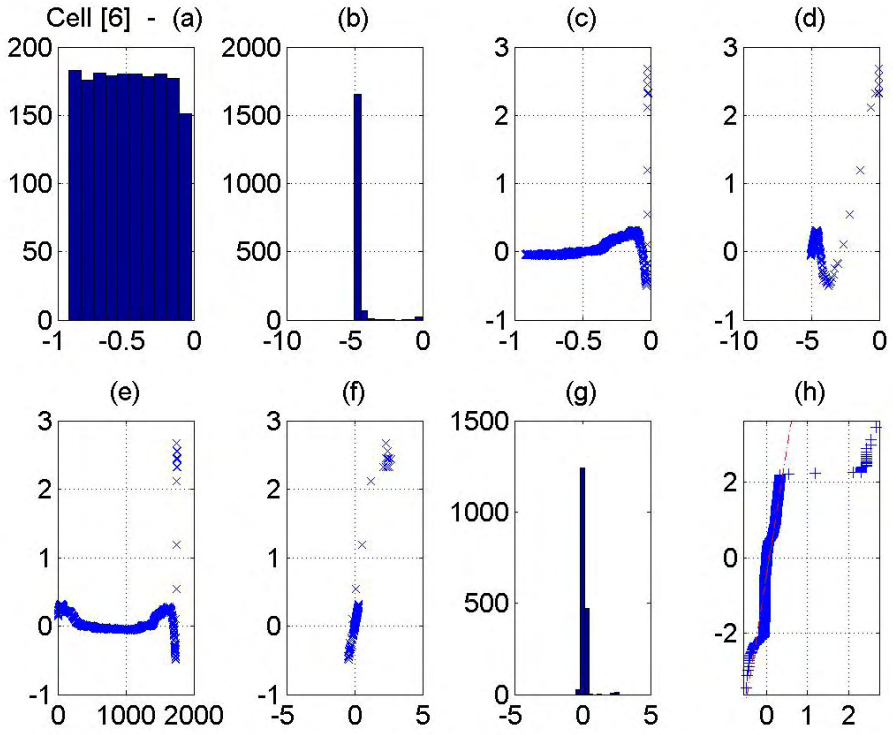

Figure 3.47: SBP 2, cell 6, plots of residuals

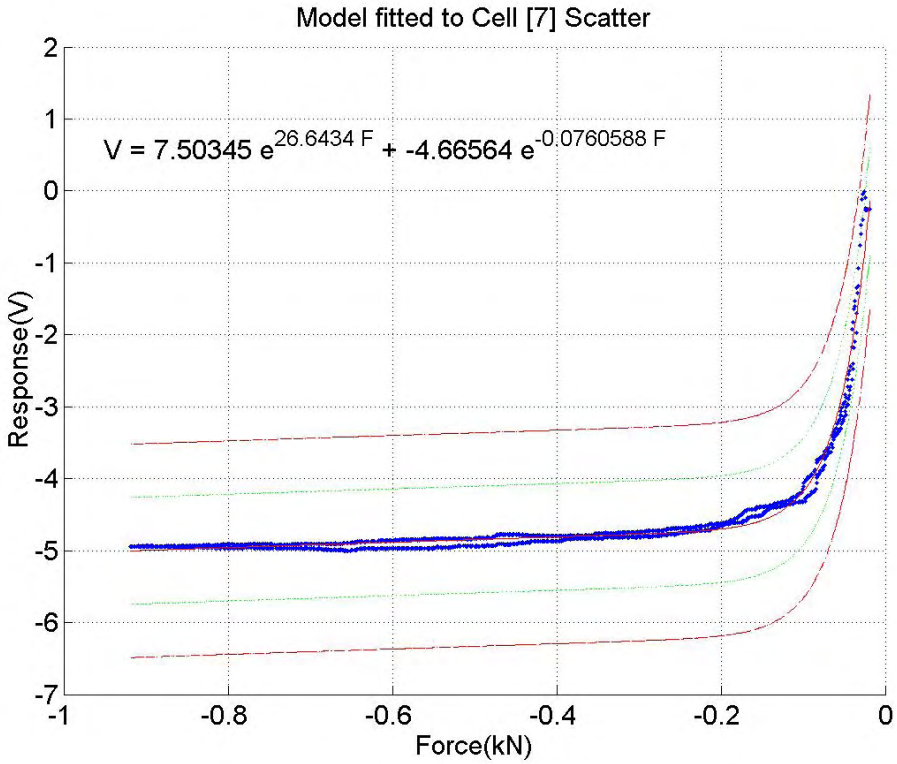

Figure 3.48: SBP 2, cell 7, model and data

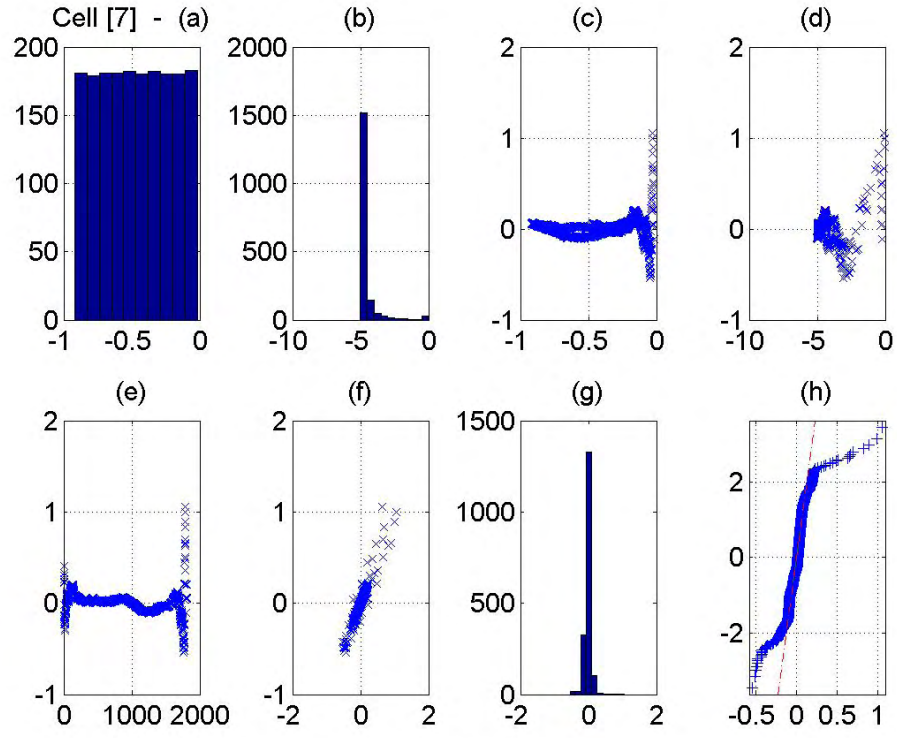

Figure 3.49: SBP 2, cell 7, plots of residuals

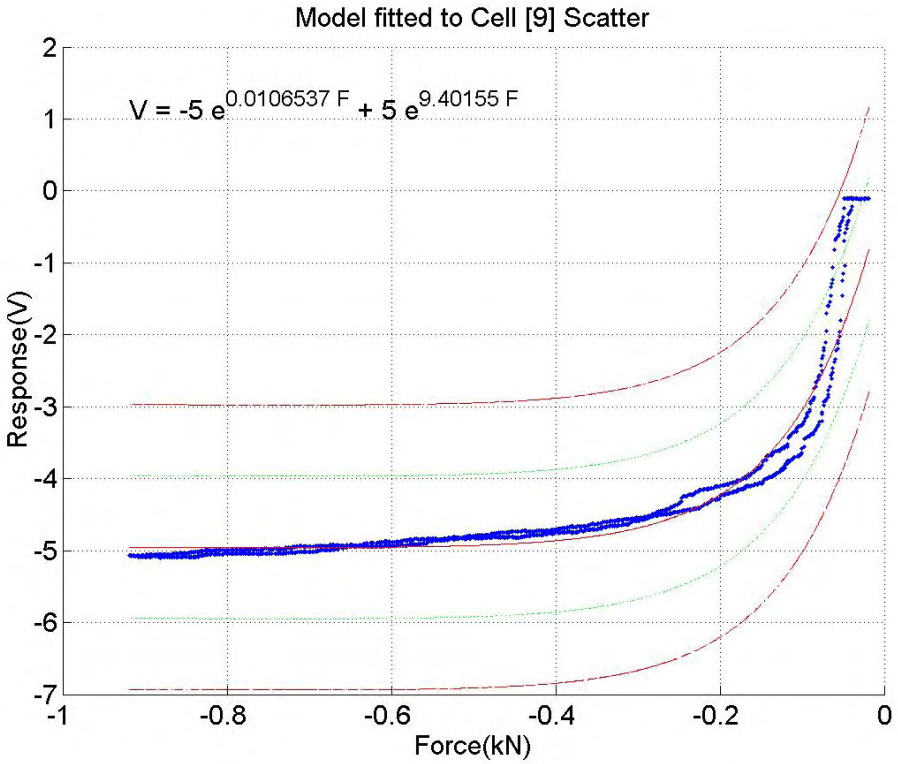

Figure 3.50: SBP 2, cell 9, model and data

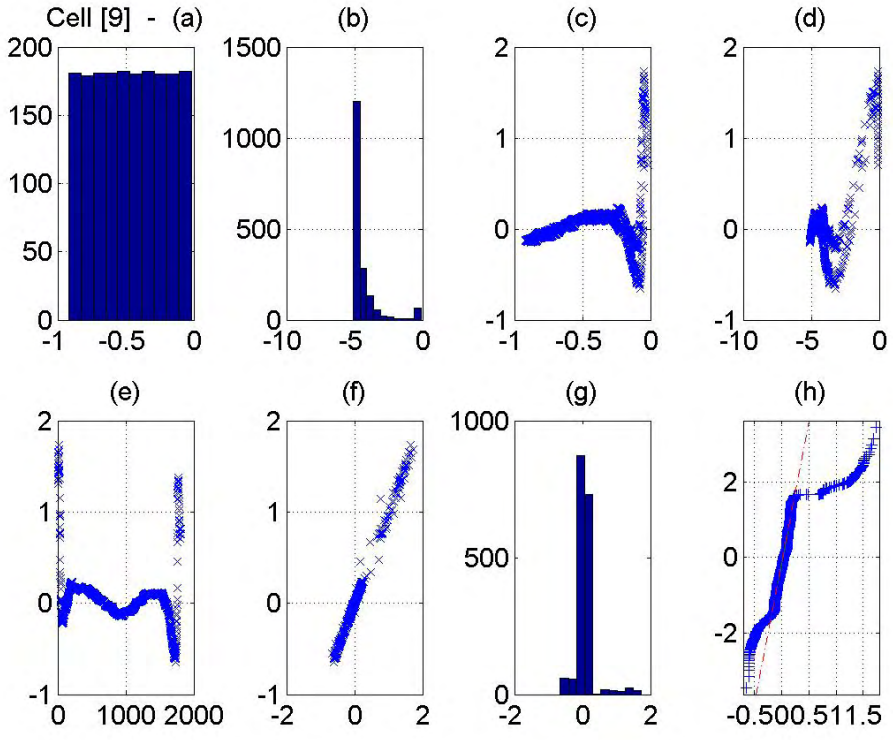

Figure 3.51: SBP 2, cell 9, plots of residuals

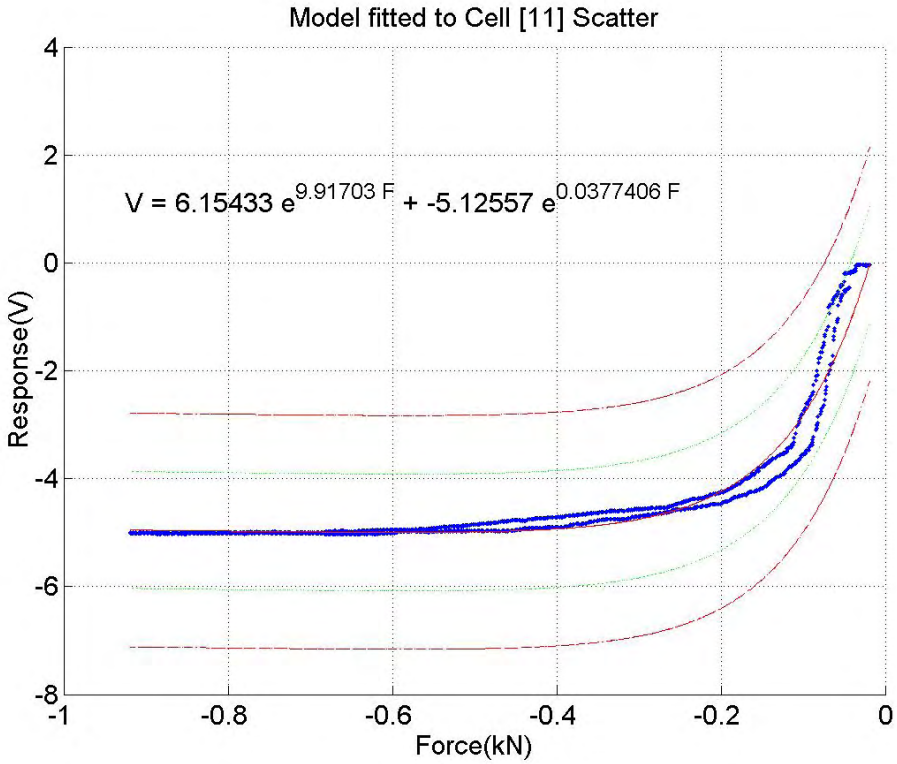

Figure 3.52: SBP 2, cell 11, model and data

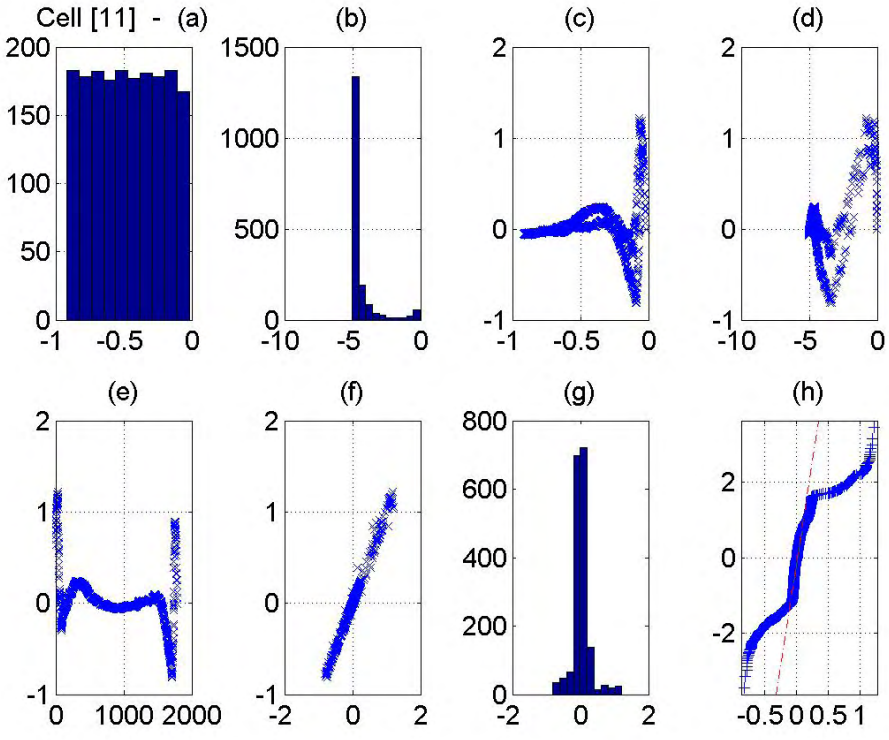

Figure 3.53: SBP 2, cell 11, plots of residuals

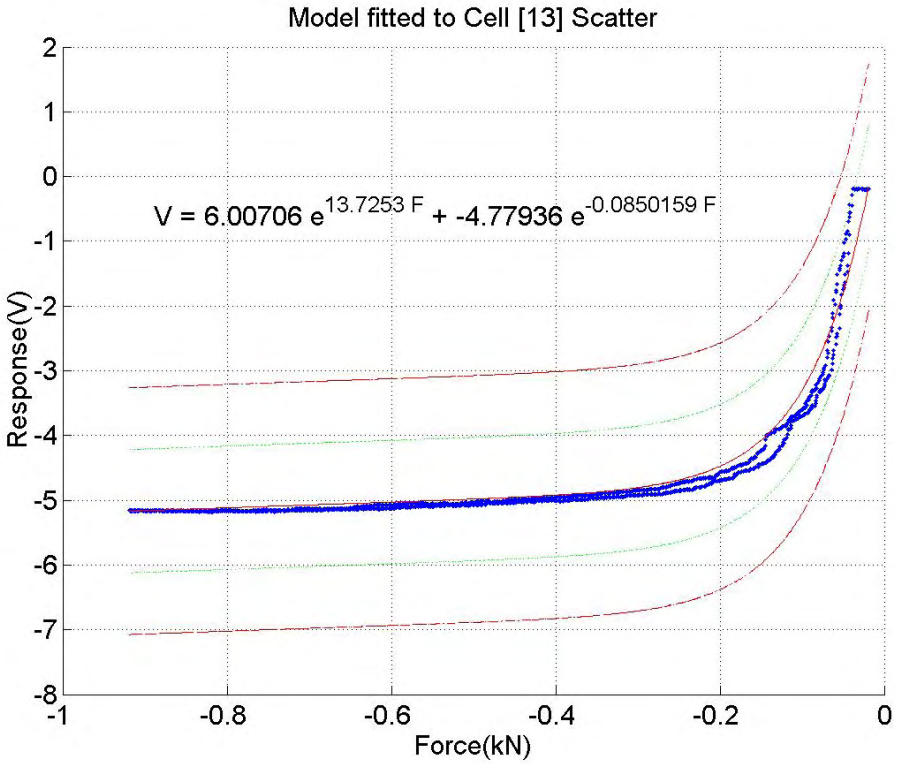

Figure 3.54: SBP 2, cell 13, model and data

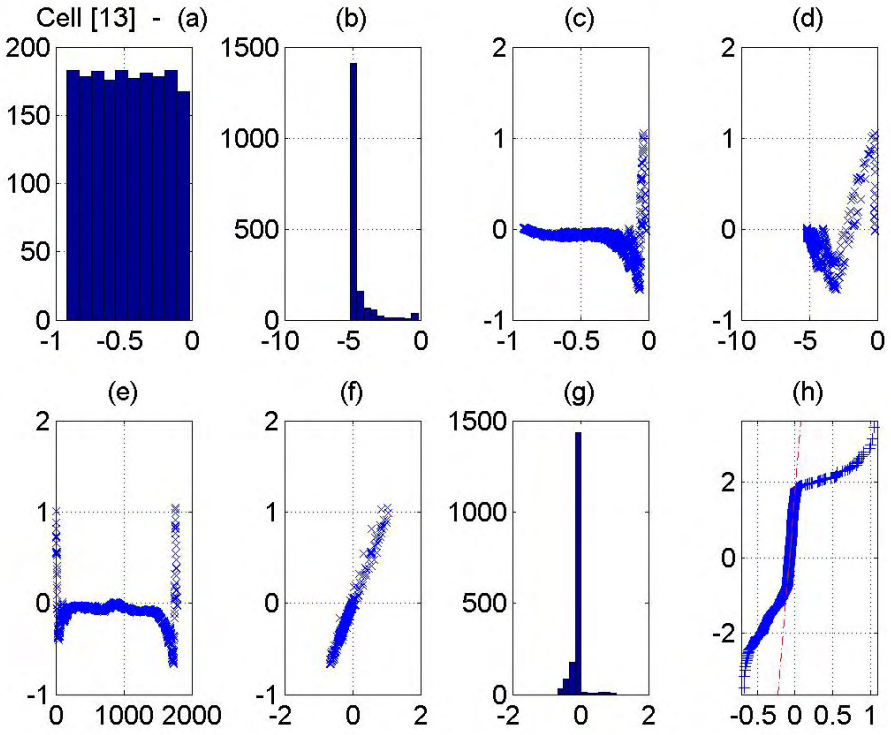

Figure 3.55: SBP 2, cell 13, plots of residuals

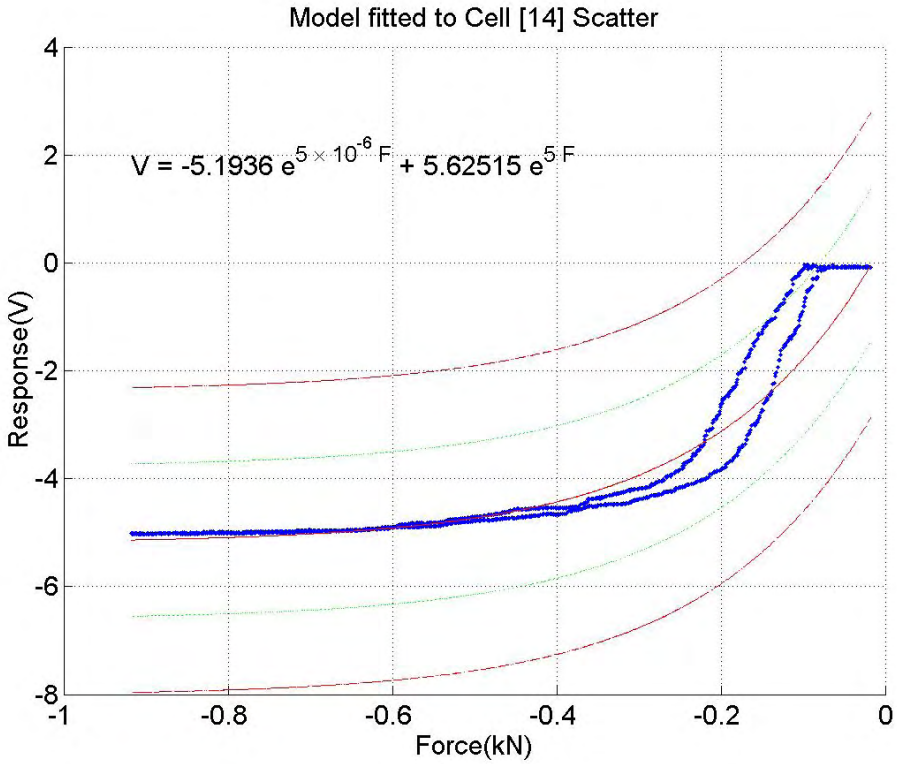

Figure 3.56: SBP 2, cell 14, model and data

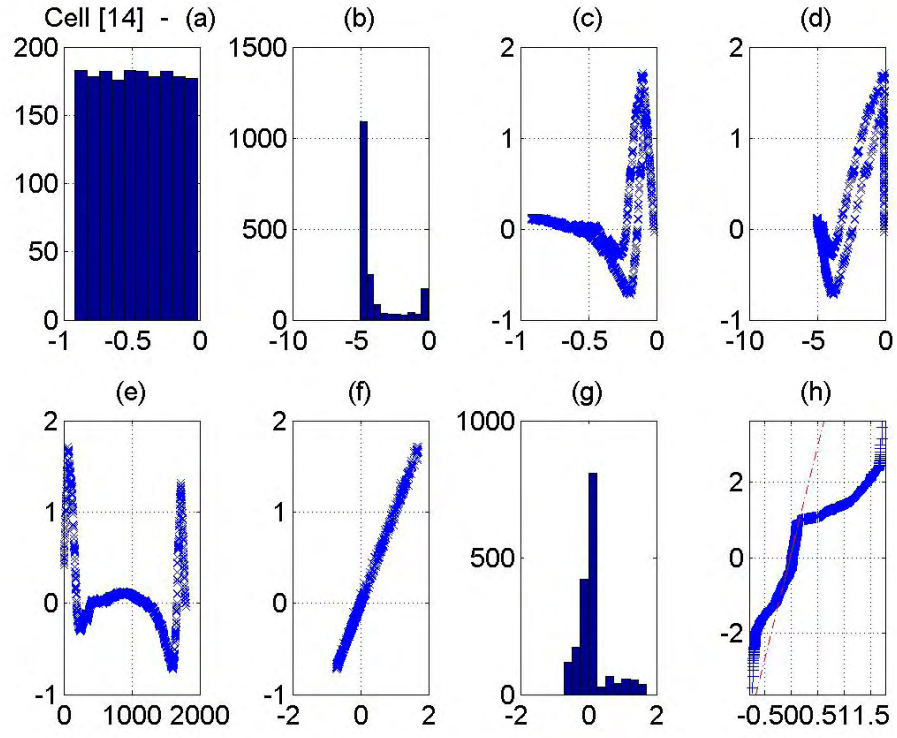

Figure 3.57: SBP 2, cell 14, plots of residuals

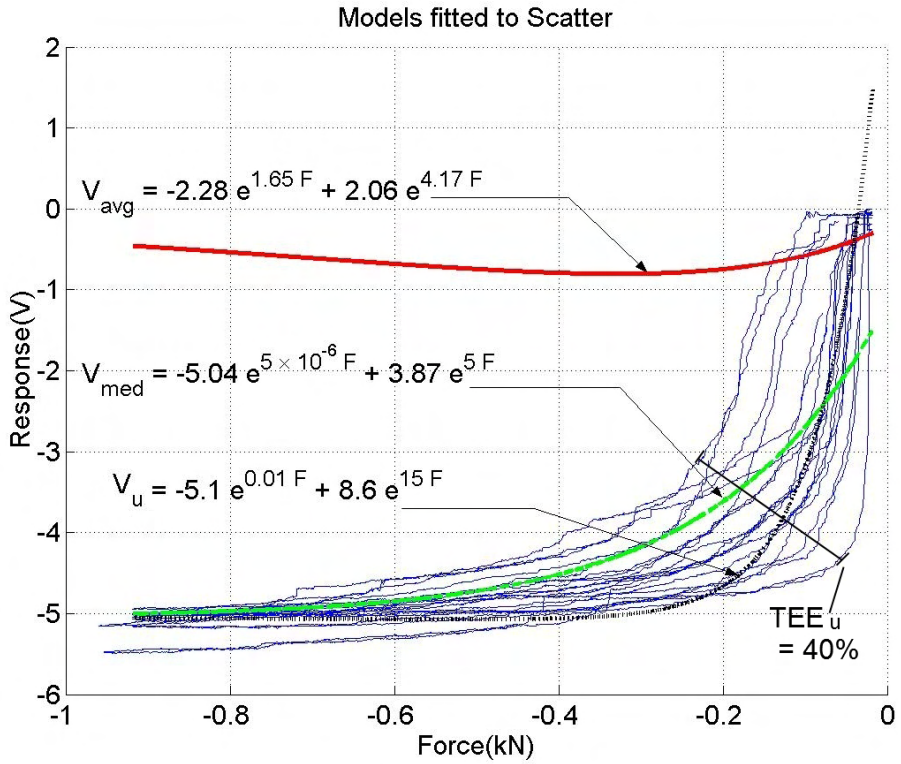

Figure 3.58: SBP 2, cells 1, 2, 3, 5, 6, 7, 9, 11, 13 and 14 with selected models

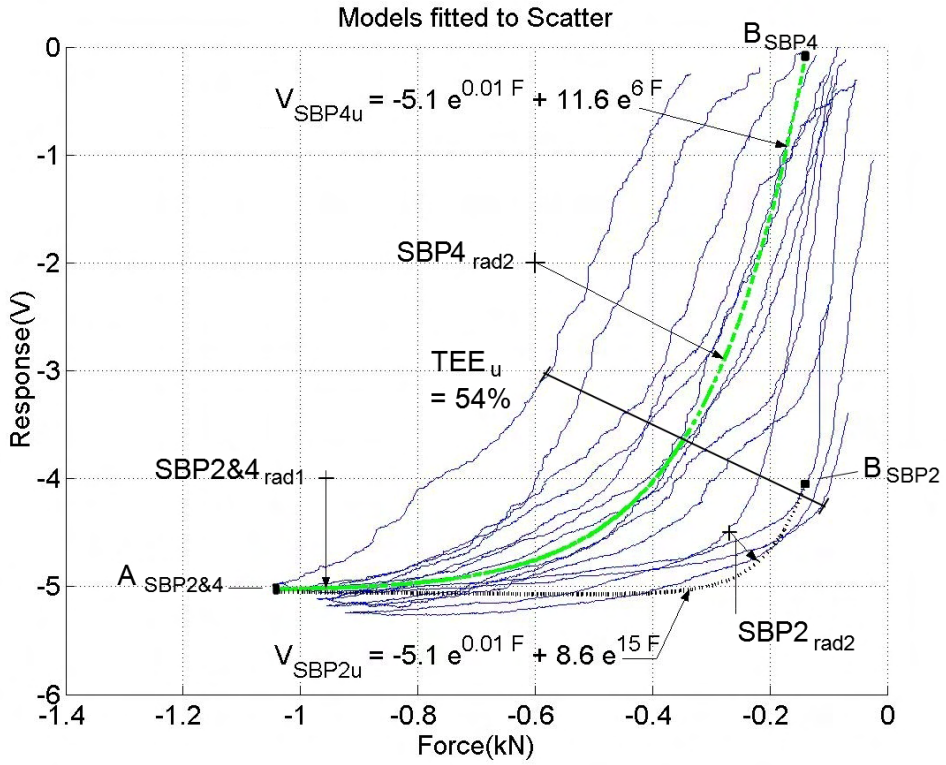

Figure 3.59: SBP 4, cells 1, 2, 3, 4, 5, 11 and 14 with selected models

(g) **Discussion and Conclusion**

In this section, we tested SBP 2 and 4 at RT with cyclic loading from 0 to 4.5 kN in compression; applied separately to each of the three pad elements. Theoretically, each of the 5 cells receive 900 N per cell. However, when processing the data it was seen that some received slightly more than others and so the results featured in Figures 3.38−3.59 have been scaled to these limits to aid the interpretation and modelling process. The response has also been scaled between 0 and -5 V. Despite these adjustments, the SBP fixture seems adequately designed for its purpose.

The solution of Equation 3.73, Equation 3.74 was first fitted[1] to SBP 2 and all of its functioning cells, the results can be seen in Figures 3.38−3.58. A summary of the results can be found in Table 3.2.

Using the individual plots Figures 3.38−3.58 we were able to find preliminary parameters for Equation 3.73 and its solution[2]. Referring to Figure 3.58, we can see the results of this exercise, with solutions: V_{avg}, V_{med} and V_u represented. Solution V_{avg}, is hardly representative of the data and this is expected since few of the cell plots have normal histograms[3] of residuals. V_{med}, is much closer, which is expected, since median values are often preferred for skew data. V_u, was developed based on the researcher's judgement resulting from analysis of the previous curves and analysis of its solution.

As a result of the SBP 2 results, SBP 4 data was only presented on one graph, Figure 3.59 with models: V_{SBP2u}[4] and V_{SBP4u}. We can see immediately that SBP 2 is much less sensitive that of SBP 4 because of the 3 volt difference in response scale between the two end points despite scaling. This increase in sensitivity is at the expense of an increase in hysteresis error which is reflected in a higher TEE_u value of 54 % compared to 40 % for SBP 2. The mechanical hysteresis in the data is believed to be caused by the sensor material and to a greater extent by non-linearity of the brake material. However, with rounding, they both end up having a tolerance of ±1 V over a FS of 5 V. These values of ±1 V are four times larger than what we specified in the SBP-SDC.

With regards to drift, it can clearly be seen that the lag plots[5] for SBP 2 have a strong linear interdependence between successive points; this implies drift. If there was no interdependence the points would be randomly dispersed. It is known that most sensors do have some level of drift, however, this seems unacceptably high. Further tests will need to be conducted on the individual cells to ascertain whether the drift is due to the cells themselves or due to being embedded into the brake pad.

Now we will analyse the components of solutions V_{SBP2u} and V_{SBP4u} using Figure 3.59 to gain a better understanding of each parameters function with regards to fitting the data. First though, we will define Equations 3.75 and 3.76 being the equivalent algebraic representations.

$$V_{SBP2u} = A_{SBP2}\, e^{\beta_{1\,SBP2}} + B_{SBP2}\, e^{\beta_{2\,SBP2}} \tag{3.75}$$

[1] The data was fitted using the Simplexe minimization routine in MatLab. The routine was developed by Jean-Luc Dellis [59]

[2] A spreadsheet of average and median values of equation parameters can be found in Appendix G

[3] Plot (g) of the residual plots

[4] In Figure 3.58, simply known as V_u

[5] Plot (f) of the residual plots

Table 3.2: SBP 2 and 4 uncertainty analysis

SBP 2

Cells	TEE 95 (%)	TEE 68 (%) [Error = +/- ½ TEE]	TEE u (%)	Tol 95 (V) [Error = +/- Tol; FS = 5 V]	Tol 68 (V)	Comments – general and with regards to residual plots
1	108	54	n/a	3	1	Good. Hysteresis, poor fit at right and has drift
2	74	37	n/a	2	1	Good. Hysteresis, poor fit at right and has drift
3	64	32	n/a	2	1	Good. Hysteresis, poor fit at right and has drift
4	X	X	n/a	X	X	Faulty
5	85	42	n/a	2	1	Good. Hysteresis, poor fit at right and has drift
6	29	15	n/a	1	0	Good – fair. Poor fit at right and has drift
7	59	30	n/a	1	1	Good – fair. Poor fit at right and has drift
8	X	X	n/a	X	X	Faulty
9	79	40	n/a	2	1	Good. Hysteresis, poor fit at right and has drift
10	X	X	n/a	X	X	Faulty
11	87	43	n/a	2	1	Good. Hysteresis, poor fit at right and has drift
12	X	X	n/a	X	X	Faulty
13	76	38	n/a	2	1	Good. A little hysteresis, poor fit at right and has drift
14	113	57	n/a	3	1	Good – fair. Poor fit at right and has drift
15	X	X	n/a	X	X	Faulty
Med	78	39	n/a	2	1	
All used	n/a	n/a	40	n/a	1	

SBP 4

Cells	TEE 95 (%)	TEE 68 (%)	TEE u (%)	Tol 95 (V)	Tol 68 (V)
All used	n/a	n/a	54	n/a	1

Please note: There is a need to improve quality assurance to reduce uncertainty in measurement and the number of faulty sensors per production; this needs to be done for all SBP's.

Table Key	
TEE 95 (%)	Total Expected Error using the 95% CI
TEE 68 (%)	Total Expected Error using the 68% CI
TEE u (%)	Total Expected Error using the user's estimation of the CI
Tol 95 (V)	Tolerance at the 95% CI in terms of voltage
Tol 68 (V)	Tolerance at the 68% CI in terms of voltage
CI	Confidence Interval
Med	Median value
n/a	not applicable

$$V_{SBP4u} = A_{SBP4}\, e^{\beta_{1\ SBP4}} + B_{SBP4}\, e^{\beta_{2\ SBP4}} \tag{3.76}$$

Both solutions 3.75 and 3.76 which are presented in Figure 3.59 are joined at point $A_{SBP2\&4}$ (bottom left of figure). Also, points B_{SBP2} and B_{SBP4} are placed in their respective positions. The value of point A is equal to the minimum value of the sensor output, whereas point B is equal this value, plus the maximum value. The difference between B and A is not equal to the scale of the response due to the equations non-linearity. For example, for solution B_{SBP2}:

$$8.6 - |5.1| = 3.5\,V$$

Whereas, the difference between B and A is around 1 V on the response scale.

The beta values, β_1 and β_2 for either equation influence the curvature of the solution between points A and B and abide by Equations 3.77−3.79.

$$SBP2\&4_{rad1} = \frac{1}{\beta_{1\ SBP2\&4}} \tag{3.77}$$

$$SBP2_{rad2} = \frac{1}{\beta_{2\ SBP2}} \tag{3.78}$$

$$SBP4_{rad2} = \frac{1}{\beta_{2\ SBP4}} \tag{3.79}$$

It is useful to know these relationships in order to study the slope of the curves and the similarities and differences between two or more solutions.

In conclusion,

- The SBP fixture was found to be adequate despite the uneven loading between cells that was compensated for by scaling the data
- The solution, Equation 3.74 fitted the data quite well, despite the mechanical hysteresis caused by the sensor and brake pad materials
- It would be worth testing the cells individually without the SBP fixture to see what is causing the hysteresis
- The *user* values (please see Figures 3.58 and 3.59) chosen as the parameters for the general solution were found to be the best
- The error tolerance of either sensor was estimated to be ±2 V at 95 % and ±1 V at about 68 % confidence
- Drift tests need to be conducted in order to determine the amount of drift in each cell
- The general solutions for the SBP were found and one DE with two sets of different parameters for SBP 2 and 4 are as follows:

$$\frac{d^2V}{dF^2} - \beta_{Tbu}\left(\frac{h}{A_{ii}E}\right)\frac{dV}{dF} + \beta_{Tcu}\left(\frac{h}{A_{ii}E}\right)^2 V = 0 \tag{3.80}$$

Where:

For SBP 2

A_{ii}	Component of Figure 3.35 $[A_{ii} = (4.7 \times 10^{-3})(968.0 \times 10^{-6})]$
E	Modulus of elasticity of the sensor film $[E = 0.5 \times 10^{9}]$
h	Film Thickness $[h = 100 \times 10^{-6}]$
β_{Tbu}	$\lvert\beta_{1u}\rvert + \lvert\beta_{2u}\rvert\left(\frac{A_{ii}E}{h}\right)$ $[\beta_{Tbu} = 341.1 \times 10^{6}]$
β_{Tcu}	$\lvert\beta_{1u}\rvert \times \lvert\beta_{2u}\rvert\left(\frac{A_{ii}E}{h}\right)^2$ $[\beta_{Tcu} = 7.753 \times 10^{15}]$

For SBP 4

β_{Tbu}	$\lvert\beta_{1u}\rvert + \lvert\beta_{2u}\rvert\left(\frac{A_{ii}E}{h}\right)$ $[\beta_{Tbu} = 136.6 \times 10^{6}]$
β_{Tcu}	$\lvert\beta_{1u}\rvert \times \lvert\beta_{2u}\rvert\left(\frac{A_{ii}E}{h}\right)^2$ $[\beta_{Tcu} = 3.104 \times 10^{15}]$

- Lastly, we discussed the relationships between the various parameters of the solutions and the physical characteristics of their curves

(h) Thick Film Room Temperature *cell-by-cell* Compression Test

i. **Introduction**
After the first successful RT test using the TF sensor embedded into two SBP it was thought necessary to conduct a second test to determine the response of the sensor outside the SBP for the purposes of comparison and improvement.

ii. **Objectives**
A. To test the TF Sensors *cell-by-cell* to obtain their output responses whilst not embedded in a the SBP
B. To fit the G-TF-DE-V solutions to the data
C. To test for drift

iii. **Methods**
Using the MTS shown in Figure 3.60 with special purpose compression probe, apply a load between 0 and 600 N, on each individual cell. Three cycles will be performed on each cell. The data will be recorded and scaled as before.

A drift test for each individual cell will be conducted consisting of loading each cell with the maximum load and holding it there with a Set Time Frame (STF) of one minute, to see if there is any variation in output whilst kept at this constant load.

iv. **Specimens**
As seen in Experimental Set-up.

v. **Experimental Set-up**
The experimental set-up is shown in Figures 3.60−3.62.

Figure 3.60: *United* 5 kN MTS

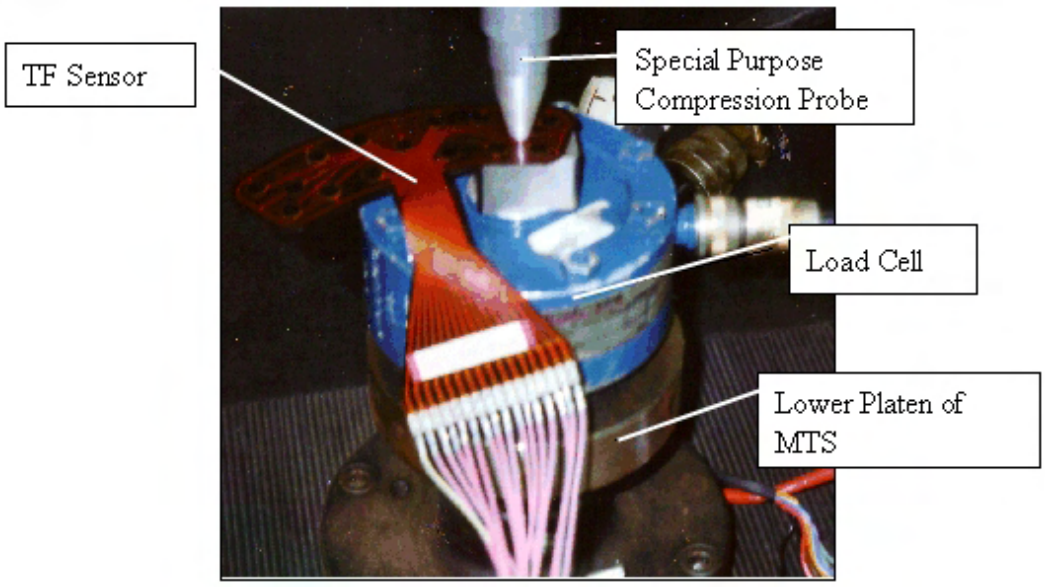

Figure 3.61: Set-up *cell-by-cell*

Figure 3.62: DAQS used for TF tests

vi. **Results**

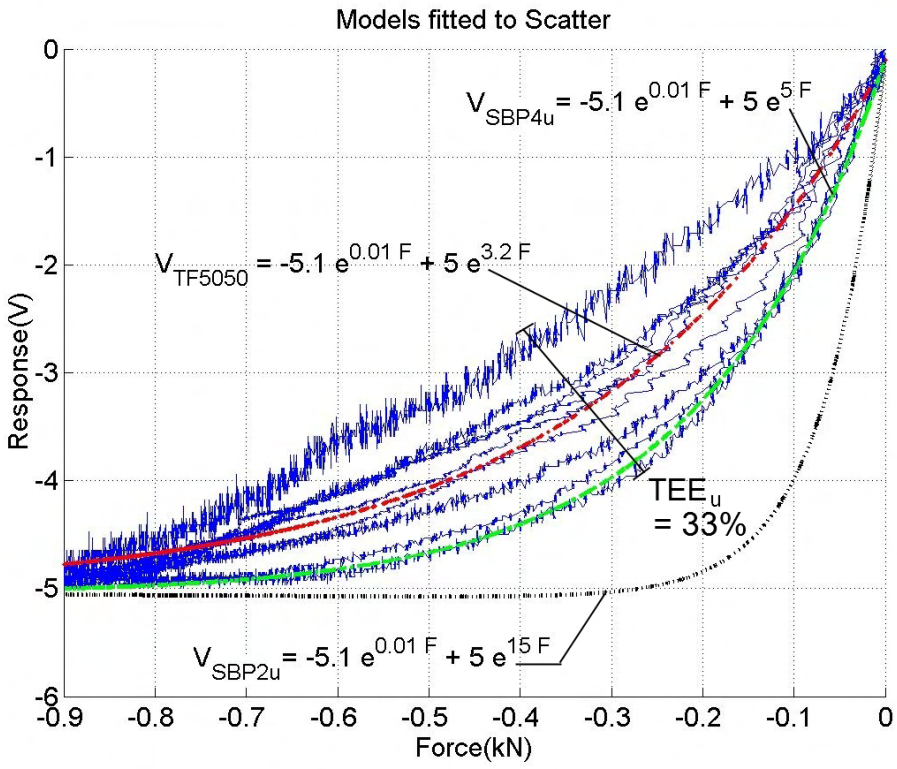

Figure 3.63: Type TF5050, cells 1, 2, 3, 4, 5, 7, 8, 13 and 14

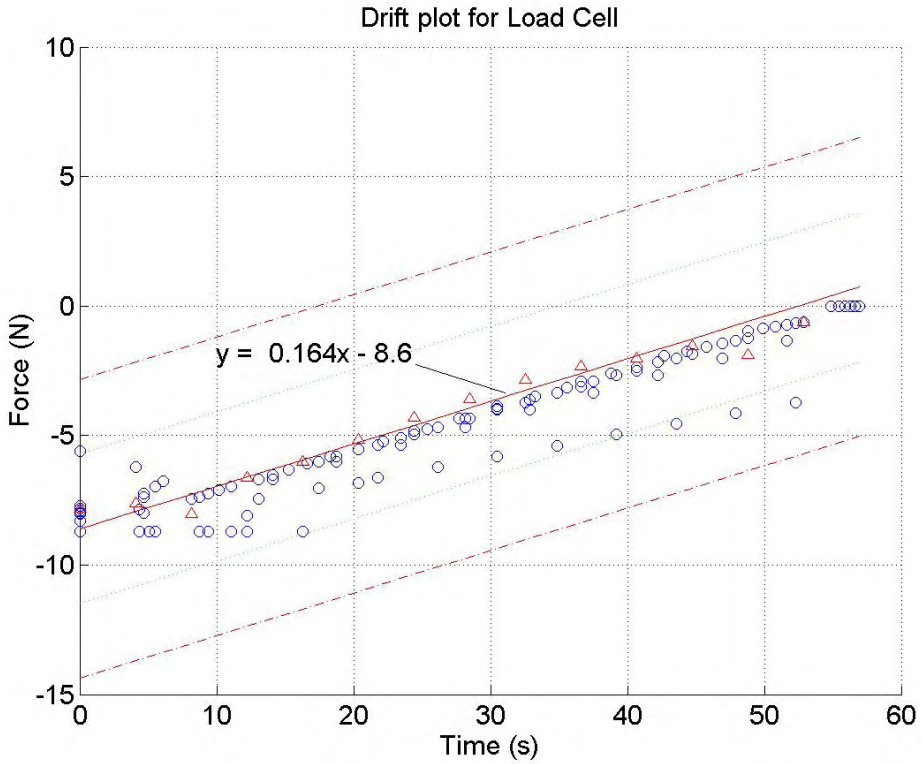

Figure 3.64: Drift of load cell used with TF5050

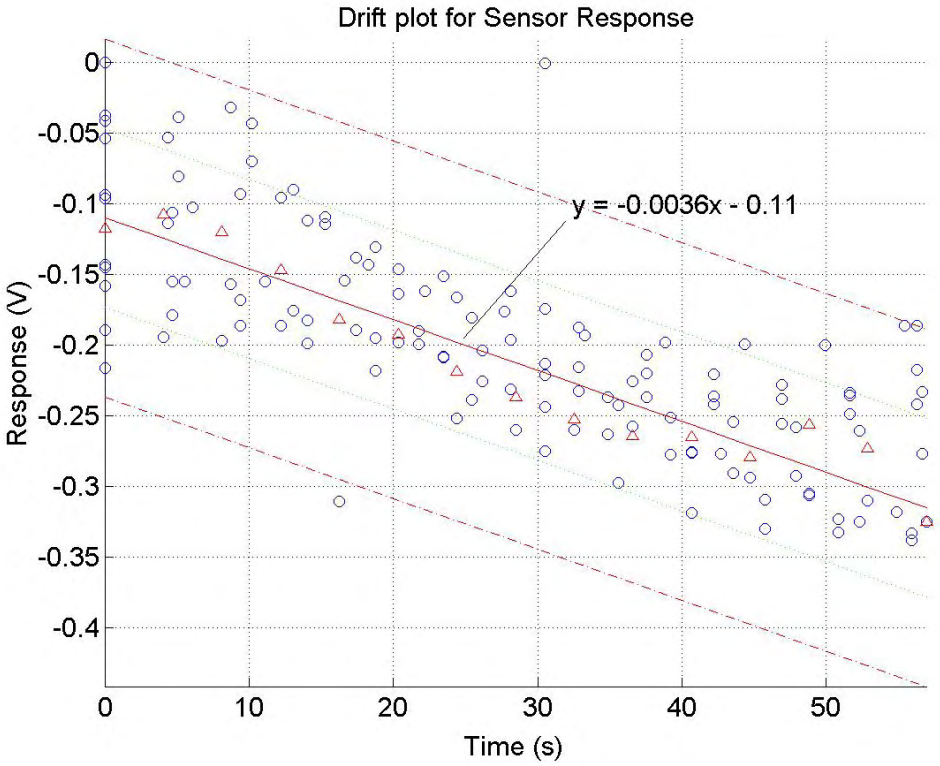

Figure 3.65: Drift of TF5050 sensor response

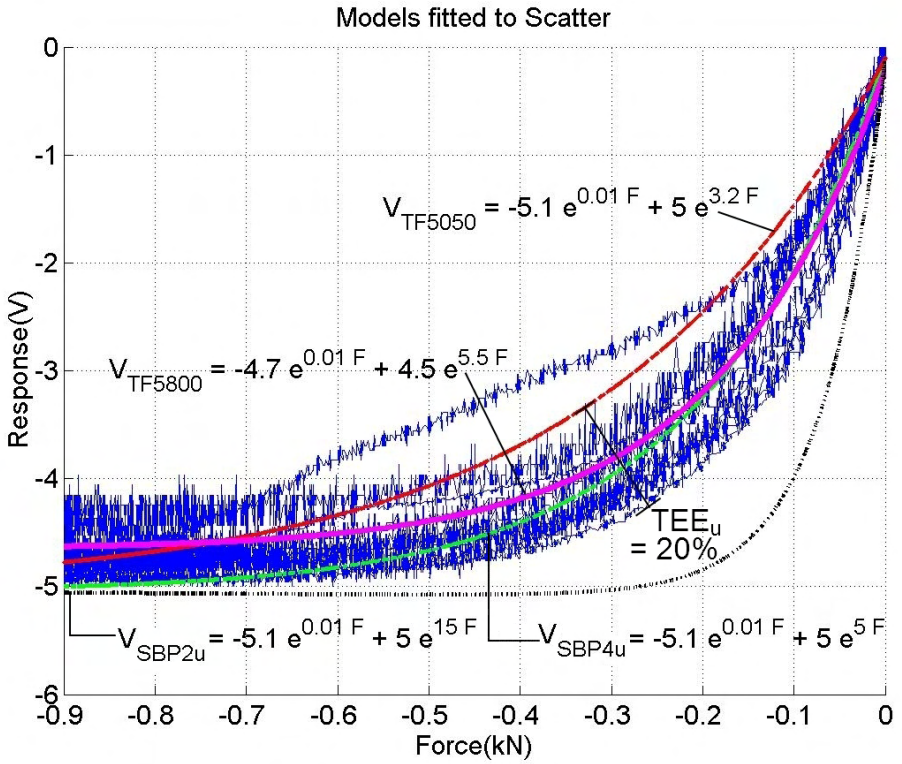

Figure 3.66: TF5800, cells 1, 2, 3, 4, 5, 7, 8, 11, 13, 14 and 15

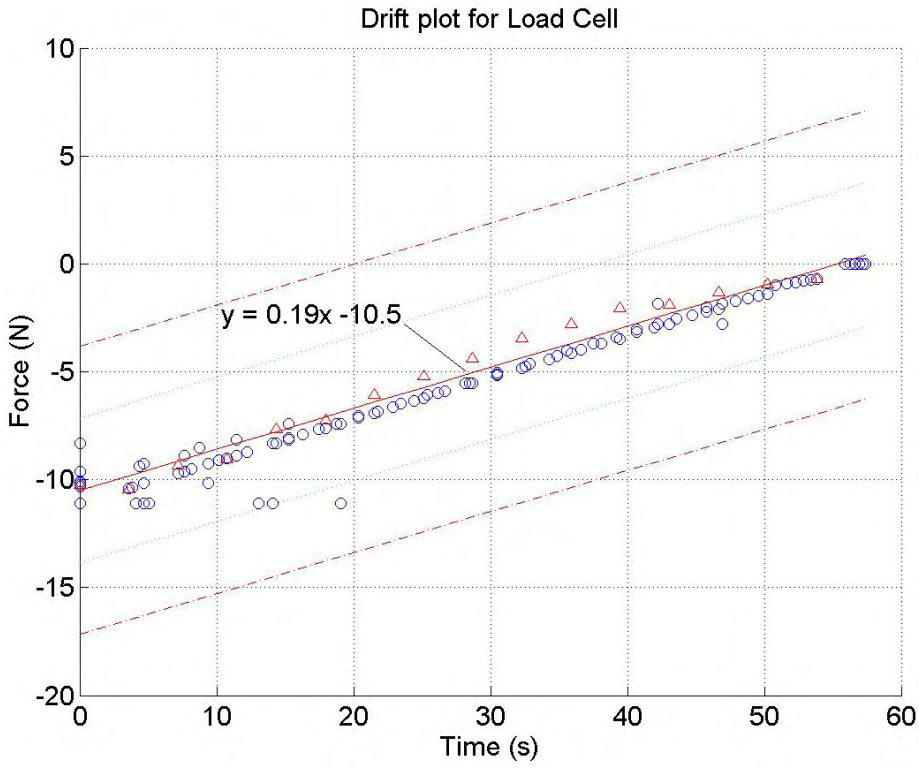

Figure 3.67: Drift of load cell used with TF5800

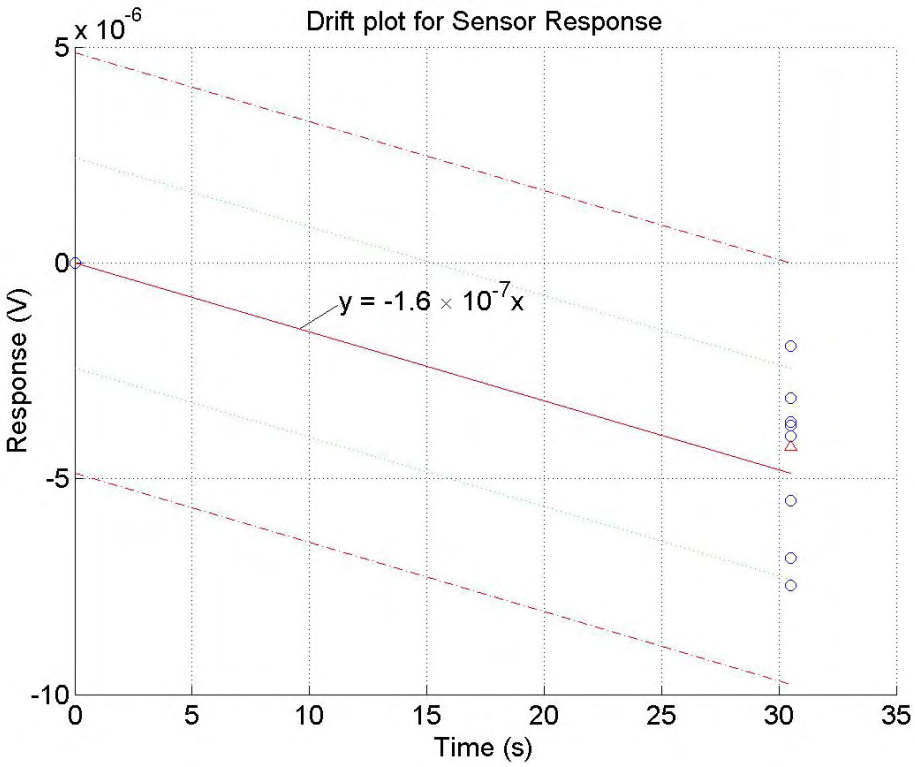

Figure 3.68: Drift of TF5800 sensor response

vii. **Discussion and Conclusion**

In these experiments the results are noisy and the curves jagged, this is attributed to the backlash in the screw type MTS we used in these experiments and should not effect the results terribly.

We tested two TF sensors one cell at a time whilst not embedded into a SBP.

For TF5050 presented in Figure 3.63 neither the V_{SBP2u} and V_{SBP4u} models fitted the data sufficiently well, though the trends were not dissimilar. A similar situation occurred for TF5800 (please see Figure 3.66). The only difference between sensors' TF5050 and TF5800 was the steepness of the user defined models, TF5050's β_2 exponent had a value of 3.2, whereas TF5800 had a β_2 exponent of 5.5 indicating that TF5050 has a flatter more linear curve. Strangely, sensor TF5050 with the flatter curve has a TEE value of 33 % compared to a lower 20 % for TF5800. It seems the effect of having either sensor embedded into a SBP is to increase its TEE value by 10 to 20 % The way to reduce this error would be to place the sensor nearer to the frictional surface as practicable thereby reducing the time it takes for the sensor to respond to changes in load.

With regards to drift, both load cells had a drift of approximately 10 N/min or 1 % per minute. Whereas, TF5050 had a drift of 0.2 V/min or 4 % per minute and TF5800 had a drift of 9.6×10^{-6} V/min or 0.0002 % per minute. So, we have mixed results. It would seem likely that the value for TF5800 is very small compared to what would be expected. This is probably due to the high number of repeated data points in the data. Therefore, value of 4 % per minute would seem a more likely value

for both TF sensors.

In conclusion,

- The two SBP models had a similar trend to that of the data but neither fitted well
- Two different *user* models were fitted to both TF sensors. The TF5050 had a flatter more linear curve with a higher TEE value, whereas TF5800 had a steeper more non-linear curve with a lower TEE value
- Having the sensors embedded into the SBP increases their TEE values by between 10 and 20 %. The suggested remedy is to place the sensor closer to the frictional surface thus reducing response times and associated error
- Though we received mixed results, the drift for a TF sensor is around 4 % per minute which was four times higher than a load cell used by industry

(i) Thick Film Room Temperature *glass disc* Compression Test

i. **Introduction**
We have noted in previous tests that the output is non-linear to varying degrees. This test is to see if that can be rectified by changing the geometry of the applicator.

ii. **Objectives**
- To test what effect a change in radius of the load applicator would have on the output of the sensor response
- To test the ability of the chosen glass to withstand loading without breakage. Glass is chosen as it is easily available and cheap insulator

Please note: This test was actually performed after one of the first heat tests thus the need for an insulator emerged.

iii. **Methods**
Load one cell to a maximum load of 600 N and return with the convexity of a solid glass disc[1] fitted into the concavity of the sensors' surface. Record loads as before.

iv. **Specimens**
Similar to that depicted in Figures 3.70 and 3.71.

v. **Experimental Set-up**
Similar to that shown in Figures 3.60−3.62.

[1] lens

vi. **Results**

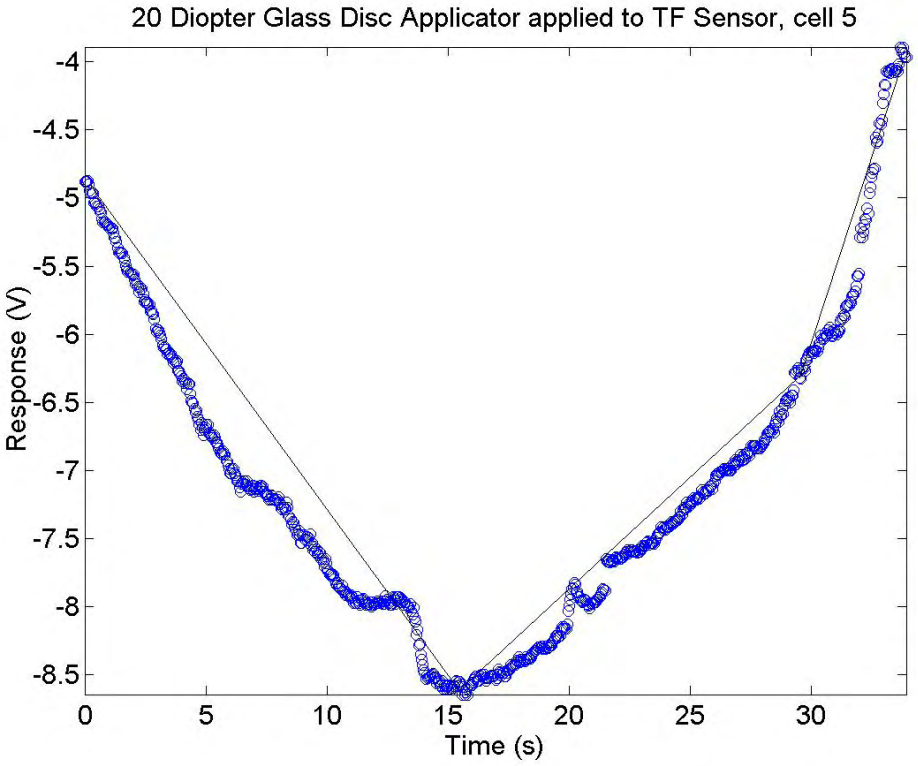

Figure 3.69: TF RT *glass disc* Compression Test

vii. **Discussion and Conclusion**

Here we applied a load applicator in the form of a glass disc to the concavity of a TF sensor cell five. We then applied a load and the glass disc broke during the test. The results shown in Figure 3.69 indicate that the radius of the disc change the linearity of the sensor response from a non-linear output to a relatively straight one as can be seen by comparing the data to the straight lines in the figure. As the glass disc broke during testing other materials need to be sought that can withstand the rigours of testing and are likely to be small enough to fit into the confines of the SBP.

(j) Thick Film Room Temperature *metal disc* Compression Test

i. **Introduction**
In the last test using a load applicator in the form of a solid 20 diopter glass lens we applied one loading cycle to cell five of a TF sensor and were able to show an apparent change in linearity due to the convexity of the load applicator. The glass disc cracked during testing indicating an alternate material needed to be found. Here we use a number of metal discs with various radii to see what effects the various radii have on the sensors response.

ii. **Objectives**
- To test what effect a change in radius of the load applicator would have on the output of the sensor response

Note: In the experiments we tested two TF sensors but since the same type of TF sensor was used only one set will be shown here.

iii. **Methods**
This involves five separate steps. At each of the five steps a bronze disc of a different radius will be used between the TF sensor and the load applicator. These steps follow:

A. Load one cell of a TF sensor to 850 N in compression at different frequencies using a flat disc and return to zero. Apply five cycles per sensor. This process will be repeated for the remainder of the discs.
B. Using a disc with a 20 mm radius (R20).
C. Using a disc with a 15 mm radius (R15).
D. Using a disc with a 10 mm radius (R10).
E. Using a disc with a 5 mm radius (R5).

iv. **Specimens**
Please see Figures 3.70 and 3.71. TF sensors were used as per previous tests.

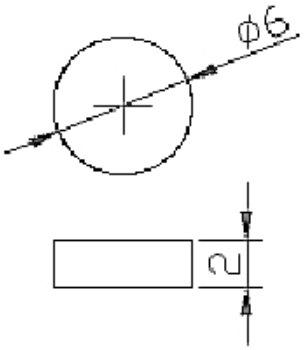

Figure 3.70: Metal flat disc applicator

v. **Experimental Set-up**
Similar to that in Figures 3.60−3.62.

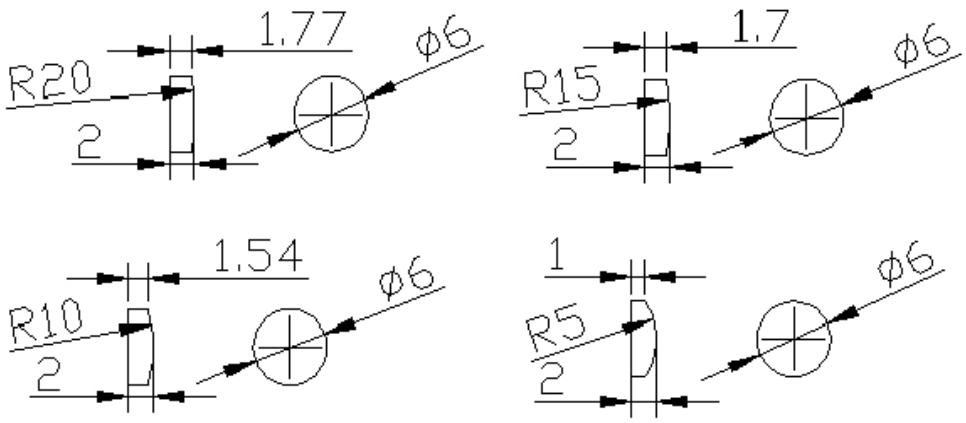

Figure 3.71: Metal disc applicators with various radii

vi. **Results**

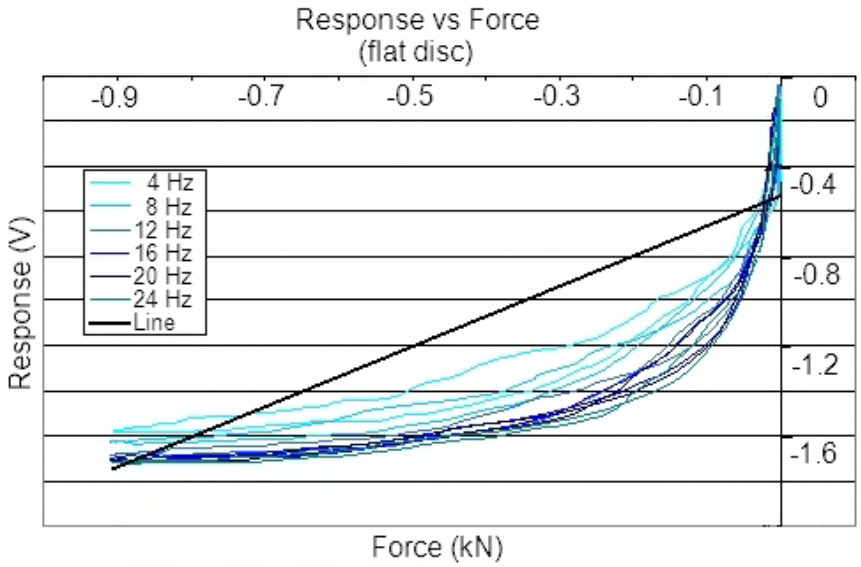

Figure 3.72: Flat disc applicator

vii. **Discussion and Conclusion**

We tested all five discs and discovered that a small radius disc produced a more linear response though at the expense of greater hysteresis in the results (please see Figures 3.72−3.77 for comparisons). In all these figures there is a straight line fit placed next to the 4 Hz data, this is to show how linear the results are. Not to be used as a calibration curve.

Figure 3.77 shows us that with increased loading frequency there is virtually no difference in the response of the sensor. The figure also shows us that the magnitude of response with a flat disc is higher than that with small radius of 5 mm. This would make sense when thinking about the construction of the sensor, since a smaller radii applicator causes a greater amount of residual stress and thus takes longer to return to its original shape. If the radius is too small it may permanently damage the

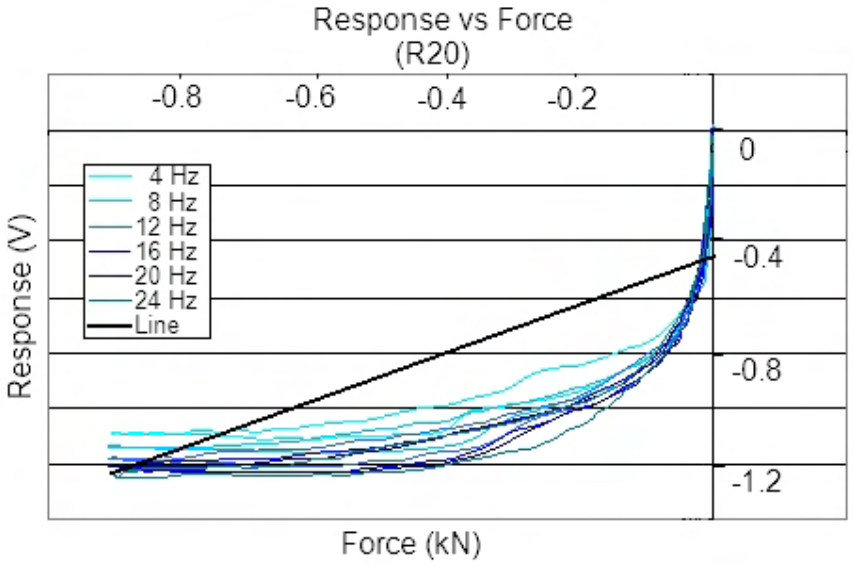

Figure 3.73: R20 applicator

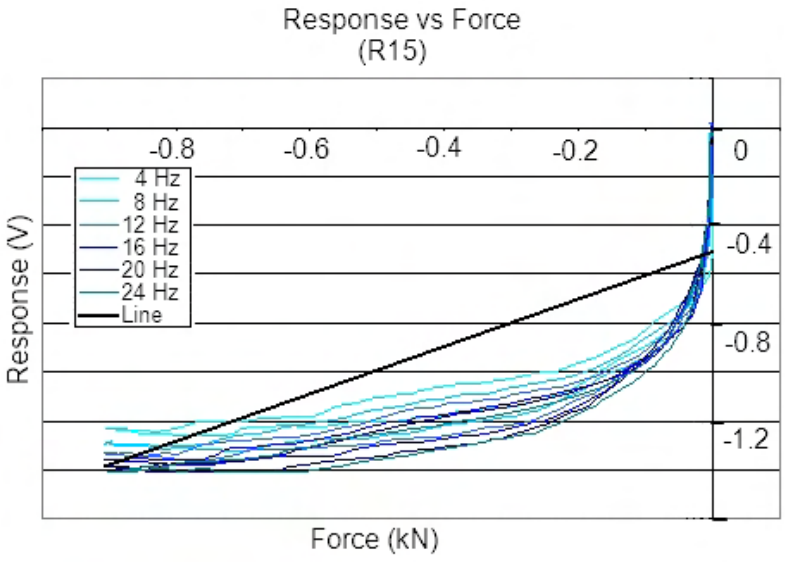

Figure 3.74: R15 applicator

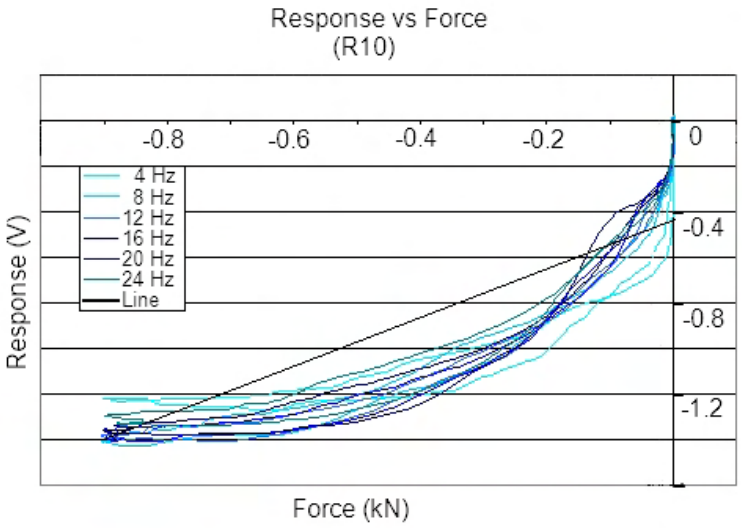

Figure 3.75: R10 applicator

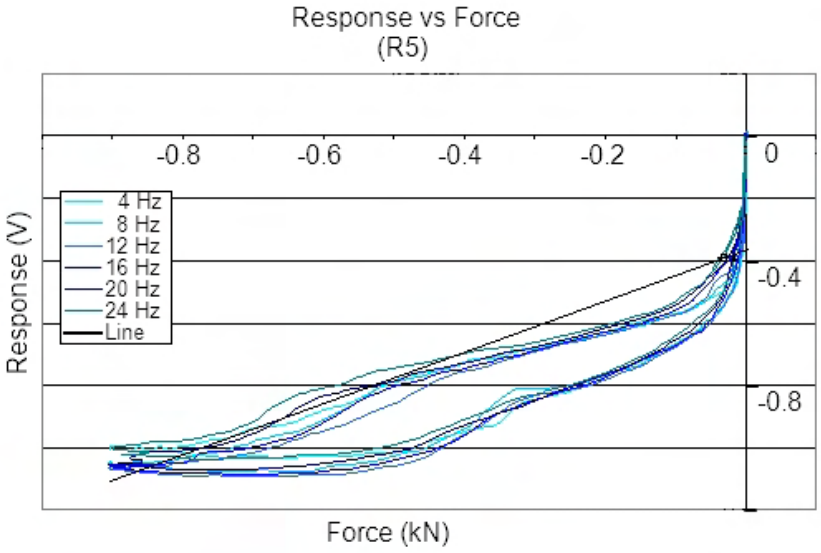

Figure 3.76: R5 applicator

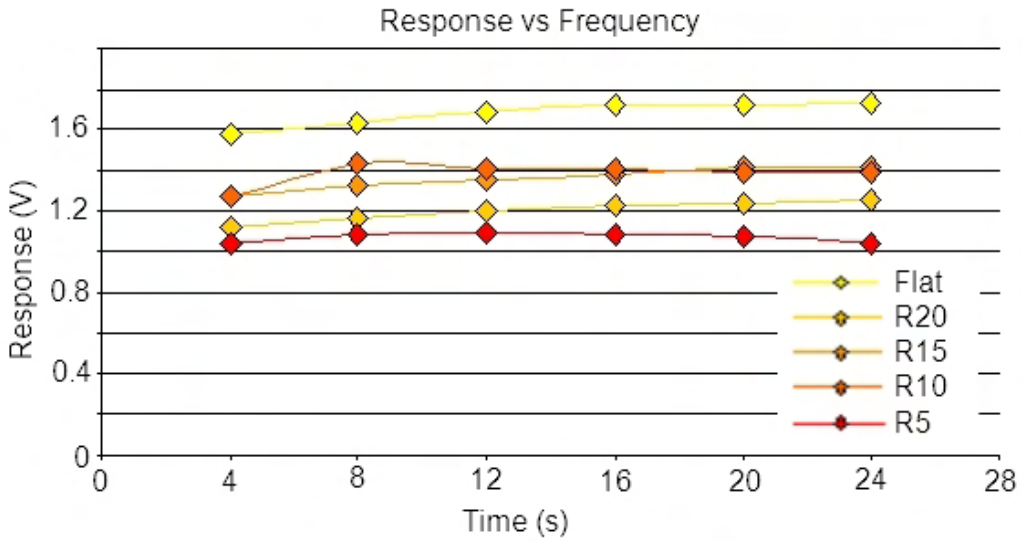

Figure 3.77: Different radii tested at different frequencies

sensor.

In conclusion,

- A smaller radius disc produces a flatter more linear response compared to a flat disc
- A disc with a smaller radius digs into the material taking it longer to *spring back* producing a curve with greater hysteresis; so it is better to use a flat disc and have less error.
- Varying the loading frequency for discs of different radii produces no great differences. However, flatter discs have a higher magnitude on the response scale.

3.4.6 Thick Film Smart Brake Pad Elevated Temperature Tests

3.4.6.1 Introduction

Once the RT tests were completed the ET tests were done, these include:

(a) Thick Film Smart Brake Pad Elevated Temperature Compression Test

(b) Thick Film Smart Brake Pad Elevated Temperature Test Compression using Insulators

These tests follow.

(a) Thick Film Smart Brake Pad Elevated Temperature Compression Test

i. **Introduction**
After the completion of a thorough examination of the SBP and TF at RT the next step was to test the SBP at ET. This experiment is our first ET test of the SBP.

ii. **Objectives**
- To test the TF sensor embedded whilst embedded in the SBP at ET

iii. **Methods**
With TF sensor embedded into SBP starting at RT and raise the temperature to a maximum of 125^o C in even increments. The test is completed using an environmental chamber attached to a 100 kN MTS.

iv. **Specimens**
TF sensors were used as per previous tests.

v. **Experimental Set-up**
A 100 kN MTS with an environmental chamber was used. The environmental chamber shown in Figure 3.78 was used to heat the specimens.

Figure 3.78: An environmental chamber for a 100 kN hydraulic MTS

vi. **Results**

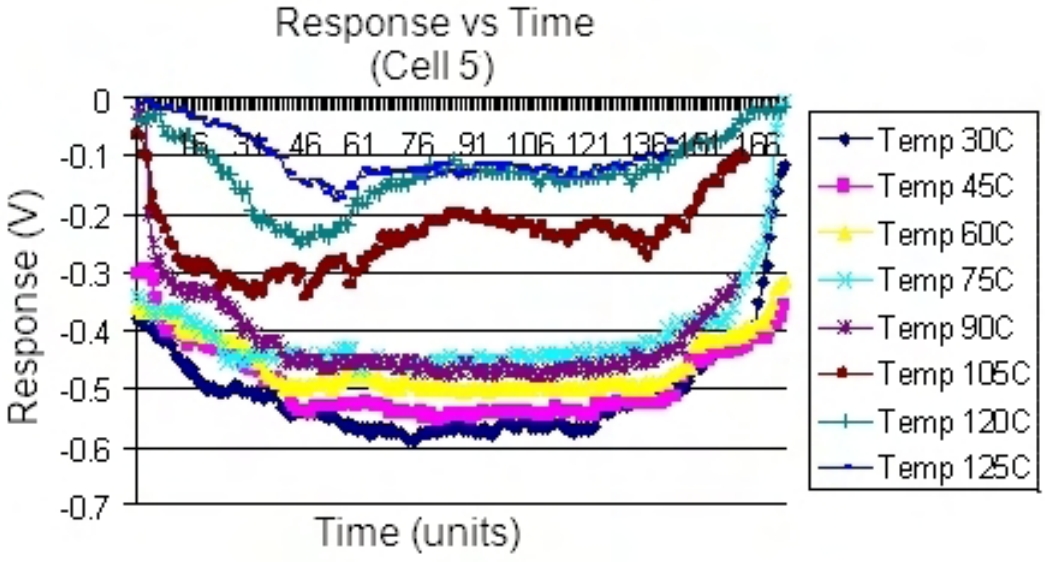

Figure 3.79: Cell 5, wires melted

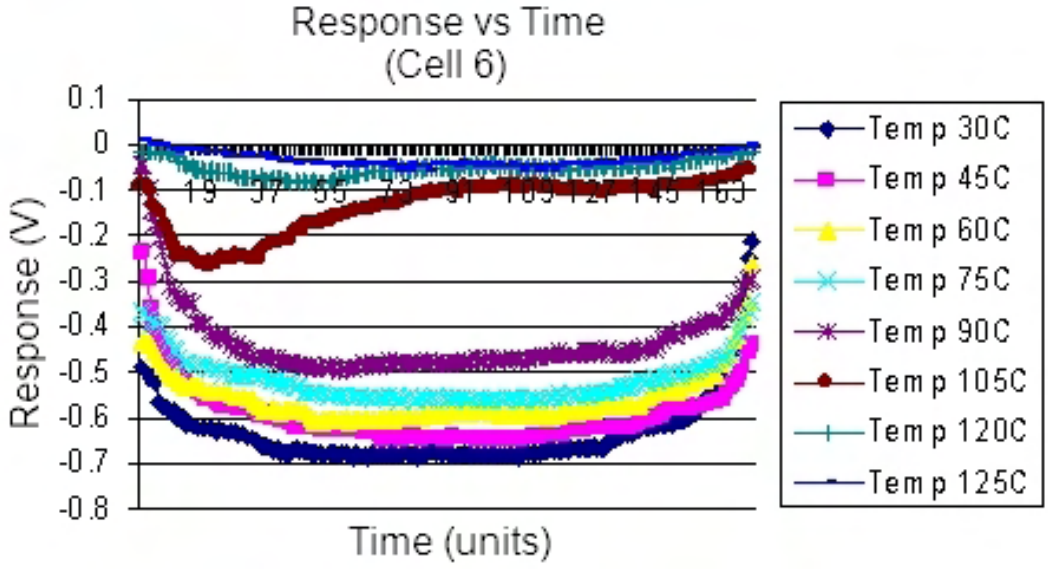

Figure 3.80: Cell 6[1], new wires

vii. **Discussion and Conclusion**

In our first attempt at this test (please see Figure 3.79) there is a noisy response, this resulted from using soldered connections and low temperature wiring to connect the DAQS with the TF sensor.

In our second attempt, we replaced the wiring and used mechanical clips rather than soldered joints, this resulted in a low noise response (please see Figure 3.80).

On first inspection of 3.80 it would seem at 105^{o} C the sensor response had decreased to almost zero, however we can see in Figures 3.81 and 3.82 that the response is present but greatly reduced in magnitude. The

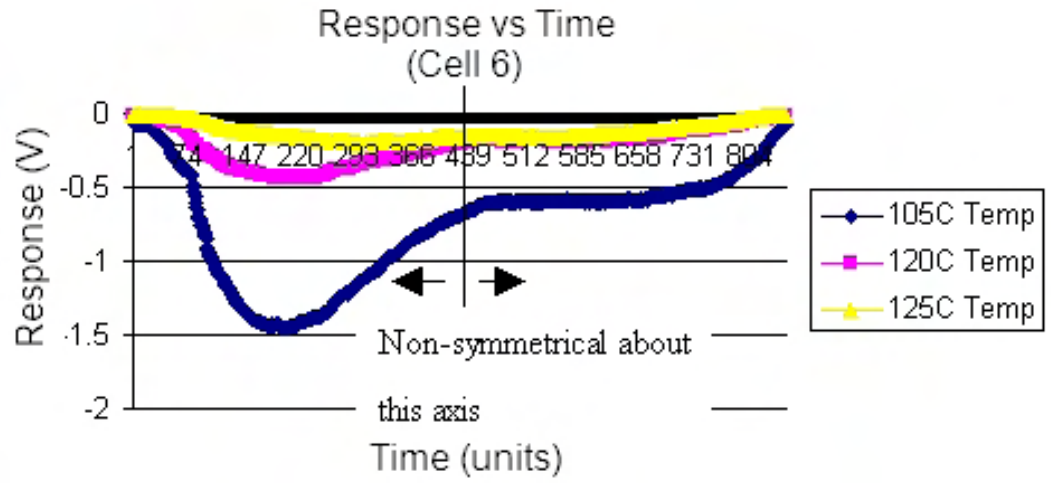

Figure 3.81: Cell 6, new wires, close-up of selected temperatures

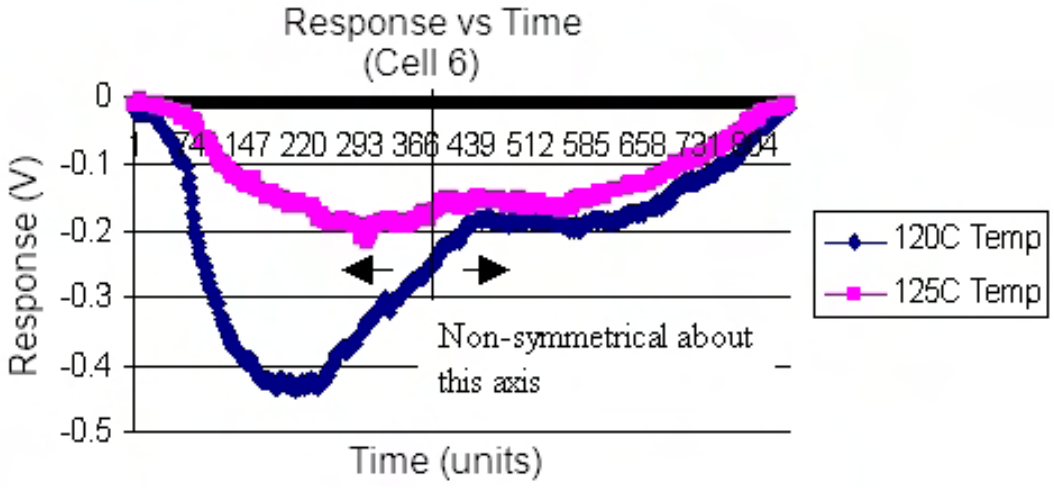

Figure 3.82: Cell 6, new wires, a further close-up of selected temperatures

other notable difference that occurs at 105^o C is the cooling part of the curves is not symmetrical with a similar temperature during the heating phase. This non-symmetrical nature, may be caused by friction material abnormalities or the fact that the cooling phase is initiated via the use of liquid nitrogen injected into the environmental chamber.

In conclusion,

- We successfully tested the SBP with TF sensor embedded to 125^o C, however, at 105^o C the magnitude of response decreases greatly and becomes non-symmetrical as temperature increases above this threshold. A non-symmetrical response would make calibrating the sensors difficult.
- It is suggested that insulating materials be used between the brake pad and the TF sensor to increase the operating temperature of the sensor

(b) Thick Film Smart Brake Pad Elevated Temperature Test Compression using Insulators

i. **Introduction**
In our previous test we tested a SBP to 125^o C, however above 105^o C there was a non-symmetrical response that would make future calibrations difficult.

In this test we try to increase the operating temperature of the SBP via the introduction of insulating materials above and below the sensor.

ii. **Objectives**
- To attempt to raise the operating temperature of the SBP by shielding the TF sensor from heat via use of insulating materials above and below the sensor

iii. **Methods**
Using a 100 kN MTS fitted with environmental chamber raise the temperature of the SBP through one heating and cooling cycle starting at RT through to a maximum temperature of 200^o C back to zero. Manually record temperature at 15^o C steps.

Please note: The cooling cycle was removed as it was not deemed necessary to complete because of the non-symmetrical response of the sensor.

iv. **Specimens**
TF sensors were used as per previous tests.

v. **Experimental Set-up**
Similar to previous ET test.

vi. **Results**

The data in Figures 3.83 to 3.86 is separated into three temperature measurements per plot. The data has been zeroed symmetrically about the mid point of the time scale since the offsets were uneven above and below the x axis.

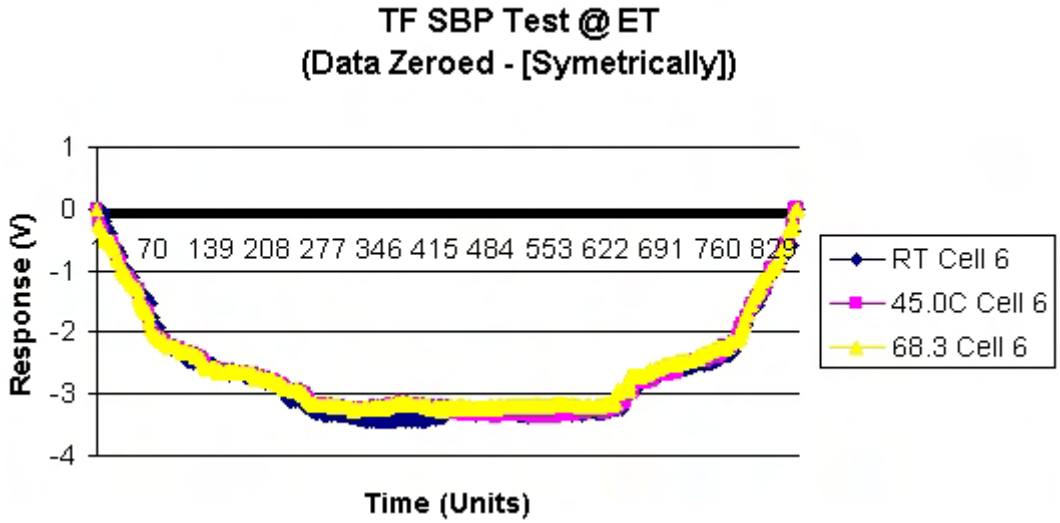

Figure 3.83: Cell 6, RT to 68.0^o C

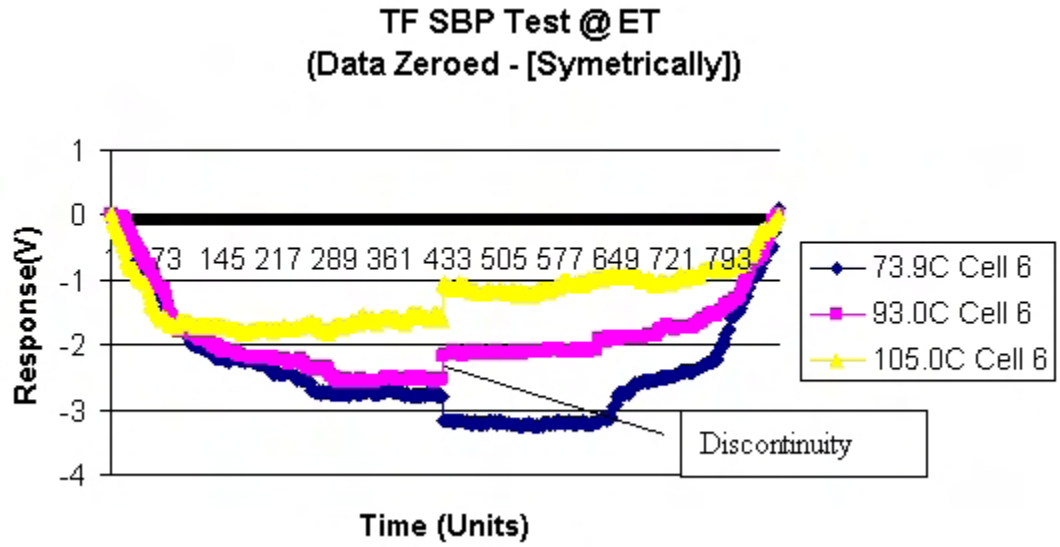

Figure 3.84: Cell 6, 73.3^o C to 105.0^o C

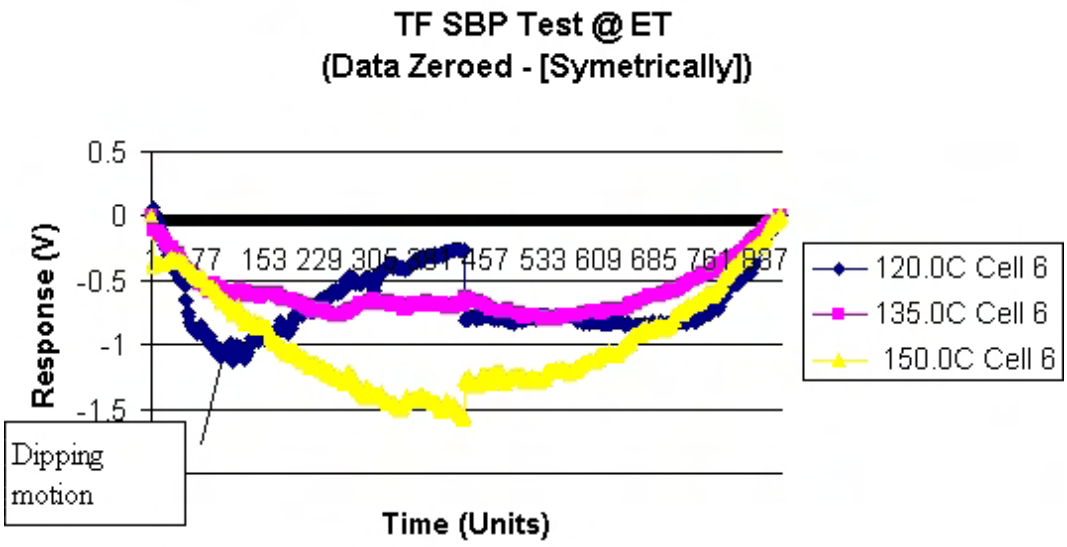

Figure 3.85: Cell 6, 120.0^o C to 150.0^o C

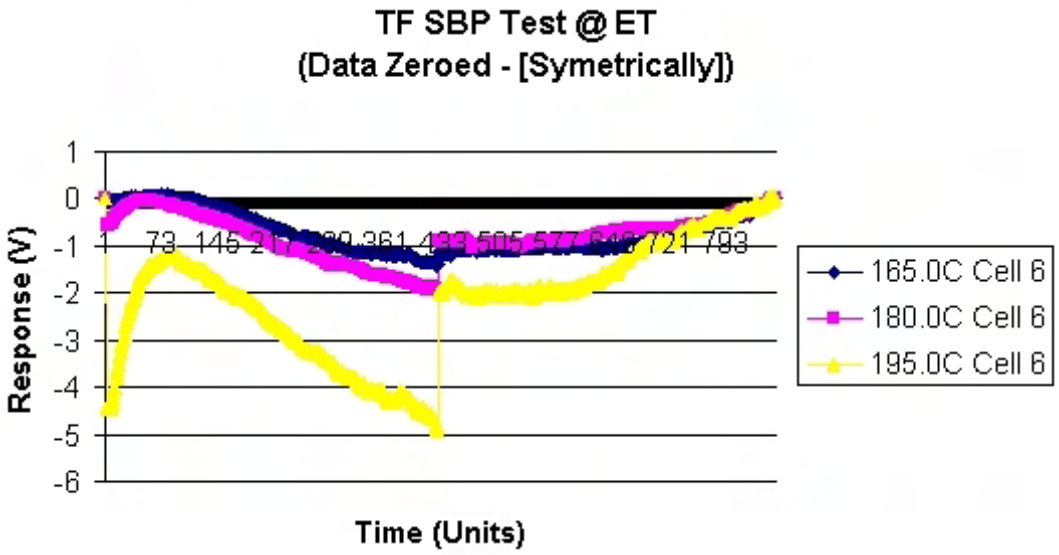

Figure 3.86: Cell 6, 165^o C to 195^o C

vii. **Discussion and Conclusion**

As shown in Figure 3.83 there is not much variation in response between the different temperatures.

As the temperature is raised through 73.9 to 105^o C shown in Figure 3.84 we see a discontinuity emerging between first half of the test and the second half of the test.

As the temperature is raised to 120^o C we see a strange sinusoidal type movement, this occurs on and off up till 195^o C. The crushing of the Mica[1] sheeting which has a square cross-sectioned honeycomb structure was the reason for the unusual response.

In conclusion,

[1]The insulating material used in these tests

- We successfully raised the temperature of the SBP to 195^o C however the sensor with this type of insulator could only be used to 180^o C with any accuracy
- Other insulators need to be investigated that resist crushing, such as: Kapton Film, Nomex^R brand paper [type 410, 20 Mil] and or small balls of A-800-3G high temperature vacuum bag sealant tape. The small balls of sealant tape would also assist in ensuring even pressure is applied to each cell and at the same time insulate the TF sensor against temperature

3.4.7 Discussion and Conclusion
- Thick Film Investigation -

In this section we summarised the SBP design process along with the sensor development. We also developed a mathematical model for the sensor.

We successfully applied the TF theory (please refer to Equation 3.73) to the SBP and cell-by-cell RT tests. Though the general trend was similar from test to test, a different solution was required for each case.

During testing we tested the SBP's and later the sensors by themselves at RT, to see what was causing the high TEE levels in the SBP tests. By reviewing these results, embedding the TF sensors underneath the friction material nearest the backing plate, causes them to have a higher TEE values than does having them nearer the rubbing surface, since they take longer to respond. Placing the TF sensors nearer the rubbing surface would be at the cost of an increase in the operating temperature. Since the friction material itself is an insulator.

The TF sensors like the FSR [18] have a higher amount of drift compared to their industrial *load cell* counterparts, in our case, four times higher.

Testing the SBP's at ET revealed that they did not function well above 105^o C without insulation. A final test was conducted by insulating the sensor with Mica sheeting that crushed during testing, though it allowed us to reach a non-symmetrical maximum of 195^o C! Certainly, high temperatures ought to be achievable by using more durable insulators, such as those previously mentioned.

In conclusion,

- We developed an analytical model for a TF sensor and tested it with experimental data whilst embedded and not embedded into a SBP with good results
- Despite the many advantages of the caged method, high TEE values can be expected. Whilst embedding TF sensor into friction material is not practical.
- Though temperatures of up to 195^o C were achieved, different insulating materials need to be implemented if the TF SBP were to be used in dynamometer testing. Since, the results were non-linear and non-symmetrical making calibration at elevated temperature very difficult
- The TF sensor has a high amount of drift and though this does not matter during MTS testing, it would make results difficult to understand if the TF SBP was used in a brake dynamometer
- Other sensors need to be investigated to fulfil the SBP-SDC

3.5 Fibre Optic Investigation

3.5.1 Introduction

In the last section we investigated *thick film sensors* and concluded that other sensors need to be investigated to fulfil our specifications.

In this section, we will investigate *fibre optic sensors* and cover the following sub-sections:

(a) Special Data Analysis Terminology

(b) Fibre Optic Smart Brake Pad Design Summary

(c) Smart Brake Pad Test

(d) Finite Element Analysis

3.5.2 Special Data Analysis Terminology

As a contingency plan, we tested two types of fibre optics sensors simultaneously. The design of both the Senko Advanced Components (SAC) and Blue Road Research (BLUERR) sensors contain bi-axial FBG. The reason for the *bi*, rather than simply, *axial*, is because the sensors' are designed to measure both temperature and load simultaneously. The difference between the two sensors, is that a bi-axial gratings has two peaks, whereas, an axial grating has one peak.

With any sensor, what we are trying to extract is the best correlation between the measured and that special characteristic of the transducer. i.e. resistance, capacitance, conductivity or optical properties, such as *peak shifts* (please see Figure 3.87. The figures are: a. Left peak shift, b. Right peak shift and c. Peak separation). In our case, it is load and peak shifts. Once we have this type of data, we may represent and reference it in different ways. For simultaneous load and temperature measurement, we could assign the *peak separations* to load measurement and the *peak shifts* to temperature measurements. If the sensors do not work as prescribed here, and for instance no peak separations are detected with successive loading, then the load measurement can easily be assigned to the peak shifts and the temperature measurements can be assigned to another sensor or other device.

The primary objective of this research is to design a sensor that will enable the dynamic measurement of pressure between brake pad and disc. This design achieves this through discrete measurement of force in several places over the brake pad surface, through use of multiple sensor points[1].

3.5.3 Fibre Optic Smart Brake Pad Design Summary

After discussions we decided that a probe would be the best option for embedding the sensor into brake pad. The method would involve drilling holes in the brake pad and inserting probes that could easily be removed and reused in another pad. So the hunt began for a suitable method to bury the optical fibre into a material that would:

[1] Multiple Fibre Bragg Gratings (FBG's)

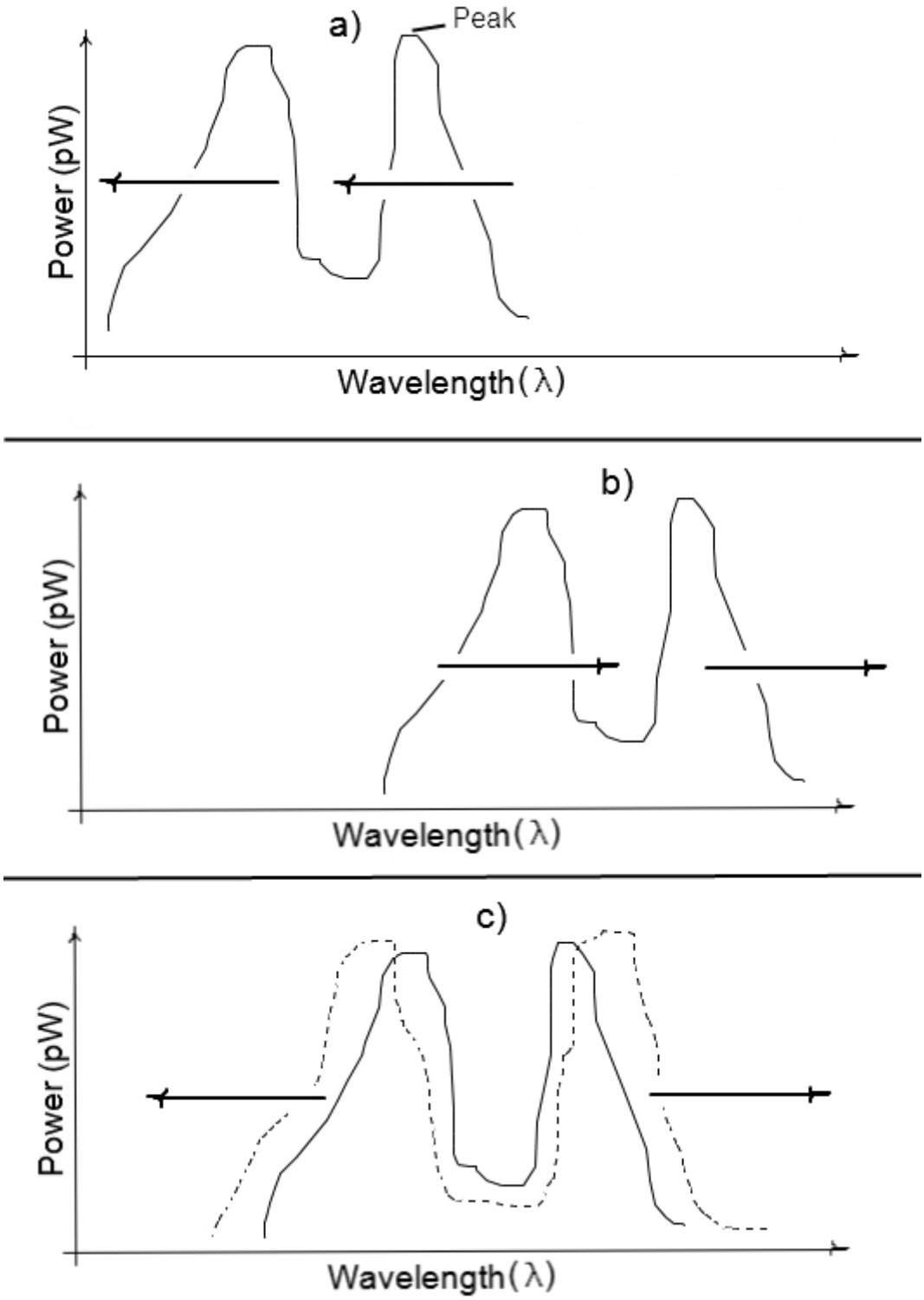

Figure 3.87: *Peak shifts*

- Decrease the influence the measurement process had on braking performance
- Would be easy to make at a low cost
- Meet the requirements of the SBP-SDC

The initial designs for the Smart Probe (SP) for the SBP are over viewed here briefly:

- A piece of metal in the shape of a straight bladed sword with blunt edges and a point, the fibre would rest on the middle of the blade and would be held in place by a resin coating. The *sword* would be the backbone of the device
- A steel rod with a flat milled on top of it and the fibre to rest in the middle of the milled flat. Like that of the *sword type* a coating of resin would be applied to the top of it
- A circular steel rod with a groove milled down the centre of it and the fibre this time would be held in location by the groove. The whole assembly would be held in place by a resin coating
- A slit in a circular rod of steel so that the load would be transferred directly to the fibre. A variation of this design involved using a spring steel *split pin*[1], fibre in middle with resin
- Using stainless steel syringe needle tubing and threading the fibre up the middle of the tubing and sucking resin around the fibre using the syringe. This was taken as novel, but rejected as it was believed that the stainless steel casing would be too stiff for the optical fibre to strain adequately in order to measure a strain using the embedded FBG sensor
- Using a cast epoxy cured in a length of plastic vacuum tube. A V shaped groove was to be milled down the centre where a fibre could be laid in. The groove would be then filled in using more epoxy
- The accepted design involved embedding the fibre directly into a probe made of resin or other appropriate material cast using a simple mould

Figures 3.91−3.89 are the SP and its uses for both the inboard and outboard brake pads. The final design used was similar to what is presented here.

Please see Appendix H for: "Resin Probe Manufacturing Process", and "The Trial Assembly of SBP's into a Brake Calliper." See Appendix I for: "Methods for replacing the Buffer Coating once Stripped."

[1] A split pin is a hollow spring steel pin with a slit in it allowing it to conform to a range of different hole diameters

3.5.4 Smart Brake Pad Test

(a) **Introduction**
In these series of experiments we attempt to calibrate two different types of FO SP's in an attempt to meet the SBP-SDC better than TF technologies.

(b) **Objectives**

i. To test the *bare* and *embedded* SP for the effects of heat (test a)

ii. To test the SP effectiveness of measuring load whilst embedded into a brake pad (test b)

iii. To test both sensors for the effects of heat and load on the output response whilst embedded into a brake pad (test c)

(c) **Methods**
The experiments were conducted with a 15 kN MTS with portable heating platen. Loads and or heat was applied to test specimens as indicated in Figures 3.93 to 3.97 and described in the following sections.

Test a Each bare SP was heated incrementally to 200^o C at each increment peak shifts were recorded. Two cycles were completed for each sensor. One test was completed with the probe bare and the other whilst embedded into the frictional material of the brake pad.

Test b SP were embedded into brake pad as displayed in Figures 3.96. The specimen was loaded between 0 and 5 kN at 400 N increments and return to zero load. At each 400 N increment the test was stopped. A peak search was performed to locate the two highest peaks on the Optical Spectral Analyser (OSA) screen. The peak positions were then recorded. The test was completed twice for each of the SP.

Test c SP were embedded into a brake pad as displayed in Figure 3.97. The SBP was heated from RT to 200^o C in 300^o C increments. At each temperature level the specimen was loaded between 0 and 5 kN at 400 N increments and return to zero load. The data was manually recorded. Each sensor was tested separately.

In Figure 3.90, a broad band light source is launched into a fibre which is coupled to the sensor cable and OSA with 0.05 nm resolution. Measurements are made manually, after each successive load cycle. The Bragg gratings are being interrogated in the reflection mode.

The MTS is controlled by an analogue test controller, which can be controlled *manually* rather than automatically which has been the case previously. This is achieved by setting the load rate, pressing *start*, and watching the illuminated indicator on the front of the chassis displaying the load in Newton's. When the display, shows the required load, the operator would press *stop*. When the operator presses stop, this gives a chance to record the readings from other instruments such as OSA. After a reading is taken the test is then resumed by pressing start and so on.

(d) **Specimens**
Please see Figures 3.91−3.92 for the approximate test specimens used.

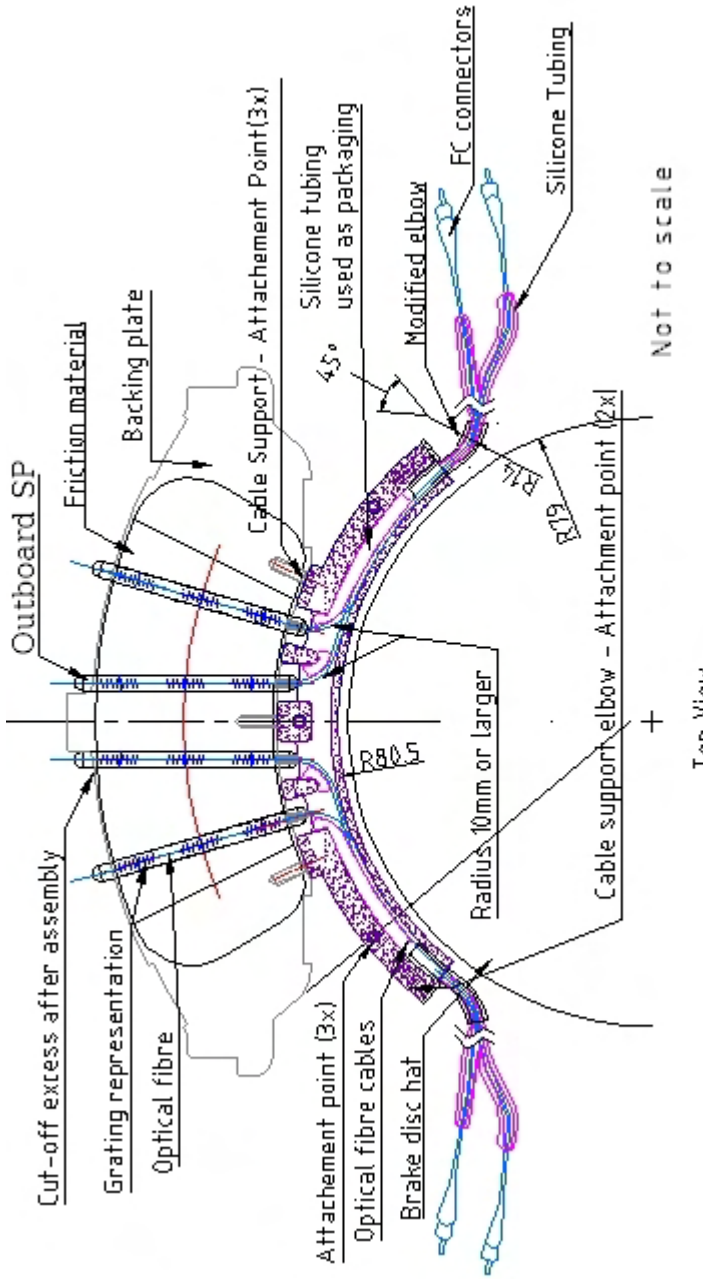

Figure 3.88: Outboard BLUERR-SP embedded into pad

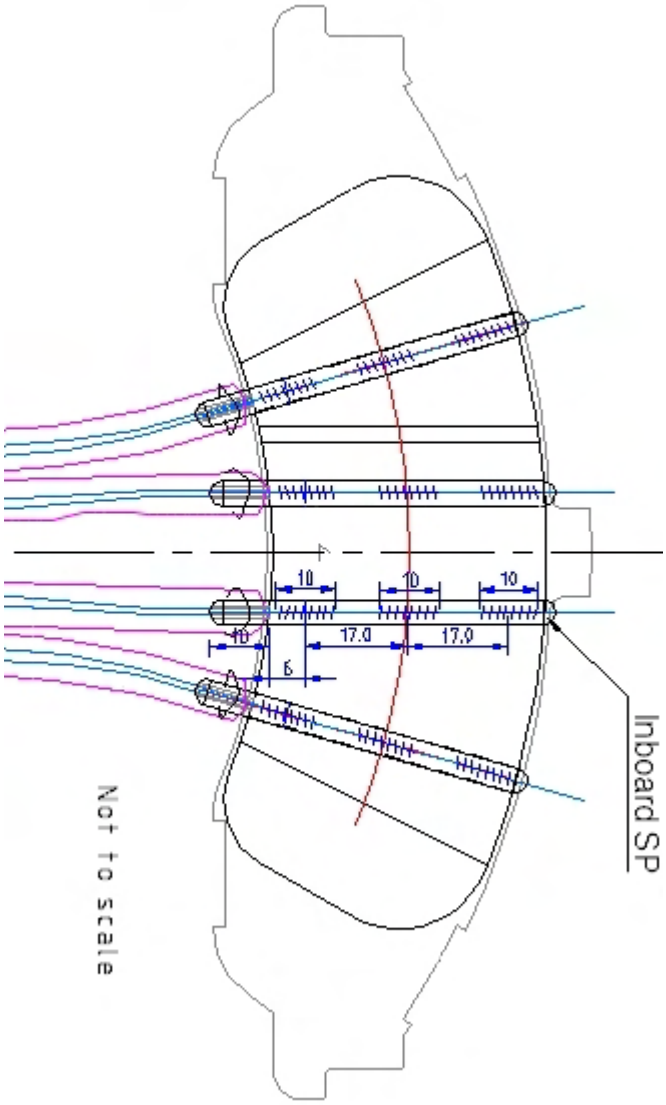

Figure 3.89: Inboard BLUERR-SP embedded into pad

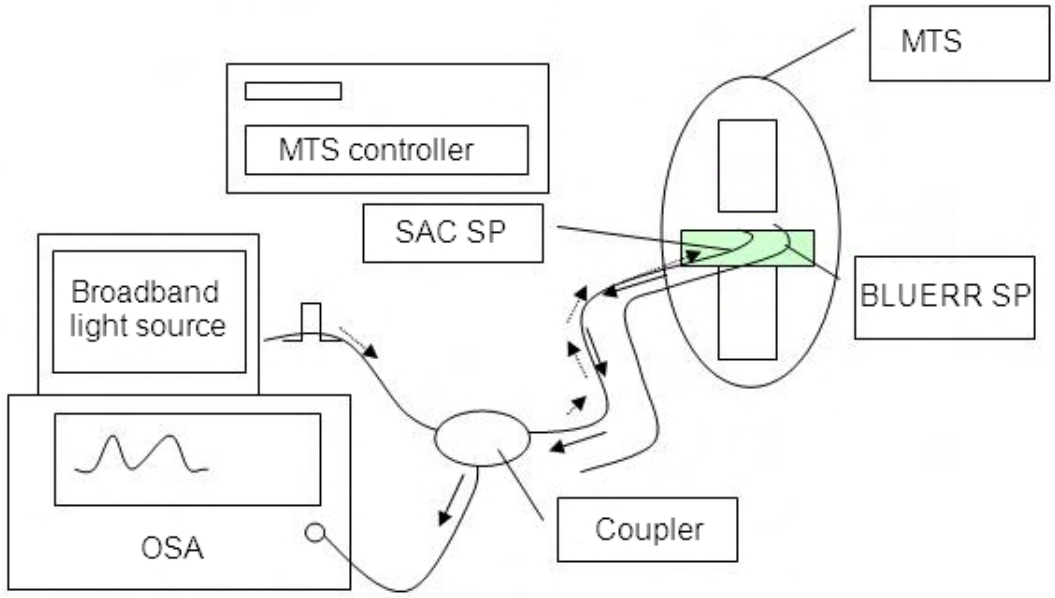

Figure 3.90: Functional experimental set-up

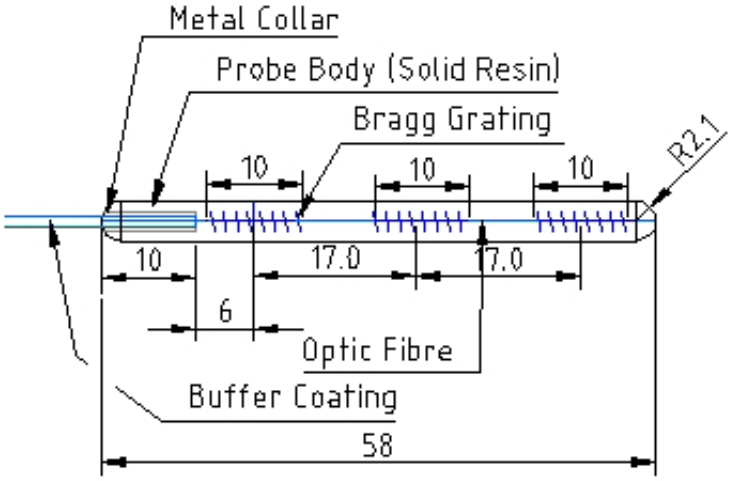

Figure 3.91: BLUERR SP

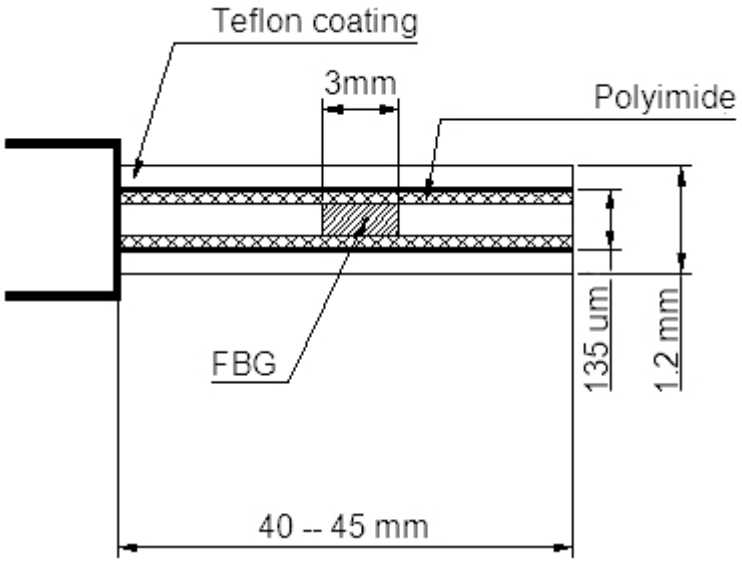

Figure 3.92: SAC SP

BLUERR SP A bi−axial FBG sensor is an optical sensor capable of measuring transverse strain orthogonal to the longitudinal axis of the fibre. It is 135 μm in diameter[1] and has a polyimide coating for improved temperature resistance. The sensor is fitted with an FC connector. The sensor is embedded in a solid resin[2] probe measuring approximately 4.2 mm in diameter, which is then inserted into a brake pad for testing. For the tests this sensor was inserted without adhesive for easy removal and later re-use.

SAC SP A bi−axial FBG sensor is an optical sensor capable of measuring transverse strain orthogonal to the longitudinal axis of the fibre. This custom sensor is approximately 2 mm in diameter and has a teflon coating. The sensor is fitted with a FC connector. This sensor was embedded into the brake pad with silicone adhesive which is mechanically bonded to the teflon coating which made it easier to remove.

[1] A similar thickness to human hair, though much more delicate
[2] Derakane 370−400

(e) **Experimental Set-up**

Figure 3.93: 15 kN MTS with peripheral equipment

Figure 3.94: Close-up, of 15 kN MTS

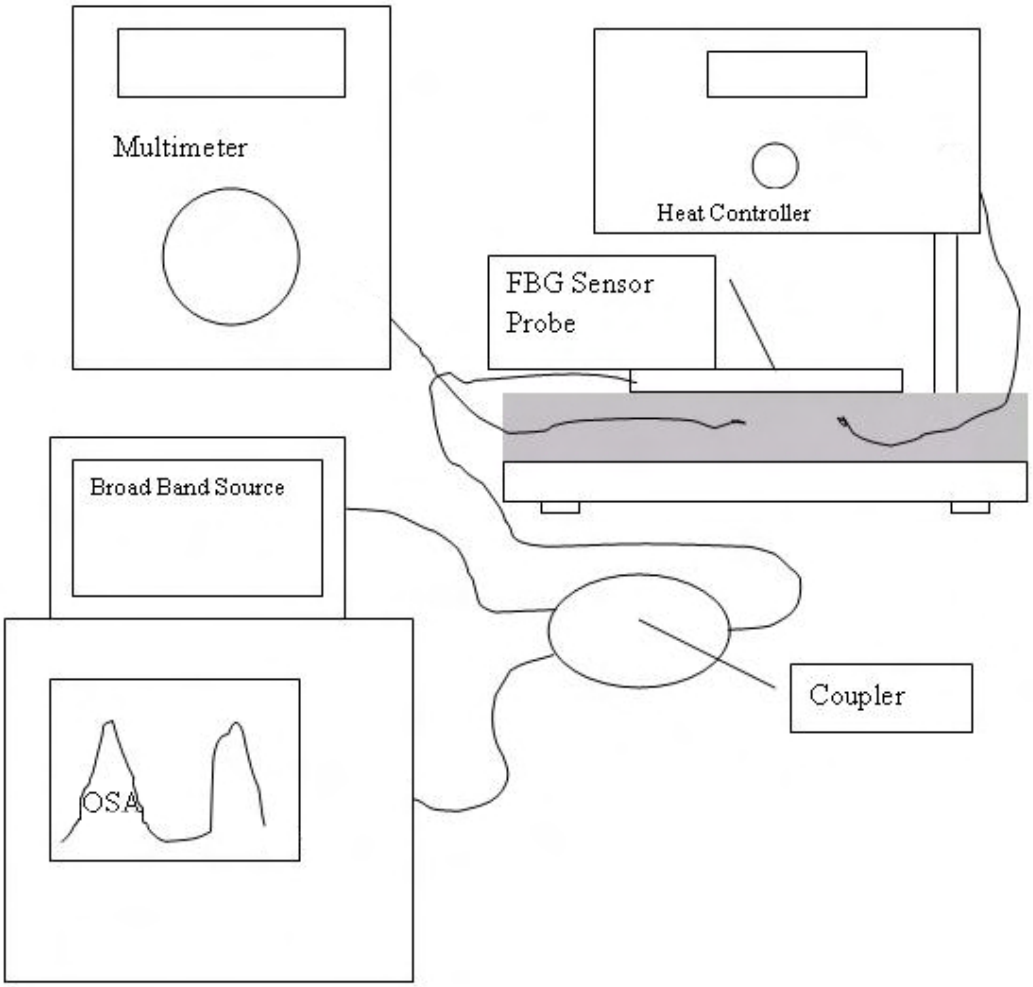

Figure 3.95: Experimental set-up for the bare fibre SP tests

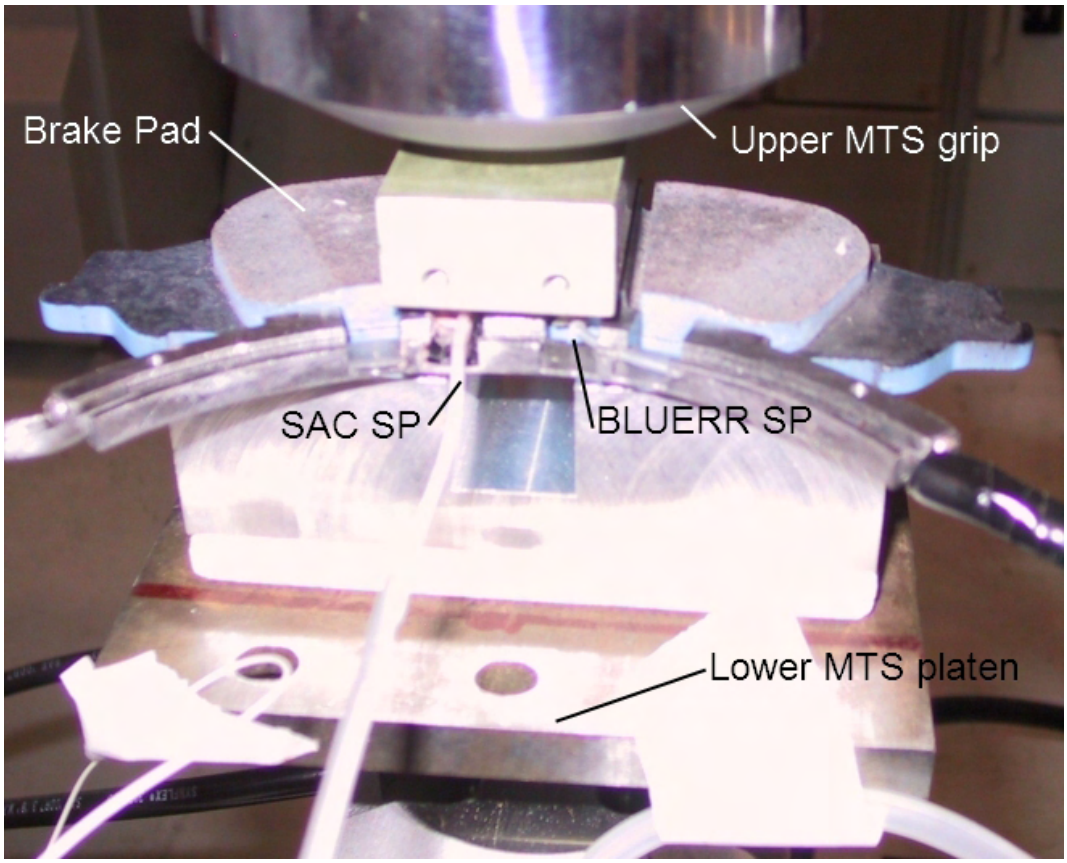

Figure 3.96: RT set-up

(f) **Results**

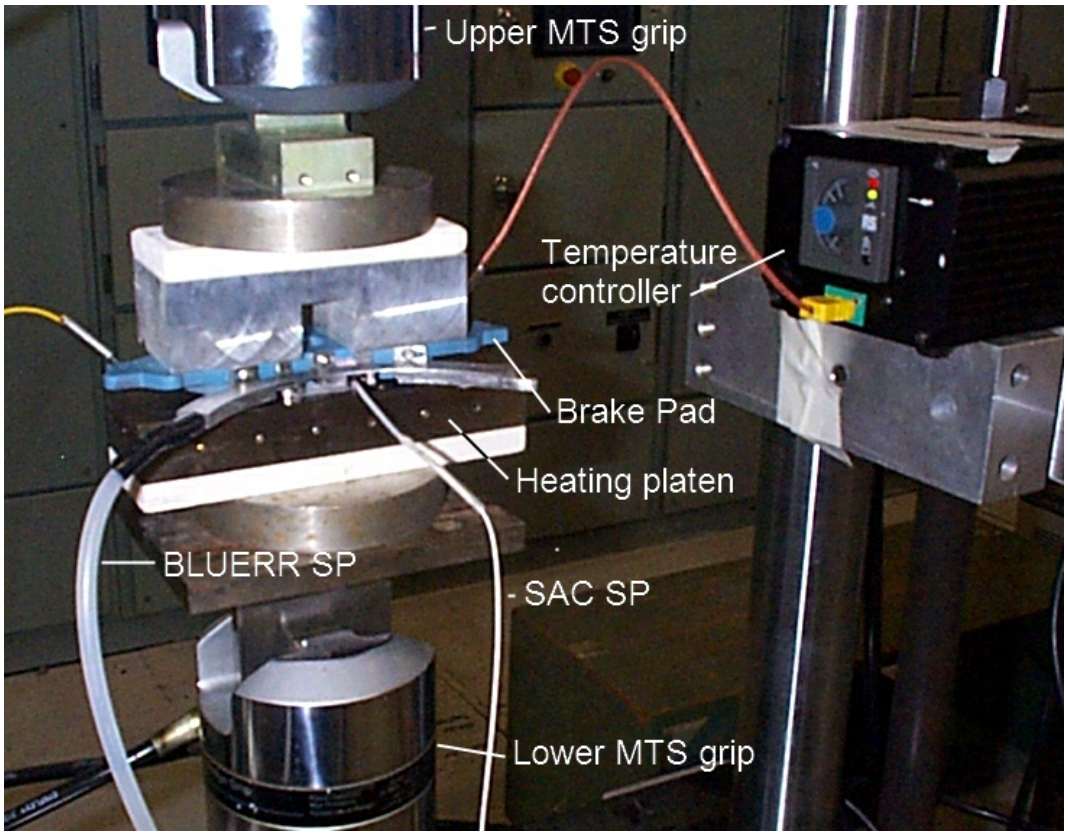

Figure 3.97: ET set-up

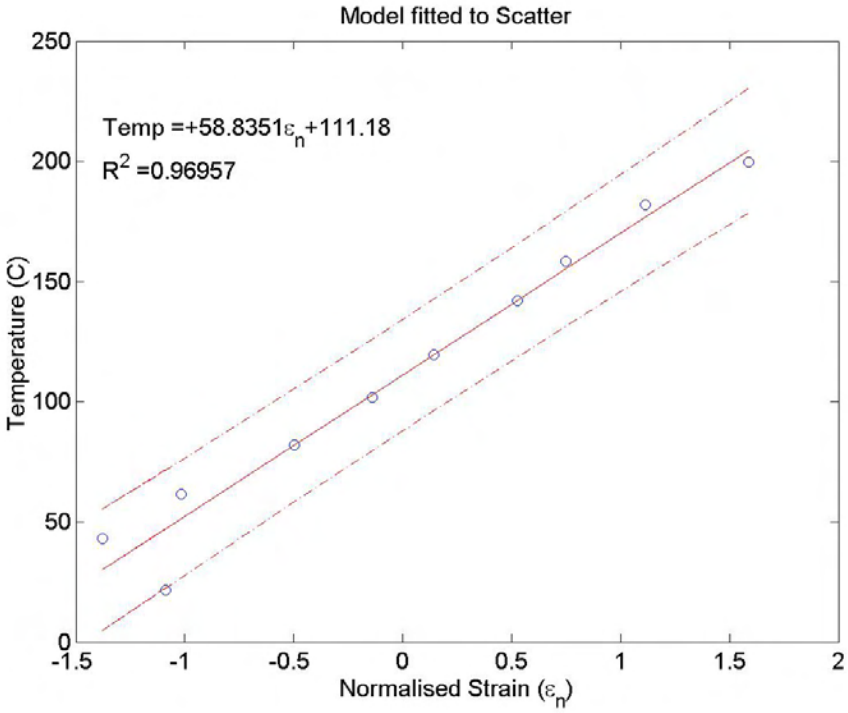

Figure 3.98: Test a, SAC bare SP, model

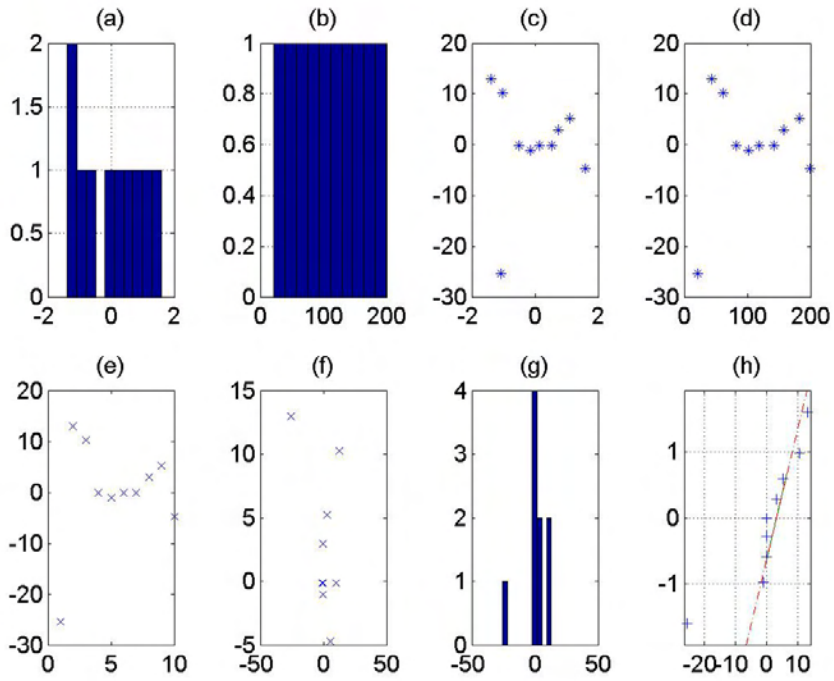

Figure 3.99: Test a, SAC bare SP, residuals

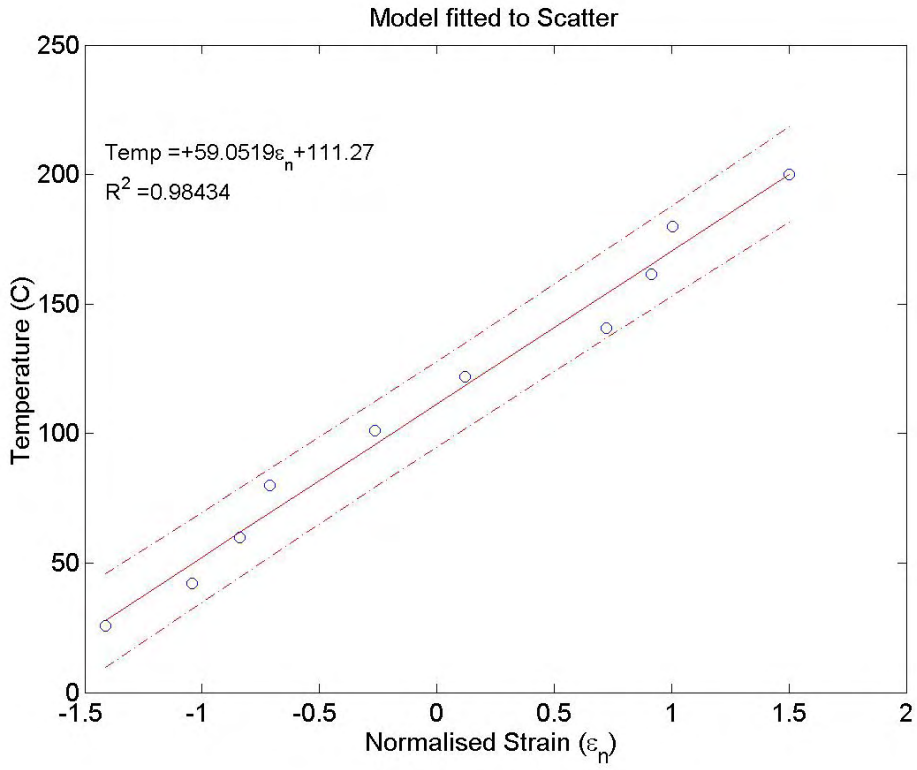

Figure 3.100: Test a, BLUERR bare SP, model

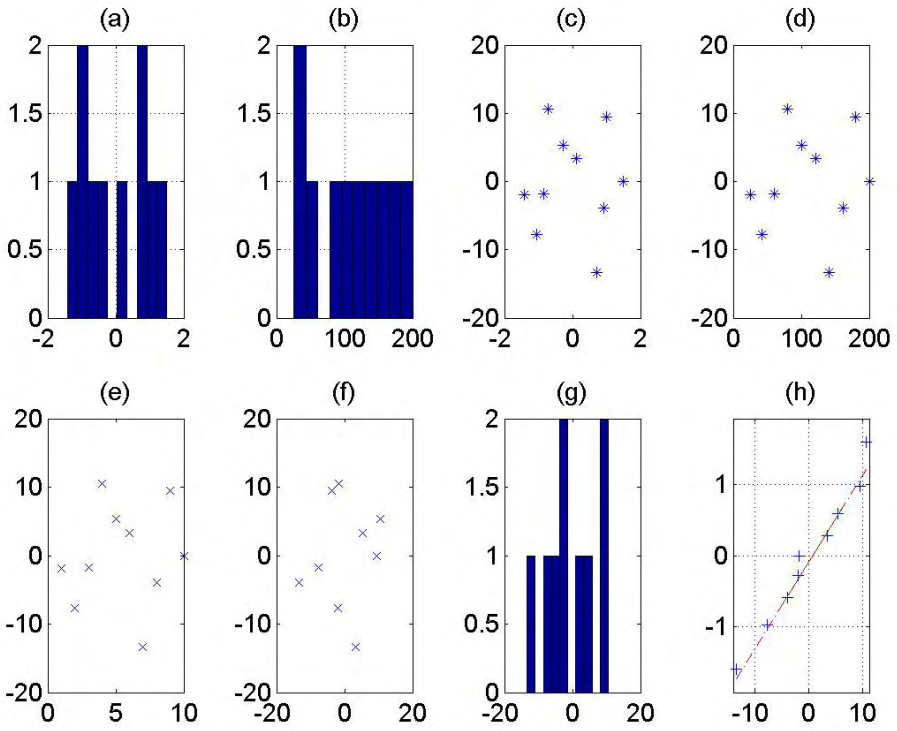

Figure 3.101: Test a, BLUERR bare SP, residuals

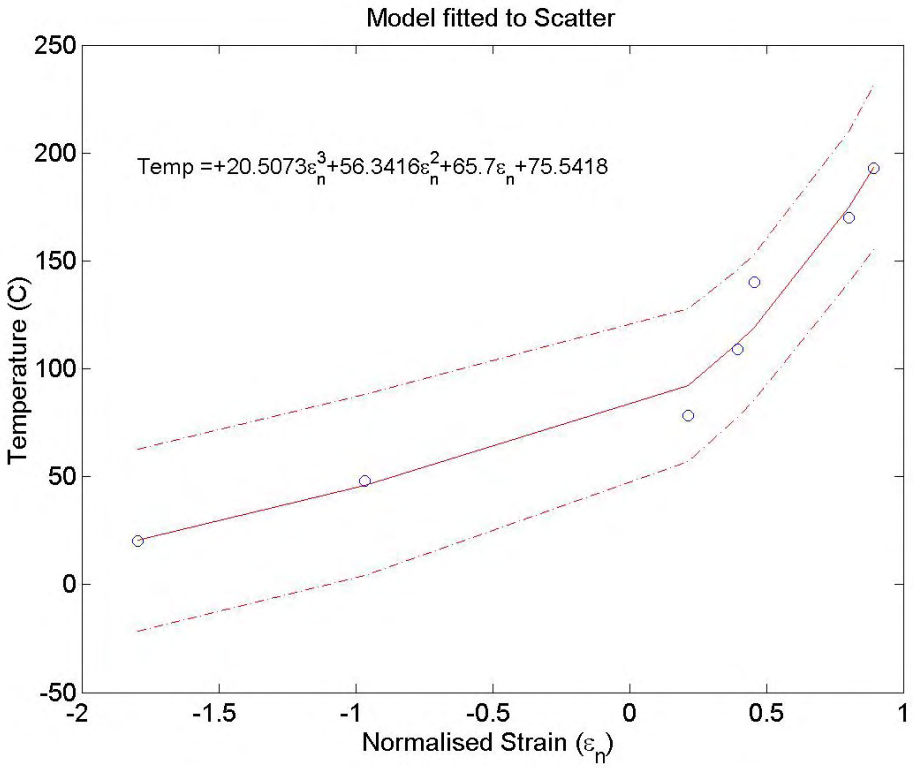

Figure 3.102: Test a, SAC embedded SP, model

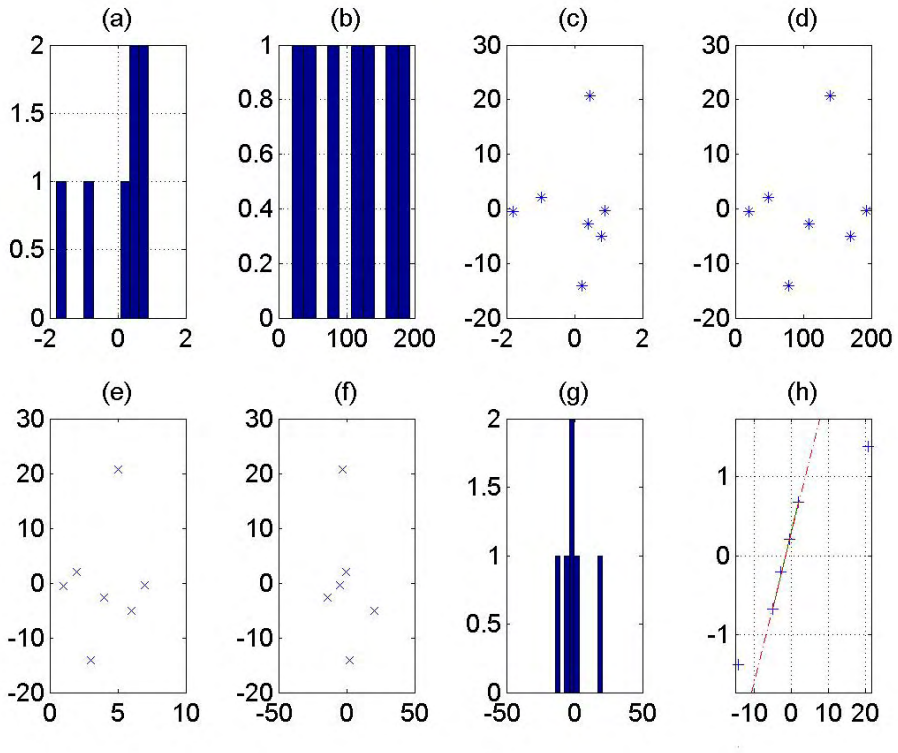

Figure 3.103: Test a, SAC embedded SP, residuals

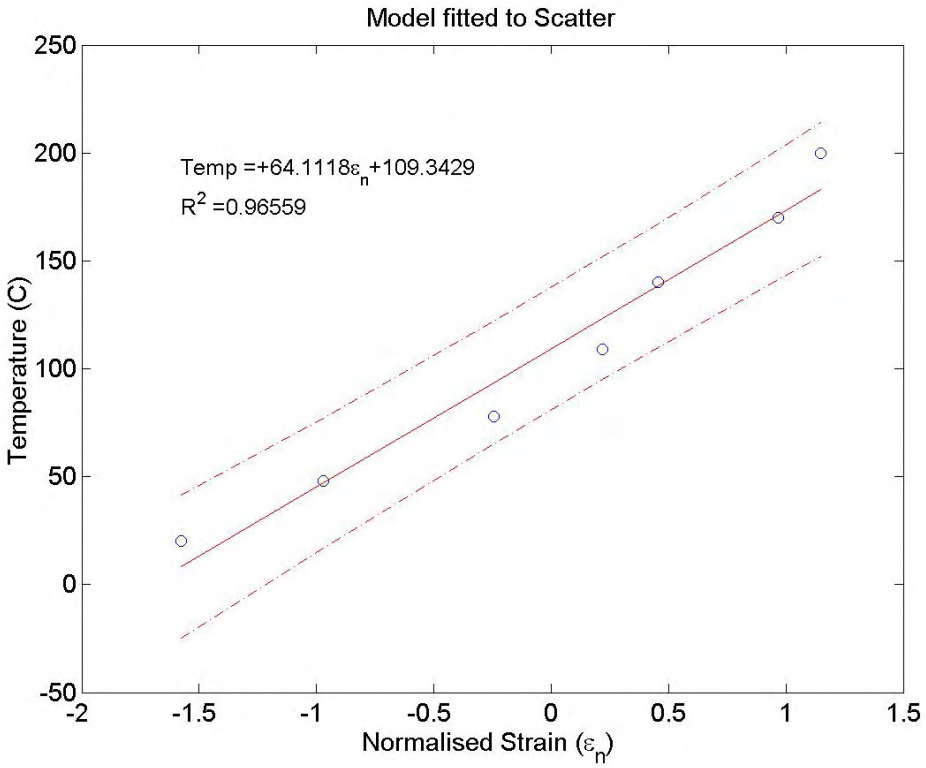

Figure 3.104: Test a, BLUERR embedded SP, model

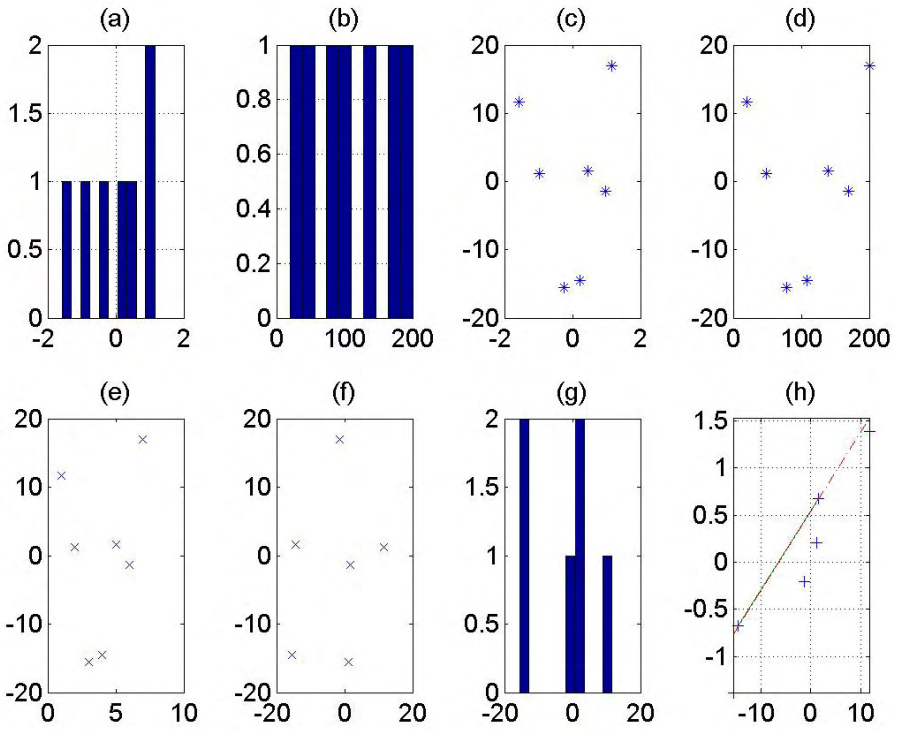

Figure 3.105: Test a, BLUERR embedded SP, residuals

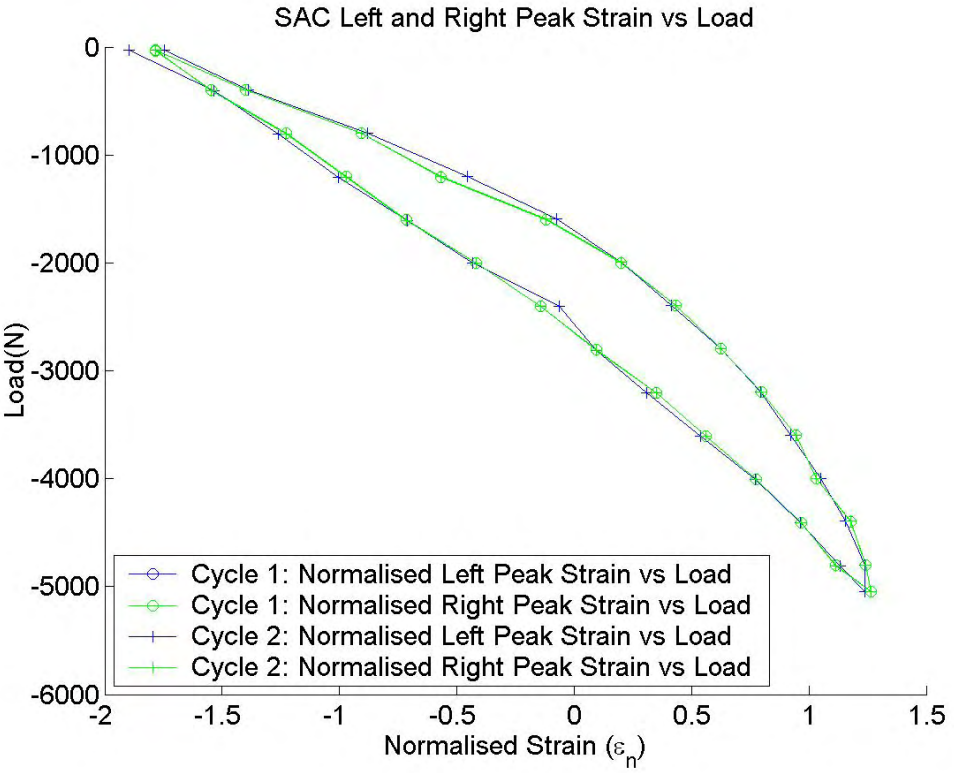

Figure 3.106: Test b, SAC embedded SP, RT, two cycles of LPSt and RPSt

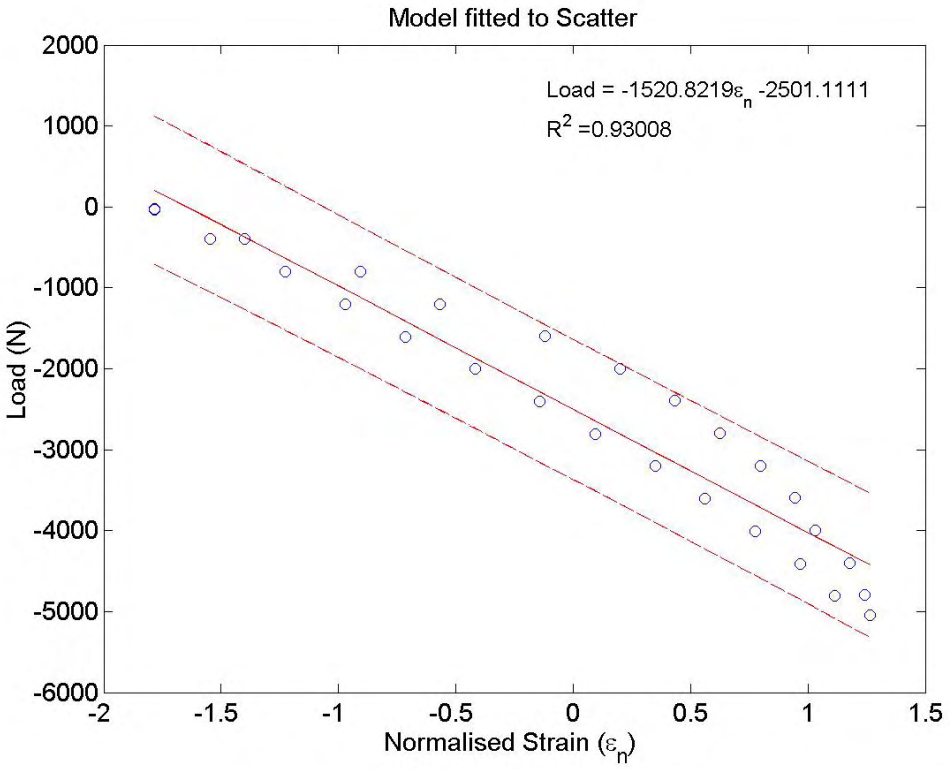

Figure 3.107: Test b, SAC embedded SP, RT LPSt

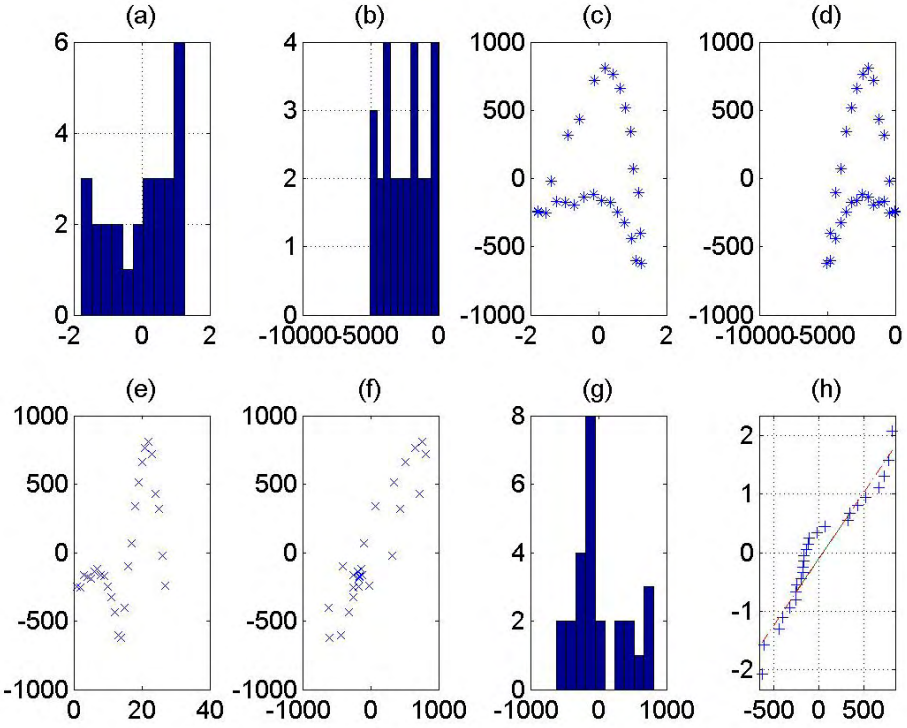

Figure 3.108: Test b, SAC embedded SP, Residuals

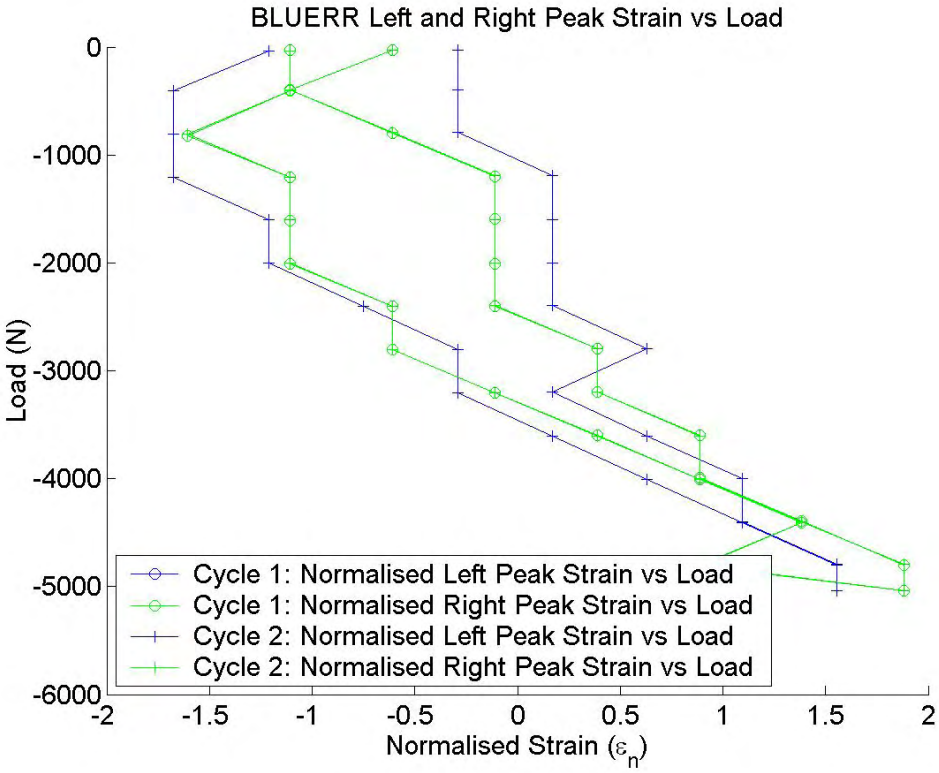

Figure 3.109: Test b, BLUERR embedded SP, RT, two cycles

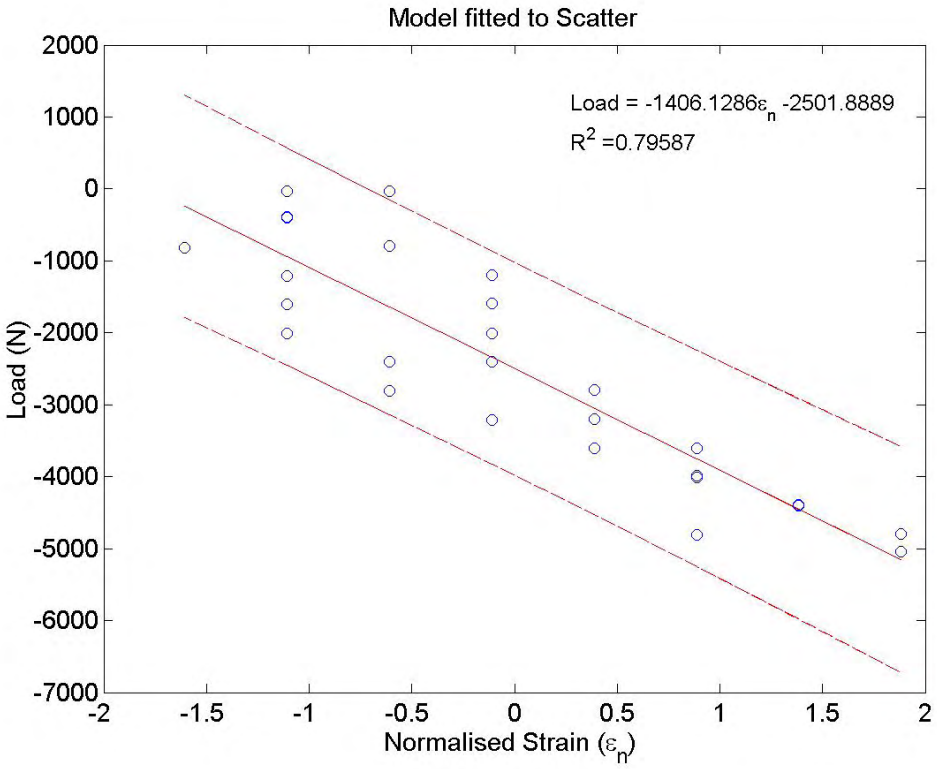

Figure 3.110: Test b, BLUERR embedded SP, RT LPSt

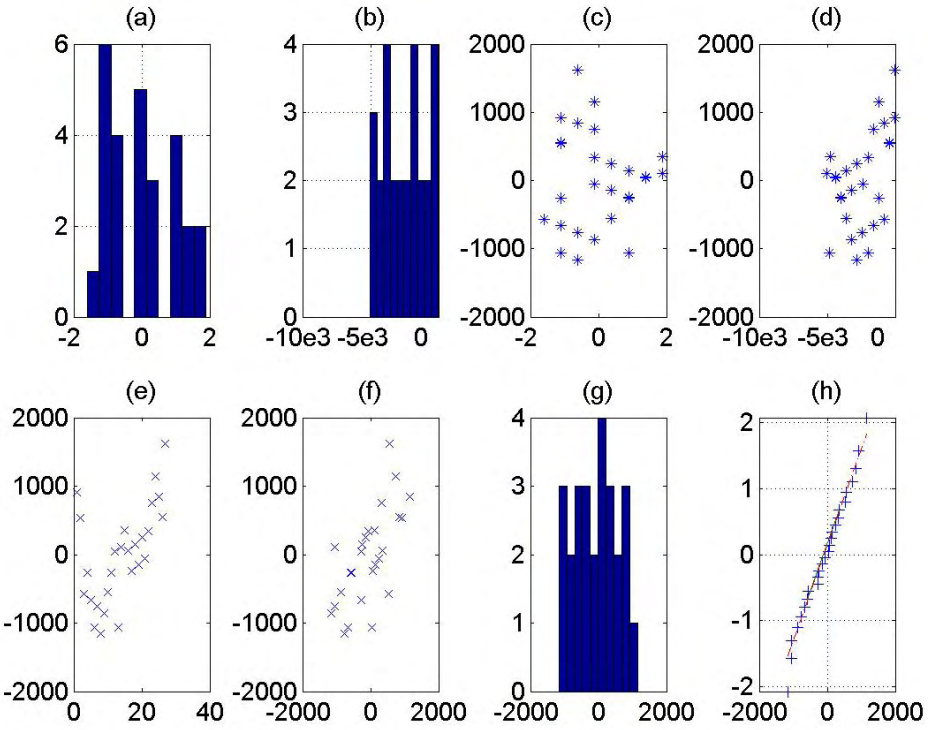

Figure 3.111: Test b, BLUERR embedded SP, Residuals

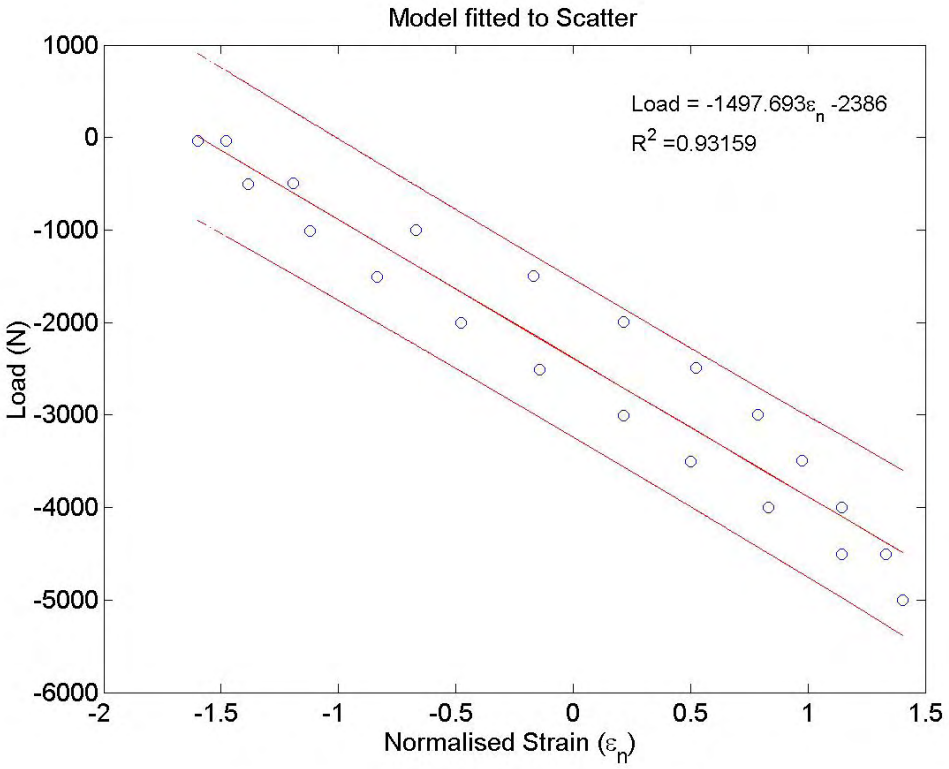

Figure 3.112: Test c, SAC embedded SP at 20^o C

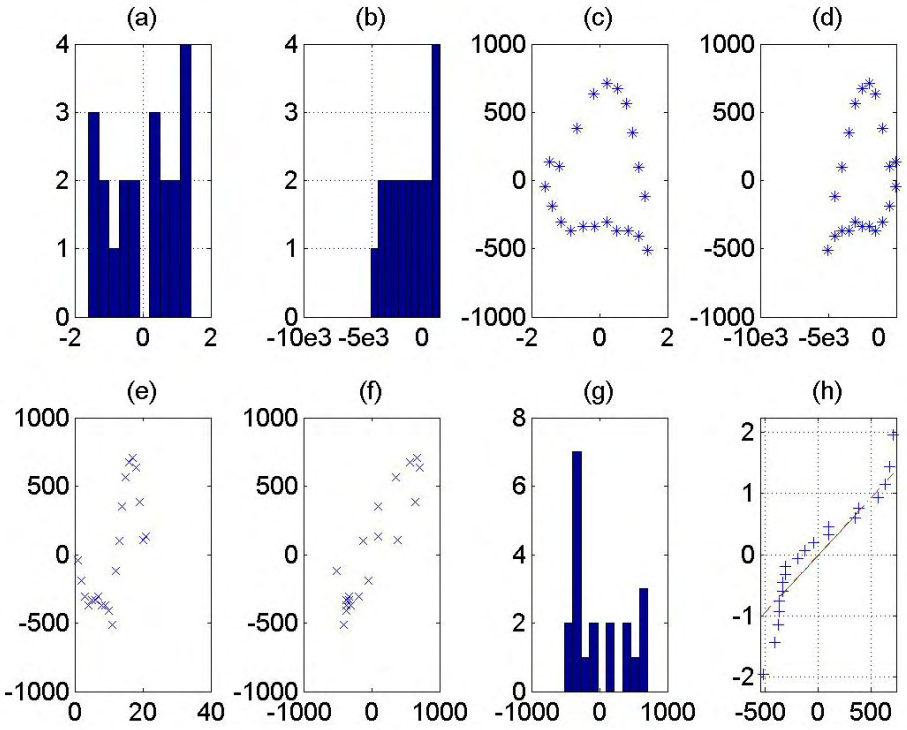

Figure 3.113: Test c, SAC embedded SP at 20^o C, residuals

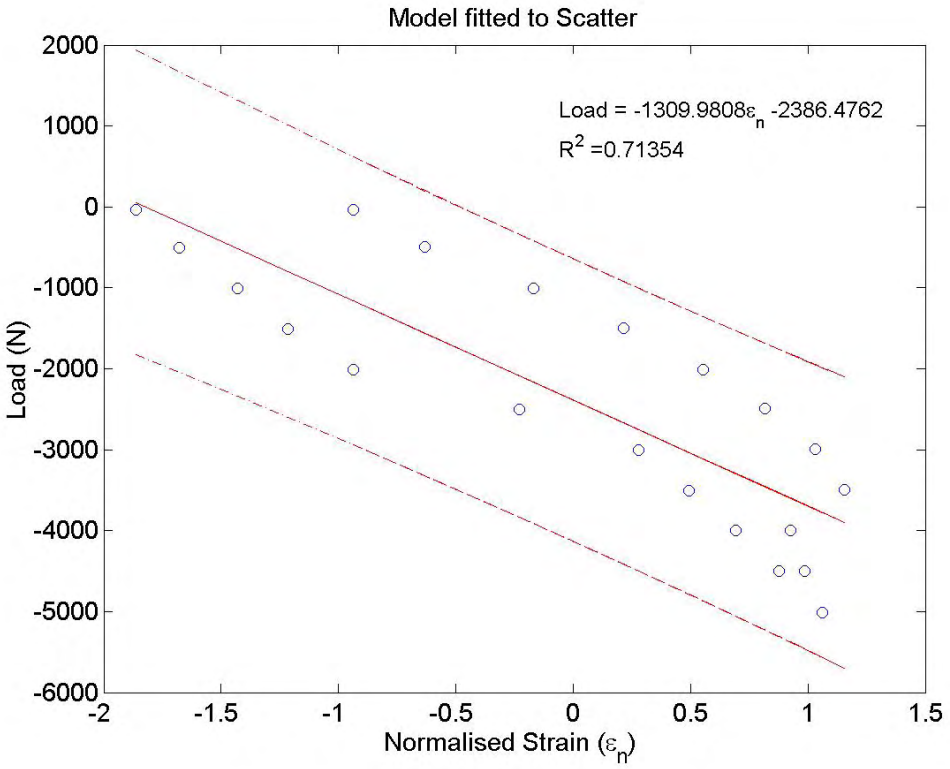

Figure 3.114: Test c, SAC embedded SP at 50^o C

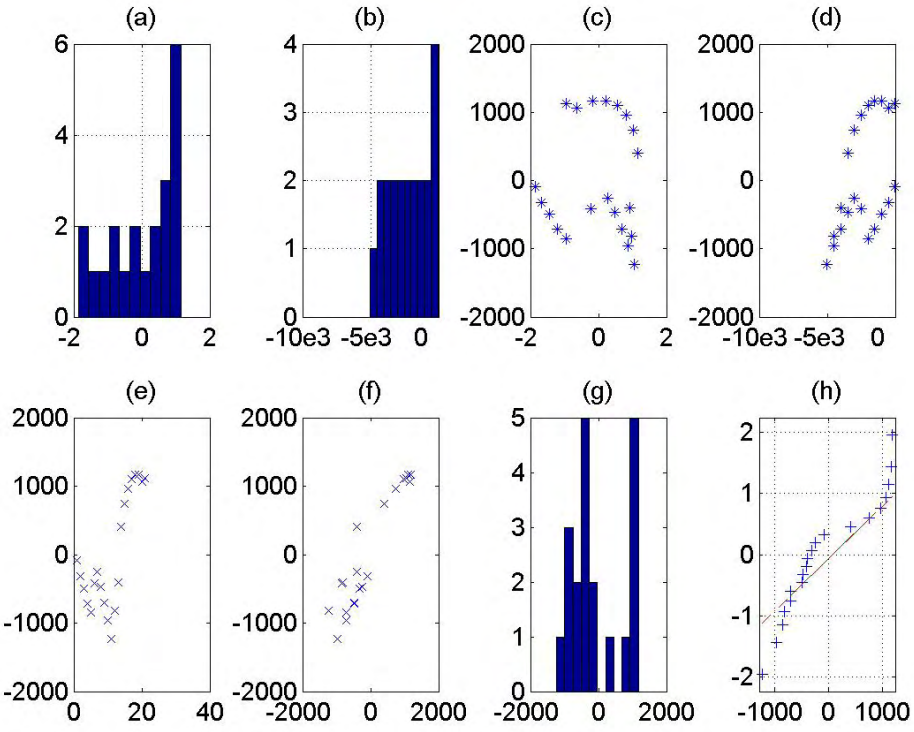

Figure 3.115: Test c, SAC embedded SP at 50^o C, residuals

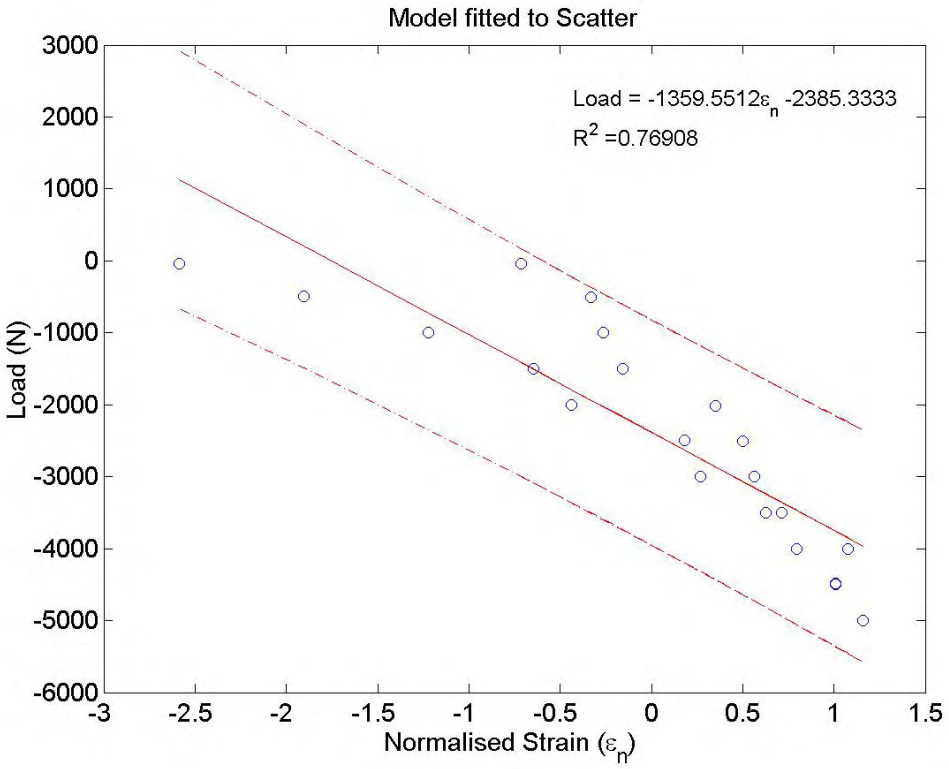

Figure 3.116: Test c, SAC embedded SP at 80^o C

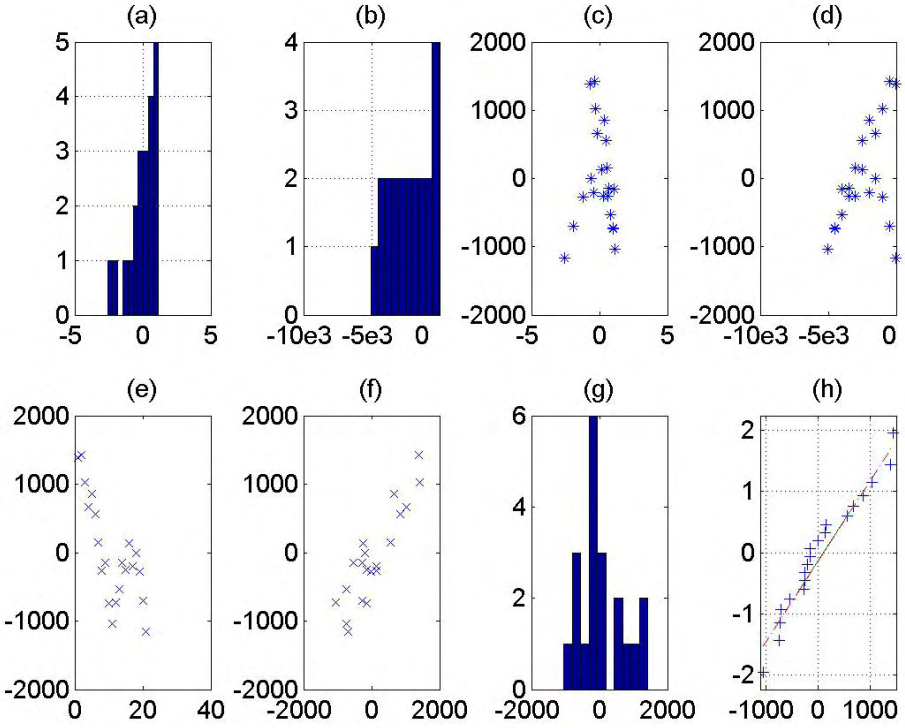

Figure 3.117: Test c, SAC embedded SP at 80^o C, residuals

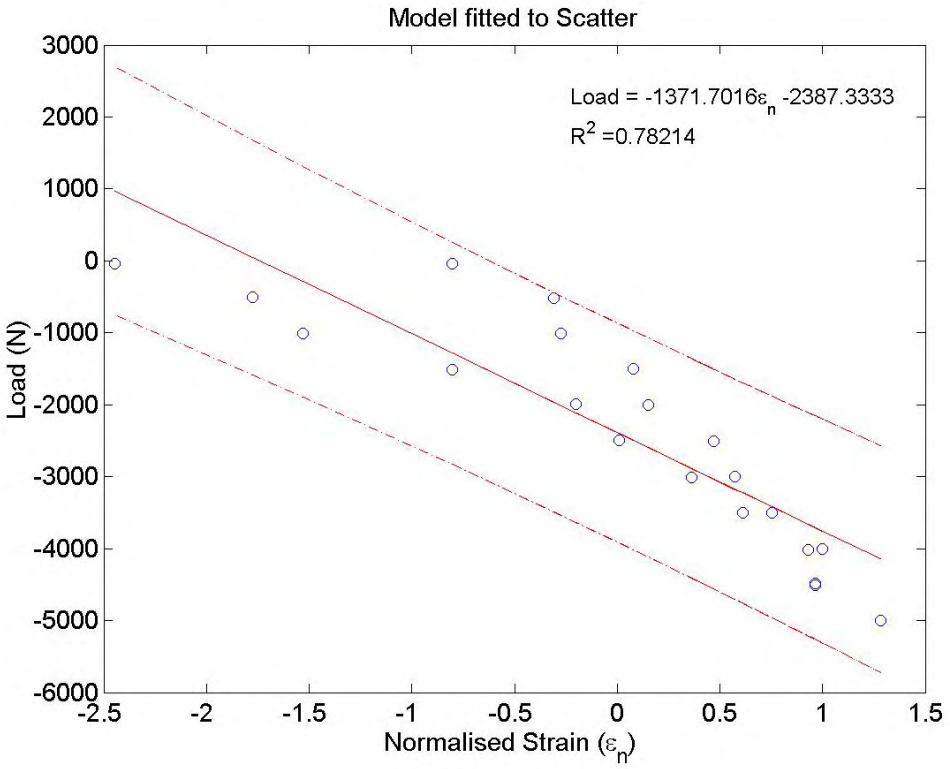

Figure 3.118: Test c, SAC embedded SP at 110^o C

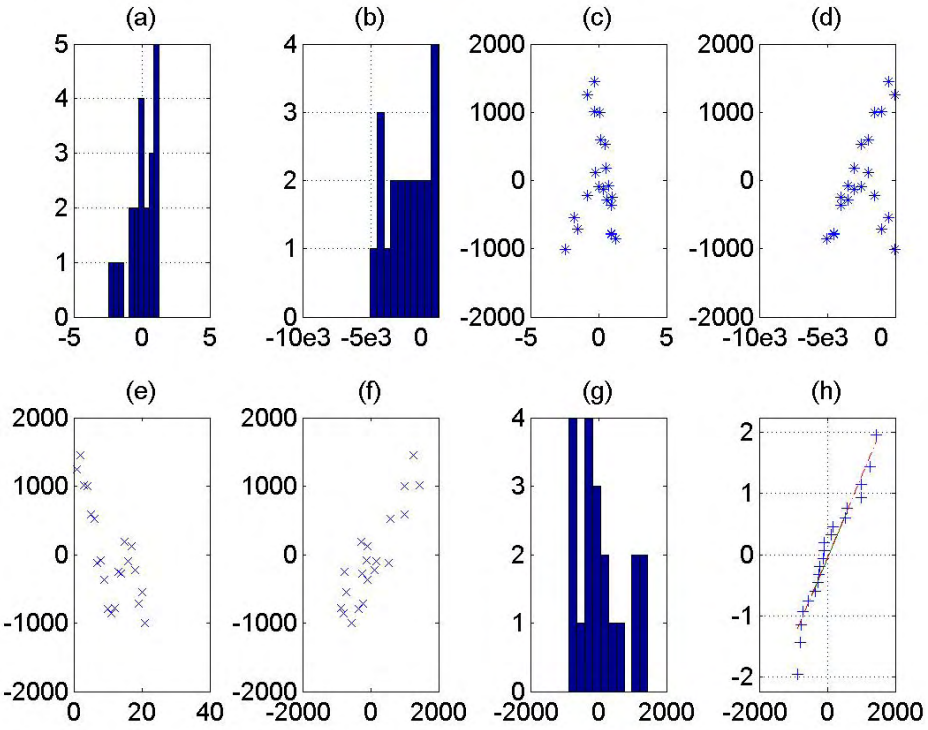

Figure 3.119: Test c, SAC embedded SP at 110^o C, residuals

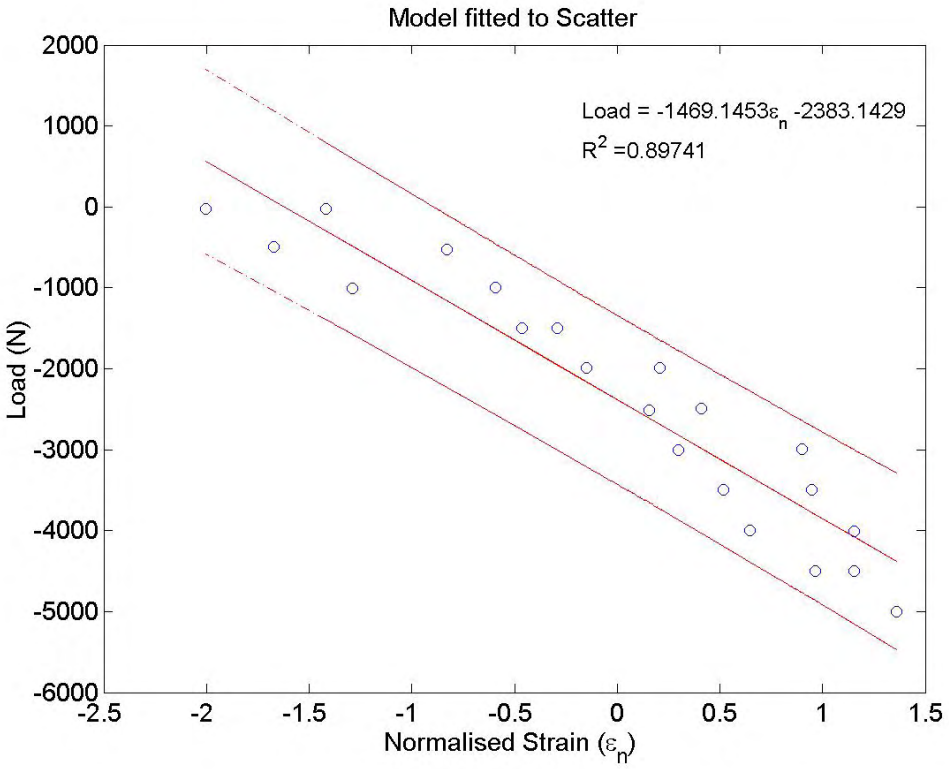

Figure 3.120: Test c, SAC embedded SP at 140^o C

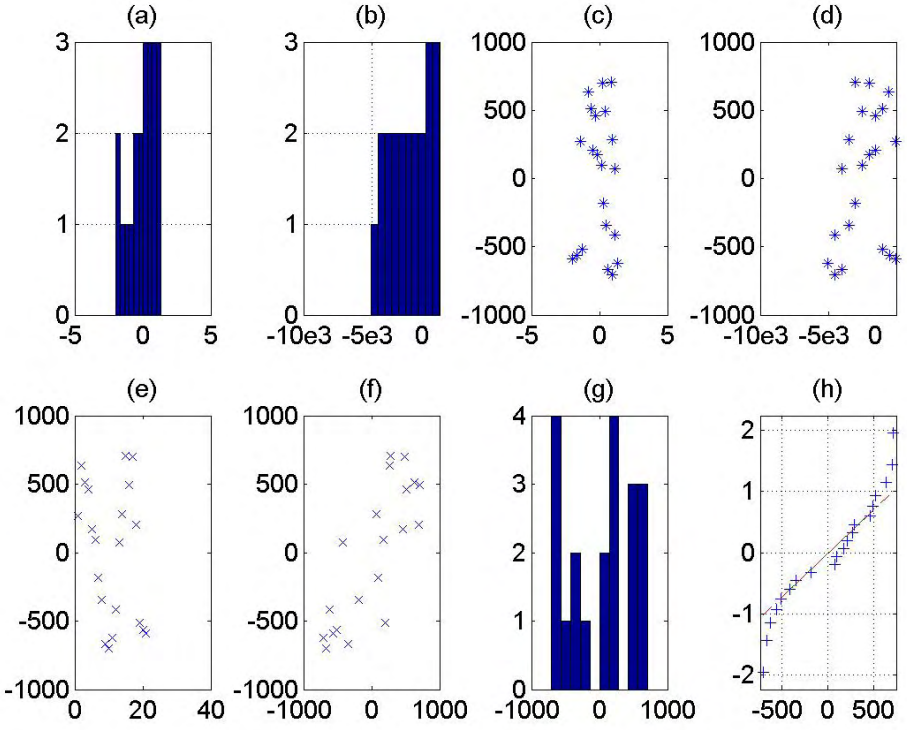

Figure 3.121: Test c, SAC embedded SP at 140^o C, residuals

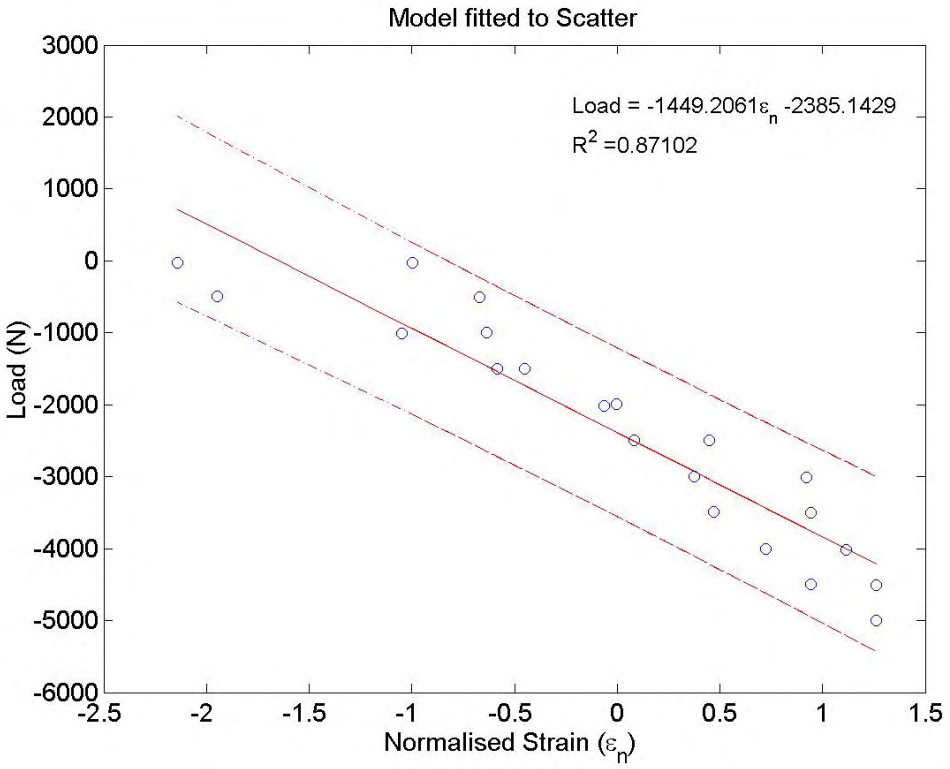

Figure 3.122: Test c, SAC embedded SP at 170^o C

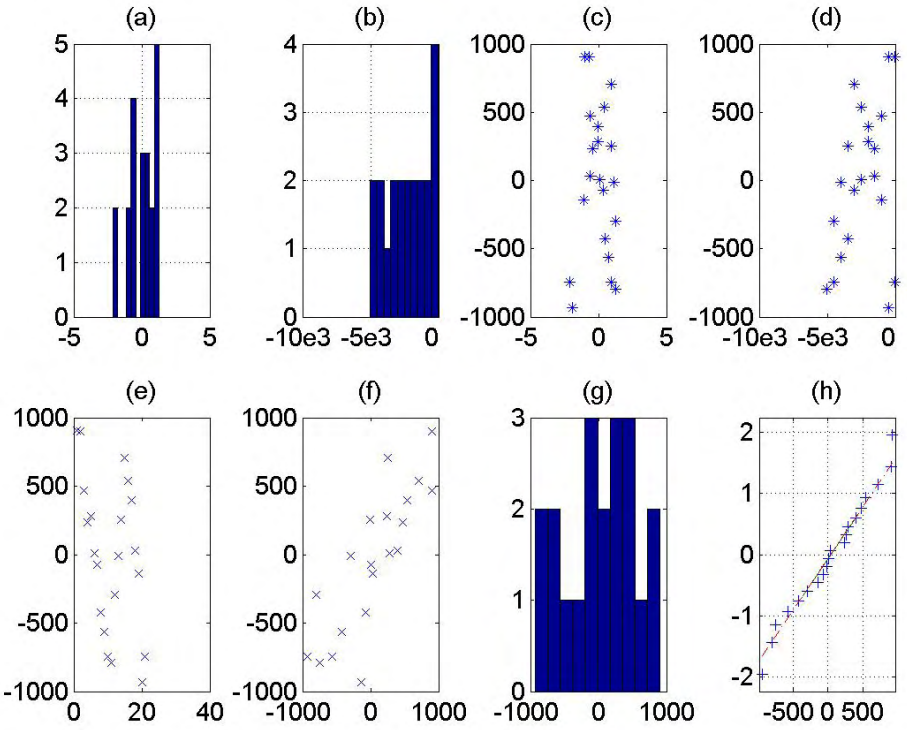

Figure 3.123: Test c, SAC embedded SP at 170^o C, residuals

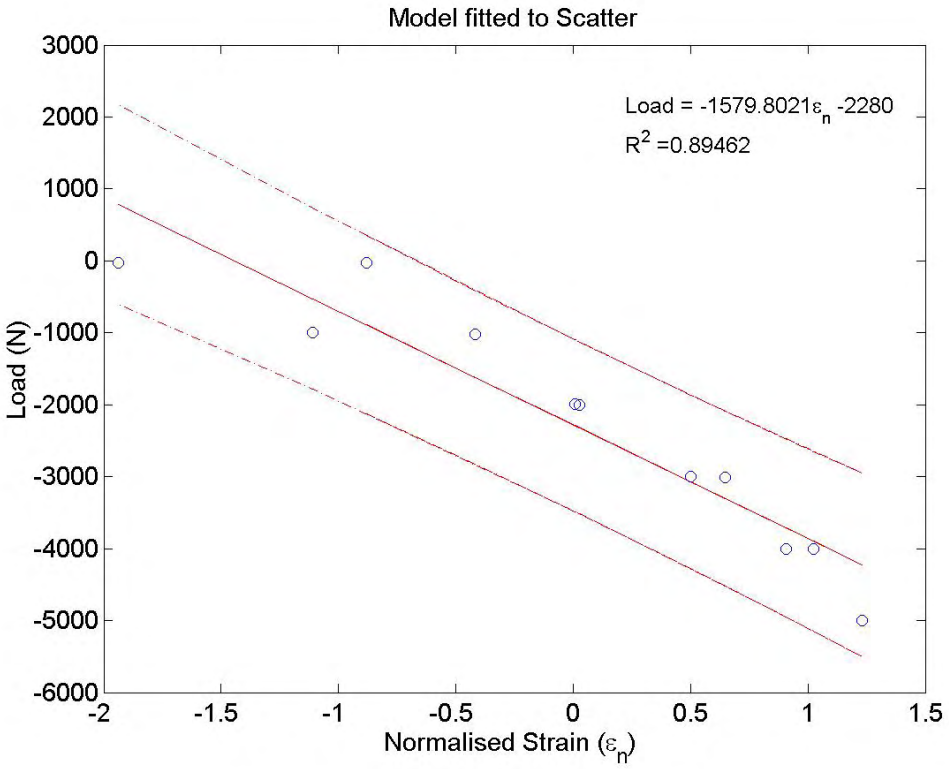

Figure 3.124: Test c, SAC embedded SP at 200^o C

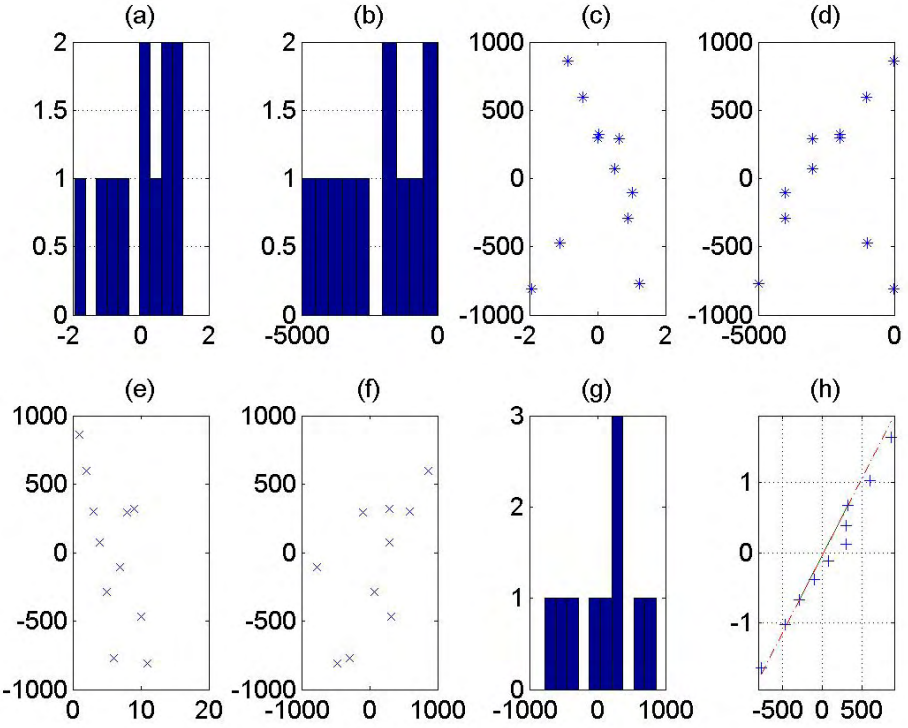

Figure 3.125: Test c, SAC embedded SP at 200^o C, residuals

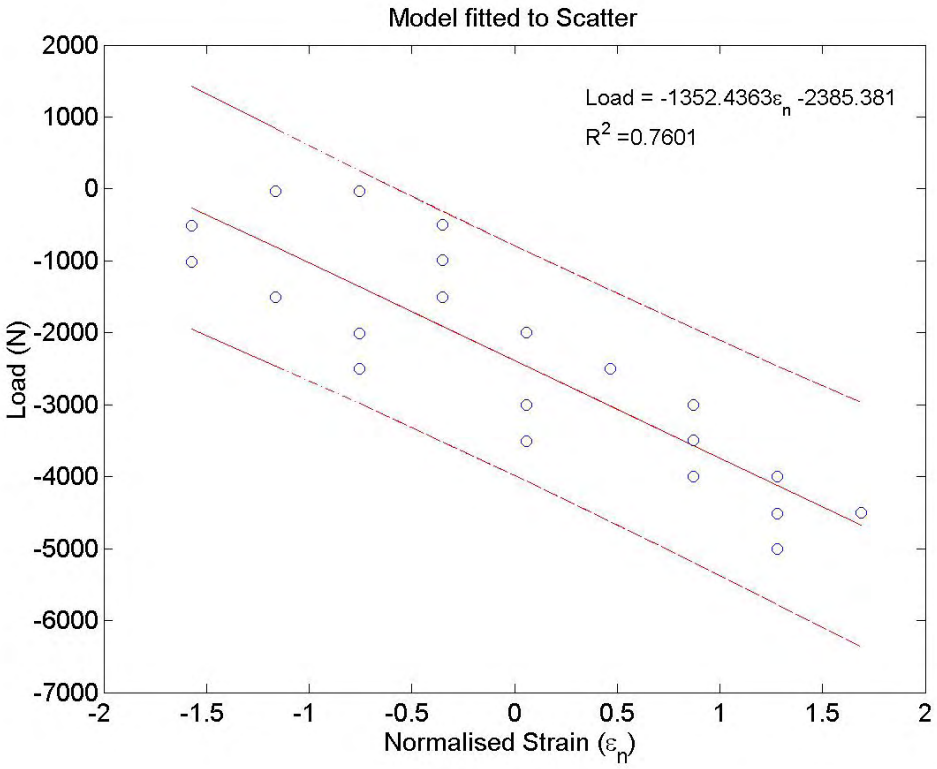

Figure 3.126: Test c, BLUERR embedded SP at 20^o C

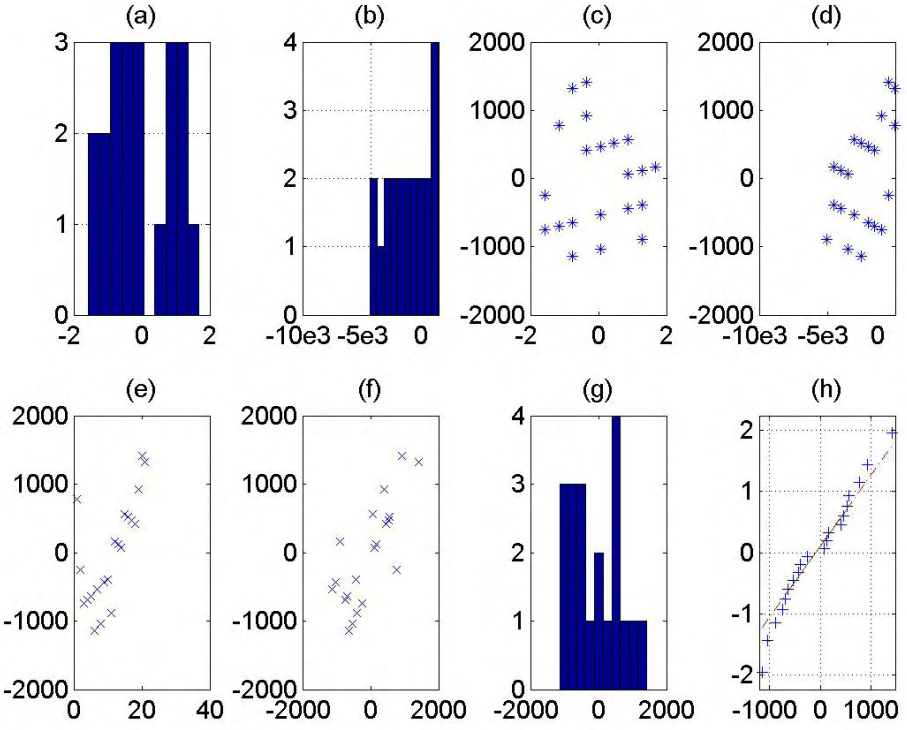

Figure 3.127: Test c, BLUERR embedded SP at 20^o C, residuals

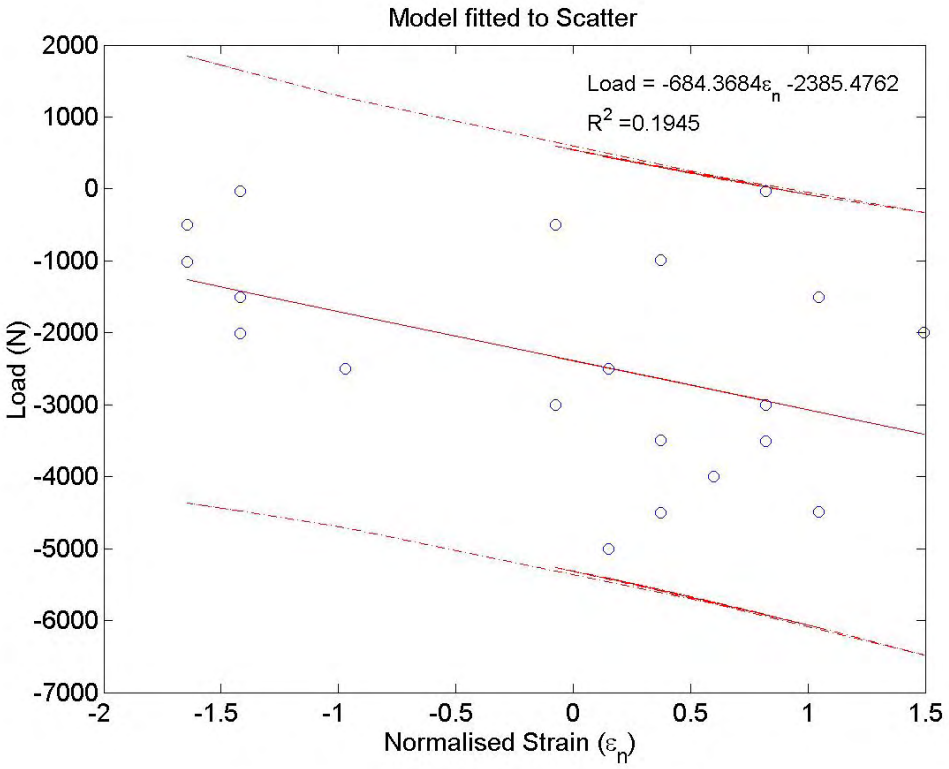

Figure 3.128: Test c, BLUERR embedded SP at 50^o C

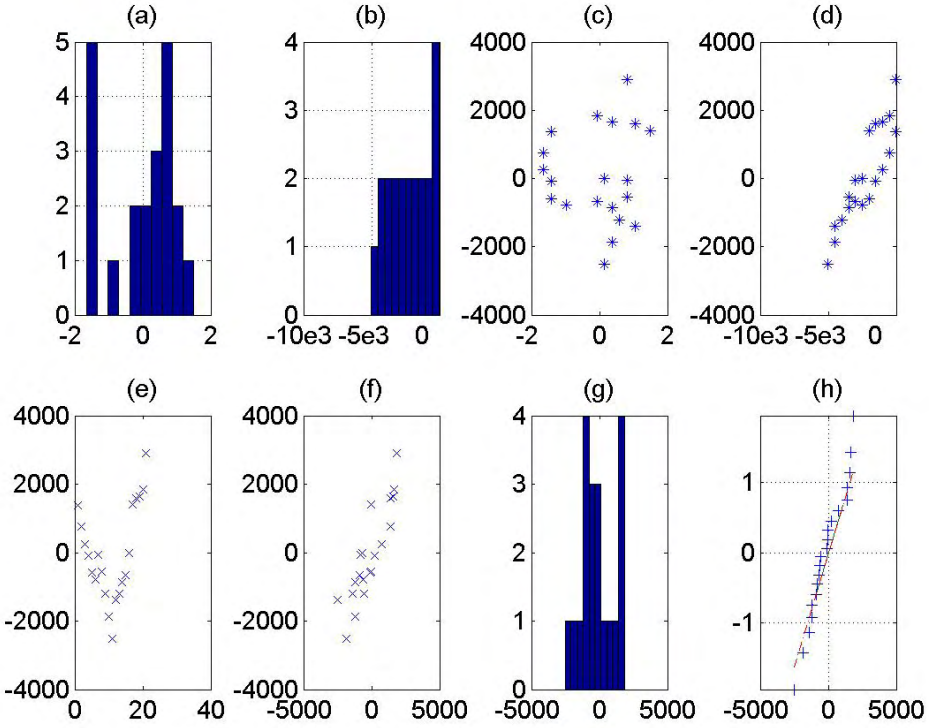

Figure 3.129: Test c, BLUERR embedded SP at 50^o C, residuals

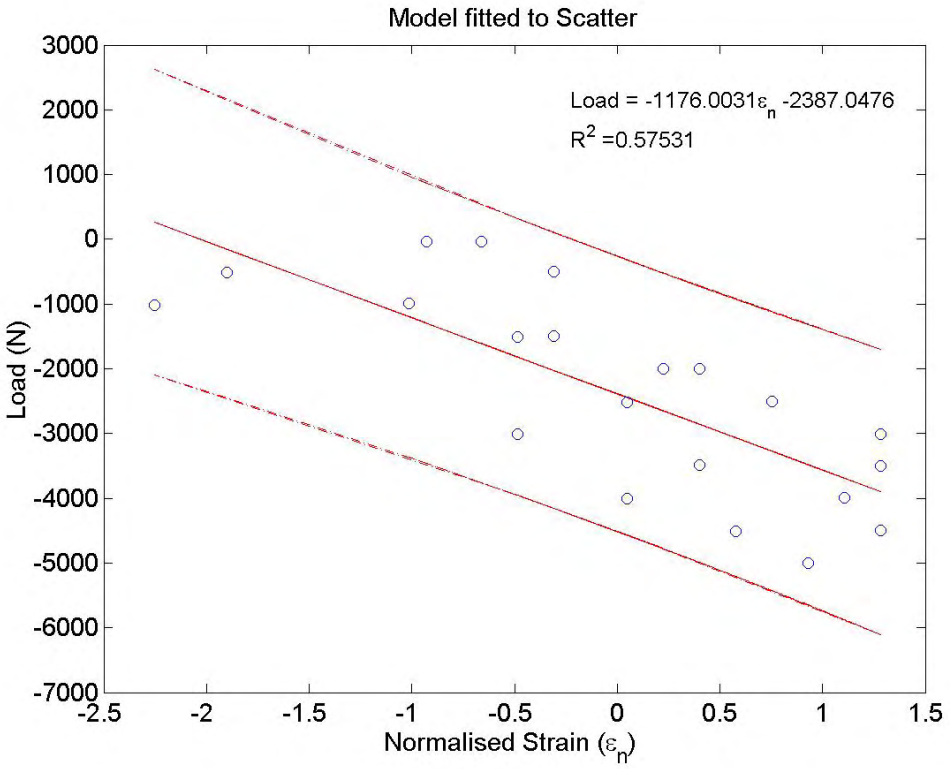

Figure 3.130: Test c, BLUERR embedded SP at 80^o C

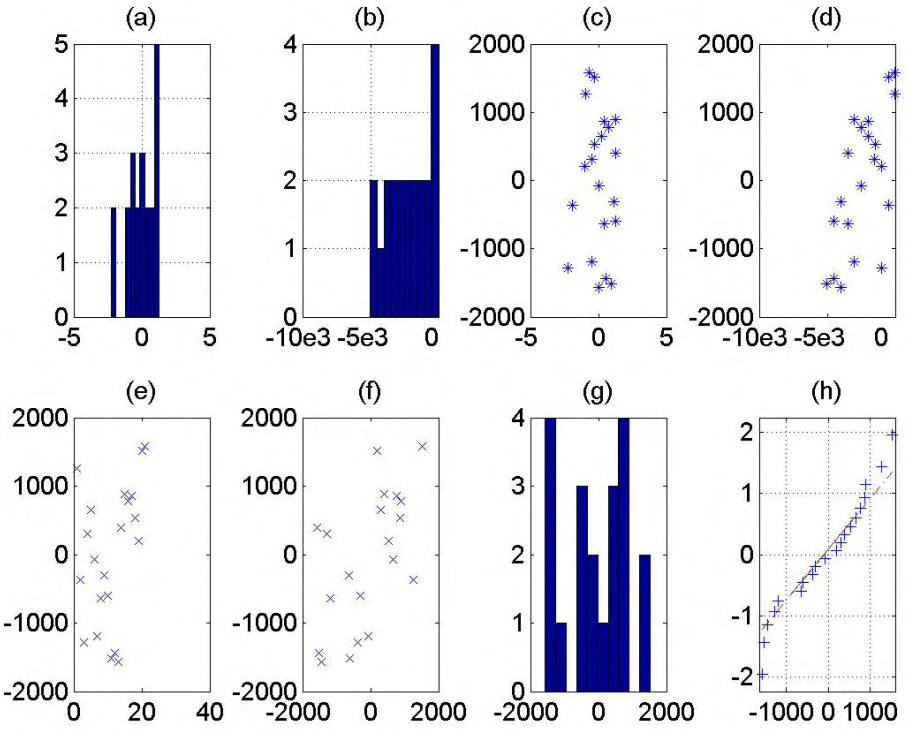

Figure 3.131: Test c, BLUERR embedded SP at 80^o C, residuals

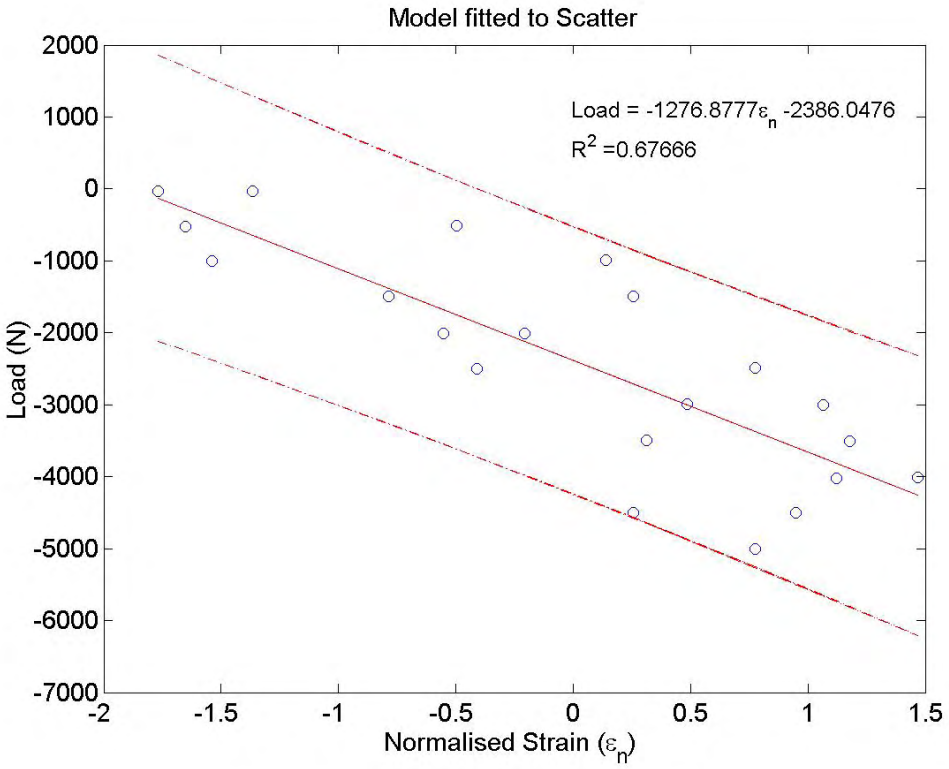

Figure 3.132: Test c, BLUERR embedded SP at 110^o C

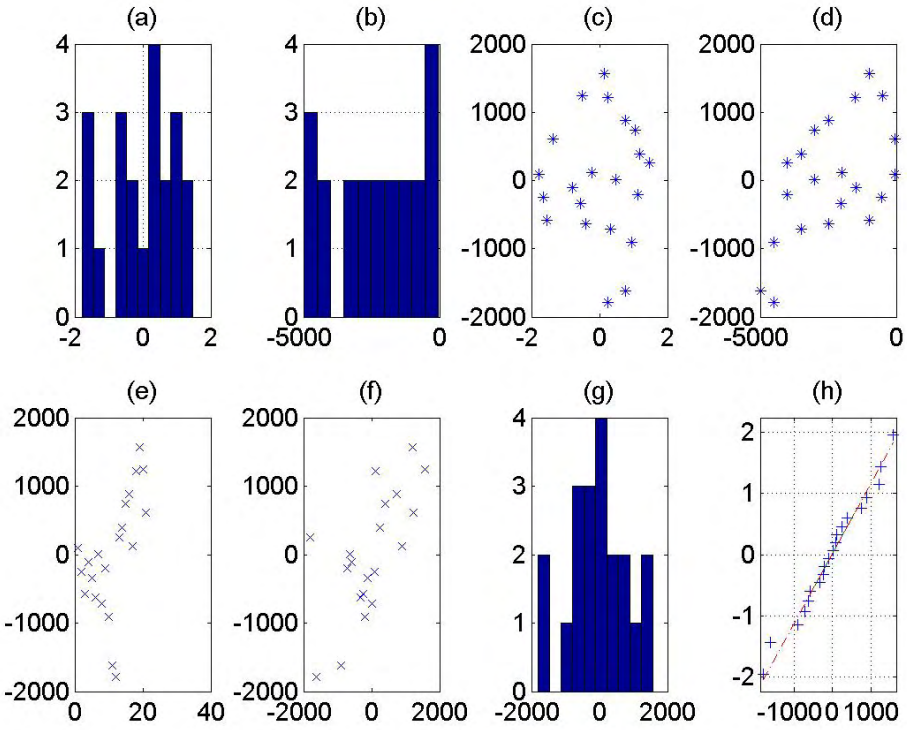

Figure 3.133: Test c, BLUERR embedded SP at 110^o C, residuals

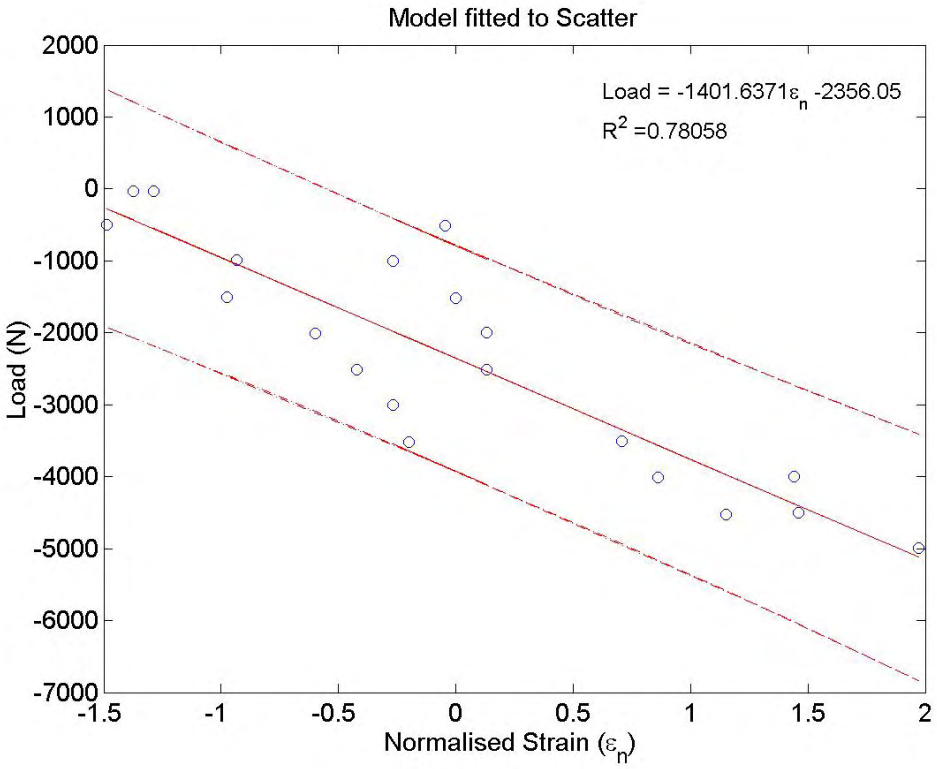

Figure 3.134: Test c, BLUERR embedded SP at 140^o C

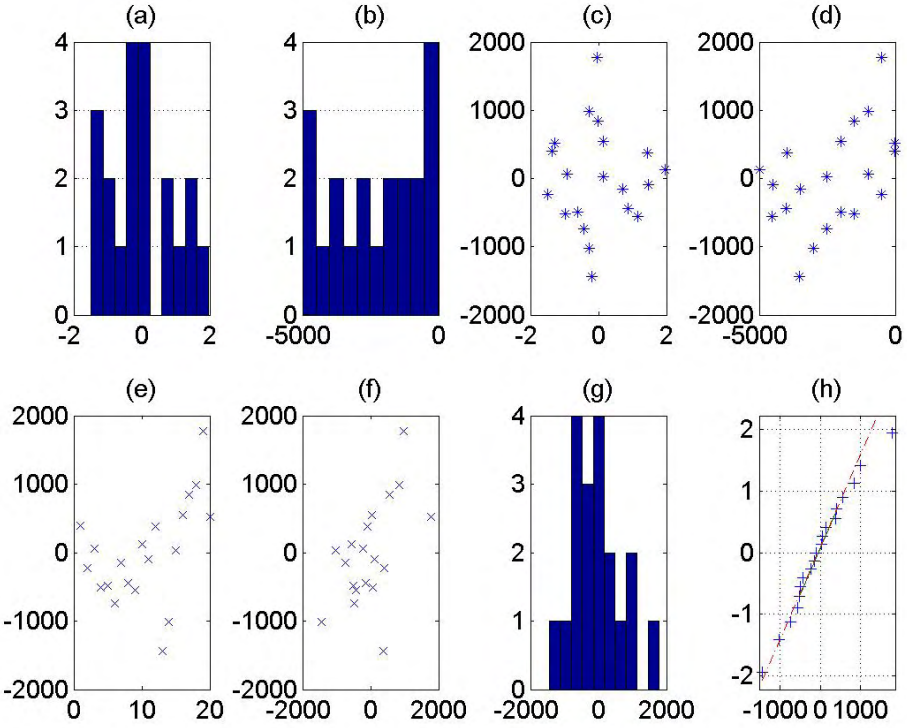

Figure 3.135: Test c, BLUERR embedded SP at 140^o C, residuals

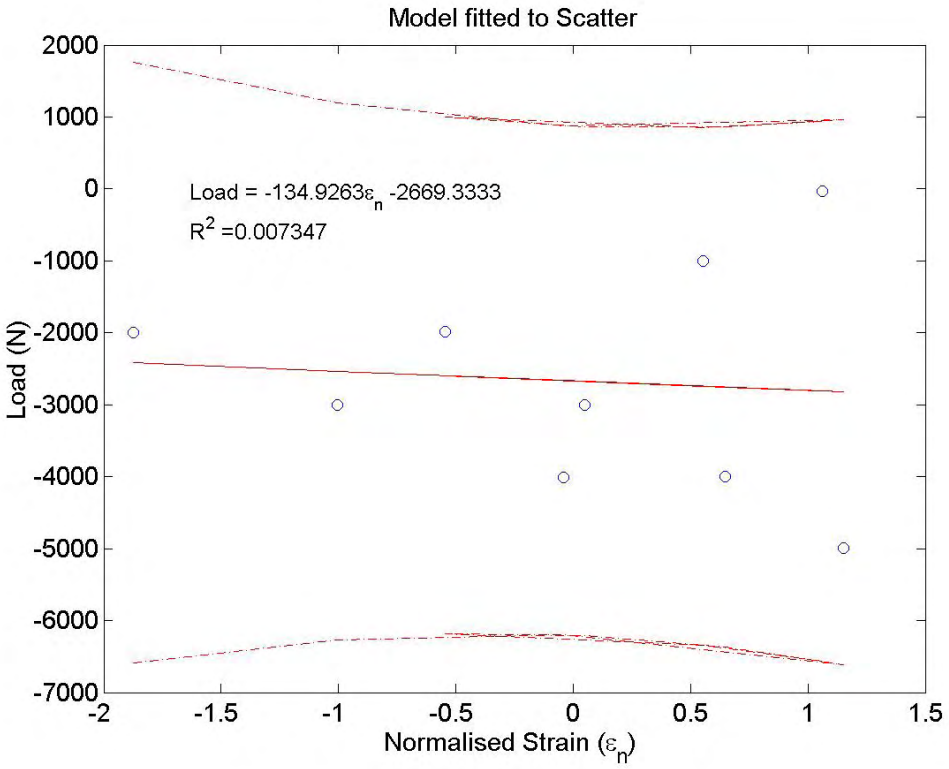

Figure 3.136: Test c, BLUERR embedded SP at 170^o C

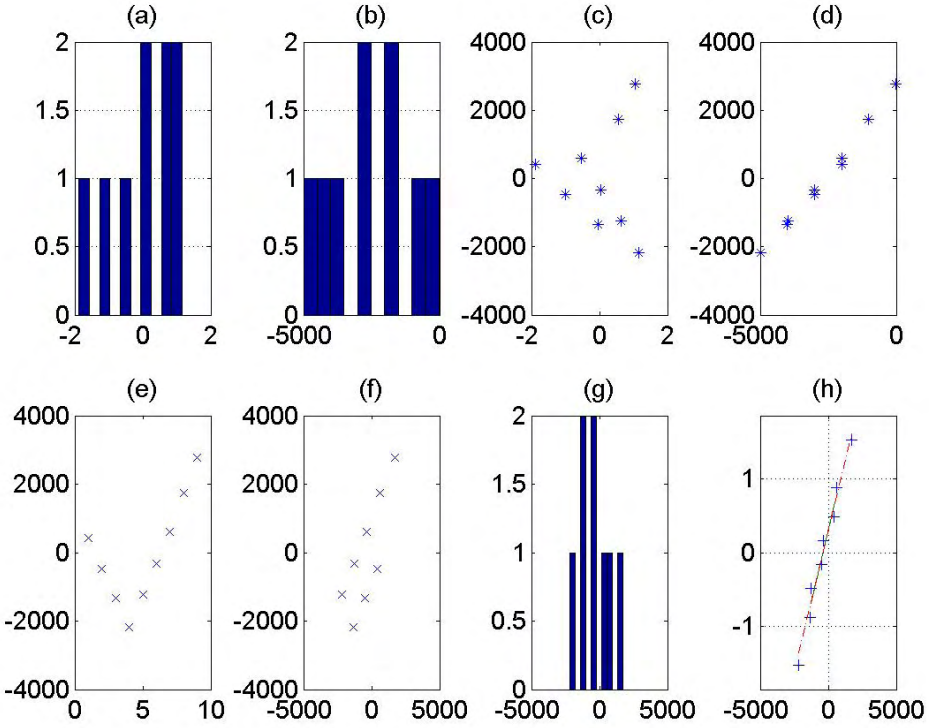

Figure 3.137: Test c, BLUERR embedded SP at 170^o C, residuals

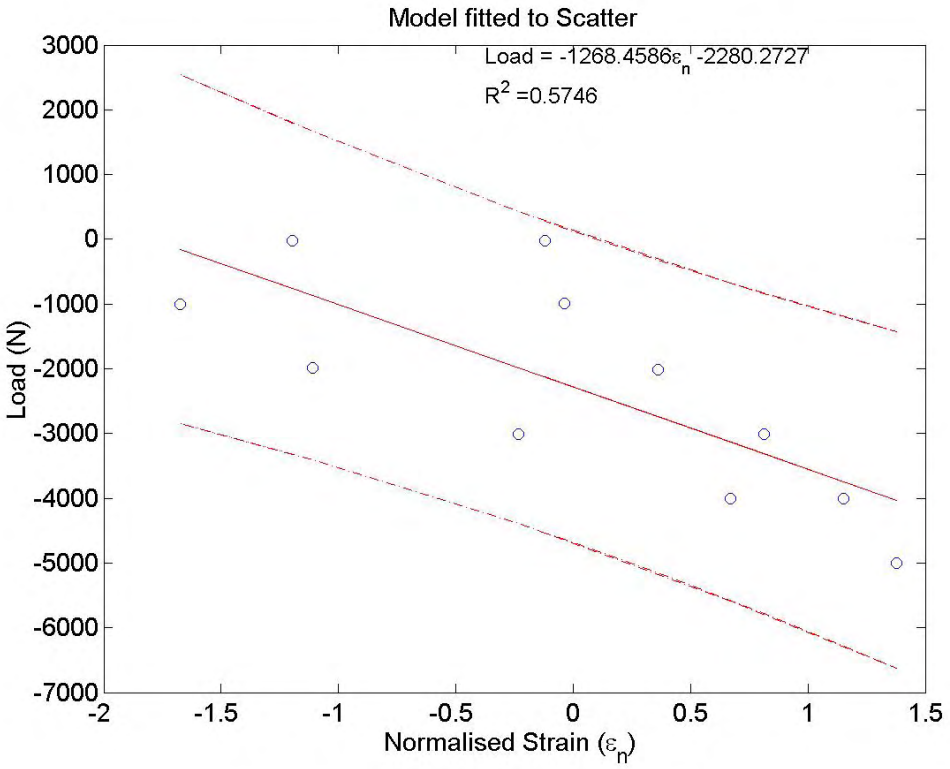

Figure 3.138: Test c, BLUERR embedded SP at 200^o C

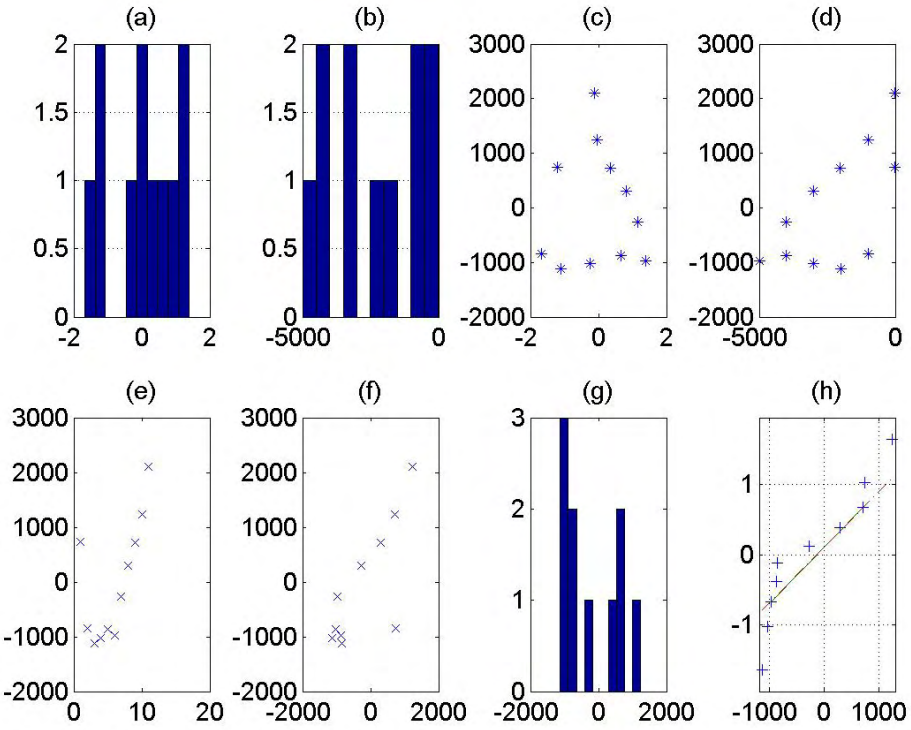

Figure 3.139: Test c, BLUERR embedded SP at 200^o C, residuals

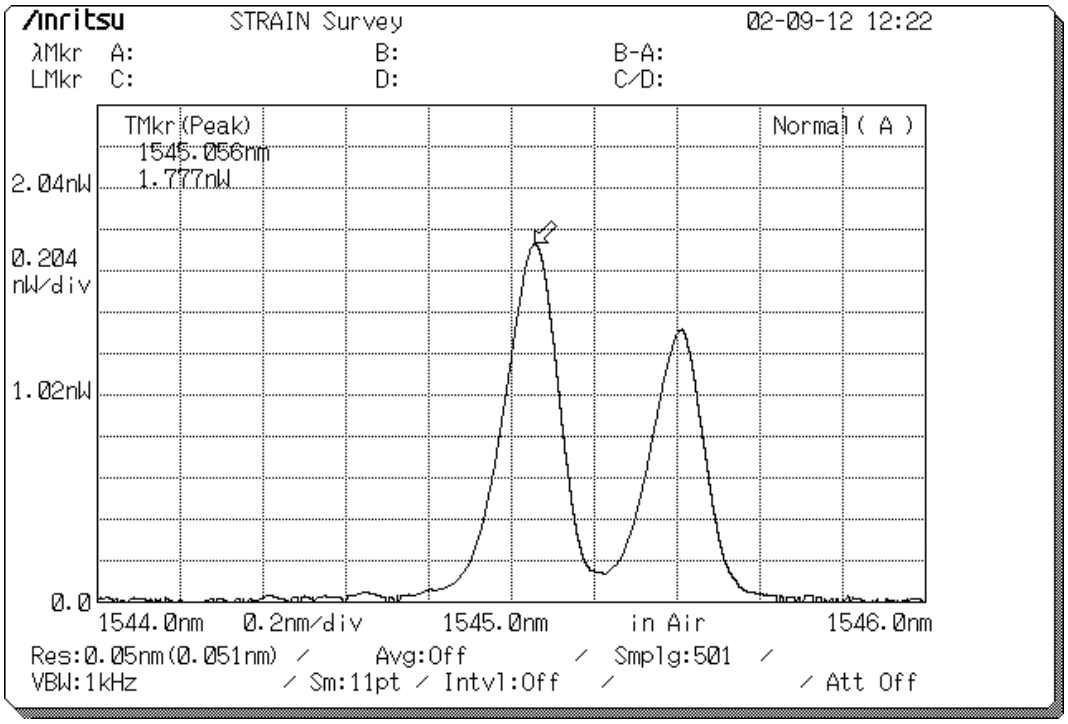

Figure 3.140: Test c, SAC, Day 1, 50^o C, no load, spectrum

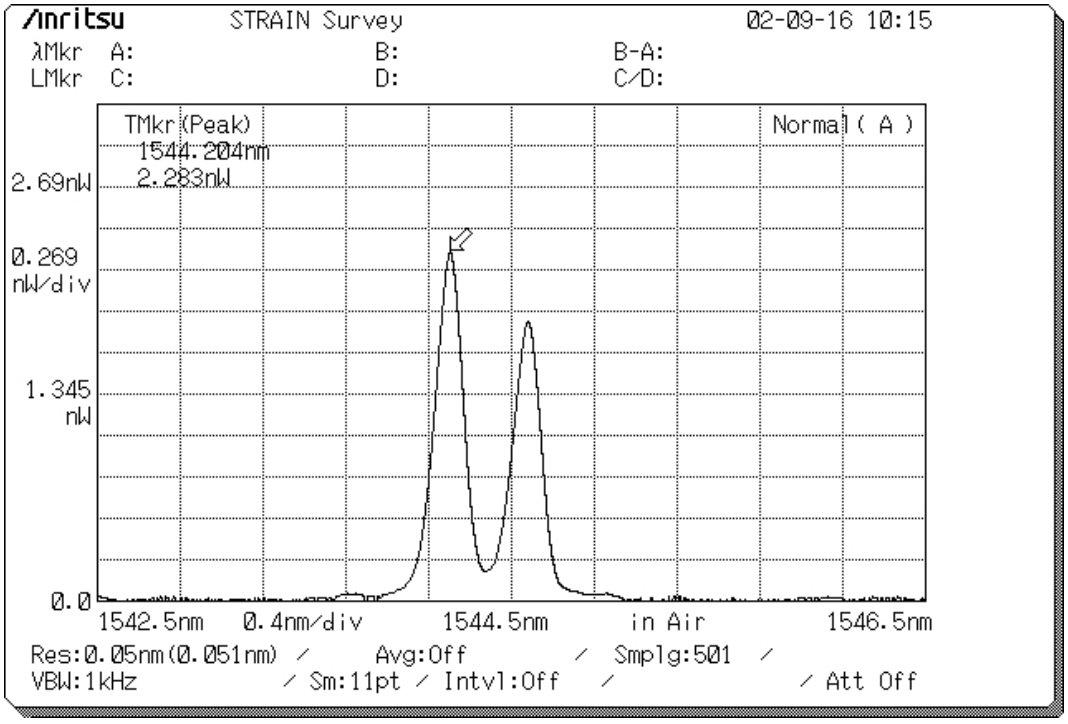

Figure 3.141: Test c, SAC, Day 2, 21^o C, no load, spectrum

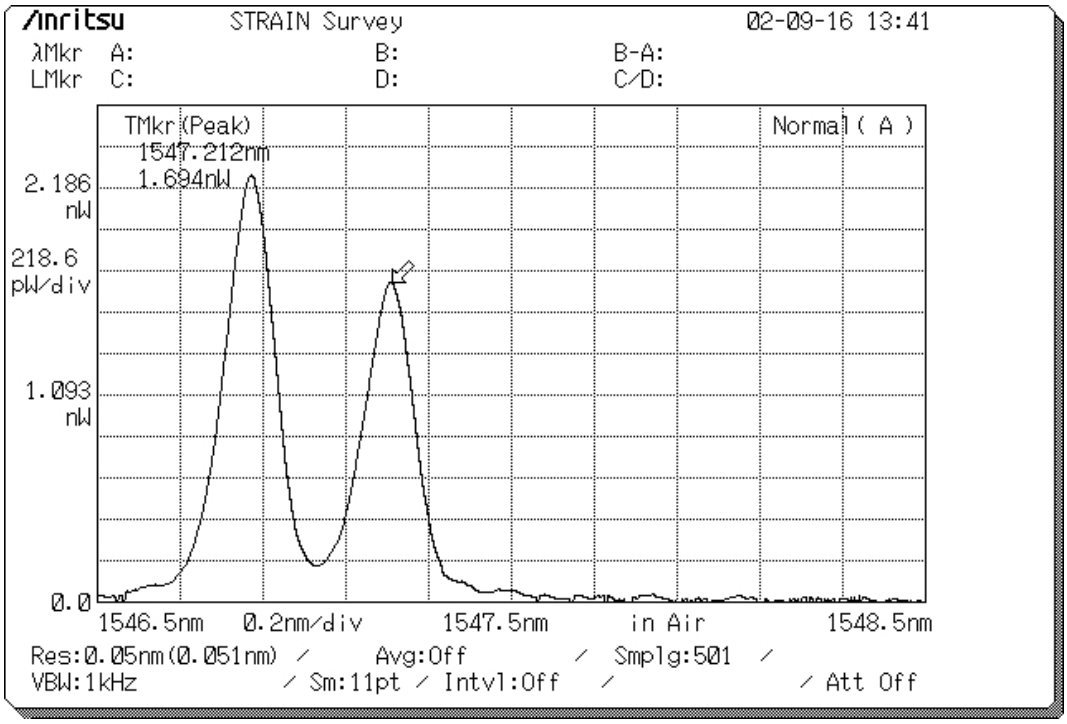

Figure 3.142: Test c, SAC, Day 2, 200^o C, no load, spectrum

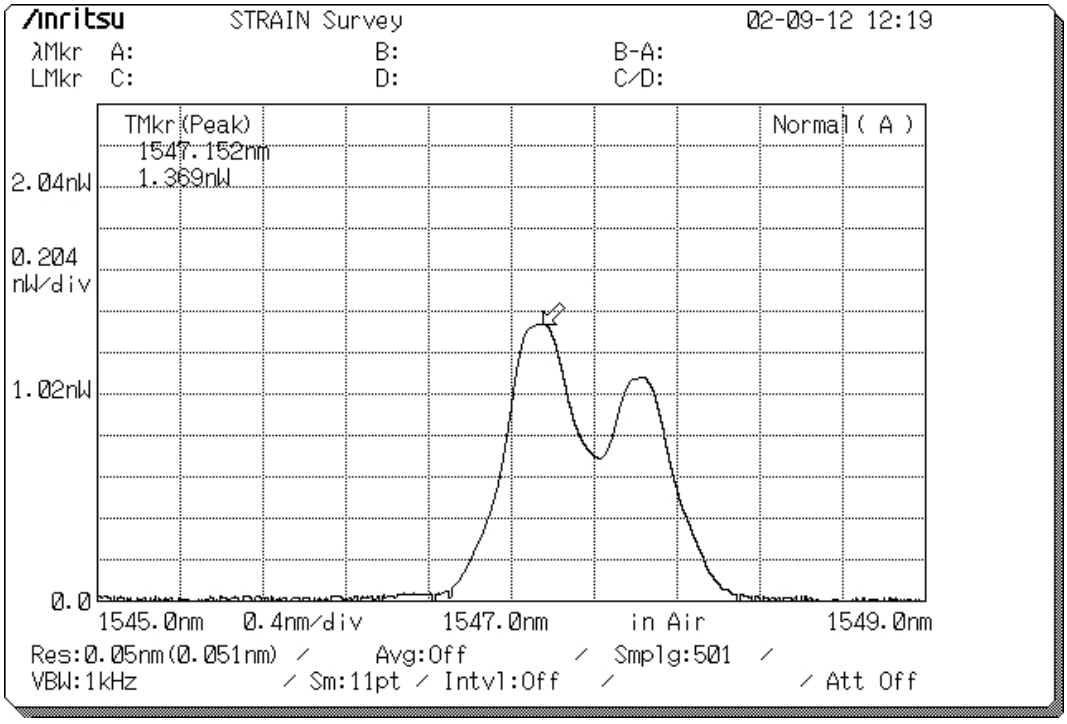

Figure 3.143: Test c, BLUERR, Day 2, 50^o C, no load

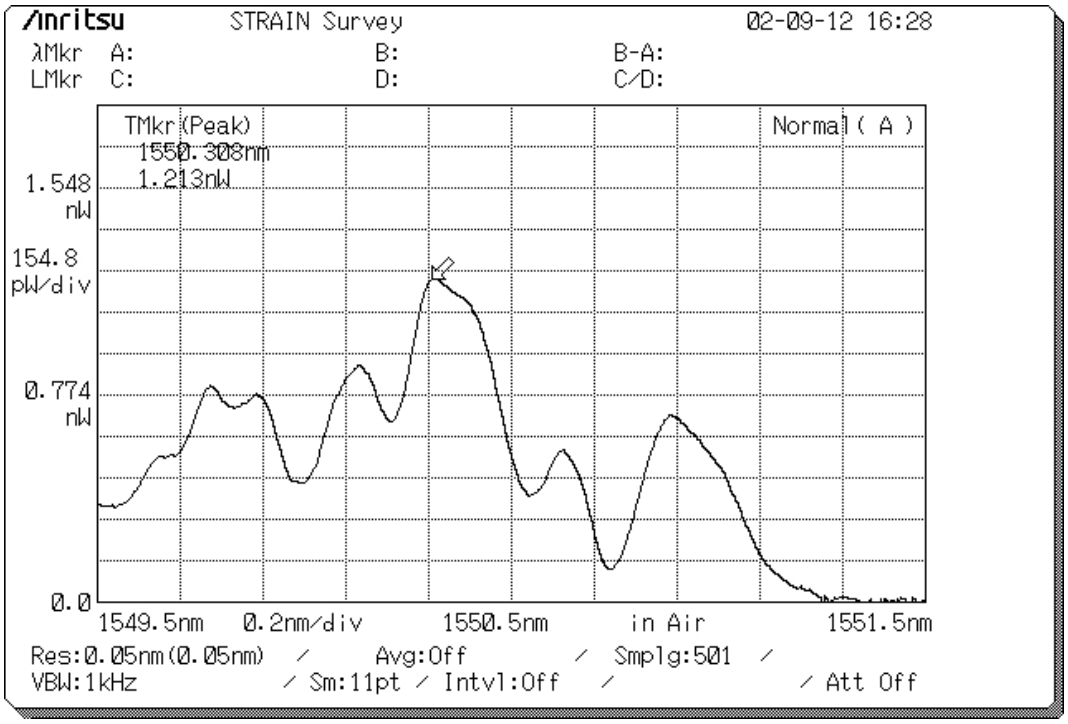

Figure 3.144: Test c, BLUERR, Day 1, 115^o C, no load

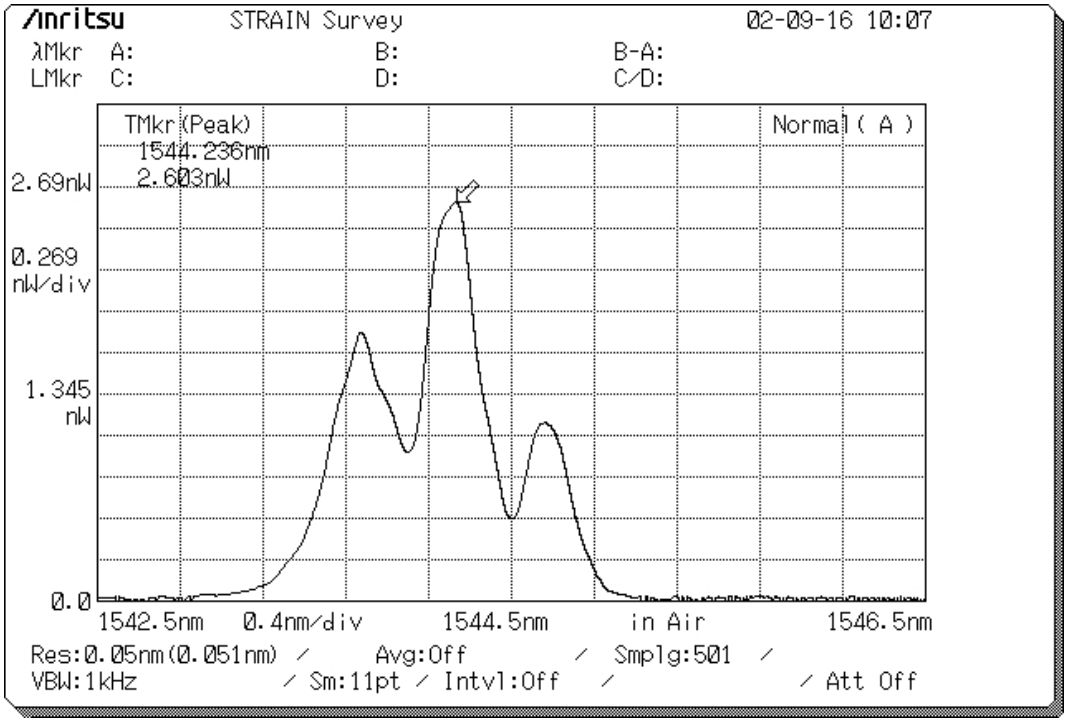

Figure 3.145: Test c, BLUERR, Day 2, 21^o C, no load

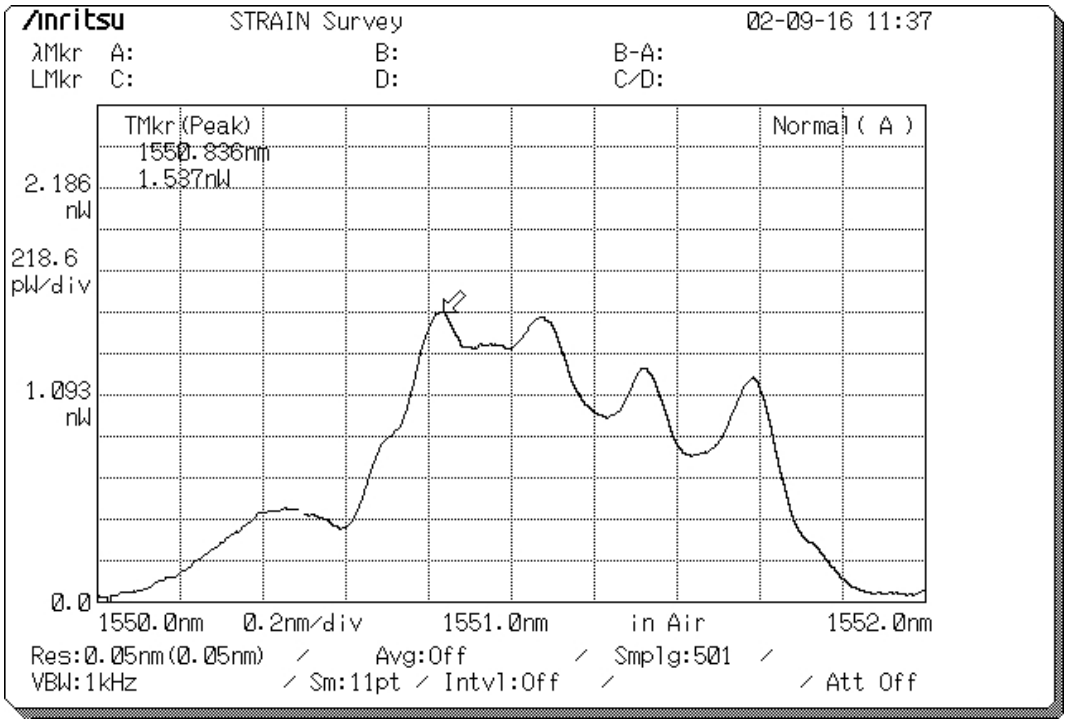

Figure 3.146: Test c, BLUERR, Day 2, 140^o C, 3000 N

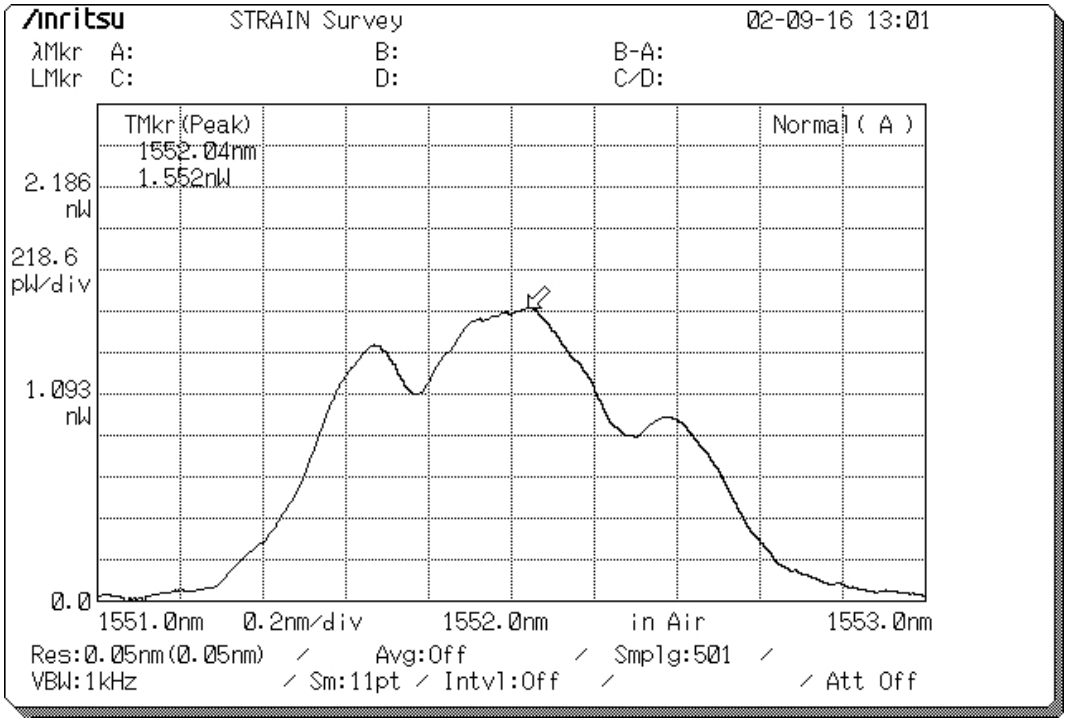

Figure 3.147: Test c, BLUERR, Day 2, 170^o C, 30 N

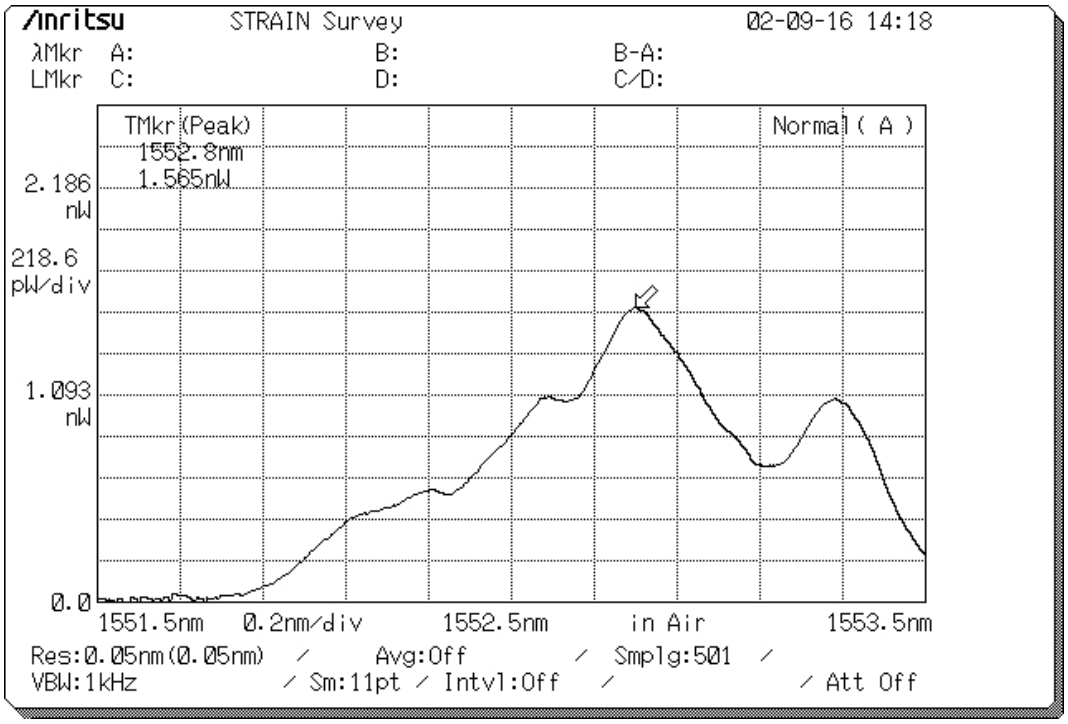

Figure 3.148: Test c, BLUERR, Day 2, 200^o C, 5000 N

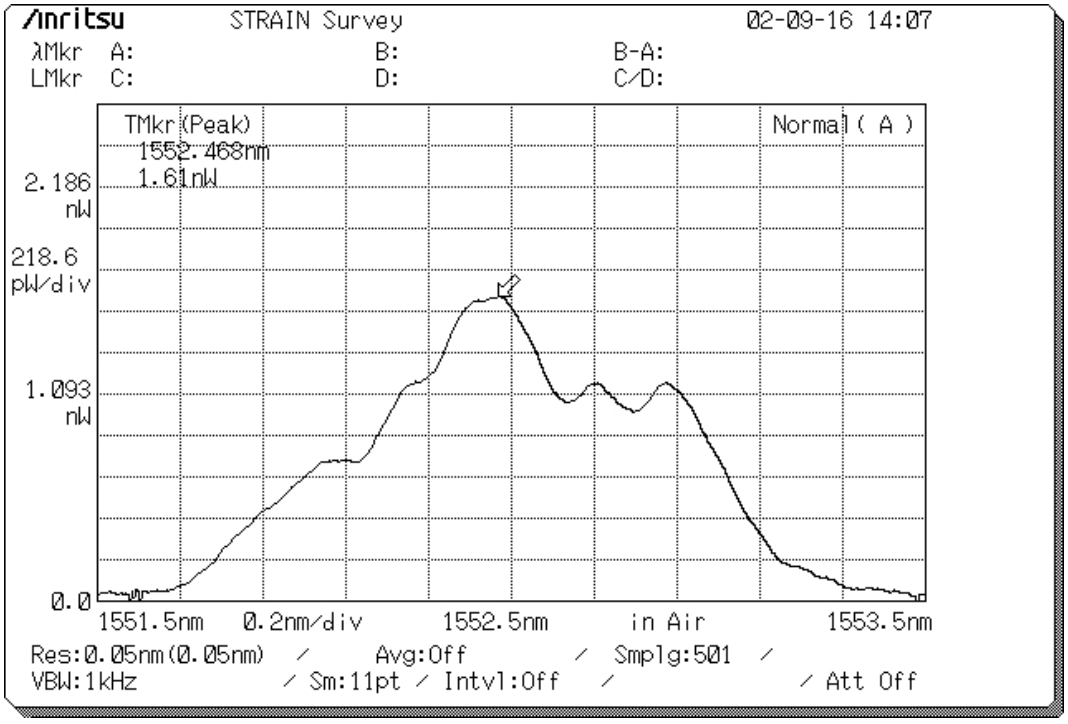

Figure 3.149: Test c, BLUERR, Day 2, 200^o C, 25 N

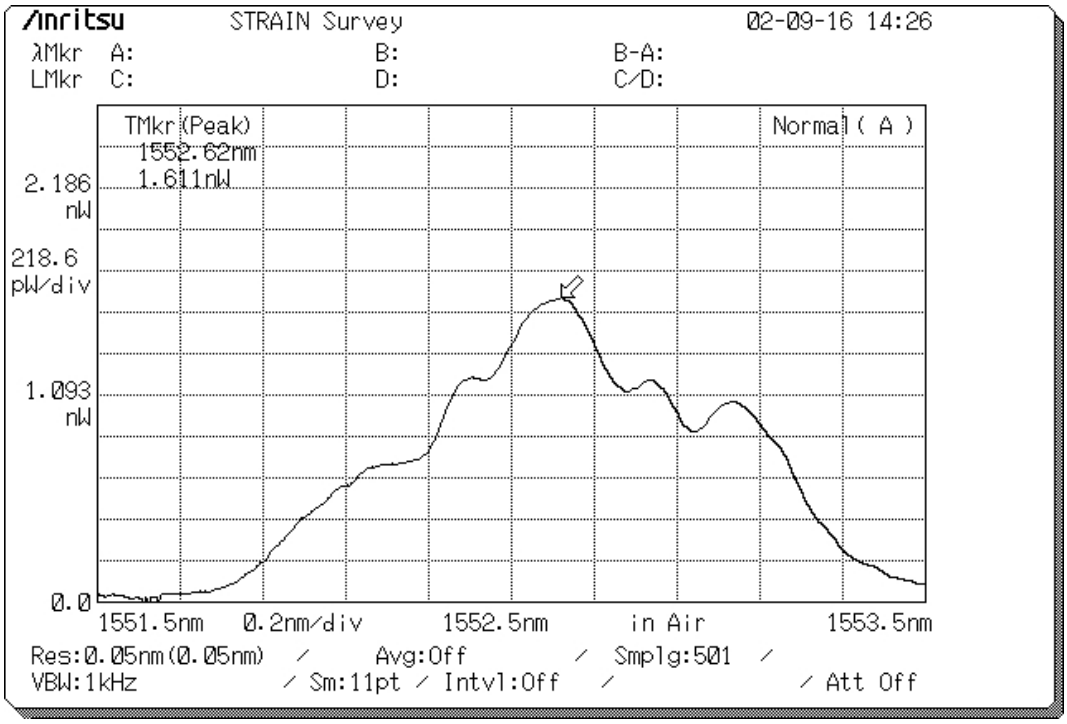

Figure 3.150: Test c, BLUERR, Day 2, 200^o C, 25 N

Temperature (°C)	SAC	TEE 95 (%)	BLUERR	TEE 95 (%)
20	good	34	ok	66
50	poor	83	faulty	x
80	ok	56	faulty	x
110	ok	55	poor	84
140	ok	37	ok	60
170	ok	43	faulty	x
200	ok-poor	45	faulty	x
Total	**n/a**	**353**	**n/a**	**210**
Median	**n/a**	**45**	**n/a**	**66**

Figure 3.151: Test c, SAC and BLUERR TEE values

(g) **Discussion and Conclusion**

In these series of experiments we have attempted to calibrate two different types of SP, by performing three different tests, namely:

i. To test the *bare* and *embedded* SP for the effects of heat (test a)

ii. To test the SP effectiveness of measuring load whilst embedded into a brake pad (test b)

iii. To test both sensors for the effects of heat and load on the output response whilst embedded into a brake pad (test c)

A discussion of these results follow:

Test a The SAC bare SP had a linear response with a TEE value of 20 %. The R^2 value[1] of 0.96957 indicates the fit is very good, however the plot of residuals suggested the fit was good despite one outlier. Again for the BLUERR bare SP the results are linear, except this time with a lower TEE value of 16 %, a very good R^2 value and residuals.

Embedding the Senko Advanced Components Smart Probe (SAC-SP) into the SBP caused the linear response in the *bare* test, to be become non-linear, whereas the Blue Road Research Smart Probe (BLUERR-SP) was not effected as much. Like the TF tests, embedding the SP's causes an increase in TEE values by a factor of 2 for the SAC-SP and 1.6 for the BLUERR. The stiffer less pliable resin coating of the BLUERR-SP has resulted in the more linear output compare to that of SAC-SP (please refer to Figures 3.98−3.105 for Test a results).

Test b Though not shown, the peak separations for both SAC and BLUERR SP's under load were found not to be present. Therefore, peak separations will not be use. The two cycles LPSt and RPSt for the SAC and BLUERR sensor were mostly identical therefore we will only use LPSt's for calibration (please refer to Figures 3.107−3.111 for Test b results).

Comparing the accuracy of the linear models between the embedded SAC and BLUERR SP's, the SAC probe had a TEE value of 3 % whereas the BLUERR-SP had a TEE value of 55 %. This result is odd, since in *Test a*, the BLUERR-SP had a lower TEE value for the bare and embedded tests. The stepped results in Figure 3.109 are believed to be caused by the stiffness of the resin coating. The resin coating unlike the teflon coating of the SAC-SP does not strain in a continuous movement thus the stepped results.

Test c Referring to Figure 3.151, we can see by using the TEE value as a primary indicator, that the SAC-SP is better than the BLUERR-SP. The median TEE values for the SAC-SP was 45 % and for the BLUERR-SP was 66 %. These values are much higher than 10 % that would be the equivalent TEE value for the SBP-SDC. However, when considering the other components of the SBP-SDC, such as the operating temperature, the ability to measure compressive loads, mounting considerations, sensor thickness, number of sensors per pad etc, the SAC-SP has the ability to

[1] A common statistical measure of goodness of fit for linear functions only. The closer R^2 is to 1 the better the fit is

comply with all of these other factors (please refer to Figures 3.112−3.139 for Test c results).

In addition to these factors, if we look at selected results for the SAC and BLUERR SP spectrums[1], we can see some of the fascinating underlying sensor characteristics of the SP (please refer to Figures 3.140−3.150.

For the SAC-SP if we compare Figure 3.140 on the first day, with that of Figure 3.141 on the second, though there is 30^o C difference the overall shape of the two peaks is clean and smooth with two easily definable peaks. Analogously, we could say, that from one day to another the SAC sensor has good well defined characteristics despite a rise in temperature. For the BLUERR-SP if we compare Figure 3.143 with 3.145, we can see that the characteristics of the BLUERR-SP on the first day is not as well defined as that of the SAC-SP. Though on the second day, the spectrum of the BLUERR-SP developed an extra peak which made it difficult to tell which peak we were tracking. As a result of this, the BLUERR-SP is not suitable for automatic FBG interrogation a necessity for brake dynamometer tests. The remainder of the selected SAC-SP results indicates it has a stable well defined characteristics making it well suited to automatic FBG interrogation.

The multiple peaks (please refer to Figure 3.146) of the BLUERR-SP spectrum is probably due to a differential temperature gradient produced as a result of the eccentric cross-section of the resin probe and the fibre not running true with the core of the probe. Thus one part of the fibre is seeing more heat and or strain than another thereby effecting the reflective properties of the gratings.

In conclusion,

- If heat is applied to the SAC and BLUERR-SP at RT whilst not embedded in a brake pad there is not much difference in performance between them
- If the SAC and BLUERR-SP is inserted into SBP then heated with no load this increases the TEE values from between a factor of 2 and 1.6 times greater than if they were not embedded, respectively
- The SAC-SP has a more stable character at RT and ET and throughout loading cycles compared to the BLUERR-SP
- The SAC-SP because of its stable well defined character would be ideal for use with an automatic FBG interrogation system that would be used for brake dynamometer or road testing of a SBP

[1] On the first day of tests we tested the BLUERR and SAC SP to about 115^o C. At each temperature level, one SP was tested then the cables were swapped and the other SP was tested; simultaneous testing was not possible. We found out that this method did not work very successfully, so on the following day we repeated the tests to 200^o C by testing each sensor sequentially. The figures given and the descriptions that follow are from the second day of testing; though, in the discussion of the spectrums we have included some day one results.

3.5.5 Finite Element Analysis

(a) **Introduction**

In this section we develop an FEA model of a SP embedded into a SBP. Typically, empirical modelling is all that is used when describing results from FBG sensors. Nevertheless, some are beginning to use FEA to model the behaviour of the embedded fibres holistically in preparation for better designs.

Here we utilise commercial software for both the creation and analysis of a model using MSC.Patran® and MSC.Nastran® for linear static analysis.

(b) **Objectives**

i. To create a quarter section model of a SAC-SP embedded into a SBP

ii. To apply the maximum braking pressure to the model and see if the highest stress concentration is centered around the teflon coating and the optical fibre contained within it

(c) **Model**

As you can see from Figure 3.152 we are modelling a quarter section model. The teflon coating of the SAC-SP has a similar E value as the friction material in which it is embedded, enhances the effects of Poissons ratio thus directing the strain along the length of the fibre enhancing the measurement. As the model illustrated in Figure 3.152, is so small, this raises a number of modelling challenges such as, compensating for the change in edge length between the optical fibre cross-section and the coating cross-section and finding the right elements to compensate for this great change.

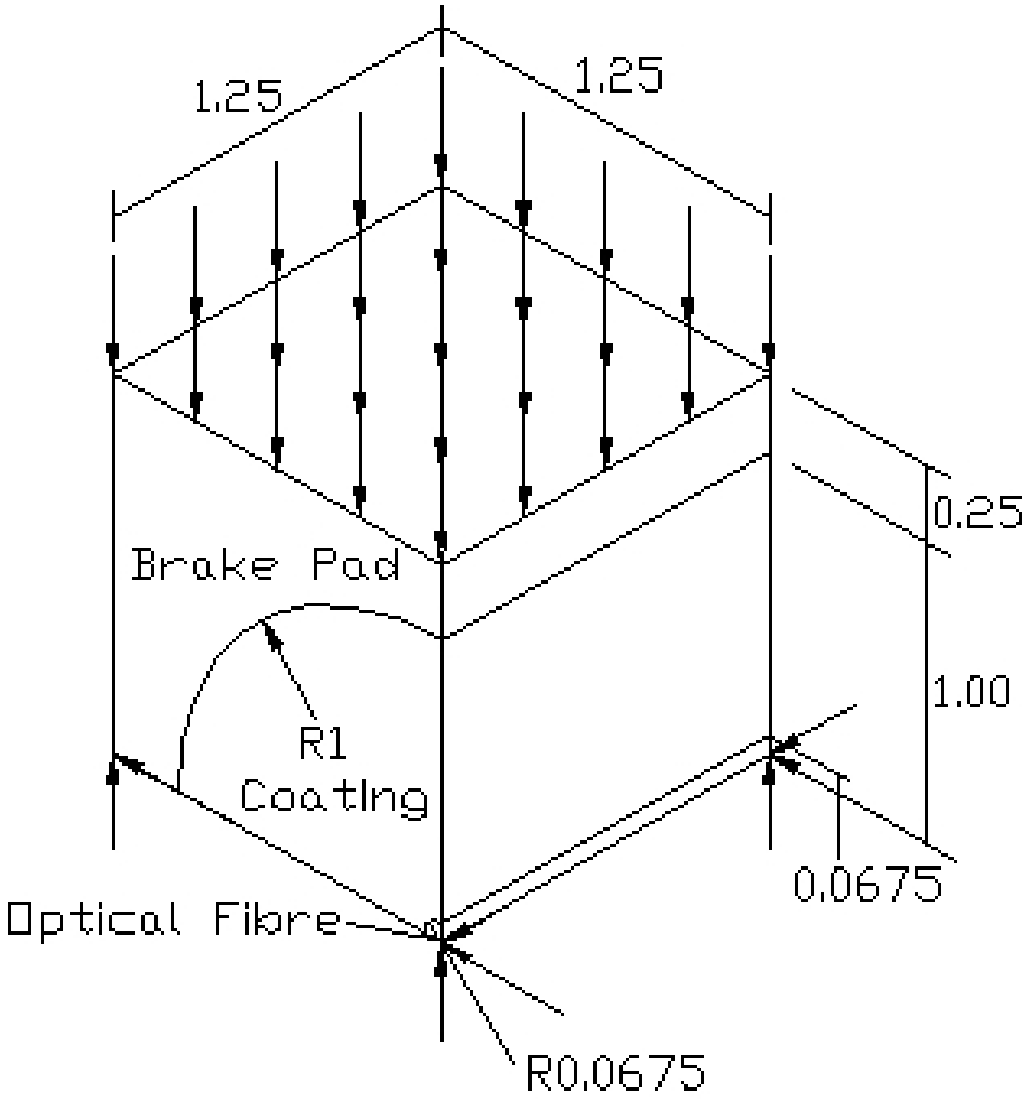

Figure 3.152: Quarter section FEA model of a SAC-SP

(d) **Results**

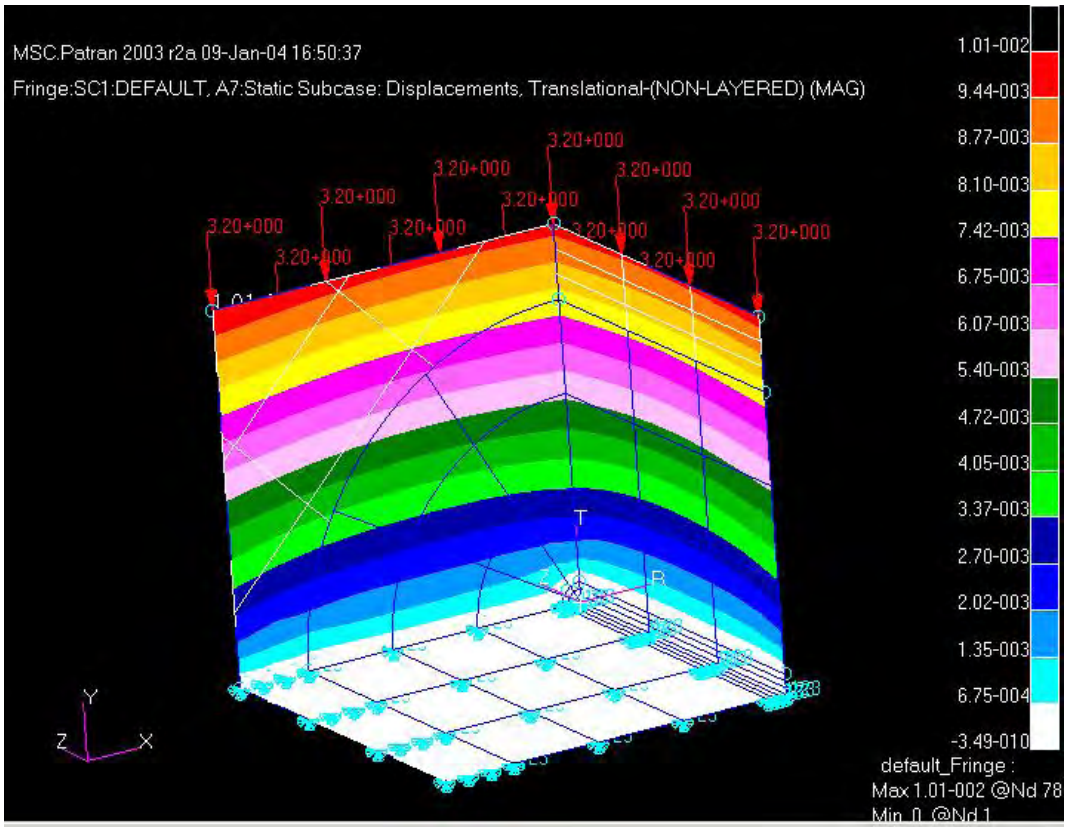

Figure 3.153: Displacements after the application of a pressure of 3.2 N/mm^2 with fixed-fixed-fixed base constraints

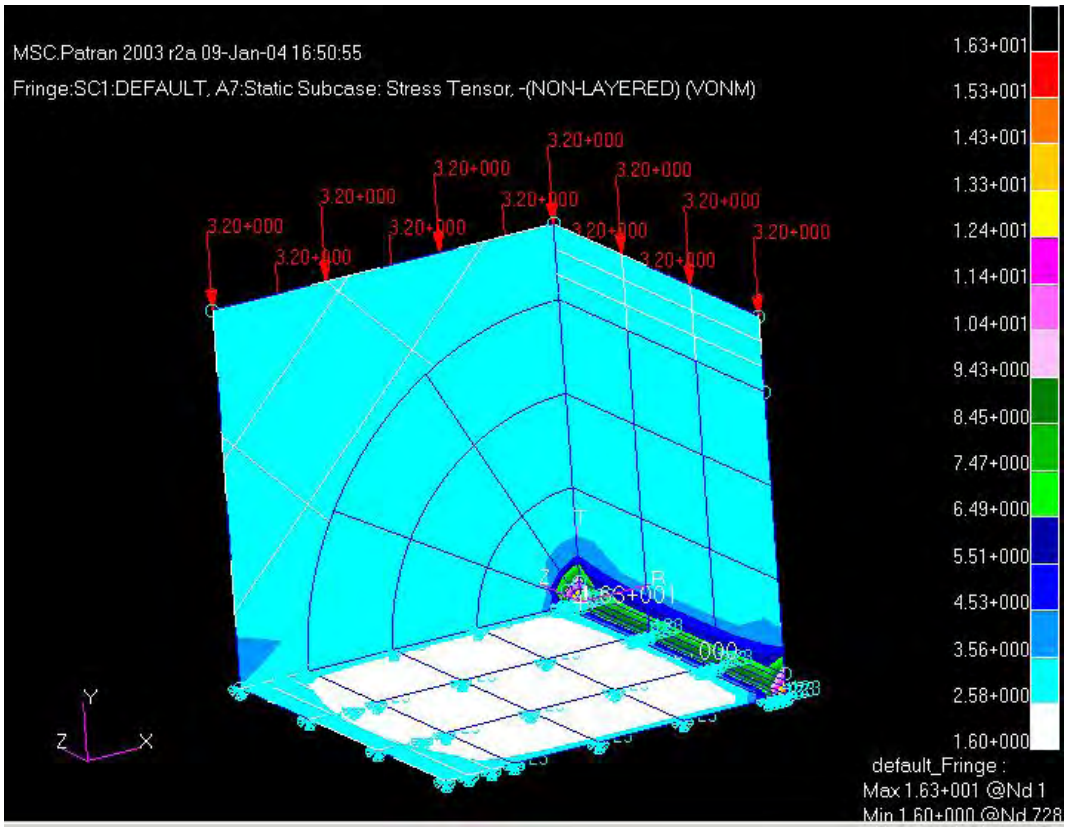

Figure 3.154: Stress tensors

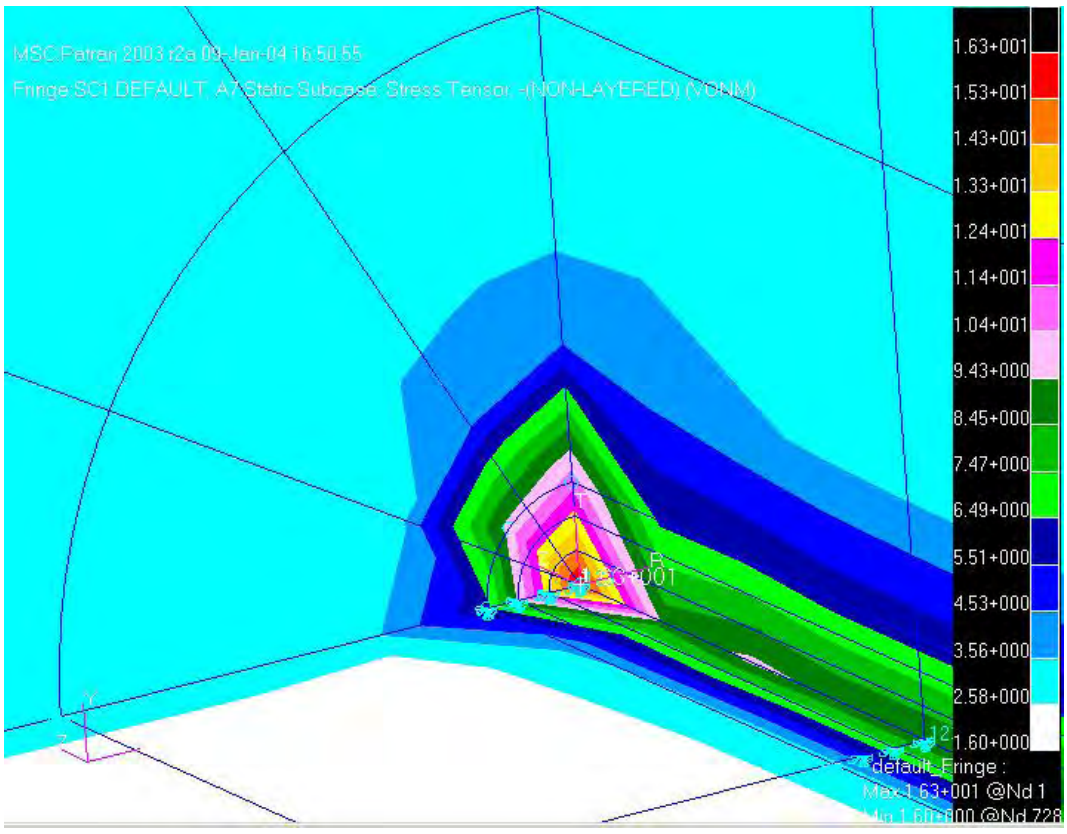

Figure 3.155: Stress tensors; close-up

(e) **Discussion and Conclusion**

There are three basic components of this model: The friction material, the teflon coating and the optical fibre. With small displacements, all three material remain linear elastic, though in reality, the friction material's E value does change between loading and unloading. The optical fibre is much stiffer than the other two components, thus we would expect overall there to be much less displacement than the other to materials. This can be seen in Figure 3.153.

However, in Figures 3.154 and 3.155 the stress in the optical fibre is greater than the rest of the model. This is expected, since it is placed at an edge and it is commonly known that the stress is higher along edges or corners.

Nevertheless, there are two lower edges opposing the applied pressure and the one with the teflon coating, is by far the greater, as can be seen by closeness of fringes and intensity of colouring at this edge. This model clearly verifies visually our theory with regards to the influence of the teflon coating on the optical fibre. Also, the figures verify that the stress is greatest at each end of the fibre, since we have Fixed-Fixed-Fixed boundary conditions, the fibre has *no where to go* thus has increased pressure at its ends.

We can also see that we have been successful in dealing with the great changes in edge length which has enabled us to obtain these results.

Furthermore, the teflon coating concentrates the stress in the area of the optical fibre, however, this may be a *double edged sword*; the sensor is now more sensitive to the friction materials hysteresis and possibly the hysteresis of the teflon coating.

In conclusion,

- This FEA model confirms our belief that the stress is more greatly concentrated in the region of the teflon coating and optical fibre contained within it
- Future models that should be considered are:
  i. A linear static model with varying loads to verify the RT tests
  ii. A coupled analysis heat and loading, to simulate the ET tests
  iii. Modelling different friction materials and optical fibre coatings to see their effects on an embedded SP

3.5.6 Discussion and Conclusion
- Fibre Optic Investigation -

We used elements of the Special Data Analysis Terminology and one of the designs from the Fibre Optic Smart Brake Pad Design Summary to complete the SBP Test and develop an FEA model.

The SBP tests showed us that the SAC-SP is superior to that of the BLUERR-SP; even though the BLUERR's spectrums containing multiple peaks were fascinating.

The FEA model confirmed our suspicion that the greatest concentration of stress is directed around the SP. In addition, a number of models were proposed for future investigations.

In conclusion,

- From the experiments performed, the SAC-SP was found to be the best technology to be used with a SBP to best fulfil the requirements of the SBP-SDC and the research questions
- FEA modelling was found to be a useful technique to check the stress concentrations around an embedded SP. Future models could also be used to check the validity of experimental results or in combination with other modelling techniques

3.6 Discussion and Conclusion
- Smart Brake Pad Investigation -

Based on extensive research and systematic development over many years which consisted of bringing together intellectual, financial and philanthropic resources towards building a SBP. The SBP is a tool that will enable engineers to better understand the root causes of DTV. It is also a tool that will enable engineers to better understand the initiators of low and high frequency vibration.

The development of the SBP is a great feat in collaborative engineering and research.

The process of developing the SBP involved creating a SBP-SDC which consisted of a list of desirable specifications that we wished the SBP to have. Whilst developing the SBP-SDC we also thoroughly discussed accuracy and tolerances of sensors; whereby we developed the TEE method to simplify the specification process. The beauty of the TEE method is that it can be used on all sensors no matter of their linearity; ensuring consistent comparisons between sensors and enabling better choices with less complexity.

Using the SBP-SDC we reviewed force measurement technologies, where we initially found TF sensors were mostly on par with their compatriots. Upon testing these sensors it became evident that a different sensors needed to be investigated. So in parallel, we started to review and experimentally investigate FO sensors.

As a result of these reviews and investigations it becomes clear that FO sensors are a winner in terms of functionality. Though, TF sensors were tested successfully to 195^o C they became non-linear and non-symmetrical between loading and unloading cycles making it difficult to fit mathematical models to the data. They also have high drift. Whereas, the embedded FO sensors were functional up to 200^o C with good solid well defined characteristics and lower drift. These qualities making them ideal for automatic FBG interrogation systems that would need to be used when testing a SBP in a simulated test environment, such as in a brake dynamometer or on a test track.

In addition, a preliminary theoretical model was developed for the TF sensor and the parameters for the model were found from experiment at RT. Though, different parameters are needed for different sensors.

Furthermore, a small 1.25 mm^3 three dimensional FEA model of an embedded SAC SP at RT was developed. The model showed on application of load, most of the stress was concentrated towards the edge of the model which formed the centre of the probe. Since the ends of the model were fixed, the increased strain along the Z axis (which the centre of the probe ran along) resulted in increased pressure at the probes ends. This result confirmed that the fibre was strained longitudinally; thus confirming the operation of the sensor and the influence of the coating. The straining of the fibre longitudinally changed the FBG properties, enabling a change of wavelength, and a measurement of load. The model is novel since FEA is only just starting to be used to study FBG and related sensor technologies.

In conclusion,

- A great feat in collaborative engineering research called an *SBP* was developed
- A SBP-SDC was developed which can be used to guide selection of applicable sensor technologies for a SBP

- A new method called the TEE method was also developed to simplify the sensor specification process to ensure consistent comparisons were made between sensors. This was also done to ease the complexity between choosing between different types and technologies
- A review of force measurement technologies suitable for use with a SBP was conducted. The review looked at the main technologies, techniques, history, types, construction and operating principals rather than simply a review of the current literature. This type of review was necessary since the knowledge gained enabled the best sensor to be chosen to match the SBP-SDC
- TF and FO sensors were investigated. TF sensors were cheap to buy and used traditional DAQS though they could not meet the requirements SBP-SDC as well as the more expensive FO sensors. The FO sensors were successfully tested up to 200^{o} C with a good solid well defined characteristics. It is believed the FO sensor as part of a SBP will enable in time for the answering of all research questions proposed in this research program and more
- A novel theoretical mathematical model was developed and successfully tested at RT for the TF sensor
- A novel three dimensional FEA model was also developed for the FO sensor for the RT tests

Chapter 4

Scanning Laser Doppler Vibrometer Test

4.1 Introduction

In Chapter 3 we investigated the SBP here we investigate an alternative option to the SBP called a S-LDV. Though either technology measures a different property, i.e. The SBP measures the pressure distribution whereas a S-LDV will give us the Animated Operational Deflection Shape (AODS). From the AODS we ought to get the profile of the pressure distribution assuming that where there is higher pressure, there is more wear, and therefore, more displacement.

The main purpose of this test is to measure the calliper/pad displacements to see if we can produce a AODS and gain insight into the pressure distribution between brake pad and disc.

4.2 Objectives

To obtain:

- The environmental vibrations present in the brake dynamometer testing facility
- Insight into the pressure distribution between brake calliper and disc

4.3 Methods

This test uses a brake dynamometer (dyne) and an S-LDV the methods used for both these pieces of equipment follow.

4.3.1 Methods used with Brake Dynamometer

With the brake disc and calliper assembly in the brake dyne with peripheral equipment, as shown in 4.1−4.4, we conducted a *judder test* which included five stops over a twenty minute period.

The judder test involved having the dyne sped up to an equivalent car speed of 130 km/h and applying the brakes at a set pressure equivalent to someone braking from high speed. The brakes are applied automatically, as soon as the embedded thermocouples in the friction material of the brake pad reach 100^o C. The brakes are continued to be applied at a constant pressure until the dyne slows to 60 km/h. At 60 km/h, the brakes are released and the dyne is returned to 130 km/h and allowed to spin freely until the brake pads have cooled. This sequence is repeated five times, being for five stops.

4.3.2 Methods used with the Scanning Laser Doppler Vibrometer

Initially we planned to send a signal to the brake solenoid of the brake dyne to start braking, that same signal would then be used to start scanning over the twenty points spread over the rear of the brake pad/calliper surface (please refer to Figure 4.3). Unfortunately, due to a technical challenges we had to initiate scanning manually.

Manual scanning consisted of starting and stopping the S-LDV scanning when a *click* from the solenoid controlling the brake line pressure on the brake dyne was heard. This meant of course, that there would be no certainty of when the S-LDV was started and stopped and thus trying to find a link between DTV and pressure distribution would be difficult as a result of these tests. Another setback was that the rate of scanning achievable by the S-LDV was much slower than anticipated, so slow in fact, that it would take one to two minutes to scan each point! This was too slow for scanning through all points during each stop. So as a *work around* we had to do one point per stop, thus twenty points and therefore twenty stops; this is the method we used.

4.4 Specimens

Brake disc[1] assembly; no separate photos available.

4.5 Experimental Set-up

The experimental set-up is contained within Figures 4.1–4.4:

The dots in Figure 4.3 are the scanning points for the laser. The scanning points were manually selected by applying pieces of special reflective tape where we wanted to take a measurement. The S-LDV was then trained to measure at each of the points in a sweep type scanning movement from the top of the picture down. With this set-up, both the pad and calliper were measured simultaneously. The two circles indicated where the pad displacements were measured.

The background noise measurement was achieved by pointing the S-LDV onto what was believed to be the noise producing source and a *point measurement* was taken.

[1]The brake disc in this experiment already has an amount of DTV

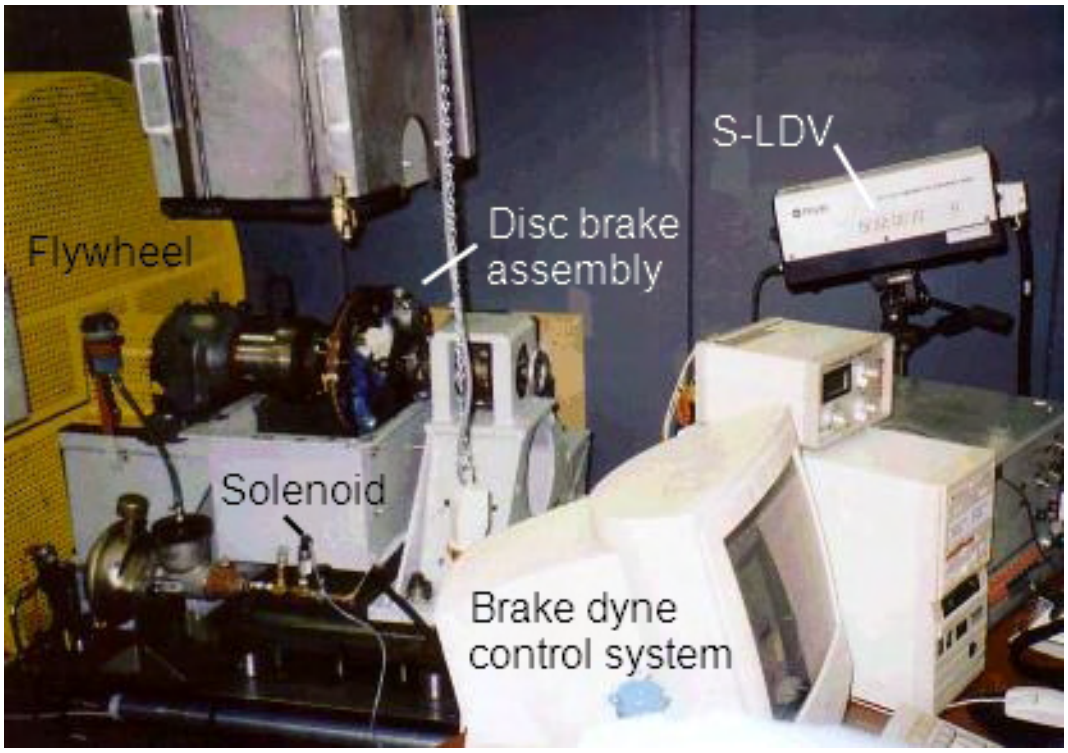

Figure 4.1: S-LDV set-up overview

4.6 Results

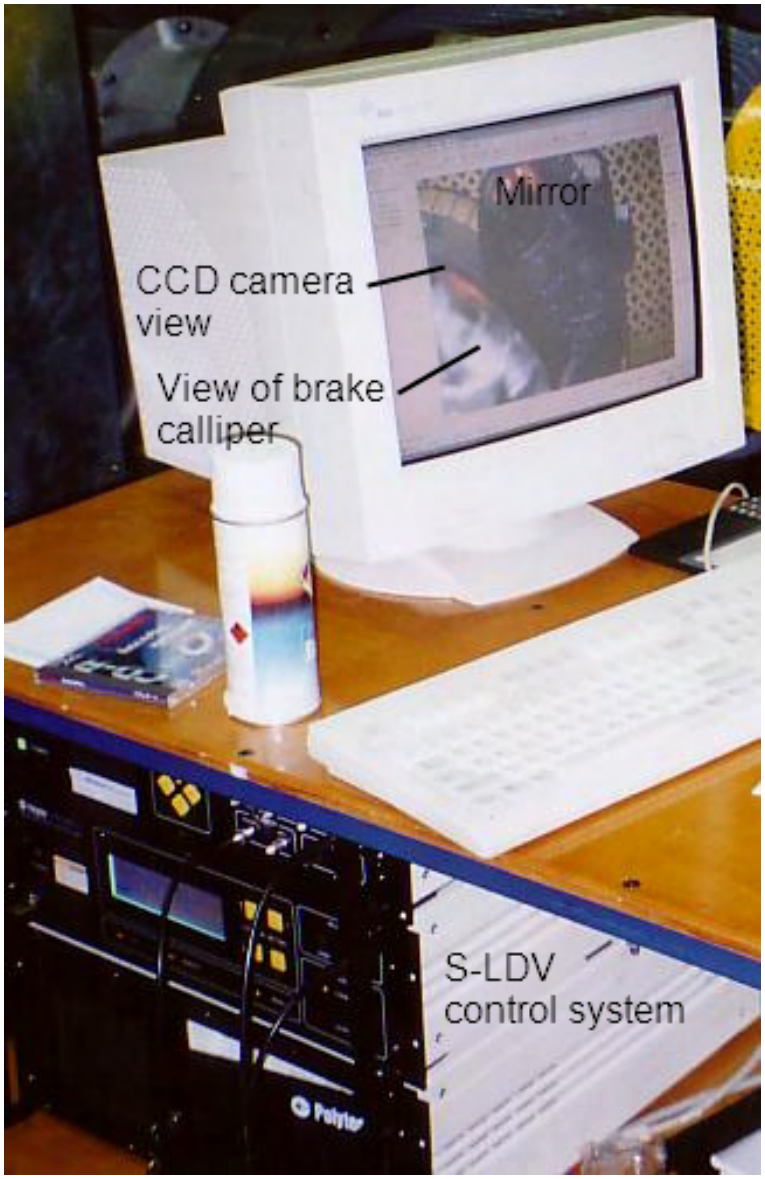

Figure 4.2: S-LDV control system

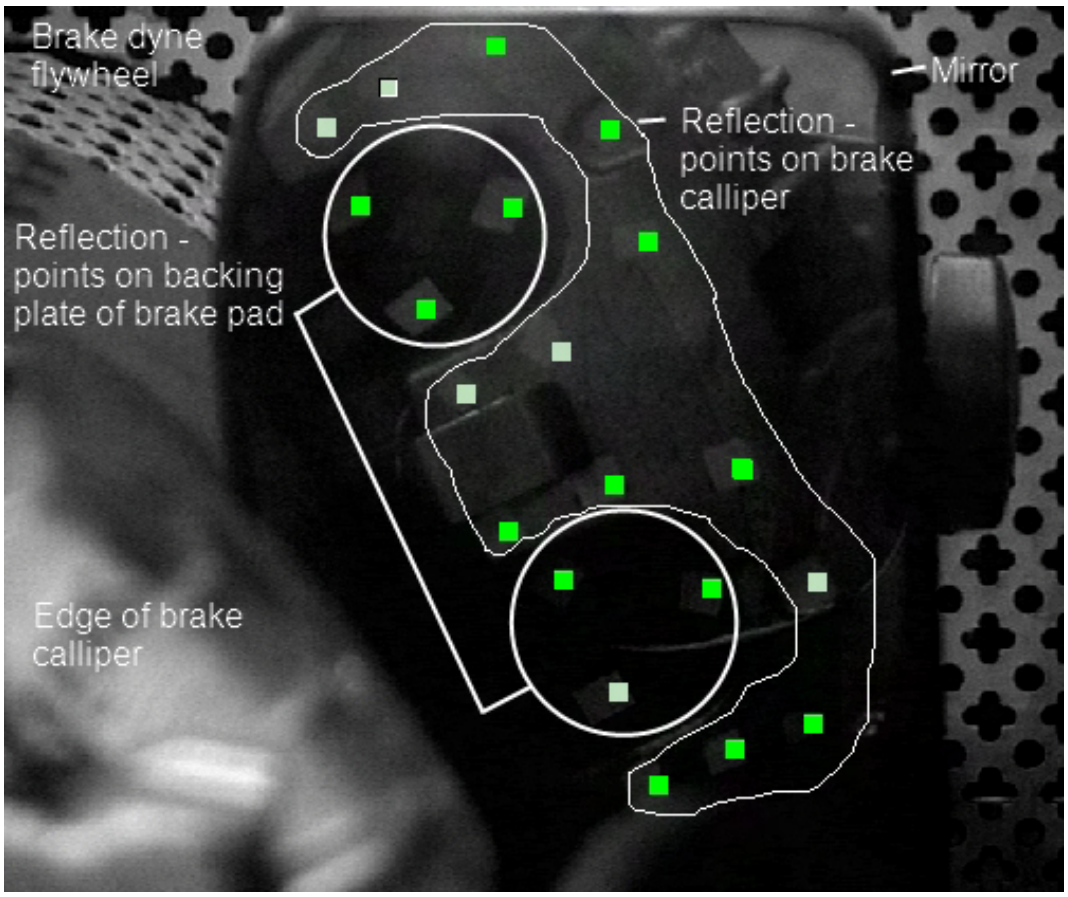

Figure 4.3: S-LDV control system; CCD camera view

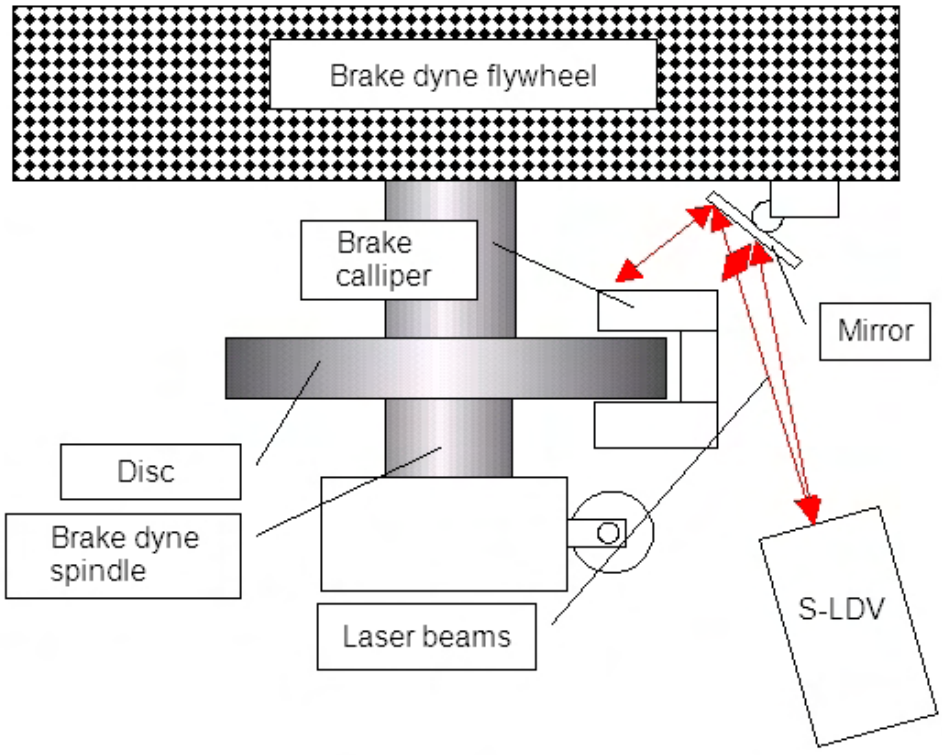

Figure 4.4: S-LDV set-up

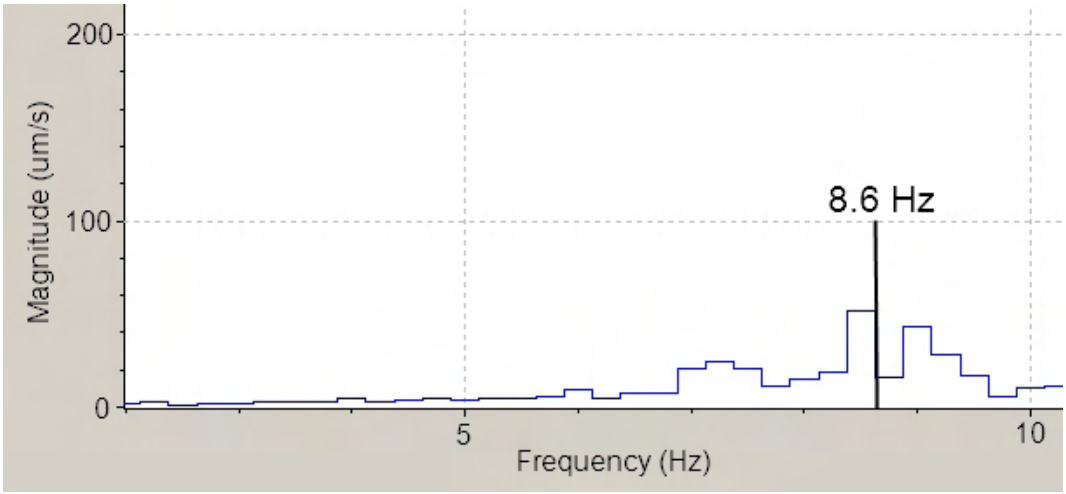

Figure 4.5: Brake dyne cooling fan off

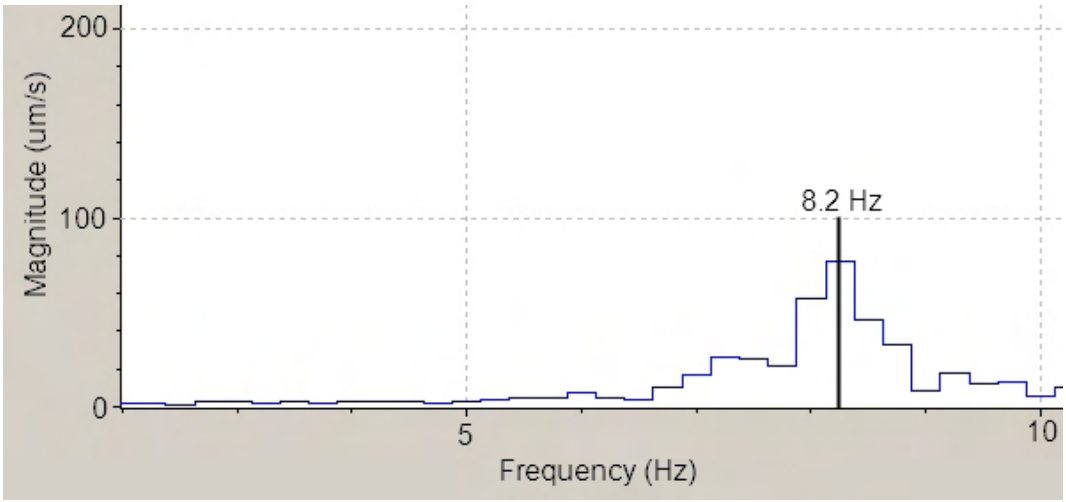

Figure 4.6: Brake dyne cooling fan low

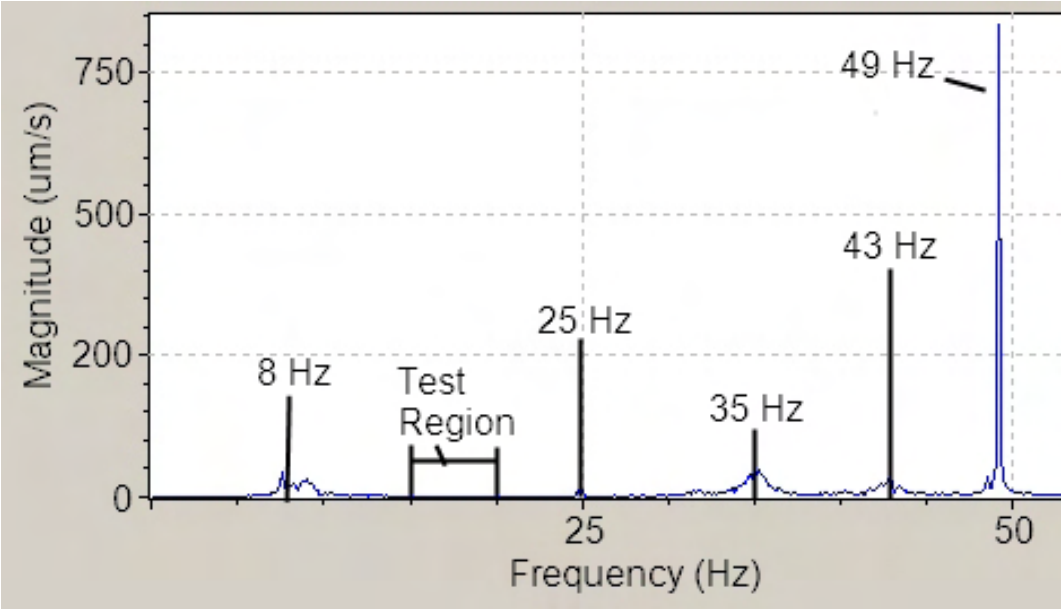

Figure 4.7: Background vibration spectrum. Fan in normal position

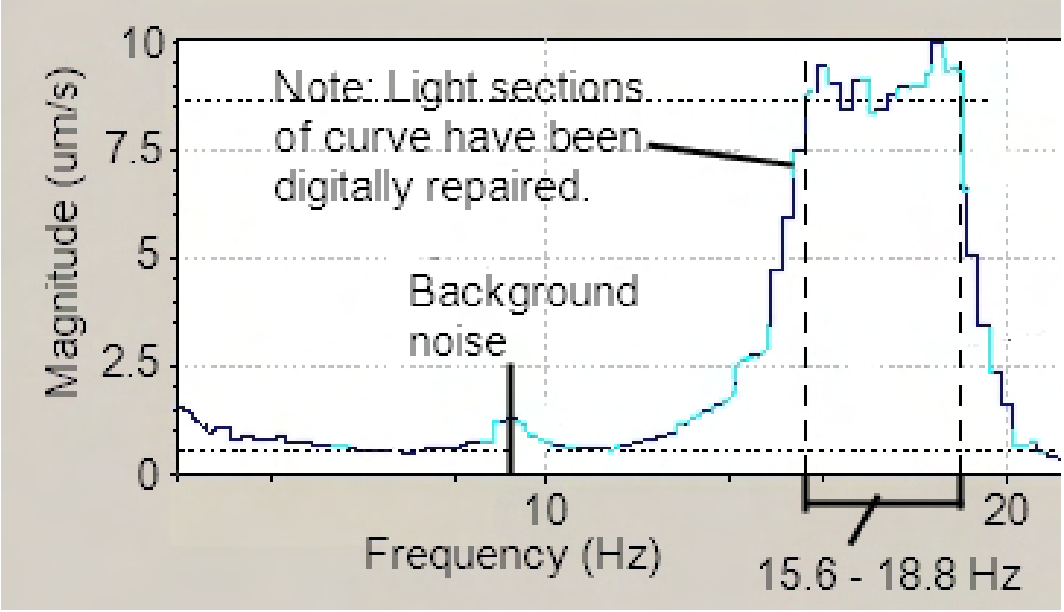

Figure 4.8: Average calliper displacements measured during brake judder

In Figure 4.8 we see the average calliper displacements during brake judder taken during the dyne test. From this we can estimate equivalent car speeds with different wheel diameters. For a 15 inch wheel this equates to juddering occurring between 92 km/h and 76 km/h. For a 17 inch wheel it would equate to between 82 km/h and 68 km/h. These car speed estimates are based on the wheel diameters and the idea that wheel speeds are directly related to vibration frequency. There is a maximum average displacement of 7.9 μm of travel between the horizontal dashed-lined-sections of Figure 4.8.

The AODS in Figure 4.9 was composed using the twenty different stops for each point of the twenty points depicted in Figure 4.3. A changing surface was then

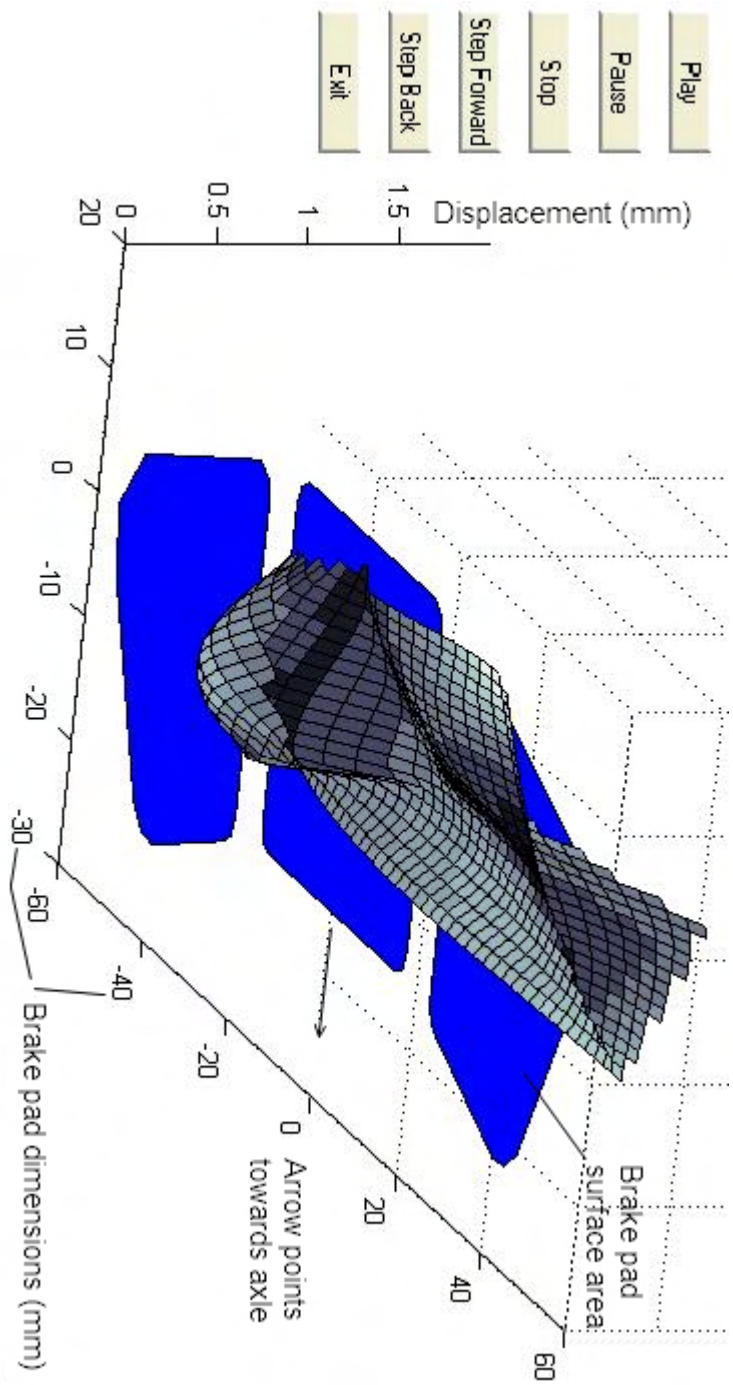

Figure 4.9: AODS of juddering outboard pad of a brake calliper

produced by interpolating over the twenty points and updating the information at a constant interval using a custom MatLab^{TM} script. Though produced from twenty different stops, it is assumed that as the stops are controlled, thus the sequence of events ought to be similar; this may have been true if we could have initiated automatic triggering of the S-LDV using the brake line solenoid. The other flaw is that there is no reference laser. Therefore there is no way of telling whether a particular point is *up or down* except to assume that the brake pad and calliper always come to rest in a similar position.

4.7 Discussion and Conclusion

- Laser Doppler Vibrometer Test -

Before conducting the brake dyne test the environment of the brake dyne was tested for vibration as no previous information was available. Figures 4.5 and 4.6 tell us that there is a noise of between 8.6 and 8.2 Hz in the testing environment which is reduced when the dyne fan is switch between the *off* and *low speed* position. In Figure 4.7 we can see that the fan further reduced at roughly 8 Hz is still present, but the dominant frequency is a large 49 Hz which is possibly a result of an *earth loop*[1]. Figure 4.7 also tells us that the testing region between 15 and 20 Hz is free from disturbance.

The brake dyne test was conducted with the experimental equipment in Figures 4.1−4.4. As discussed in the method, the original plan of five stops in twenty minutes was changed to twenty stops, due to the much slower than expected scanning rate of the S-LDV. We expected that the S-LDV would be able to scan through all points in Figure 4.3 during each stop, however, *on the day* we had to scan through a single point in each stop. This coupled with the fact that when we did scan through a single point we had no way of knowing whether a point was *up or down*. If future tests were conducted with such equipment a reference laser (Ref Laser in Figure 4.4) or alternatively another S-LDV would be needed in order to have a reference line for each point to be measured as suggested in Figure 4.4.

Though we conducted the tests without a reference laser we could have possibly 60 % confidence, at a guess, that the extremes of displacement of the brake calliper would be approximately the same between subsequent tests[2]. This said, Figures 4.10 is a stem plot of the extremes in displacement between the outer and inner radius. From this figure we can see that the equilibrium is roughly between 2 and 2.5 on the displacement scale and the extremes are between 6 and 10 on this same scale. Figure 4.11 is more useful as it shows a clearer relationship between displacement and position on brake pad surface. This figure suggests that the outer radius is moving more than the inner radius thus following the DTV that is already present on this disc.

Figure 4.8 shows the average calliper displacements during juddering brakes. This figure confirms the well known relationship between wheel speed and vibration frequency; thus DTV and brake judder are directly related.

In conclusion,

- We were able to accurately measure the existing background vibration levels
- The testing region used to perform the S-LDV tests on the brake dyne was found to be relatively free of external interference
- We were able to get the AODS which may help us with the shape of the pressure distribution though with two major assumptions:
  - The same testing environment and parameters are present in twenty individual stops

[1] An electrical fault caused by incorrect grounding of electrical equipment and accessories
[2] This is assumption is based on the action of the brake calliper

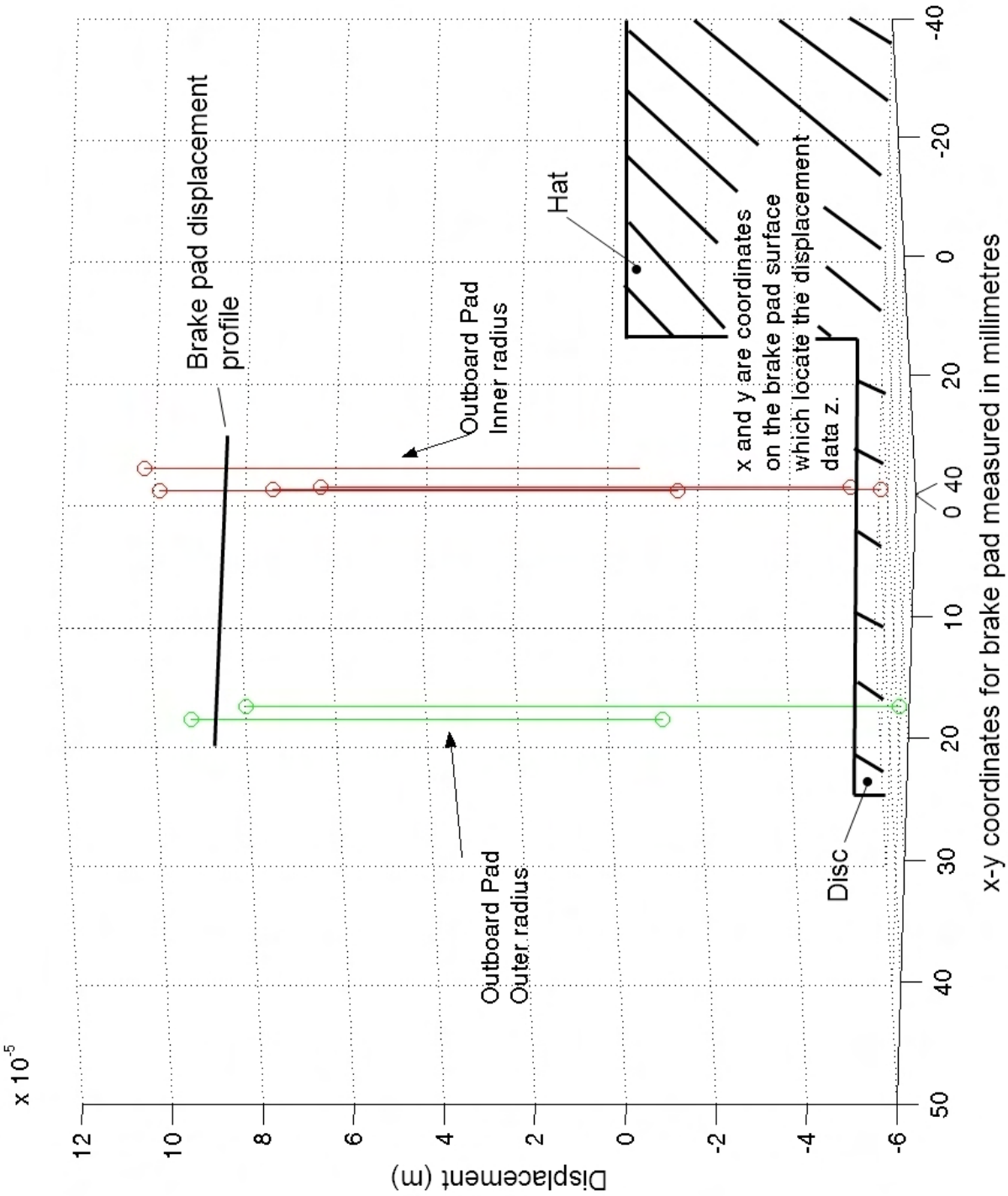

Figure 4.10: Stem plot of extreme calliper displacements

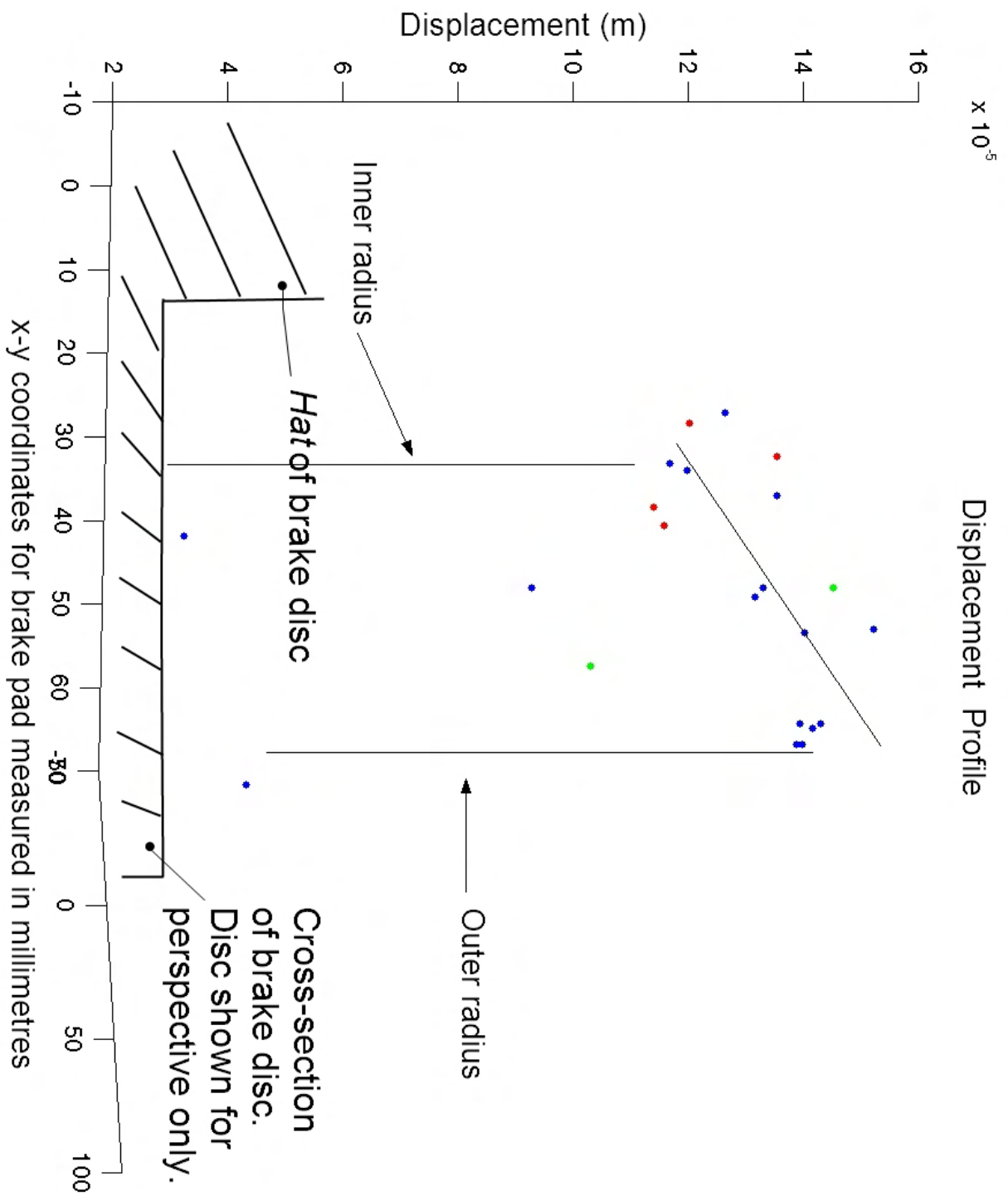

Figure 4.11: Displacement profile for inner[a] and outer radius of a brake pad

[a]The inner is closest to the hub of the wheel

  - The calliper returns to approximately the same equilibrium point after each brake application and more importantly that the extremes of displacement of the calliper have the same sign (±)

- Confirmed the relationship between wheel speed and brake judder frequency of between 18.8 and 15.6 Hz when braking, from a speed of 130 km/h to approximately 60 km/h

- Suggested the following recommendations for future work:

  - To further the development of LDV technologies by increasing the scanning rates to the point where the whole pad can be scanned at a rate of 50 Hz or greater

  - Use a reference laser or multiple S-LDV set-up

From the work discussed in this Chapter we can see that the SBP investigated and developed in Chapter 3, at present is the best technology available that is likely to lead us to the root causes of DTV in motor vehicle brakes.

In the next Chapter we trial the SBP in a brake dyne to see how it performs during simulated driving conditions.

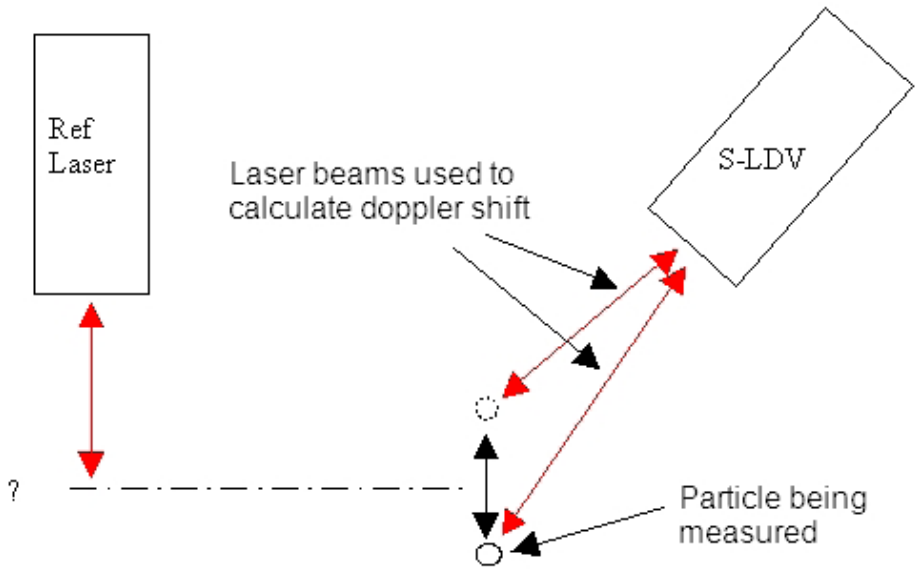

Figure 4.12: The tracking of a single particle using a S-LDV for the purpose of measurement

Chapter 5

Application of Smart Brake Pad

5.1 Introduction

In this Chapter we calibrate then trial a SBP in simulated driving conditions using a brake dyne. As a result of these tests we hope to answer the first research question: "Is it possible to measure the contact pressure between brake pad and disc dynamically?"

The ability to answer this question fully in time will enable future researchers to answer all research questions proposed in this research program.

This Chapter contains the following topics:

(a) Smart Brake Pad Calibration Test

(b) Smart Brake Pad Brake Dynamometer Test

5.2 Smart Brake Pad Calibration Test

5.2.1 Introduction

The objective of these tests is to calibrate the SBP in preparation for the dyne test.

This requires us to measure three variables:

- Strain ϵ from the SP embedded into a SBP
- Temperature from conventional Thermocouple (T/C) embedded as close as possible to the SP
- Load measured using a load cell connected to an MTS

This data is then use to produce a *two dimensional look-up table*, when plotted looks similar to Figure 5.1.

The two dimensional look-up table used to produce Figure 5.1 can then be used to find the equivalent forces given a strain at a particular temperature (please refer to Equation 5.1).

$$F_{Temp} = f(F, \epsilon_n, Temp) \tag{5.1}$$

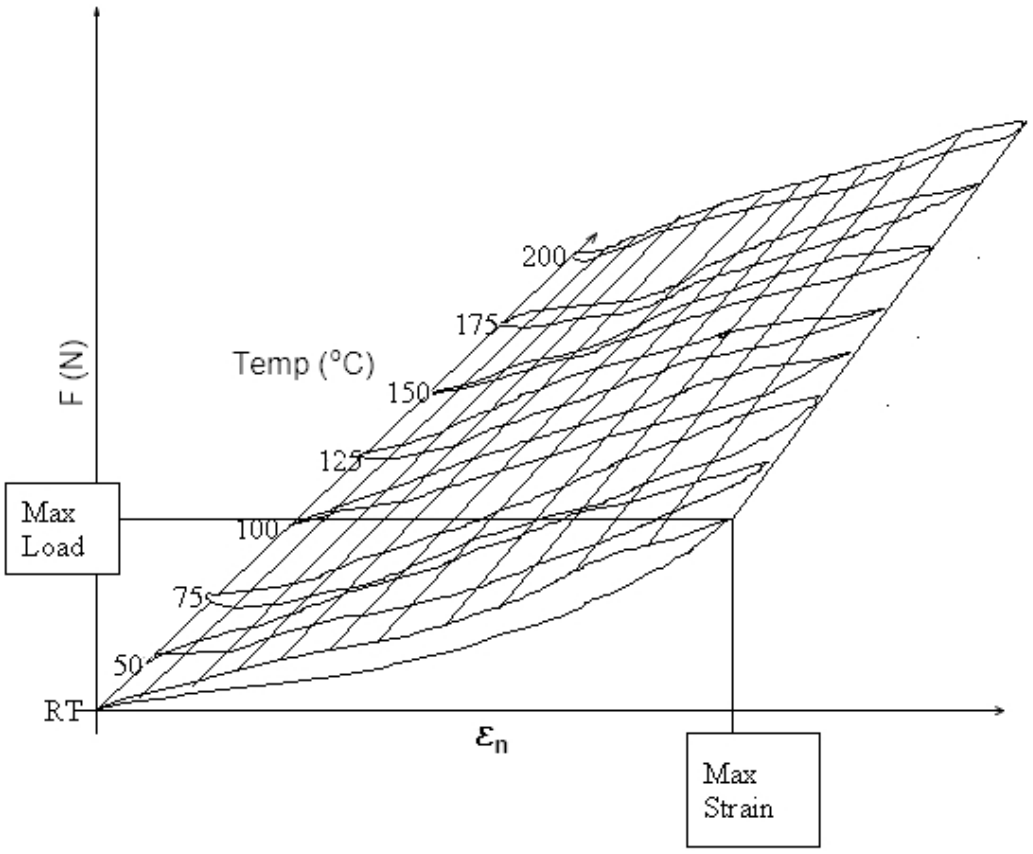

Figure 5.1: Representative three dimensional calibration plot

5.2.2 Objectives

The objectives are to, conduct a:

(a) Smart Brake Pad Room Temperature and Compression Test

(b) Smart Brake Pad Elevated Temperature Test

(c) Smart Brake Pad Elevated Temperature and Compression Test

Objective three ought to be the only test that is needed to produce the two dimensional look-up table. Here we will analyse only what is needed.

5.2.3 Methods

In turn each of the two SBP is put through one of the following Experiments.

SBP RT and Compression Test The test is conducted at RT; six loading cycles from 0 to 5 kN in compression are applied to the specimen. The MTS DAQS records the loads from the load cell for the test. The Micron Optics Interrogation System (MOIS) records the optical data from the SP.

SBP ET Test The test starts at RT then moves through to 200^o C recording temperature via SP-Temp and T/C (See Figure 5.2 for T/C-Pad). A separate DAQS measures the temperature from T/C in the pad and the MOIS measures the data from the SP.

SBP ET and Compression Test The test starts at RT, moving through to 200^o C in 25^o C degree increments. At each temperature level six loading cycles are applied from 0 to 5 kN in compression. At each of these levels the temperature is recorded to compensate for temperature fluctuations[1]. Both the load and temperature measuring SP data is interrogated using the MOIS and the data is recorded directly to a laptop pc using its ethernet port. The MTS' load cell and T/C data are recorded using its in-built DAQS on the MTS.

5.2.4 Specimens

There are two SBP to test each with two SP, see Figure 5.2 and their descriptions here:

(a) SBP_1 contains two SP [manufacturer 1]

  i. SP-Load: One bi-axial SAC SP from the Chapter 3 tests

  ii. SP-Temp: Two mono-axis FBGs on separate fibres in the one hole

(b) SBP_2 contains two SPs [manufacturer 2]

  i. SP-Load: Three mono-axis FBGs on one probe

  ii. SP-Temp: Two mono-axis FBGs on separate fibres in the one hole

Figure 5.3 details the interfaces between each set of probes[2].

[1] As the probes are highly sensitive

[2] The nominal wavelength is 1550 m; each grating has a different wavelength which can be thought of as a unique address

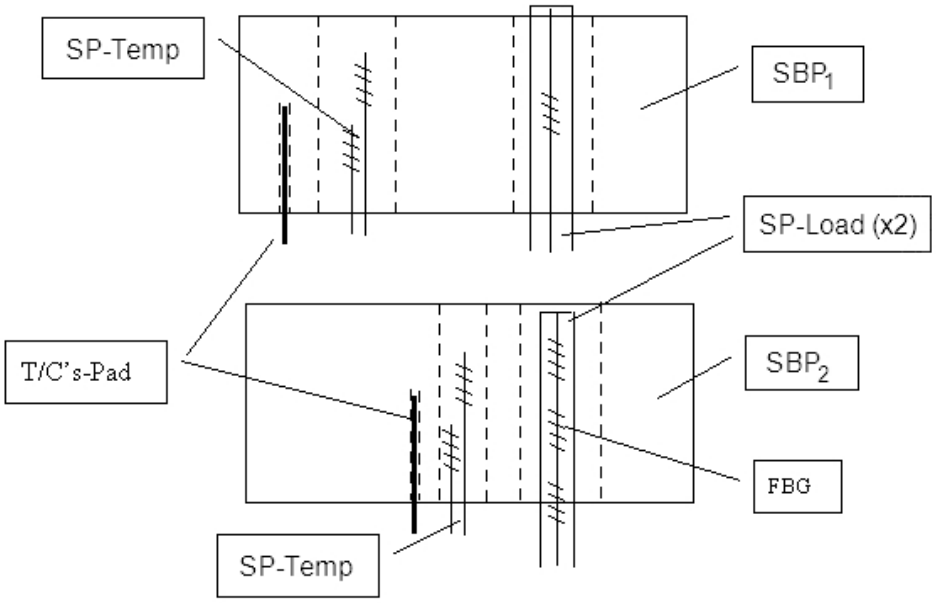

Figure 5.2: SBP's layout; aerial view

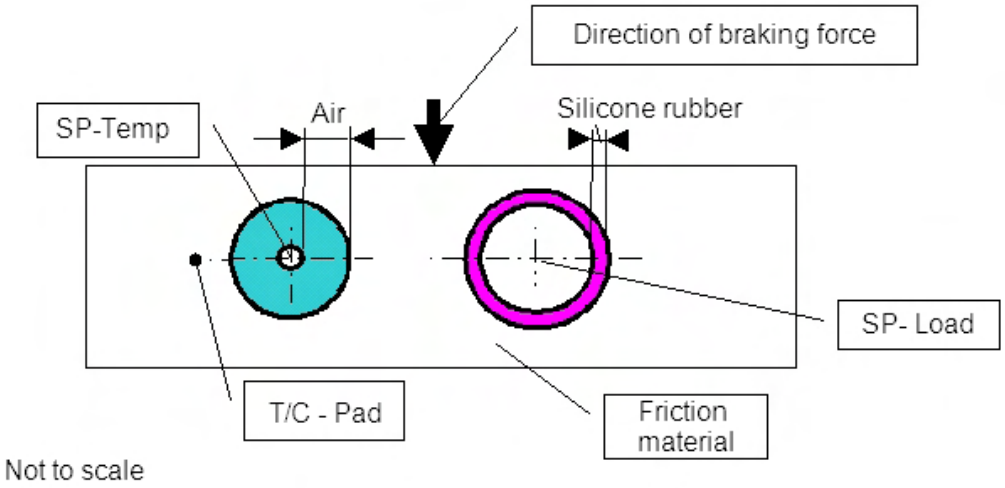

Figure 5.3: SBP's interfaces; end view

5.2.5 Experimental Set-up

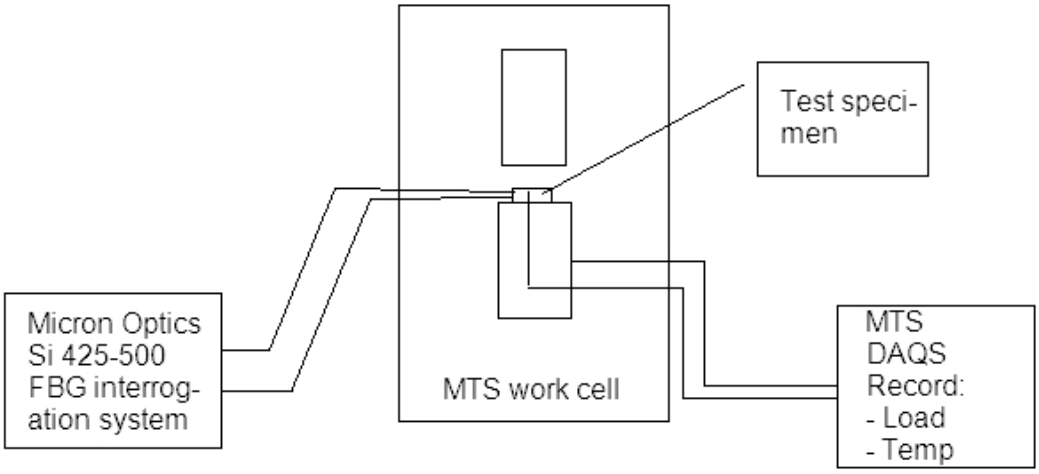

Figure 5.4: Overview of experimental set-up for calibration tests

The detailed set-up of the compression platens is similar to that in Chapter 3.

5.2.6 Results

All 3 tests were successfully completed and it ought to be possible to produce a 2D look-up table and plot in order to fulfill the calibration obligations for the SBP.

Due to the magnitude of success of the SBP during the dyne test it will only be necessary to show the highlights of experiment 3.

Please note: In the following figures the *x axis* is measured in units; the *MTS load cell* has a different sampling rate to the MOIS used for the SPs this is the reason for the difference in unit values.

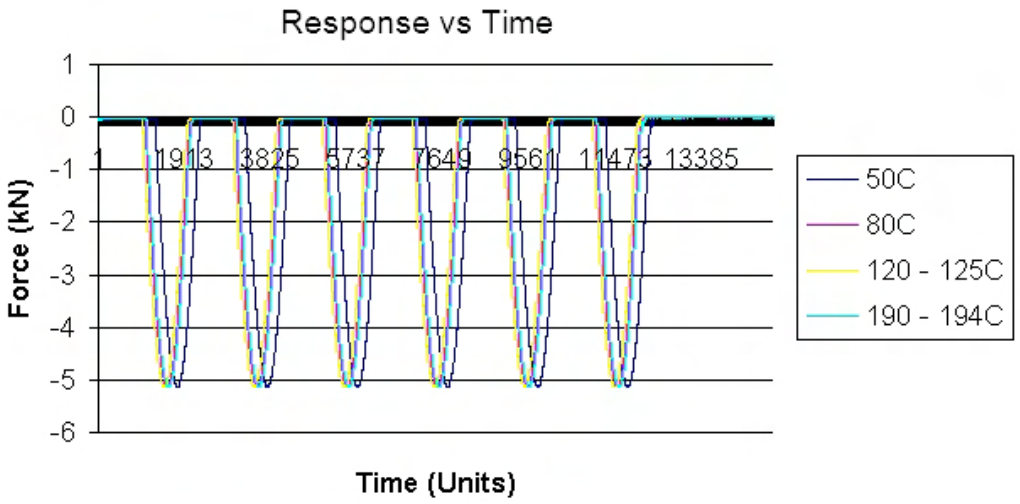

Figure 5.5: MTS load cell data recorded for SBP_1 calibration test

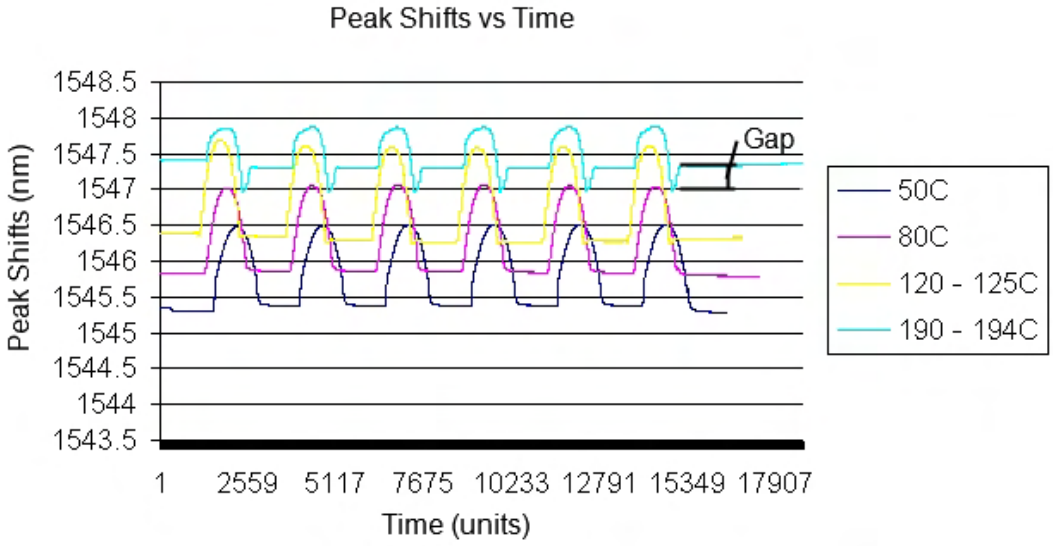

Figure 5.6: SBP_1 data

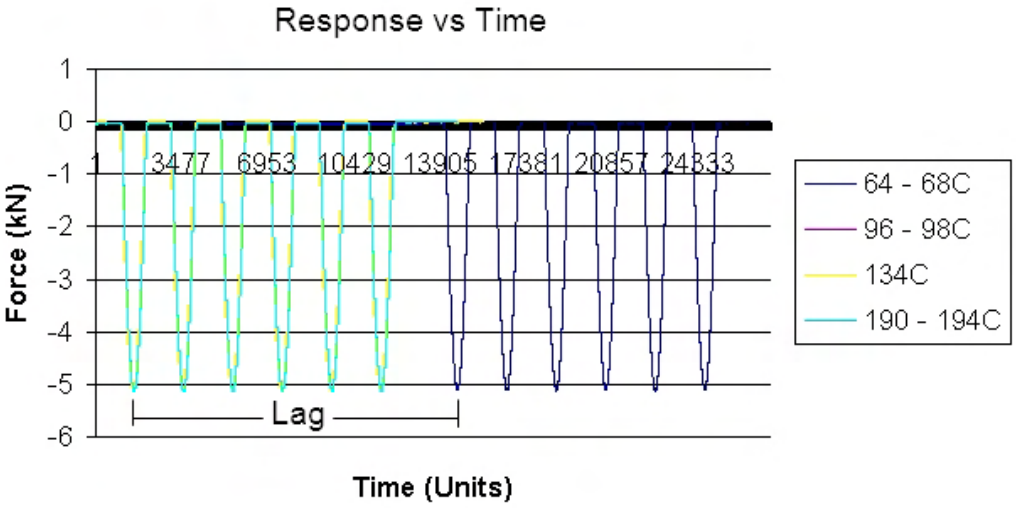

Figure 5.7: MTS load cell data recorded for SBP_2 calibration test

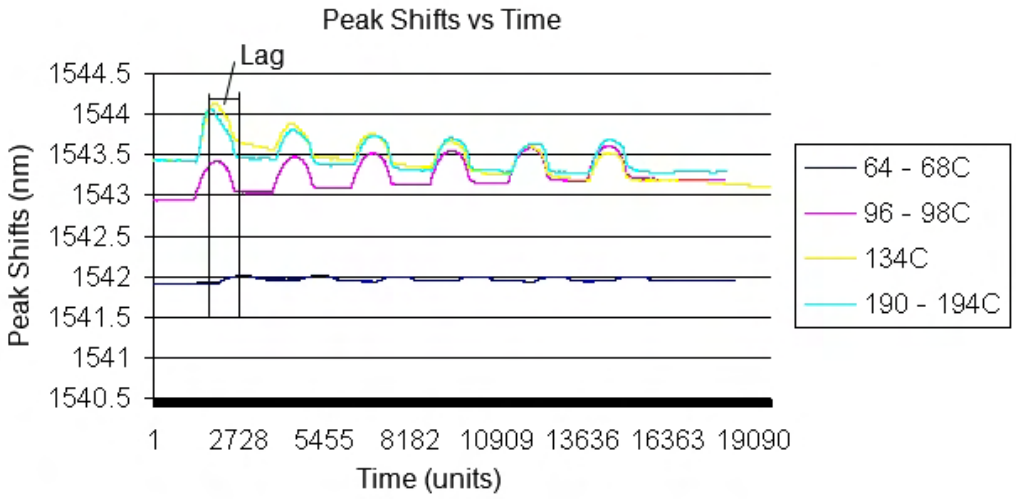

Figure 5.8: SBP_2 data

5.2.7 Discussion and Conclusion

- Smart Brake Pad Calibration Test -

On inspection the main observable difference between the load cell output (please refer to Figure 5.5) and the SP-Load output (please refer to Figure 5.6) is the linearity; the load cell is practically linear whereas the SP is not; but this is expected as was found in the previous tests in Chapter 3. As the temperature raised above 50^o C we get a softening of the brake pad material and an increase of material hysteresis as can been seen by the *gap* between where the strain was first measured and where it was finally measured. In fact, if a compression test was performed on brake pad at RT, it could be shown that the material would show a degree of hysteresis between loading and unloading cycles. So, from the results it seems that the hysteresis gets worse upon heating, thus the increasing gap as the temperature increases.

Material hysteresis would affect SBP_1 as much as SBP_2 as they both are made of similar material, however, the sensors sensitivity to this hysteresis would be different since they both have different constructions and different types of coating. SBP_2 in fact appears to be less affected by hysteresis than SBP_1, possibly due to a slightly thinner and stiffer coating; the time *lag* that is present between the lower and higher temperature data is simply due to the application of the load at a later time as can be seen by the presence of the lag in both Figures 5.7 and 5.8[1].

So in conclusion,

- From the data highlighted for SBP_1 and SBP_2 it seems that both these pads could be calibrated with a differing degree of error due to material hysteresis and different sensor constructions
- SBP_2 seems to have less hysteresis than SBP_1

[1]The apparent difference in size of lag is caused by the different data sampling rates

5.3 Smart Brake Pad Brake Dynamometer Test

5.3.1 Introduction

The aim of this test is to trial the SBP's developed in this research program and discussed in the previous section.

5.3.2 Objectives

The objectives of these test are to:

- Trial a simplified SBP in a simulated driving condition in a brake dyne
- To answer the first research question
- To learn what we can from the trial in order to improve the parameters for future trials

5.3.3 Methods

(a) The test will be split into two parts. Both specimens will be tested simultaneously. The two tests are:

   i. A *judder test* comprising of five judder stops in thirty minutes

   ii. A *squeal test* comprising of applying a constant load[1] at constant slow speed the equivalent of 5 to 10 km/h for one minute.

5.3.4 Specimens

As per calibration.

5.3.5 Experimental Set-up

Two SBPs' fitted inside a brake calliper. The brake calliper is then mounted onto the disc brake assembly. The disc brake assembly is then placed inside the testing chamber of the brake dynamometer ready for testing.

[1] 2.5 MPa Brake line pressure

5.3.6 Results

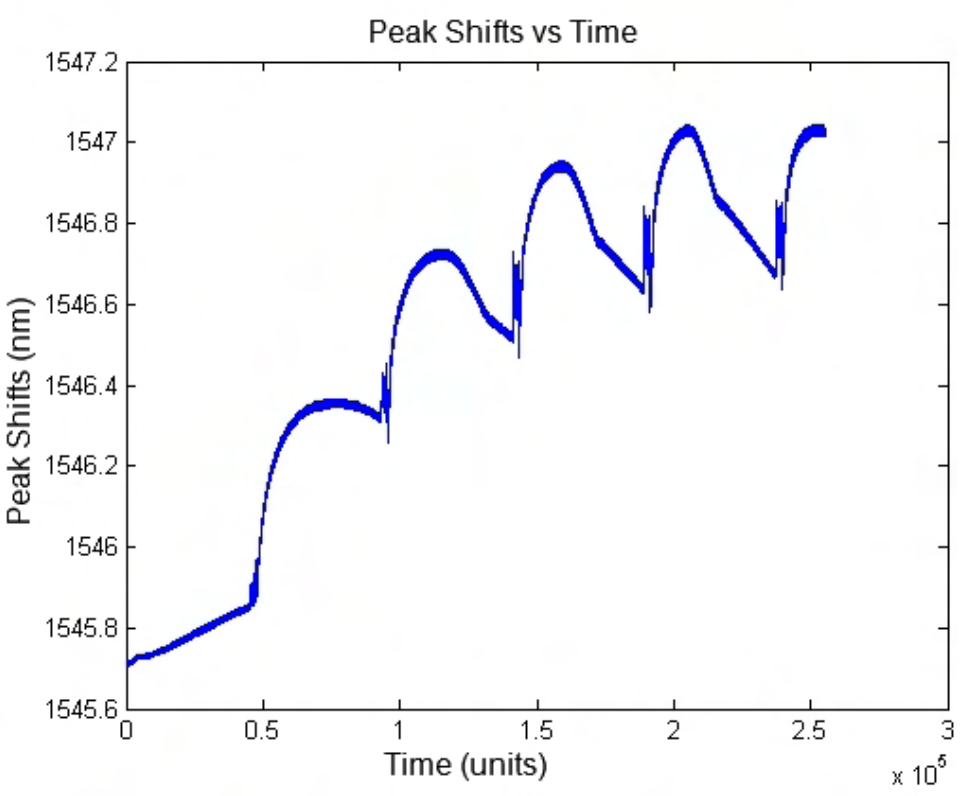

Figure 5.9: SBP output; snap-shot one

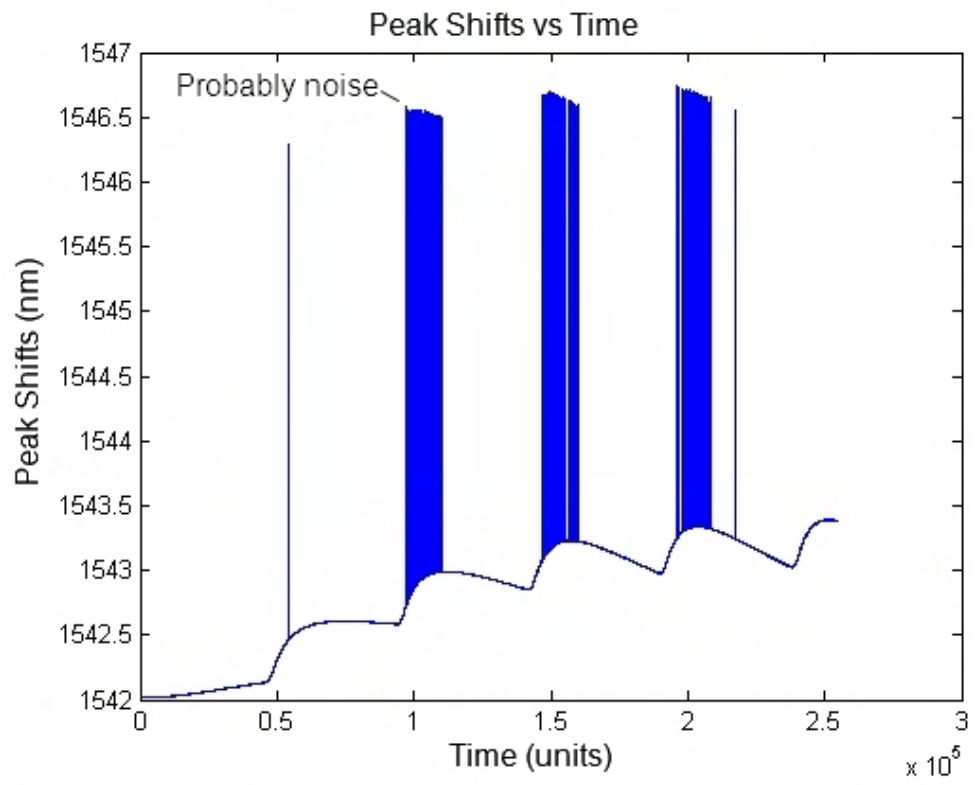

Figure 5.10: SBP output; snap-shot two

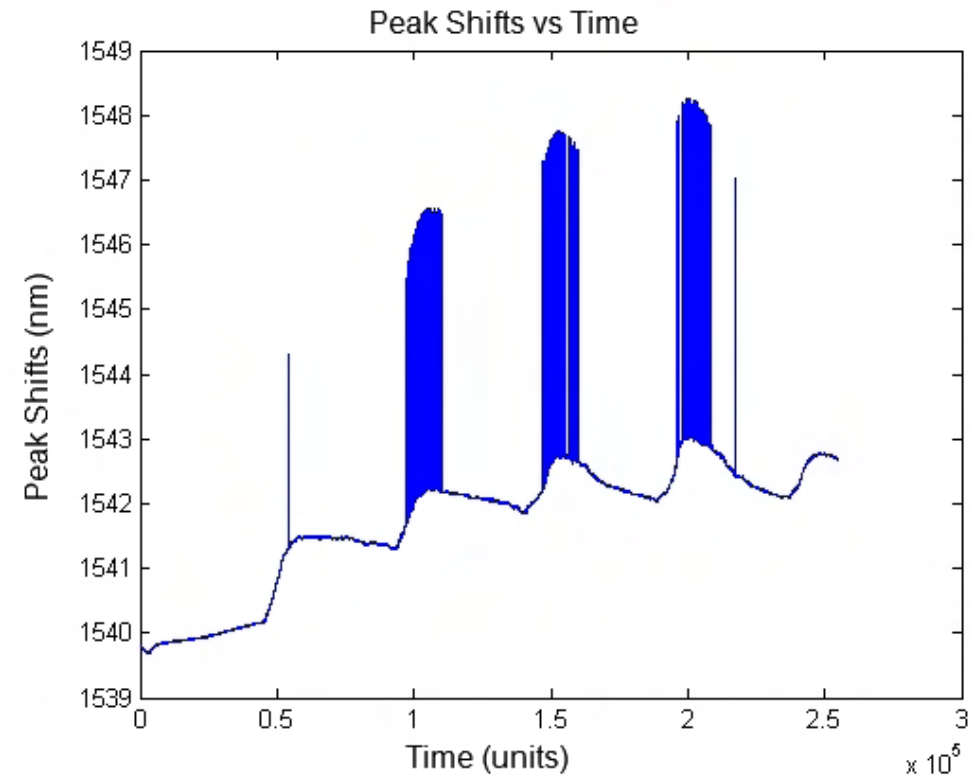

Figure 5.11: SBP output; snap-shot three

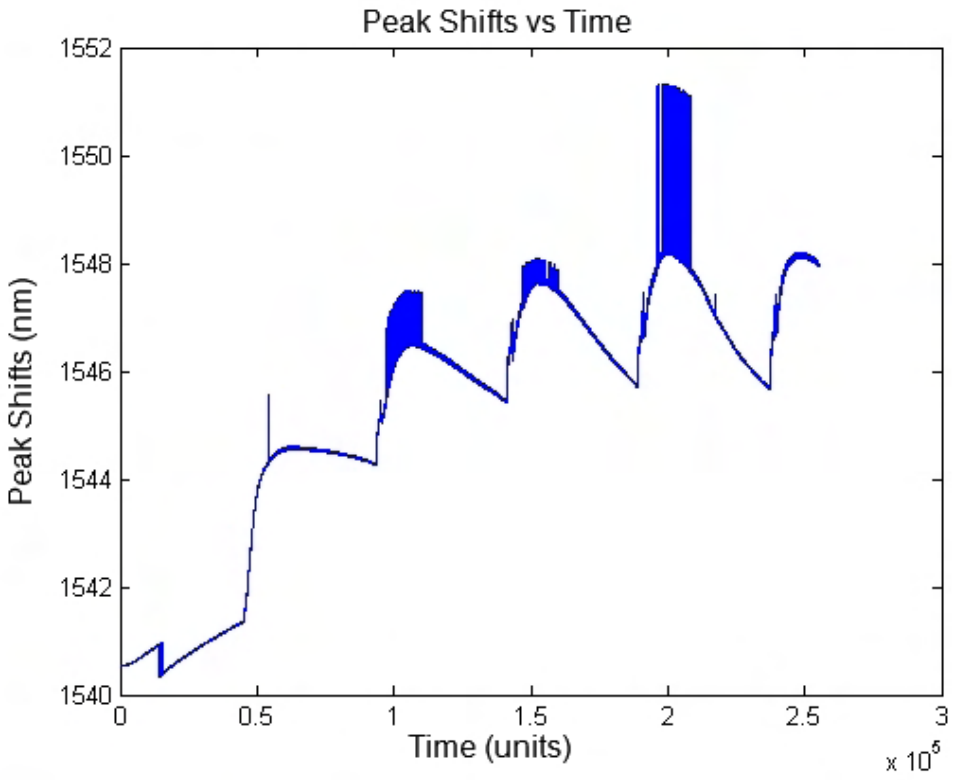

Figure 5.12: SBP output; snap-shot four

5.3.7 Discussion and Conclusion

- Smart Brake Pad Brake Dynamometer Test -

The objectives of these test were to:

- Trial a simplified SBP in a simulated driving condition in a brake dyne
- To answer the first research question
- To learn what we can from the trial in order to improve the parameters for future trials

Overall the tests were a great success. We successfully examined two SBPs simultaneously under simulated driving conditions; during a shudder stop. However, only *snap-shots* of the data could be presented (please see Figures 5.9−5.12) due to a DAQS failure in the MOIS. In Figures 5.9−5.12 it appears that the brakes are juddering, nevertheless, it would be impossible to tell from a snap shot what this means with regards to DTV generation in brakes. Yet, these snap shots are enough, they prove it is possible to measure the surface pressure between the brake pad and disc dynamically; thereby answering our first research question, a great achievement.

In conclusion,

- Successfully tested a set of SBPs in a brake dyne and obtained results
- Answered our first research question
- Propose the following improvements for future tests:

- More tests using modified MOIS software
- A greater number of SPs and different types of brake pad materials would need to be tested in order to get to the root cause(s) of DTV

5.4 Discussion and Conclusion

- Application of Smart Brake Pad -

Chapter 5 completes a major accomplishment in team work, tenacity and creativity towards the objective of finding the root causes of DTV that is the successful trial of a SBP.

In the first part we successfully conducted the tests and received the necessary data to allow us to calibrate two SBPs, nevertheless due to the magnitude of success of the following dyne tests we chose not to calibrate the two SBPs but rather show highlights from either tests. From the highlights of experiment three of the calibration, we concluded that both SBPs work well enough in order to satisfy the requirements for calibration, though they both suffered from differing amounts of hysteresis which was expected.

As a result of the dynamometer tests we were able to gauge the effectiveness of the MOIS to obtain data from SPs embedded into the SBP. In addition, we were able to successfully answer the first research question for the research program, that is: "Is it possible to measure contact pressure between brake pad and disc dynamically?" We concluded that it is now possible.

In future post-research program tests we hope to answer the remainder of the research questions, namely:

- How does the brake contact pressures effect DTV development in motor vehicle brakes?
- How do the experimental results compare to the analytical computer modeling of the brake pad and disc system?
- What measures are needed to minimize or eliminate DTV generation in motor vehicles disc brakes?

Though we were unable to answer these questions experimentally within this research program, they will be further discussed in Chapter 6.

Chapter 6

Discussions, Conclusions, Recommendations and Directions for Future Work

- Thesis -

6.1 Discussions and Conclusions

The focus of this research program has been to experimentally investigate the causes of DTV in motor vehicle brakes through the theoretical and experimental development of a new tool called a *Smart Brake Pad*.

The successful development and validation of the Smart Brake Pad is a great feat in engineering research, collaboration and of the human spirit that was achieved through an extensive research and systematic development over several years. Which consisted of bringing together intellectual, financial and philanthropic resources towards building and testing this device in simulated driving conditions.

The Smart Brake Pad is a tool that will enable engineers to better understand the processes which occur between the brake pad and disc whilst braking. It is also a tool that will enable engineers to better understand the causes of DTV and stick-slip the initiators of low and high frequency vibration in motor vehicle brakes.

The Smart Brake Pad can equally be used to solve many other still remaining riddles in automotive, aerospace, rail or anywhere where two surfaces may come in contact.

To drive the Smart Brake Pad, we initially designed, developed and tested a thick film sensor array in a special purpose environmentally friendly *sandwich design* Smart Brake Pad. We tested the device at room and at elevated temperature. To better understand the operation of the sensor we developed a mathematical model to describe its function. The mathematical model we developed is called a, *General Thick Film Differential Equation for Voltage Output (G-TF-DE-V)*. It was successfully tested against data obtained at room temperature.

Though, the thick film sensors were tested successfully to 195^o C they became non-linear and non-symmetrical between loading and unloading cycles making it difficult to fit the mathematical model to the data. They also have high drift making dynamic measurement hard to interpret.

As a result of this, in parallel we developed two new fibre Bragg grating smart probes; one with a solid resin coating and the other with a teflon coating. The

probes were temporarily inserted into the friction material by drilling holes into the friction material parallel to the rubbing surface of the brake pad and disc ready for testing. The teflon probe was held in place with a silicon glue. Both smart probes were rigorously tested at room and elevated temperatures up to 200^o C. The teflon coated smart probe out performed the resin coated smart probe. The teflon coated probe has a good solid well defined character, and virtually no drift making them ideal for automatic interrogation systems using in dynamic testing. This probe was further developed and used in the final smart brake pad used in simulated driving conditions. In addition, a Finite Element Analysis model was created for the smart probe whilst embedded into a smart brake pad demonstrating stress resulting from the action of a applied load on the fibre Bragg grating smart probe.

The teflon smart probes can also be used in other applications where load needs to be measured at room and elevated temperatures in confined spaces. Since fibre optics sensors were used, the teflon smart probes can be applied to such diverse applications as measuring loads on bridge pylons, the recoil of artillery pieces or in Smart Brake Pads

Nevertheless, to improve the performance of thick film sensors at temperature, different materials need to be investigated to insulate the sensors from heat; a number have been suggested within the thesis. To reduce the mechanical hysteresis in either sensor technology it is suggested that the sensors be placed as near as possible to the rubbing surface between the friction material and disc.

Using a S-Laser Doppler Vibrometer we were able to confirm the relationship between wheel speed and judder frequency. We were also able to obtain some valuable information about the testing environment. Furthermore, we were able to gain an insight into the shape of the pressure distribution via a Animated Operational Deflection Shape.

Though the concentration of this research program has been the development of the Smart Brake Pad and allied sensor technologies it has become clear that there is no singular scenario that produces DTV. Rather, there are a number of different scenarios that can produce DTV which are vehicle dependent. The two main scenarios to produce DTV are:

(a) Off brake wear (Off-BW)

(b) Vibration Induced Wear (VIW)

In Chapter 2 we discussed Off-BW. Here we introduce a new term called Vibration Induced Wear. If a brake disc was spinning about its axis and the friction material is thought of as a sanding block on either side of the disc. If the calliper was applied and released at a frequency of 18 Hz then you would produce DTV. The judder resulting from this DTV would also be at 18 Hz. This theory we could call Vibration Induced Wear and the law which describes it as Vibration Induced Wear Law (VIWL).

It is known from previous studies mentioned in Chapter 2 that some suspension systems may go into a state of resonance around this frequency. It is assumed in these studies that the brake system is the initiator of this vibration. However, a body may resonate if acted upon by an unbalanced force which produces a vibration that is equal to that of the natural frequency of the body. In some motor vehicles, such a force could be produced by the car hitting a bump in the road.

So, either Off-BW or VIW could produce DTV in motor vehicle brakes; though this is not conclusive without further tests using the Smart Brake Pad that we have developed in this research program.

In conclusion,

- A revolutionary tool called a Smart Brake Pad was developed and validated that will enable engineers to better understand the causes of DTV and stick-slip the initiators of low and high frequency vibration in motor vehicle brakes
- Thick film and fibre optic smart probes were successfully developed and tested at room and elevated temperatures. The teflon coated smart probes were used in the validation of the Smart Brake Pad in simulated driving conditions using a brake dynamometer
- The teflon smart probes can be applied to such diverse applications such as measuring loads on bridge pylons, the recoil of artillery pieces or in Smart Brake Pads
- A new mathematical model was developed for the thick film sensor and plotted against experimental data. A novel Finite Element Analysis model was developed for the fibre optic sensor
- A scanning laser doppler vibrometer was successfully used to understand the test environment better and confirm the link between wheel speed and judder frequency an important linkage in the understanding of DTV. It also was able to give us insight into the possible shape of a pressure distribution that may be present between brake pad and disc
- A new scenario and accompanying law was introduced to explain DTV development in motor vehicle brakes

6.2 Recommendations and Directions for Future Work

The recommendations follow three main avenues:

(a) Investigate DTV further by using Smart Brake Pad diagnostic technology

(b) As DTV is not a safety issue, then reduce or isolate the occupant from the its effects

(c) Use other braking systems

Descriptions of these follow:

(a) Investigate DTV further by using Smart Brake Pad diagnostic technology
It is recommended that the improved Smart Brake Pad and *Micron Optics Interrogation Systems* is transformed into Smart Brake Pad diagnostic technology by:

- Incorporating a secure web updatable database of all known brake problems collected throughout the world
- Add to this database by gathering data using the Smart Brake Pad and Micron Optics Technology via a series of tests, using different materials, driving styles etc
- Creating a software program called, *Smart Brake Pad Diagnostics* that would use logic and neural networks to link brake problems either typed in at the command line by a technician as a set of presented problems from a given vehicle or measured using Smart Brake Pads attached to a vehicle

The final product could then be sold to vehicle manufacturers world-wide under the name of *Smart Brake Pad diagnostic technology* and the database could be leased as it would be continually growing as new information arrived via brake technicians in the field.

(b) DTV is not a safety issue It is known that occupants have become more aware of noise and vibration related problems as a result of improved cabin design. It is also known that DTV is often *felt rather than heard*, in this case insulate or isolate the steering mechanism and or brake pedal so that the occupant is unaware of there being a vibration problem. This reduction in awareness would not pose any danger to an occupant i.e. if the vibration is caused by something else apart from DTV then the affect would certainly be noticed by the reduction in performance of the vehicle during stopping and this reduction could be monitored.

(c) Use other braking systems The simplest alternative to a traditional braking system is to use a floating disc of cast iron. A floating disc may consist of a two piece brake disc consisting of a disc and the hat (please see Figure 6.1). The hat would be isolated from the disc via a two by four gasket system. The four gasket system, would consist of two outer gaskets fabricated from teflon and two inner gaskets moulded from *bellows shaped* rubber. The teflon gaskets are used to reduce heat transfer from the disc to the hat and friction. Whilst the bellows shaped rubber gaskets will absorb vibration and allow the discs to float horizontally. The assembly would be held in place by shoulder bolts. The self aligning properties of the floating disc system would reduce the possibility of DTV generation by *vibration induced wear* or *off brake wear*.

A completely different method would be to use an electromagnetic braking system being composed of alternating coils. The main advantage of this system is that it could also generate electricity whilst the brakes are not in use.

Which ever option is chosen, the sensor system developed in this research program is a universal tool that is not limited to DTV analysis. It can also be utilised to investigate many different phenomena and brake designs to achieve the optimal result for the comfort of the motorist.

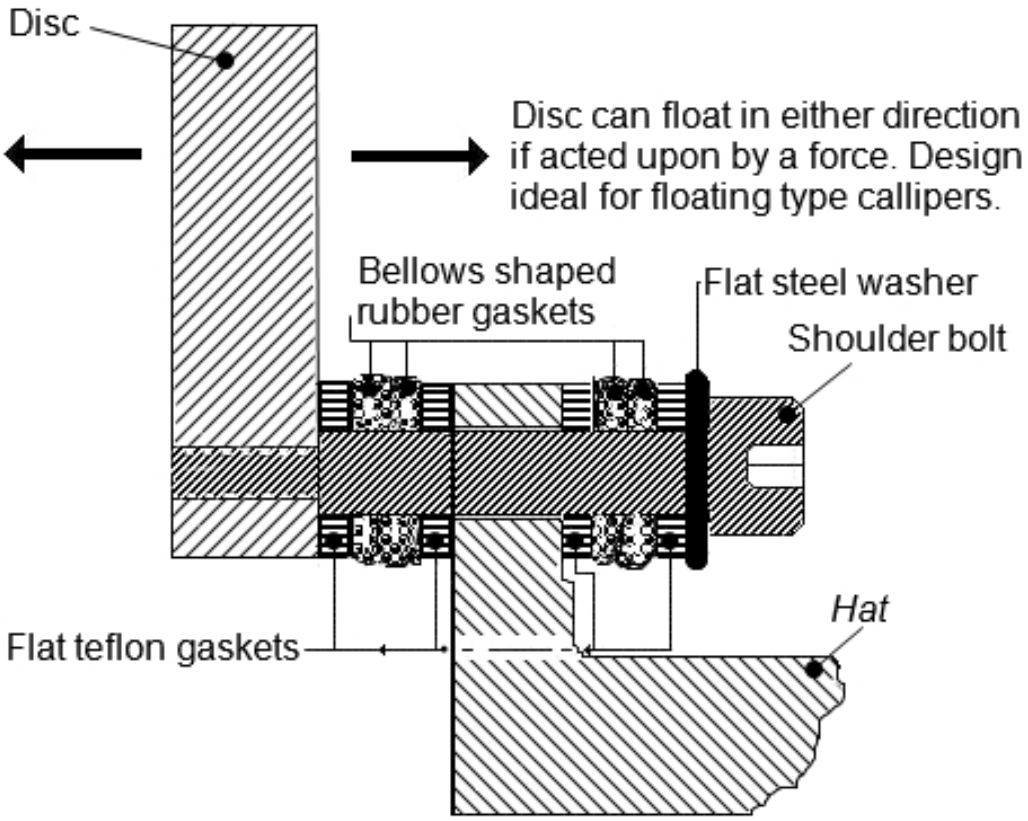

Figure 6.1: Floating disc

Appendix A

A brief Introduction to Analytical Techniques

There are two main approaches to finding a solution to engineering problems using analytical techniques, they are, either: classical or numerical analysis (please see Figure A.1).

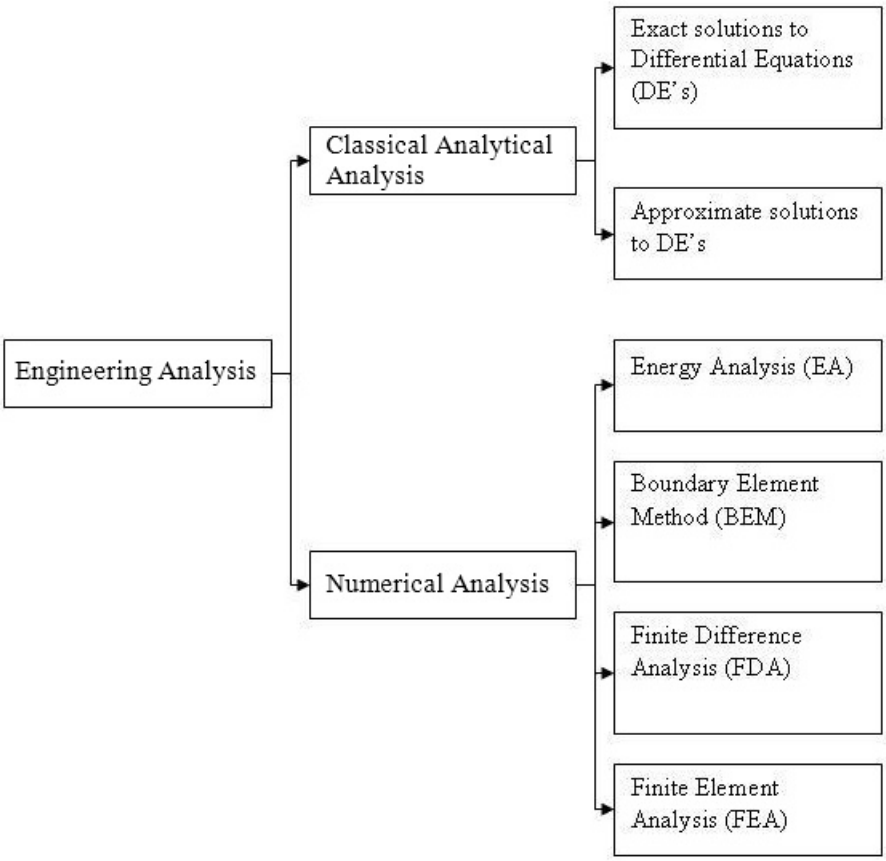

Figure A.1: Analysis techniques in Engineering [60]

A brief description of the techniques follows:

Classical Analytical Analysis

- Only simple problems can be solved using exact or approximate analytical techniques.

Numerical Analysis

- In EA problems, an expression in terms of potential energy is found and minimised. This technique is only useful for simple problems (limited number of Degrees of Freedom (DoF)).

- In Boundary Element Modelling (BEM) problems, a Partial Differential Equation (PDE) which governs the domain (boundary and volume) is reformulated by using another equation which is mathematically equivalent but represents the boundary alone; thus drastically simplifying the computational resources needed to solve the problem. However, the method is only suitable for particular problems. It is particularly useful in solving Computational Fluid Dynamics (CFD), acoustical and electromagnetic type problems [61].

- In Finite Difference Analysis (FDA) problems, differential equations with boundary conditions are found then replaced with the equivalent finite difference equations. The method is limited as it cannot represent irregularly shaped structures or complicated boundary conditions [60].

- In FEA problems, there are two different approaches Force and Displacement methods. "In both methods, equilibrium, compatibility, and stress-strain relationships are used to generate a system of equations that represent the behaviour of a structure [60], p. $2-4$."

Of these techniques, FEA has become the most popular numerical analysis technique due to its ability to be generally applied across a broad range of problems.

Since the 1960s, Numerical Analysis has gained popularity since the invention of the computer. The methods can be implemented by direct coding, with computer languages such as:

- FORTRAN (developed circa 1950)
- C (developed circa 1970)
- ADA (developed circa 1983)
- C++ (developed circa 1985)
- PYTHON (developed circa 1990)
- JAVA (developed circa 1994)

Of these FORTRAN is still widely used in the numerical analysis community. Though many researchers now use Scientific Computing Environments (SCE) that include special toolboxes and libraries geared towards the solution of particular mathematical problems; the most common of these are:

- MatLab (developed circa 1970 - via Mathworks in 1984)
- Mathematica (developed circa 1986)

In these SCEs the solution to simple equations can be done at the command line whilst more complex problems can be solved with the SCEs' built-in computer language.

Apart from writing your own code whether it be using a computer language or SCE there are many packages available today that specialise in a particular Numerical Analysis method. Of these, the following are the most suitable commercial FEA packages for engineering analysis:

Development of Mesh *(Mesher)*

- MSC Patran
- Hypermesh

Analysis of Model *(Solver)*

- MSC Nastran
- MSC Dytran
- ABAQUS
- ANSYS
- ADINA

There is also a number of free open-source FEA styled packages available for download on the internet.

Appendix B

Data Acquisition Terms and Plotting Errors

This is a list of common data acquisition terms and plotting errors that users of various sensors ought to be familiar with. The first four will be briefly discussed here aided by several figures; the last two are discussed in Chapter 3.

- Null or voltage Offset
- Null Temperature Shift
- Sensitivity Temperature Shift
- Linearity Error
- Drift Error
- Hysteresis Error

Null or Voltage Offset

The *null or voltage offset* is the amount to which the zero point is offset on a calibration curve (please refer to Figure B.1).

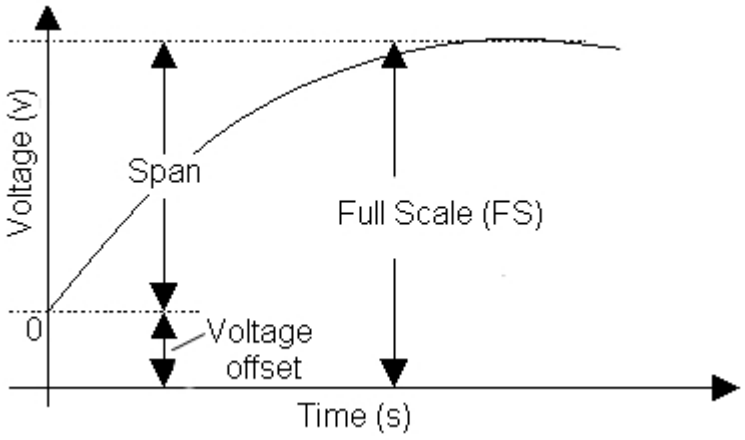

Figure B.1: Null or voltage offset

Null Temperature Shift

The *null temperature shift* is the amount by which the zero point of a calibration curve is influenced by temperature (please refer to Figure B.2).

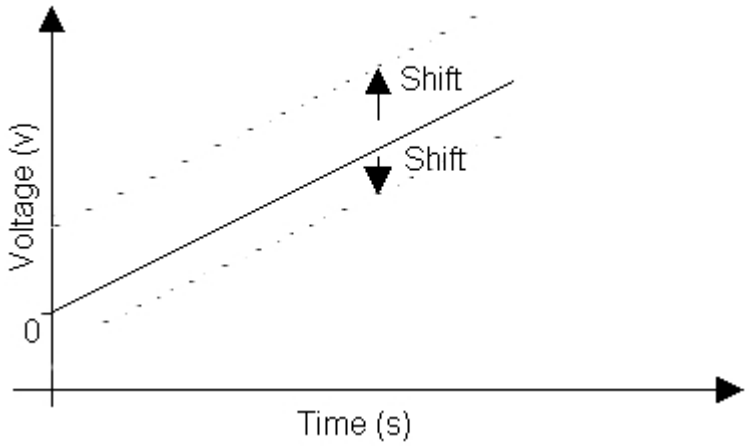

Figure B.2: Null temperature shift

Sensitivity Temperature Shift

The *sensitivity temperature shift* is the shift in a calibration curve due to the influence of temperature on the sensor (please refer to Figure B.3).

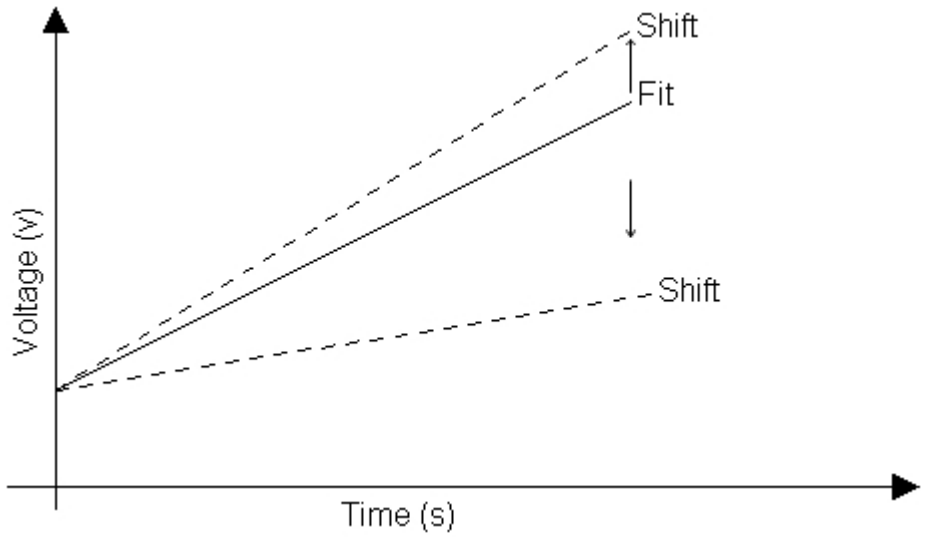

Figure B.3: Sensitivity temperature shift

Linearity Error

Linearity error is only an error if we expect a linear output. Descriptively, it is the deviation from a, Line of Best Fit (LoBF), which passes through a set of data

points (please see Figure B.4). Linearity ℓ is expressed mathematically in Equation 1; Linearity is most often expressed as a percentage.

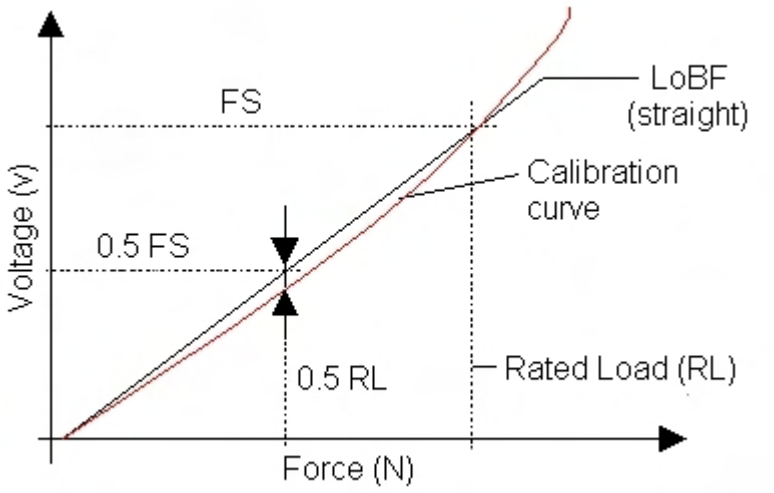

Figure B.4: Linearity

$$\ell = \frac{0.5FS - 0.5RL}{RL} \tag{1}$$

Linearity error can also be found using the commonly known R^2 *value* statistic via Equation 2. Linearity is also most often expressed as a percentage.

$$\ell = 1 - R^2 \tag{2}$$

Appendix C

Techniques to Manufacture Thin and Thick Films

The differentiation between thick and thin films comes down to the thicknesses of the deposited films and the methods used to manufacture them, this should not be confused with the substrate material which is also often referred to as a TF, which it is, but in this discussion, when we say, *thick film* we are discussing the deposited material not the substrate material. Thick films are silk-screen printed or some similar type of ink deposition, whereas thin films are generally made by a process of sputtering, or one of the methods of chemical vapour deposition. With respect to thickness of the films, a film is considered thick if it is above 5.00 μm and thin if it is below this thickness [62, 63]. A quick review of thick film[1] processes follow.

Screen Printing

The screen printing process has been around for thousands of years. It was first developed in China where a silk screen was used to print bold colours onto fabrics. Today, the use of screen printing is very diverse, from the clothing industry, art to thick film sensor development. What ever the application, the basic components are the same, it is just the degree of sophistication that differs.

The basic components of a silk screen printing set-up are (please refer to Figure C.1):

- Substrate
- Screen Printing Mechanism

Substrate

The substrate is the base material on which an organic or inorganic process takes place. In this case, the substrate can be a piece of polymer film, such as Kapton or Mylar, where inks are deposited.

Screen Printing Mechanism

The screen printing mechanism consists of three basic parts:

[1] Since these are the ones that are most useful to us

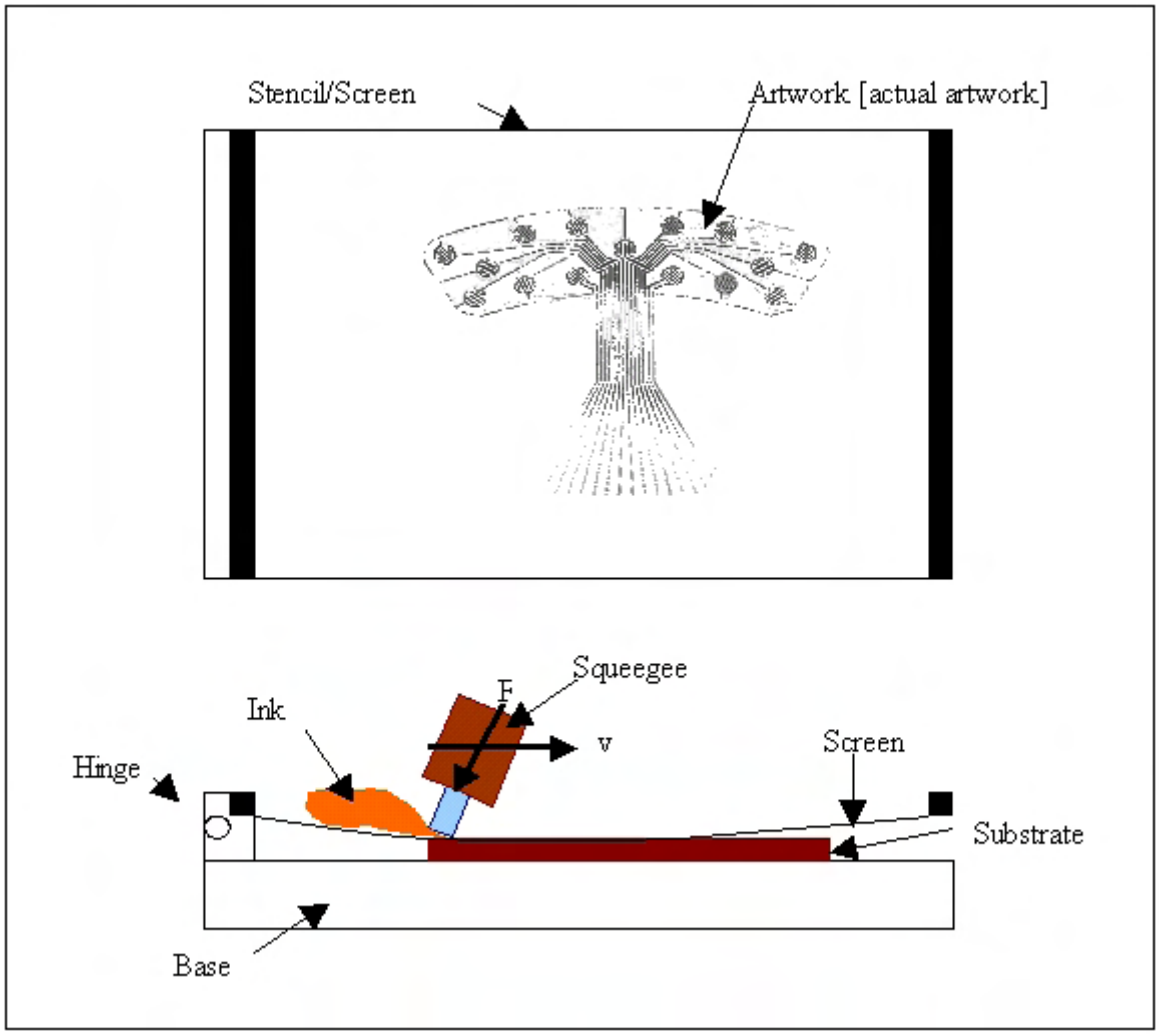

Figure C.1: The screen printing process

(a) **Machine Base**
The machine base is where the substrate is attached in preparation for the screen printing

(b) **Stencil**
The stencil[1] is a frame which has a fine mesh net stretched over it. The stencil is hinged at one end and lowered over the substrate. The screen is often photosensitive which allows a picture or photoplot of the required image[2] to be transferred to the screen. Gaps in the mesh (The darkened areas in Figure C.1) are left open to allow ink to flow through them; this is how the image is created

(c) **Squeegee**
The squeegee in its most basic form is a piece of wood with a rubber blade running across the edge of it. When producing an image, ink is fed across the top edge of the screen and applied to the mesh by sweeping the blade from the hinged point to the bottom of the frame; this has three functions:

i. To deflect the stencil
ii. To bring the stencil in to contact with the substrate
iii. To drive the ink over the mesh to produce an image onto the substrate

If a different ink or colour needs to be used, the screen needs to be washed and the process needs to be repeated.

The screen printing process is often adapted to produce circuits on a Printed Circuit Board (PCB) or polymer films since it is relatively inexpensive and the equipment is readily available. The inks used are different from traditional inks as they contain not pigment but finely ground metals such as copper or silver which are dispersed into a liquid; this liquid can be thought of as the *ink* in the traditional screen printing process.

A typical process to reproduce a circuit using the screen printing technique [3] follow:

(a) Sketch or obtain the schematic or circuit diagram of the required tracks, electrodes (sensing cells) and pads needed for the particular application

(b) Design using a computer drawing package such as AutoCAD the exact circuit diagram with track widths and pad diameters; this will be referred to as the *artwork*

(c) Convert the AutoCAD file[4] to a Gerber file[5]

(d) Print out a photoplot to check circuit

(e) Create a stencil by exposing the photosensitive mesh to light in the areas that require ink to pass through; create the mesh

(f) Place the substrate onto the base of the screen printing machine

[1] Often called a *screen or mesh*
[2] Artwork
[3] Depending on the requirements of the circuit and equipment available
[4] Artwork
[5] NC code

(g) Screen print artwork directly onto the substrate (Kapton) sheet with required inks (such as copper)

(h) Fire substrate in a furnace or specially developed device first to dry the ink, then to sinter the particles within the liquid to produce a solid film of copper or other material (being careful not to fire above the substrates operating temperature)

(i) Apply additional sheets of the substrate material, coatings or other to protect the film from damage

Lithography

General Lithography

Lithography, hence the Latin word, *litho*, involves placing an image on to a surface with an oil based medium; acid is then used to *burn* the oil into the surface, leaving an image etched into the substrate. When printing the surface is kept submerged in water[1], thus the image to be printed also repels water. A roller with an oily based ink is then rolled over the surface leaving ink attached to the oily image and clean everywhere else. Then when this surface is brought into contact with a substrate the image is transferred onto this surface; however, it transfers both the image and the water to the substrate, thus a producing a wet substrate. To avoid a wet substrate a *dummy substrate*[2] with a rubber surface is pressed against the wet image transferring the image to that surface and at the same time removing the water, it is this image that is transferred to the substrate for the purposes of printing, leaving a clean accurate image with minimum moisture.

Photo Lithography

Photolithography was developed for the manufacture of microchips; it is also used for the manufacture of Micro Electro Mechanical Systems (MEMS), which thick and thin films can be considered a part of; if you consider the thickness of the films, they are measured in microns. Many different substrate materials are used, though, silicon lithography, is considered the most advanced.

The procedure usually involves some combination of etching, chemical deposition and chemical treatments in repeated steps on an initially flat substrate. A typical procedure would be as follows:

(a) Sketch or obtain the schematic or circuit diagram of the required tracks, electrodes (sensing cells) and pads needed for the particular application.

(b) Design using a computer drawing package such as AutoCAD the exact circuit diagram with track widths and pad diameters

(c) Print out a photoplot of the artwork

(d) Determine your substrate material, such as silicon

[1] As oil repels water
[2] An Offset Roller as in Offset- Lithography

(e) Deposit a layer of conductive metal several nanometres thick on the substrate

(f) Deposit a layer of *photo resist*[1] on top of the conductive metal layer

(g) Use the photoplot to create a *mask*[2]

(h) Place the mask in a machine called a *stepper* which allows light to shine through certain exposed areas of the mask on to the substrate; this selectively hardens the places which are touched by light. The image produced via a stepper is either the same size as the Artwork or slightly smaller

(i) Place the substrate into an etching solution to remove the areas which were not hardened. Then remove it

(j) Place the substrate into another etching solution which finishes the process and which leaves you with the metal with the same pattern on it as the mask or photoplot. The photoplot is often the negative, black and white image of your CAD schematic; so the clear areas are the tracks and dark areas will be removed via chemical etching

(k) Sintering[3] may follow this

Other Techniques

A relatively new technique used in manufacturing for quick development of three dimensional models using Computer Aided Manufacturing (CAM) techniques is *rapid prototyping* this method is finding its way into microelectronics as a fast way to produce circuits. There are two basic techniques:

(a) **Subtractive**
In this technique you would start out with a solid block of material and use a Computer Numerical Controlled (CNC) machine to physically mill out the block to reveal the shape hidden within its surface, rather like, *a sculptor hacking away at a block of marble*. This method is not used for sensor development as yet.

(b) **Additive**
Uses a special three dimensional printer which applies layers of plastic or other material on to a substrate to successively build up layers of cross-sections to produce a three dimensional model. It is this method that can be used in sensor development.

[1] A chemical that hardens when exposed to light
[2] Which is usually made of metal
[3] A process similar to baking a cake in the oven

Appendix D

The History of Light

Fibre optics relies on the fundamental principals of light developed over the centuries since Before Christ (BC). The Greeks were responsible for many early developments in pure and natural philosophy. One of them, Democritus ($460-370$ BC) suggested that: "light travels as a particle from the source of light [64], p. 195."; the suns' rays for example, which was fairly close to the truth as we now consider it. Later Aristotle ($384-322$ BC) said that, "light is a property of the medium between the source of light and the eye [64], p. 195"; this also has some merit when considering the refractive index of light in various mediums, but it does not explain the nature of light itself. Forty years following Euclid the father of geometry suggesting that, "light travels from the eye to the object [64], p. 195"; this is true to some extent if considering the reflection of light from an object, but the eye is definitely not the source of that light; rather the receiver of reflected light; otherwise we could see in the dark! The great renaissance artist, engineer and philosopher Leonardo da Vinci ($1452-1519$) noted that "light could be reflected like sound waves [64], p. 195" this is an important contribution to our early understanding of light as it hints towards the wave properties of light.

What follows from these early discoveries, is a contest between the greatest minds to get to the truth behind light[1]. The two camps were the, *particle people* and the *wave people*. The particle people, Rene Descartes ($1596-1650$) and Isaac Newton ($1642-1727$); suggested that light consisted of high speed particles (corpuscles) this could explain, straight line propagation, reflection, refraction and dispersion of light. Whereas the wave people Grimaldi ($1618-1663$), Hooke ($1635-1702$) and later Christian Huygens (1629 - 1695) suggested that light travels as waves; the wave theory could explain why a shadow of a circular disk does not have a sharp well defined outline when projected against a flat surface; whereas the particle model could not. Wave people were later followed by Thomas Young ($1773-1829$) who added further proof of the wave properties of light with his famous *double slit* experiment. He was able to explain the presence of dark and light bands that were produced as a result of shining a light through a double slit mask onto a glass screen by using Huygens's principle and the principle of superposition. Augustine Fresnel ($1788-1827$) repeated some of these experiments and improved on young's work by developing a microscope with a higher accuracy for viewing the interference pattern (dark and light bands) and developed a mathematical theory to explain interference, diffraction, polarization and double refraction of light [64].

Simeon-Denis Poisson[2] (1781 - 1840) added further weight towards the wave prop-

[1] If only they realized that light was not an *either or* situation but rather *and* one

[2] Better known by Engineers for his work in mechanics

erties of light by using Fresnel's theory and predicting that a bright spot ought to appear in the centre of the shadow coinciding with the maxima of the intensity profile of the shadow - the spot is knows as *Poisson spot*. Finally, in 1862 Foucault[1] using a rotating mirror and light passing through a long tube of water was able to show that the velocity of light in air was greater than light in water; this was confirmation of the wave properties of light [21, 64, 65].

The next greatest leap for our understanding of light came from the progression of knowledge from Lord Kelvin[2] and more readily acknowledged Michael Faraday $(1791 - 1867)$ discovered electromagnetic induction and found "that a changing magnetic field gives rise to a changing electric filed [64], p. 199." He also found that "the plane of polarization of light can be rotated in a magnetic field [64], p. 199." These discoveries suggested a link between light and magnetism. In 1872 James Clerk Maxwell published his Electromagnetic theory. In this mathematical model, light is a form of electromagnetic radiation which is produced by oscillating charges and their associated electric fields which travel at right angles to each other. The waves travel at the speed of light. In 1886 Heinrich Hertz conducted an experiment which confirmed Maxwell's theory by using a simple oscillating charge emitter and a loop of wire with a gap between the two ends as the detector; a spark produced at the emitter was transmitted to the receiver which induced a voltage in the loop of wire creating a spark across the gap of the receiver; this is illustrates how EM waves are used to transmit and receive radio, TV and radar signals. Hertz was able to show EM waves traveled at the speed of light (confirming Maxwell's theory), can be reflected, refracted, polarized and can interfere with each other [64].

In 1900 Max Planck $(1858-1947)$ whilst studying the radiation of hot bodies noticed that radiation left these bodies in packets of energy; this was the birth of Quantum mechanics [3]. The energy of each pulse or photon is proportional to the frequency of the photon, where h is Planck's constant and f is the frequency of the photon:

$$\Delta E = hf \tag{3}$$

Using Einstein's theory of special relativity[4]:

$$\Delta E = mc^2 \tag{4}$$

and noting that the Quanta have wave properties,

$$\nu = f\lambda \tag{5}$$

and the Newton's linear momentum of a particle[5] is given by,

$$p = m\nu \tag{6}$$

we arrive at the momentum of a photon being a combination of wave and particle properties giving[6],

[1] Also known for his contributions to our understanding of relative motion in mechanics
[2] Inventor of the strain gauge
[3] Quanta Latin for 'packet' (pre- 1900 is considered classical physics)
[4] Developed for overcoming the difficulties of optics in motion [65]
[5] Which is still valid when dealing with photons
[6] Noting that the velocity ν of a photon is equal to the speed of light c

$$\overrightarrow{p} = \frac{h}{\lambda} \tag{7}$$

Equation gives us completion to say that both the wave *and* particle people were right.

Visible light is just one small section of what is called the *Electromagnetic Spectrum*; see the middle of Figure 6.2 for visible light. The wavelength of light that optical communications and fibre optics sensor technology commonly occupies is between 1300 nm and 1550 nm, which is not specifically indicated on this drawing but it is the visible light side of infrared; hence Near-Infrared[1].

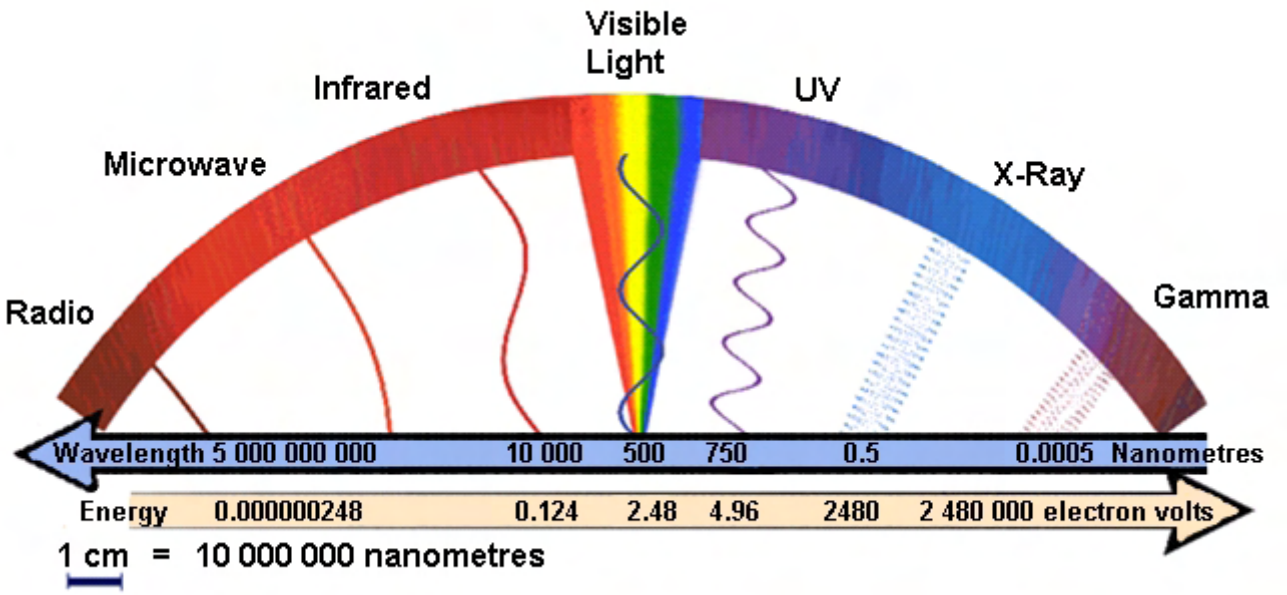

Figure D.1: The electromagnetic spectrum

Claude Chappe in 1790 invented the *optical telegraph* with manned operators using semaphores[2] on telegraph poles enabling them to send messages to each other. In the 1840s, Swiss physicist Daniel Collodon and French physicist Jacques Babinet showed that light could be guided along jets of water for fountain displays. Fourteen years later in 1854 John Tyndall[3] the well known scientist, educator to the masses and supporter of Darwinism demonstrated a similar feet in front of the Royal Society by showing that light could be guided by a curved jet of water coming out of a hole in a tank [22]. Alexander Graham Bell in 1880 developed the *photophone* a device for transmitting voice through the air via light; later abandoned in favour of copper cables. In 1888 William Wheeler developed an innovative lighting system that worked by channeling light produced by an electric lamp in the basement of a house down highly reflective tubes to different areas around home. In 1895 French Engineer Henry Saint-Rene used a series of bent glass rods in an attempt to produce the first television[4]. Using a similar technique, 1898 American David

[1] NIR 700 to 5000 nm

[2] Alphabetic code sent via flags or optical signals still sometimes used in boating for communicating between ships

[3] He is also known as one of founders of the *Greenhouse Effect* [22]

[4] Transmission of images

Smith applied for a patent on a surgical lamp. In the 1920s, John Logie Baird in England and Clarence W. Hansell in the United States patented the idea of using arrays of hollow pipes or transparent rods to transmit images for television or facsimile systems. Following this, German Heinrich Lamm, in an effort to view the inaccessible recesses of the human body, used bundles of unclad optical fibres, to transmit the image of a light bulb. The image produced by the apparatus was poor due to the unclad fibres [66, 67].

Please note: This section was written as revision material and a further background to our study of fibre optic sensors in Chapter 3.

Appendix E

An Introduction to Fibre Optics

It was not until six years after WWII, in 1951 that A. C. S. Van Heel, Harold Hopkins and Narinder Kapany independently introduced a light carrying flexible fibre which they called a *flexible fibre-scope* for use in practical instruments .

The main uses for fibre optics are in: medical instruments, telecommunications and more recently, in fibre F-P and FBG sensors.

There are typically two types of fibre (please refer to Figure E.1):

- Single mode
- Multimode

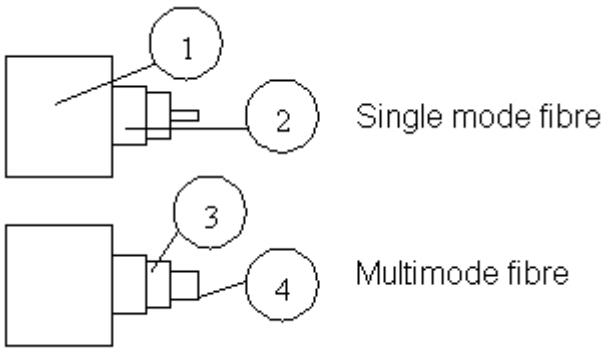

Figure E.1: Single and multimode fibres

Referring to Figure E.1, the numbered items are as follows:

(a) Protective jacket

(b) Protective coating

(c) Cladding

(d) The core

The descriptions of these and the types of fibres follow.

Protective jacket Plastic or rubber coating that protects the fibre during handling.

Protective coating Protects the fibre from mechanical and or heat stress.

Cladding Typically, made of silica glass or doped silica glass. Helps keep a beam of light within the core via the process of Total Internal Reflection (TIR)[1].

The core Normally, made of silica glass like the cladding, except the refractive index n of the glass, must be such so that the velocity of light traveling in the core, is less than that in cladding, so that the light stays within the core, and follows Snell's law.

Single mode fibre Have a smaller diameter core and only allows a single *beam of light at a particular phase*[2] through it at one time.

Multimode fibre Have a larger diameter core and allows multiple beams of light through it at different phases. These types of fibres are normally used in telecommunications.

The way light is guided by an optical fibre[3] is found by following the principle of TIR. Please refer to Figure E.2 and Snells law, Equation 8 which follows.

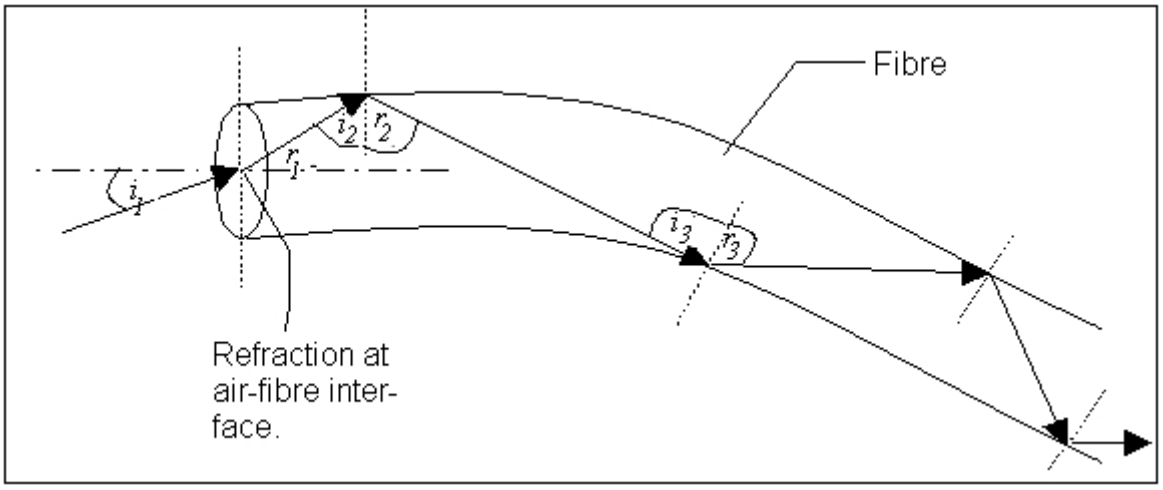

Figure E.2: The operation of an optical fibre via the laws of *total internal reflection*

$$n = \frac{\sin(i)}{\sin(r)} = \frac{\nu_1}{\nu_2} = \frac{\lambda_1}{\lambda_2} \tag{8}$$

Where:

n	the refractive index
i	the angle of incidence
r	the angle of refraction
ν_1	the velocity of waves in the first medium
ν_2	the velocity of waves in the second medium
λ_1	the wavelength in the first medium
λ_2	the wavelength in the second medium

[1] To be discussed shortly
[2] Mode
[3] Also known as: *waveguide*

If we now look at Figure E.2, which demonstrates Snell's law at a boundary. In the figure, three incident beams b_1, b_2 and b_3 enter the fibre, at three different incident angles, i_1, i_2 and i_3. Each of these incident beams represent three different cases, these cases follow (please refer to Equation 8):

(a) **Case 1: Refraction**
If i_1 is less than what is termed the critical angle i_c, then b_{11} will be refracted, at angle r_1.

(b) **Case 2: Refraction at the Boundary**
If i_2 is equal i_c, then b_{22} will follow the boundary, at angle r_2.

(c) **Case 3: TIR**
If i_3 is greater than i_c, then b_{33} will be TIR, at angle r_3.

To calculate the critical angle i_c, we set the reflected angle r to 90^o in Equation 8, and ignore the last term; which gives us Equation 9.

$$\sin i_c = n \tag{9}$$

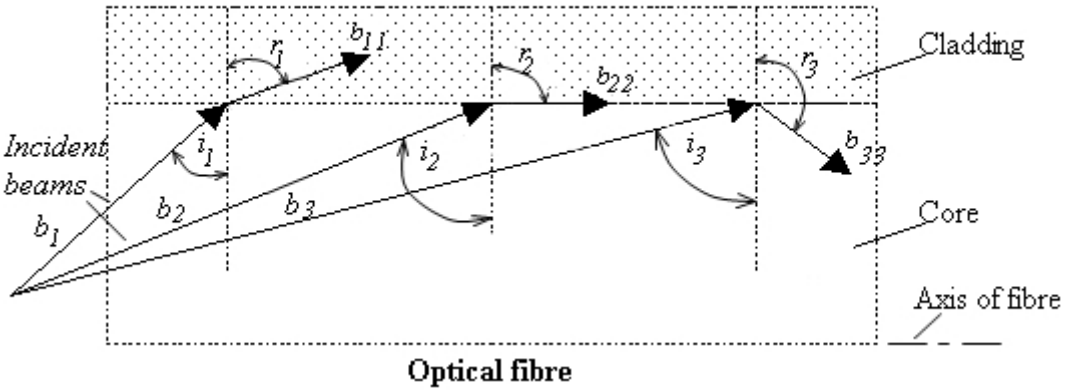

Figure E.3: Snells law at a boundary

Appendix F

Smart Brake Pad Thick Film Cell Structure Dimensions

The approximate dimensions and descriptions of the numbered components represented in Figure 3.31 are listed here:

(a) 4.7 mm

(b) 2 mm

(c) 2.2 mm

(d) 0.77 mm

(e) 3.8 mm

(f) 4.3 mm

(g) 2 mm

(h) Copper screen printed and fired finger(s)/electrode configuration

(i) 1.9 mm

(j) 5.3 mm diameter

(k) 6.35 mm diameter

(l) Kapton film

(m) Kapton film

(n) Kapton film

(o) 8 mm diameter

(p) 6.35 mm diameter

(q) Screen printed section of the Kapton film. The ink for the screen printed section is most probably a polymer dispersed with conductive particles (resistive polymer)

Appendix G

Thick Film Smart Brake Pad Room Temperature Tests - Model Parameters

Cells	A	B	Beta_1	Beta_2
Cell 1	-5.10137	6.72605	5.00E-6	5.00E+0
Cell 2	-5.5834	4.62581	5.00E-6	5.00E+0
Cell 3	-5.08E+0	3.33E+0	5.00E-6	5.00E+0
Cell 5	-5.00E+0	4.41E+0	5.00E-6	5.00E+0
Cell 6	-5.00E+0	5.00E+0	6.36E-3	3.38E+1
Cell 7	7.50E+0	-4.67E+0	2.66E+1	-7.61E-3
Cell 9	-5.00E+0	5.00E+0	1.07E-2	9.40E+0
Cell 11	6.15E+0	-5.13E+0	9.92E+0	3.77E-2
Cell 13	6.01E+0	-4.78E+0	1.37E+1	-8.50E-2
Cell 14	-5.19E+0	5.63E+0	5.00E-6	5.00E+0
Average	-7.01E-1	1.10E+0	5.03E+0	6.82E+0
Median	-5.00E+0	3.87E+0	3.18E-3	5.00E+0

beta_T_b_avg =	2.69E+8
beta_T_c_avg =	7.79E+8
beta_T_b_med =	1.14E+8
beta_T_c_med =	3.62E+5

Above, the missing cells are faulty. Below, the missing cells and outliers have been removed.

Cells	A	B	Beta_1	Beta_2
Cell 1	-5.10137	6.72605	5.00E-6	5.00E+0
Cell 2	-5.5834	4.62581	5.00E-6	5.00E+0
Cell 3	-5.08E+0	3.33E+0	5.00E-6	5.00E+0
Cell 5	-5.00E+0	4.41E+0	5.00E-6	5.00E+0
Cell 11	6.15E+0	-5.13E+0	9.92E+0	3.77E-2
Cell 14	-5.19E+0	5.63E+0	5.00E-6	5.00E+0
Average	-2.28E+0	2.06E+0	1.65E+0	4.17E+0
Median	-5.04E+0	3.87E+0	5.00E-6	5.00E+0

beta_T_b_avg =	1.32E+8
beta_T_c_avg =	1.57E+8
beta_T_b_med =	1.14E+8
beta_T_c_med =	5.68E+2

Figure G.1: SBP2 model parameters

Appendix H

Resin Probe Manufacturing Process

The resin probe manufacturing process is relatively simple.

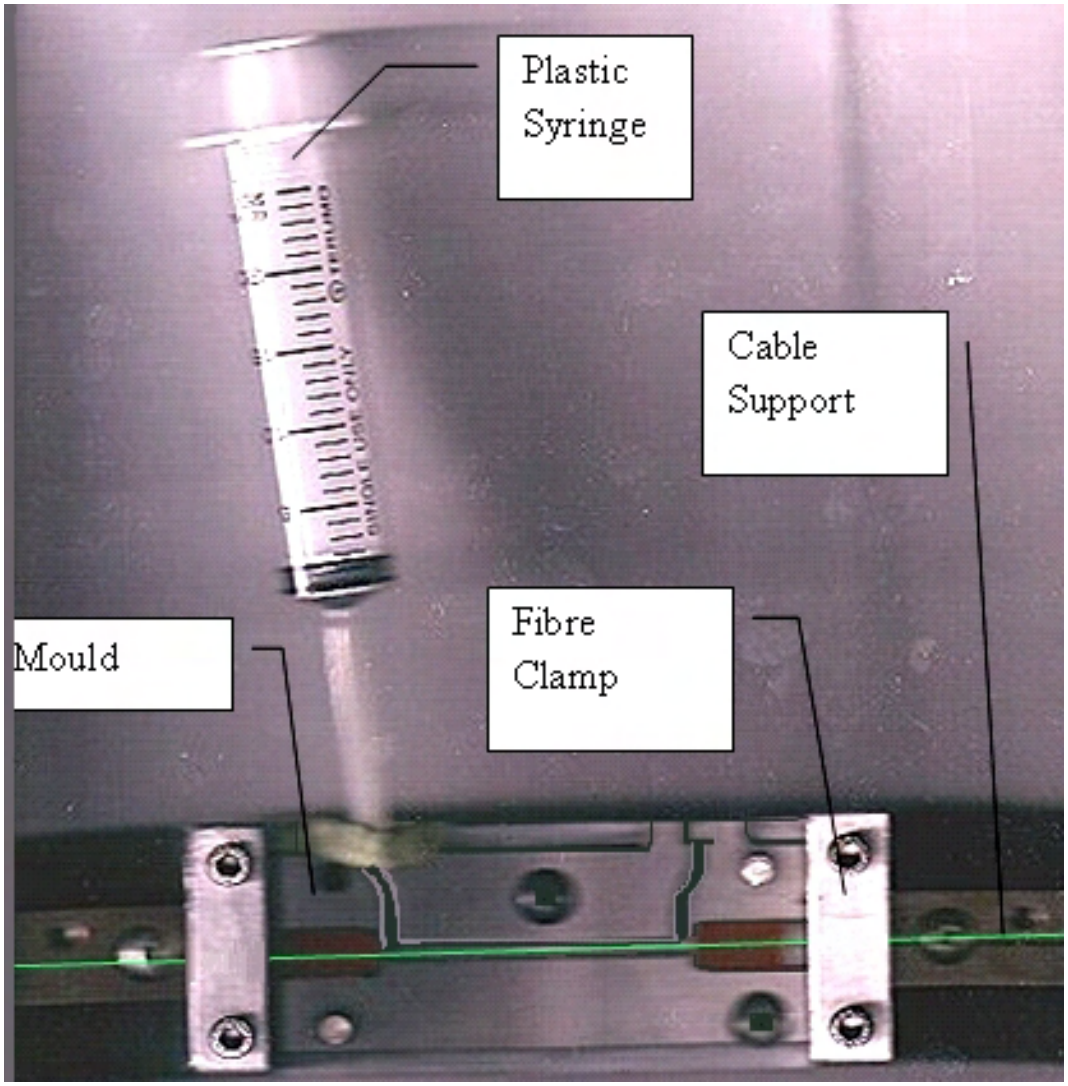

Figure H.1: Assembly of BLUERR smart probe moulding system; top platen missing

The steps to mould a BLUERR smart probe are as follows:

(a) First the mould shown in Figure H.1 was thoroughly cleaned with a cleaning solution

(b) A coating of *mould release* was then applied to prevent the moulded part from sticking to the mould when the moulding process was complete

(c) Place both halves of the open mould into an oven[1] to dry the mould release as per instruction, after this is done a second coat may be applied

(d) When the mould is ready, lay the bottom half of the mould on a table. Carefully, take pre-prepare gratings and place it on the mould between supports making sure fibre is centrally located. Clamp one side then the other with the fibre clamps - make sure a slight tension is applied

(e) Place top platen on mould watching carefully when closing mould that the fibre stays central and clamp with a sash or G-clamp

(f) Under a fume hood mix 2.5 % of Methyl Ethyl Ketone Peroxide (MekP) the (hardener) with the Resin Derakane 470−300 a Epoxy Vinyl Ester Resin (Resin)

(g) With the inlet and outlet of the mould vertical and the Syringe in place fill the syringe by removing the plunger. There should be *no need*[2] to use the plunger, though you can replace it in and apply slight pressure; it is good practice to have a short piece of clear tubing in the Outlet to observe any bubbles in the stream of the outlet; keep putting resin in until it is virtually clear. Figure H.2 displays the upper platen of mould with a piece of fibre in place for demonstration purposes; it also shows the direction of resin flow in the mould

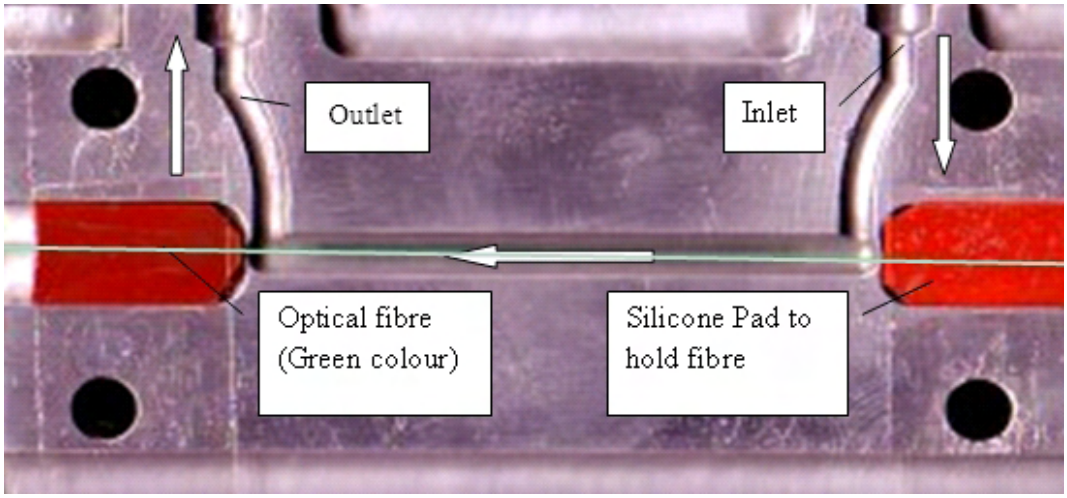

Figure H.2: BLUERR smart probe mould *top platen*

(h) The resin can dry in RT and does not require baking for cure; nevertheless, bake for one hour at 200^o C to ensure resin is completely cured and to enhance easy removal of probe. Ensure parts that are not in the mould are adequately protected from the heat

[1] One not used for eating
[2] Relying on gravity feed

(i) Using thick industrial oven gloves remove the mould and carefully place on a bench for hot objects. With care, release the clamp and separate the mould using large flat ended screwdrivers as leavers

(j) See Figure H.3 for a *dummy* probe that was manufactured using this process

Figure H.3: Dummy probe

Notice in Figure H.3 the row of bubbles along the edge of the probe this was caused by too vigorous a stirring of the resin (with hardener) prior to injection into the mould. Ideally, a vacuum set-up would be attached to the outlet of the mould to ensure fewer air bubbles were present, however such a system was not available in our lab. We were relatively happy with finished moulded probe the only concession was that the cross-section of the probe was not round but *egg shaped*[1] however this was the best the technicians were able to achieve. The probe in the figure looks slightly bent this is only an optical illusion.

Once any problems with coatings[2] were solved, we completed a trial assembly of *dummy* sensors to ensure all components fitted into the calliper and to ensure the bends were not too sharp for the optical fibre to pass light through without substantial losses (please refer to Figures H.4−H.7).

[1] 4.25 mm in one direction and 3.95 mm in the other
[2] SP materials

Trial Assembly of Smart Brake Pads

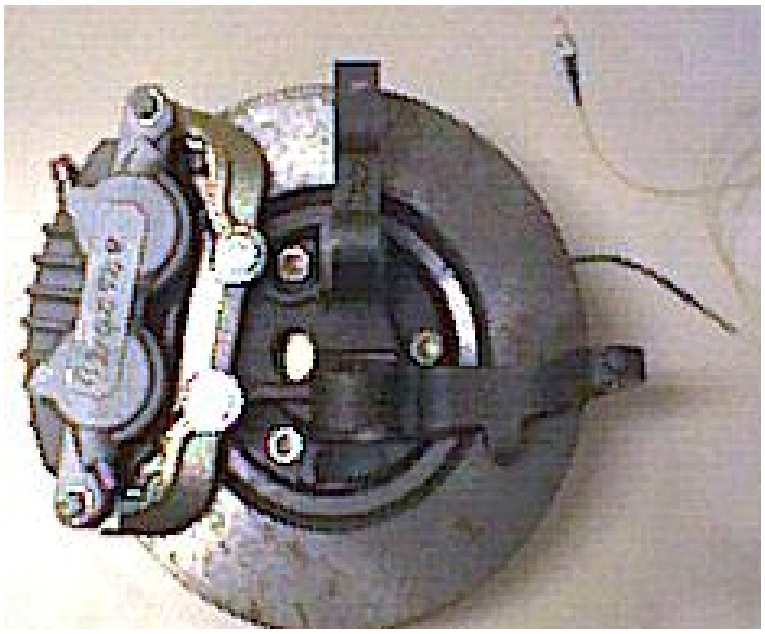

Figure H.4: Inboard side of front wheel disc brake showing fibre optic lead

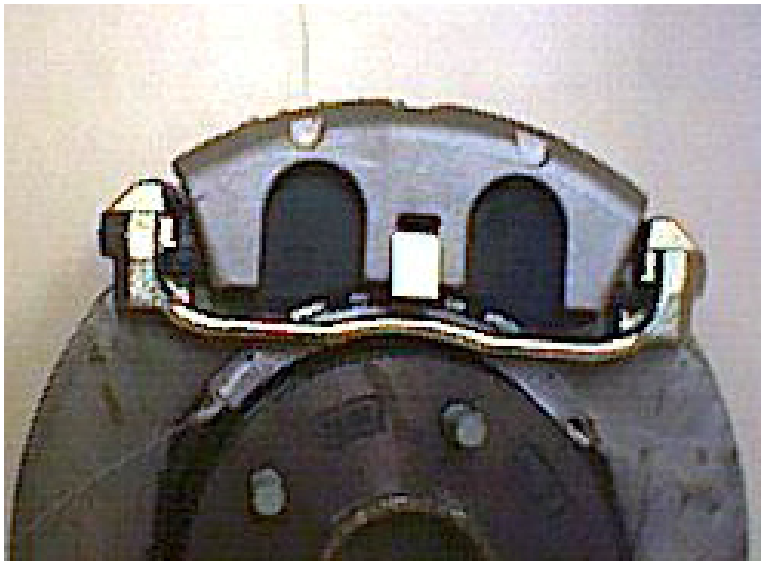

Figure H.5: Fibre optic support bracket assembled into brake calliper

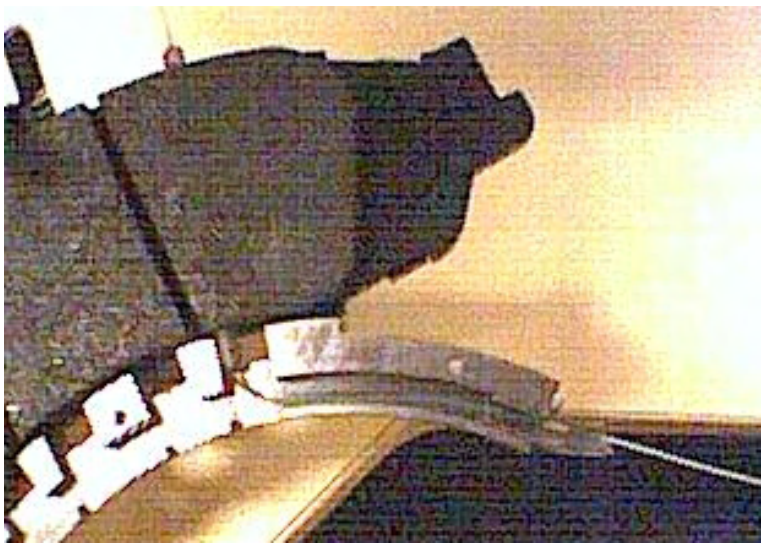

Figure H.6: Fibre optical cable support bracket installed with dummy smart probe

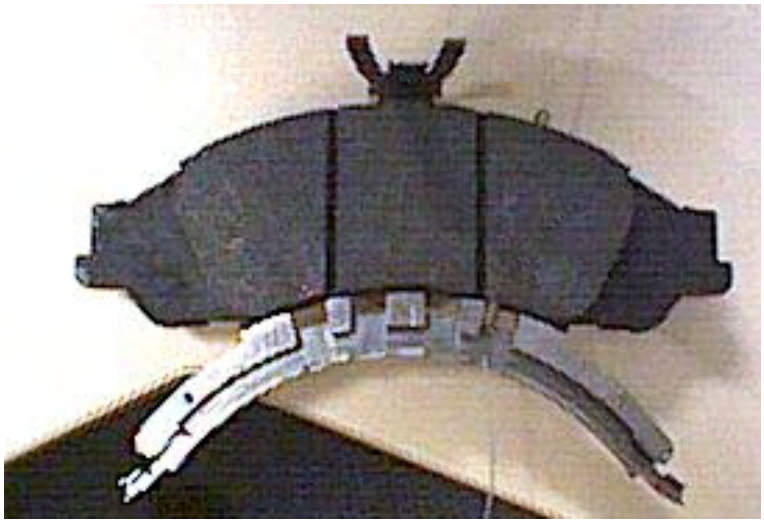

Figure H.7: Smart probe with fibre optic cable going relatively straight out of pad

Appendix I

Methods for replacing the Buffer Coating once Stripped

As mentioned previously optical fibres typically come with coatings and buffer protection. When creating sensors these commercially applied coatings are stripped back and removed by mechanical[1] or chemicals to dissolve the coating; often the chemical approach is quite messy, but has the advantage over the mechanical method since it does not score or damage the surface of the optical fibre which can often happen with mechanical strippers; this can lead to easier breakage of the fibre or reflective disturbances. Cheap mechanical strippers or fibres should be avoided; the strippers don't strip properly and the cheap fibre is protected with poor quality stiff plastic buffer which is difficult to remove, in addition the fibre itself is full of flaws and can have bubbles (air pockets) or voids like those found in cut diamonds within the fibre causing light loss and poor sensor performance; because of this these fibres are also difficult to join.

One great problem we and others' have come across is how to replace the stripped back coatings once the gratings have been written onto fibres because without the buffer coating as depicted in Figure I.1 the fibre is easily scratched or damaged during handling.

In order to overcome this challenge, we tried to re-create a tight buffer by using a simple die and some commercially available synthetic rubber coating called *Plasti-Dip* this product was quite difficult to obtain since it produces poisonous vapours[2]. Figure I.2 is a drawing of a die coating a fibre. The result of applying coating using this method, was initially a tapered coating since during overnight drying the coating sagged ever so slightly. To overcome this successive coating were applied in the opposite direction until the desired thickness was achieved. The resulting coating has high friction when rubbed against surfaces which is not desirable[3]. Though overall these coating do improve the handling properties of the fibre. Another method we found shortly after this, was to use Teflon tubing to create a lose buffer, we used this method in the end[4], rather than the Plasti-Dip method.

Nevertheless, the die method as illustrated in Figure I.2 and or slightly automated, which is quite similar in principle to what is used in industry to coat fibres and wires, could be used to re-coat both the polyimide coating and the buffer coating on top so it has quite a lot of promise to fill the void in non-commercially available coating methods.

[1] Special optical fibre stripper similar to a very precise copper cable stripper to remove the rubber or vinyl coating on copper wires

[2] Cartridge type mask must be used

[3] As it sticks to itself and other things

[4] This is commonly used as we found out later

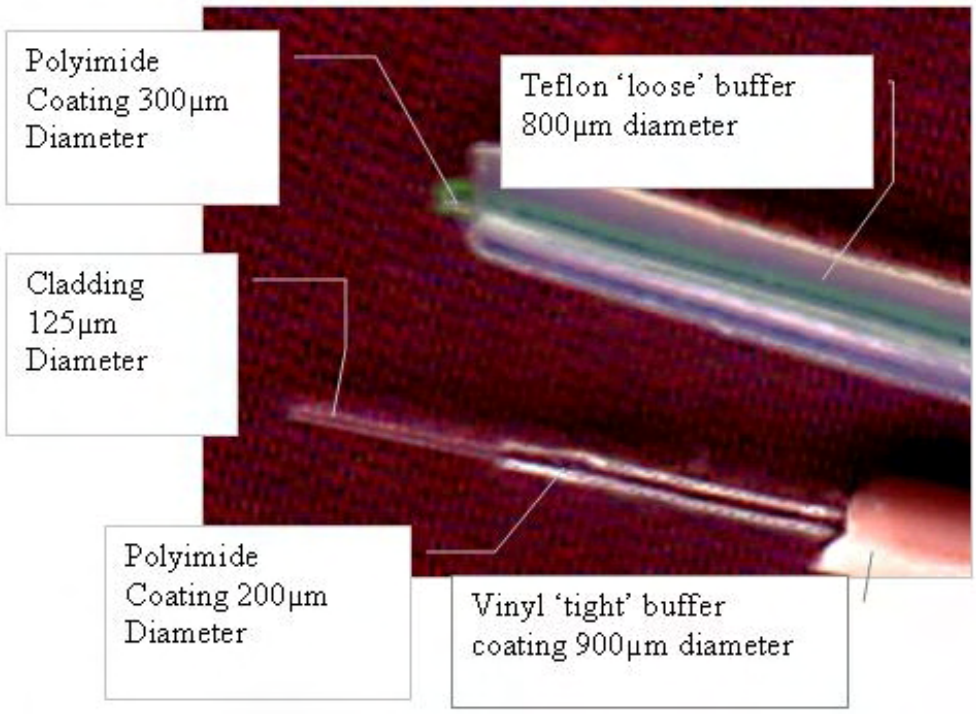

Figure I.1: Different optical fibres and their coatings

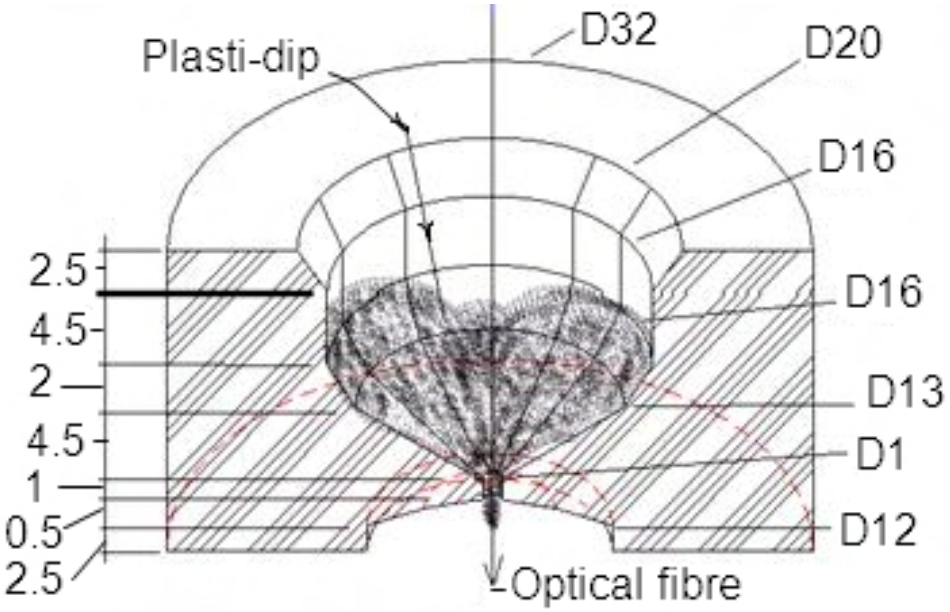

Figure I.2: Die for coating fibres

Appendix J

Rounding Errors in Computations

Rounding errors are caused by *cutting* what may seem an excessive number of decimal places at each stage of a computation. For example:

If, $a = 1.1234567891$ and $b = 1.99999999999$. First, without rounding, we add these numbers together, and we get,

$$\begin{aligned} c_1 &= a + b \\ &= 1.1234567891 + 1.99999999999 \\ &= 3.1234567891 \end{aligned} \tag{10}$$

We now round the result to one decimal places,

$$c_2 = 3.1$$

If we now perform a calculation using c_2 instead of c_1 we would be introducing an error; this error would be a *rounding error*.

References

[1] Abdelahamid, M. K., *Brake judder analysis: Case studies*, SAE, Technical Paper Series, no. 972027, 1997. iii, 1

[2] de Vries, A. et al., *The brake judder phenomenon*, SAE Technical Paper Series, no. 920554, 1992. 12, 20, 21

[3] Engel, G., H. et al., *System approach to brake judder*, SAE Technical Paper Series, no. 945041, 1994. 1, 9, 21

[4] Gassmann, S. et al., *Excitation and transfer mechanism of brake judder*, SAE Technical Paper Series, no. 931880, 1993. 13

[5] Jacobsson, H., *High speed disc brake judder – the influence of passing through critical speed*, In EuroMech – 2nd European Nonlinear Ocillation Conference, Prague, no. 2, pp. 75–78, 1996. 22

[6] Jacobsson, H., *Wheel suspension related disc brake judder*, ASME, no. DETC97/VIB-4165, pp. 1–10, 1997. 2, 21

[7] Jacobsson, H., *Frequency Sweep Approach to Brake Judder*, Licentiate of engineering, Chalmers University of Technology Sweden, 1998. ix, 9, 10, 22

[8] Jacobsson, H. SAE Technical Paper Series, no. 1999-01-1779, pp. 1–14, 1999. 2, 23

[9] Stringham, W. et al., *Brake roughness – disc brake torque variartion, rotor distortion and vehicle response*, SAE Technical Paper Series, no. 930803, 1993. iii, 1, 13, 23

[10] Lee, C., Alex et al., *Application of digital signal processing in diagnosis of noise problems during braking*, Automotive Engineering, Warrendale, Pennsylvania, v. 105, no. 9, pp. 5–8, 1997. ix, 2, 8, 22, 23, 44

[11] Barber, R., J., *Thermoelastic instabilities in the sliding of conforming solids*, Philosophical Transactions of the Royal Society A: Mathematical, Physical and Engineering Sciences, v. 312, pp. 381–394, 1969. ix, 13, 14, 15

[12] Lee, K. et al., *Frictonally excited thermoelastic instability in automotive disk brakes*, ASME, v. 115, no. October, pp. 607–614, 1993. ix, 15, 16

[13] Thoms, E., *Disc brakes for heavy vehicles*, IMechE, pp. 133–137, 1988. ix, 1, 15, 16, 19, 20

[14] Anderson, E., A. et al., *Hot spotting in automotive friction systems*, Wear, v. 135, pp. 319–337, 1990. ix, xv, 1, 17, 18

[15] Lee, K. et al., *Effect of intermittent contact on the thermoelastic instability of automotive disk brake systems*, ASME, v. 198, pp. 27–32, 1995. ix, 17, 19

[16] Fletcher, R., *Force transduction materials for human–technology*, IBM Systems Journal, v. 35, no. 3-4, pp. 630–639, 1996. ix, 26, 27

[17] Klafter, D., Richard et al., *Robotic engineering: An integrated approach*. Prentice–Hall, Englewoods Cliffs, NJ, 1989. x, 46, 48, 50, 51

[18] Yaniger, I., Dr. Stuart, *Force Sensing Resistors^{tm}: A Review of the Technology*, Interlink Electronics Inc., pp. 666–668, 1993. x, 49, 51, 52, 114

[19] Nave, R. Hyperphysics, 2000. x, 53, 57

[20] Grattan, T. V., K. et al., *Fiber optic sensor technology: an overview*, Sensors and Actuators A: Physical, v. 82, no. 1-3, pp. 40–61, 2000. x, 54, 56, 58, 60

[21] Mc Climent, R., Edward, *Physics*. Harcourt Brace Jovanovich Inc., 1984. x, 54, 55, 214

[22] Tyndall-Centre, *Who was John Tyndall?*, tyndall.ac.uk, 2006. x, 55, 215

[23] Fellay, A., *Physics of brillouin scattering*, metwww.epfl.ch, 1998. Alexandre.Fellay@epfl.ch, 1998. x, 55, 56

[24] PCB-Piezotronics-Inc., *General piezoelectric theory*, pcb.com, 2003. xv, 44, 45

[25] Barber, R., J. et al., *Implications of thermoelastic instabilities for the design of brakes*, Jnl. Tribology., v. 107, pp. 206–210, 1985. 1, 15

[26] Inoue, H., *Analysis of brake judder caused by thermal deformation of brake disc rotors*, SAE Technical Paper Series, no. 865131, 1986. 1, 20

[27] Lee, C. E. et al., *Interferometric optical fiber sensors using internal mirrors*, Electonic Letters, 1988. 1, 56

[28] Rhee, K., S. et al., *Friction–induced noise and vibration of disc brakes*, Wear, v. 133, pp. 39–45, 1989. 1, 20

[29] Kim, M.-G. et al., *Sensitivity analysis of chassis system to improve shimmy and brake judder vibration on the steering wheel*, SAE Technical Paper Series, no. 960734, 1996. 1, 21

[30] Subic, A., *No more noisy brakes*, Email: Aleksander Subic (RMIT University) – Alex Rodriguez (RMIT University), no. 21-04-05, 2005. 2

[31] Aviles, H. R. et al., *Low frequency vibration in disc brakes at high car speed. Part I experimental approach*, International Journal of Vehicle Design, v. 16, no. 6, pp. 542–555, 1995. 10

[32] Lee, K. et al., *Conditions of frictional contact in disk brakes and their effects on brake judder*, SAE Special publications, v. 1339, no. February, pp. 165–175, 1998. 12, 19, 22, 23

[33] Cole, S., *DTV Theories*, Letter Steve Cole – Alex Rodriguez (RMIT University), 1999. 12, 13

[34] Lee, K. et al., *An experimental investigation of frictonally–excited thermoelastic instability in automotive disk brakes under a drag brake application*, Journal of Tribology, v. 116, no. July, pp. 409–414, 1994. 15

[35] Abendroth, H., *A new approach to brake testing.*, SAE Technical Paper Series, no. 850080, 1985. New in vehicle data aquisition unit was described Thermal imaging via optronic measurement procedures was discussed. 19

[36] Loh, W. et al., *The application of experimental design method to brake induced vehicle vibrations*, SAE Technical Paper Series, no. 980902, pp. 133–139, 1998. 21

[37] Balakin, A., V. et al., *Dynamic processes in engagement of clutches and brakes*, Jnl. Friction and Wear, 1996. 22

[38] Metzler, H., *The brake rotor – friction partner of the brake linings*, SAE Technical Paper Series, 1990., no. 900847. 22

[39] SGL-Technologies, *High performance automotive brakes*, sglcarbon.com, 2000-2005. 22

[40] Gibbons, P., *Porsche: Installing carbon ceramic brakes (pccb) on a 911 c4s*, europeancarweb.com, 2004. 22

[41] Hohmann, C. et al., *Contact analysis for drum brakes and disk brakes using adina*, International Journal Computers & Structures, v. 72, no. 1-3, pp. 185–198, 1999. 23

[42] Holden-Ltd Meeting Chassis Group, Holden Ltd – Alexander J. Rodriguez, Port Melbourne, Australia, 1999. 23, 33

[43] Suzuki, T. et al., *Analysis of disk brake squeal*, SAE Technical Paper Series Paper, no. 971038, pp. 89–93, 1997. 23

[44] NIST/SEMATECH, *NIST/SEMATECH e–Handbook of Statistical Methods*, itl.nist.gov, 2003-2006. 35, 76

[45] Stroud, A., K., *Engineering Mathematics*. Macmillan, Hong Kong, 1994. 38, 69

[46] of Belgrade, U., *Lord Kelvin (William Thompson)*, phy.bg.ac.yu. 43

[47] Piezo-Systems-Inc., *History of piezoelectricity*, piezo.com, 1993-2002. 44

[48] Stadler, W., *Analytical Robotics and Mechatronics*. McGraw–Hill Book Co., Singapore, 1995. 48

[49] Culshaw, B., *Fibre optic sensor: Integration with micromachined devices*, Sensors and Actuators A: Physical, v. 47, no. 1-3, pp. 463–469, 1995. 56, 60

[50] Dakin, P., J. et al., *Distributed optical fibre raman temperature sensor using a semiconductor light source and detector*, Electonic Letters, v. 21, p. 569, 1985. 56

[51] Parker, R., T. et al., *Simoultaneous distributed measurement of strain and temperature from noise-initiated brillouin scattering in optical fibres*, IEEE Journal of Quantum Electronics, v. 34, p. 645, 1998. 56

[52] Kim, S.-H. et al., *A study on the development of transmission-type extrinsic fabry-perot interferometric optical fiber sensor*, Journal of Lightwave Technology, v. 17, no. 10, pp. 1869–1875, 1999. 56

[53] Fiberdynamics, *Technical Background of an FFPI Sensor*, Fiberdynamics.com, 2003. 56

[54] Davis, C., *Introduction to fibre bragg gratings and their applications in sensing*, Defence Science and Technology Organisation, 2003. 58

[55] Simpson, O., J. et al., *Innovative materials for aircraft morphing*, In SPIE'S 5th Annual International Symposium on Smart Structures and Materials, San Diego CA USA, 1998. 59

[56] Yamate, T. et al., *Thermally insensitive pressure measurements up to 300º C using fiber bragg gratings written into side hole single mode fiber*, BLUERR, 2000. 59

[57] BLUERR, *Blue Road Research publications*, bluerr.com, 1985-2001. 60

[58] MicronOptics, *Sensing – field proven solutions for optical sensing*, micronoptics.com, 2003. 60

[59] Dellis, L., J., *Fit experimental data is easy*, MathWorks File Exchange, 2004. 88

[60] MSC, *Basic MSC/NASTRAN Linear Static and Normal Modes Analysis Seminar Notes*, MacNeal Schwendler Corporation (MSC), Los Angeles, no. June, 1998. 199, 200

[61] Kirkup, S., *Bemlap: BEM for laplace problems*, boundary-element-method.com, 2004. 200

[62] Vechembre, J. et al., *Screen printed pzt thick films for sensor and actuators*, Ecole Polytechique Federale de Lausanne, 1996. 207

[63] Wheeler, D., *Prescon^{tm} thick film sensors*, International Microelectronics Research Corporation, 2002-2006. 207

[64] Christian, D. et al., *Studymate HSC Physics – Electives.* M^{c} Graw Hill Book Company Australia, 1991. 213, 214

[65] Dugas, R., *A History of Mechanics.* Dover Publications, New York, 1988. 214

[66] Bellis, M., *The birth of fiber optics*, about.com, 2006. 216

[67] Hecht, J., *A short history of fibre optics*, sff.net/people.asp, 1999. 216